Developments for transactinide chemistry experiments behind the gas-filled separator TASCA

Dissertation
zur Erlangung des Grades
“Doktor der Naturwissenschaften”
im Promotionsfach Chemie

am Fachbereich Chemie, Pharmazie und Geowissenschaften
der
Johannes Gutenberg-Universität
in Mainz

vorgelegt von

Julia Even
geboren in Warburg

Mainz 2011

1. Berichterstatter:
2. Berichterstatter:

   Tag der mündlichen Prüfung: 13.12.2011

Hiermit versichere ich gemäß § 10 Abs. 3d der Promotionsordnung vom 24.07.2007, dass ich die jetzt als Dissertation vorgelegte Arbeit selbst angefertigt und alle benutzten Hilfsmittel (Literatur, Apparaturen, Material) in der Arbeit angegeben habe.

Mainz, den 14.11.2011 _____

Das Leben muss nicht leicht sein, wenn es nur inhaltsreich ist.

-Lise Meitner-

Zusammenfassung

Die vorliegende Arbeit befasst sich mit der Entwicklung von Experimenten hinter dem gasgefüllten Separator TASCA (TransActinide Separator and Chemistry Apparatus) zur Studie des chemischen Verhaltens der Transactinide.

Zum einen wurde die Möglichkeit der elektrochemischen Abscheidung kurzlebiger Isotope der Elemente Ruthenium und Osmium auf Goldelektroden im Hinblick auf ein Experiment mit Hassium untersucht. Aus der Literatur ist bekannt, dass bei der elektrochemischen Abscheidung einzelner Atome das Abscheidepotential signifikant vom Nernst Potential abweicht. Die Verschiebung des Potentials hängt von der Adsorptionsenthalpie des abzuscheidenden Elements auf dem Elektrodenmaterial ab. Wenn die Adsorption auf dem Elektrodenmaterial gegenüber der Adsorption auf einer Oberfläche aus dem abzuscheidenen Element bevorzugt ist, so verschiebt sich das Potential zu höheren Werten und man spricht von Unterpotentialabscheidung. Möglichkeiten automatisierter Elektrochemieexperimente hinter dem gas-gefüllten Separator TASCA wurden untersucht, um spätere Studien mit Transaktiniden durchführen zu können

Der zweite Teil der Arbeit befasst sich mit der In-situ-Synthese flüchtiger Carbonylkomplexe mit Kernreaktionsprodukten. Spaltprodukte des Uran-235 und Californium-249 wurden am TRIGA Mainz Reaktor erzeugt und in kohlenstoffmonoxidhaltiger Atmosphäre thermalisiert. Die gebildeten flüchtigen Komplexe der Übergangsmetalle konnten im Gasstrom transportiert werden. Desweiteren wurden kurzlebige Isotope der Elemente Wolfram, Rhenium, Osmium und Iridium am Linearbeschleuniger UNILAC am GSI Helmholtzzentrum für Schwerionenforschung, Darmstadt, in Kernfusionreaktionen erzeugt und im gasgefüllten Separator TASCA vom Ionenstrahl und den Transferprodukten getrennt. Die Kernfusionprodukte wurden in TASCAs Fokalebene in einer Rückstoßkammer in einer Kohlenstoffmonoxid-Helium Gasmischung thermalisiert. Die so erzeugten Carbonyl-Komplexe kurzlebiger Isotope wurden mittels kernsprektroskopischer Methoden identifiziert und zum Teil gaschromatographisch untersucht. Anhand des Vergleichs mit Monte Carlo Simulationen wurde die Adsorptionsenthalpien auf Siliziumdioxid- und Goldoberflächen bestimmt. Die Monte Carlo Simulationen basieren auf bereits existierenden Programmen und wurden den Geometrien der Chromatographiesäulen entsprechend modifiziert. Alle ermittelten Adorptionsenthalpien - auf Silziumoxid sowie auf Gold – sind typisch für Physisorption. In einigen Fällen wurde auch die thermische Stabilität der Carbonylkomplexe untersucht. Hierbei zeigte sich, dass ab Temperaturen von über 200 °C die Komplexe zerstört werden. Es wurde gezeigt, dass Carbonyl-Komplex-Chemie eine geeignete Methode ist, um die Transactinide Rutherfordium, Dubnium, Seaborgium, Bohrium, Hassium und Meitnerium zu untersuchen.

Bisher war es in der Gasphasenchemie der Transaktinide nur möglich, einfache, anorganische Verbindungen zu synthetisieren. Die Synthese von Transaktinid-Carbonyl-Komplexen würde den Zugang zu einer neuen Verbindungsklasse in der Transaktinidchemie ermöglichen und einen wichtigen Schritt hin zur metallorganischen Chemie der Transactinide bedeuten.

Desweiteren können Carbonyl-Komplexe genutzt werden, um Kernspektroskopieexperimente mit chemisch präparativen Methoden durchzuführen.

Abstract

Topic of this thesis is the development of experiments behind the gas-filled separator TASCA (TransActinide Separator and Chemistry Apparatus) to study the chemical properties of the transactinide elements.

In the first part of the thesis, the electrodepositions of short-lived isotopes of ruthenium and osmium on gold electrodes were studied as model experiments for hassium. From literature it is known that the deposition potential of single atoms differs significantly from the potential predicted by the Nernst equation. This shift of the potential depends on the adsorption enthalpy of the deposited element on the electrode material. If the adsorption on the electrode-material is favoured over the adsorption on a surface made of the same element as the deposited atom, the electrode potential is shifted to higher potentials. This phenomenon is called underpotential deposition

Possibilities to automatize an electro chemistry experiment behind the gas-filled separator were explored for later studies with transactinide elements.

The second part of this thesis is about the in-situ synthesis of transition-metal-carbonyl complexes with nuclear reaction products. Fission products of uranium-235 and californium-249 were produced at the TRIGA Mainz reactor and thermalized in a carbon-monoxide containing atmosphere. The formed volatile metal-carbonyl complexes could be transported in a gas-stream. Furthermore, short-lived isotopes of tungsten, rhenium, osmium, and iridium were synthesised at the linear accelerator UNILAC at GSI Helmholtzzentrum für Schwerionenforschung, Darmstadt. The recoiling fusion products were separated from the primary beam and the transfer products in the gas-filled separator TASCA. The fusion products were stopped in the focal plane of TASCA in a recoil transfer chamber. This chamber contained a carbon-monoxide – helium gas mixture. The formed metal-carbonyl complexes could be transported in a gas stream to various experimental setups.

All synthesised carbonyl complexes were identified by nuclear decay spectroscopy. Some complexes were studied with isothermal chromatography or thermochromatography methods. The chromatograms were compared with Monte Carlo Simulations to determine the adsorption enthalpy on silicon dioxide and on gold. These simulations based on existing codes, that were modified for the different geometries of the chromatography channels. All observed adsorption enthalpies (on silcon oxide as well as on gold) are typical for physisorption. Additionally, the thermalstability of some of the carbonyl complexes was studied. This showed that at temperatures above 200 °C the complexes start to decompose.

It was demonstrated that carbonyl-complex chemistry is a suitable method to study rutherfordium, dubnium, seaborgium, bohrium, hassium, and meitnerium. Until now, only very simple, thermally stable compounds have been synthesized in the gas-phase chemistry of the transactindes. With the synthesis of transactinide-carbonyl complexes a new compound class would be discovered. Transactinide chemistry would reach the border between inorganic and metallorganic chemistry.

Furthermore, the in-situ synthesised carbonyl complexes would allow nuclear spectroscopy studies under low background conditions making use of chemically prepared samples.

Content

1 Introduction....3
1.1 Production of superheavy elements....5
1.2 Chemistry of superheavy elements and relativistic effects....10
2 Chemistry experiments with single atoms....13
2.1 General aspects....13
2.2 TASCA – TransActinide Separator and Chemistry Apparatus....20
3 Underpotential Deposition....24
3.1 The phenomenon of underpotential deposition....25
3.1.1 Thermodynamic description of underpotential deposition....28
3.1.2 Kinetics of underpotential deposition....31
3.1.3 Determining the critical potential....34
3.2 Underpotential deposition experiments....37
3.2.1 The electrolysis cell....38
3.2.2 Electrodeposition studies of ruthenium....39
3.2.3 Electrodeposition of osmium on gold....43
3.3 The ELectro – CHemistry apparatus ELCH....49
3.4 Summary and discussion of the electrochemistry experiment....55
4 Metal-Carbonyl-Complex-Chemistry - Introduction....59
4.1 Metal-Carbonyl Complexes....61
4.2 Gas-chromatography....69
4.2.1 Adsorption....71
4.2.2 Monte Carlo Simulation of gas-chromatography experiments....74
4.2.3 Thermal decomposition of carbonyl-complexes....82
4.3 Experimental studies of metal-carbonyl complexes....84
4.3.1 Carbonyl chemistry experiments at the TRIGA Mainz reactor....84
4.3.1.1 Experiments with fission products of uranium-235....91
4.3.1.2 Experiments with fission products of californium-249....100
4.3.2 Experiments at Miss Piggy....114
4.3.3 Experiments at TASCA....116
4.3.3.1 Experiments with tungsten....125
4.3.3.2 Experiments with Osmium....137
4.3.3.3 Experiments with Iridium....147
4.3.3.4 Experiments with Rhenium....153
4.3.3.5 Experiments with Platinum....159
4.4 Summary and discussion of the experimental studies of transitionmetal-carbonyl complexes....161
4.5 Outlook and perspectives of transactinide-carbonyl chemistry and applications in nuclear physics....171
5 Résumé....178
Bibliography....180
Appendix....195
A) Source codes of the Monte Carlo Simulations....195
B) Parameters used in the simulations....219
Acknowledgements....229

1 Introduction

The most important tool for every chemist is the periodic table of the elements developed independently by Dimitrii Mendeleev and Lothar Meyer in 1869. The systematics in the periodic table provides a good foundation to predict the chemical properties of an element. The tables published by Mendeleev and Meyer predicted the existence of unknown elements and their chemical behaviour, which allowed to identify these elements in nature.

A total of 90 elements were found in nature with uranium being the heaviest one (except for ^{244}Pu, of which primordial traces were found by Hoffman et al. [1] in bastnasite). All heavier elements are human made.

The first transuranium element discovered was element 93 (neptunium) [2], followed by the discovery of element 94 (plutonium) in 1940 [3]. The elements actinium, thorium, protactinium, uranium along with the first transuranium elements were first placed in the periodic table as transition metals. By 1944, Seaborg and his coworkers knew a lot about the chemical behaviour of plutonium and started their first attempts to produce and identify the elements with atomic numbers 95 and 96 [4], [5]. However, these elements showed a non-transition metal-like behaviour. Chemical separations based on treating elements 95 and 96 as trivalent lanthanide homologs succeeded in separating and identifying these new elements, subsequently named americium and curium, respectively. Based on these results, Seaborg published the actinide hypothesis. He proposed that the 14 elements following actinium (atomic number 89) should be placed in the periodic table of elements as a *5f* transition series under the lanthanide *4f* transition series. [6] Heavier actinides, like their lanthanide counterparts, would be extremely difficult to oxidize beyond their trivalent oxidation state. In the following years, heavier actinides were discovered and their chemical behaviour agreed with the predictions made based on the actinide concept. [7],[8]

Since the late 1960´s, the transactinide elements 104 (rutherfordium), 105 (dubnium), 106 (seaborgium), 107 (bohrium), 108 (hassium), 109 (meitnerium), 110 (darmstadtium), 111 (roentgenium), 112 (copernicium), 113, 114, 115, 116 , 117 and 118 were discovered in nuclear fusion reactions, while 113, 115, 117 and 118 have not been officially accepted by the International Union Of Pure And Applied Chemistry IUPAC. The systematics in the periodic table suggests

placing them in groups 4−18, see Figure 1. Currently, we know very little about the chemical behaviour of these elements (see [9],[10],[11]). As the cross sections of the fusion reactions are low and the isotopes are short-lived, experiments with these elements are very challenging. Rutherfordium, dubnium, and seaborgium have been studied in ion-exchange experiments and as thermally stable inorganic compound in the gas-phase. Bohrium has only been studied in the gas-phase as bohrium oxochloride and of hassium, only the tetroxide has been studied. Copernicium and element 114 have only been studied in their elemental state in the adsorption on gold. The relativistic effects influence the chemistry the transactinides. Due to the large proton number, the electrons are accelerated, the *s* and $p_{1/2}$ orbitals are contracted and shield the nucleus, which leads to expansion of the *d* and *f* orbitals. Classical quantum mechanical description is not sufficient, to describe the chemical behaviour of these heavy elements and relativistic effects have to be taken into account. Therefore, studying the chemical behaviour of these elements is interesting. However, due to the half-lives and production rates of the transactinides it is very challenging.

The focus of this thesis is the development of new chemistry experiments to study the transactinides. It includes developments for liquid phase chemistry experiments as well as the synthesis of a new compound class in the gas phase.

1																	18
1 H	2											13	14	15	16	17	2 He
3 Li	4 Be											5 B	6 C	7 N	8 O	9 F	10 Ne
11 Na	12 Mg	3	4	5	6	7	8	9	10	11	12	13 Al	14 Si	15 P	16 S	17 Cl	18 Ar
19 K	20 Ca	21 Sc	22 Ti	23 V	24 Cr	25 Mn	26 Fe	27 Co	28 Ni	29 Cu	30 Zn	31 Ga	32 Ge	33 As	34 Se	35 Br	36 Kr
37 Rb	38 Sr	39 Y	40 Zr	41 Nb	42 Mo	43 Tc	44 Ru	45 Rh	46 Pd	47 Ag	48 Cd	49 In	50 Sn	51 Sb	52 Te	53 I	54 Xe
55 Cs	56 Ba	57+* La	72 Hf	73 Ta	74 W	75 Re	76 Os	77 Ir	78 Pt	79 Au	80 Hg	81 Tl	82 Pb	83 Bi	84 Po	85 At	86 Rn
87 Fr	88 Ra	89+" Ac	104 Rf	105 Db	106 Sg	107 Bh	108 Hs	109 Mt	110 Ds	111 Rg	112 Cn	113 ---	114 ---	115 ---	116 ---	117 ---	118 ---

*	58 Ce	59 Pr	60 Nd	61 Pm	62 Sm	63 Eu	64 Gd	65 Tb	66 Dy	67 Ho	68 Er	69 Tm	70 Yb	71 Lu
"	90 Th	91 Pa	92 U	93 Np	94 Pu	95 Am	96 Cm	97 Bk	98 Cf	99 Es	100 Fm	101 Md	102 No	103 Lr

Figure 1: Periodic table of the elements. The actinides are marked with blue colour, the transactinides are marked yellow. The transactinide elements, which are lowered, have not been studied in chemistry experiments until now.

1.1 Production of superheavy elements

For scientists working in the field of superheavy elements (SHE), the low production rate and relatively short half-lives of these elements are big challenges. Superheavy elements are the elements heavier than Z=103. The stability of their nuclei can only be explained with shell stabilization effects. According to the liquid-drop model, these nuclei could not exist. Superheavy elements are also the transactinides. While "superheavy elements" is mainly used in physics terms and "transactinides" is the chemical name. Transactinides can only be produced in nuclear fusion reactions with relatively low cross sections. In this type of reaction, a target is irradiated with a high intensity heavy-ion beam. The beam energy has to be high enough to overcome the Coulomb barrier between the target and the projectile nuclei. When a projectile nucleus hits a target nucleus, there are three possible cases in competition with each other:

i) elastic scattering – the nuclei will not fuse

ii) deep inelastic scattering or quasi-fission, the nuclei touch each other and transfer some nucleons, but they do not form a mononucleus;

iii) the two nuclei hit central to each other, they undergo fusion and form a compound nucleus. This compound nucleus is highly excited and has two main possibilities to de-excite: neutron evaporation or fission.

We distinguish between hot and cold fusion reactions. [12], [13], [14] Hot fusion reactions are very asymmetric reactions characterized by excitation energies of 40-50 MeV. Light projectiles, e.g., oxygen, neon, magnesium, or chlorine, are used to bombard actinide targets. The compound nucleus typically de-excites by fission, however, there is furthermore the possibility to de-excite by the evaporation of four or five neutrons. Cold fusion reactions are characterized by excitation energies of 10-15 MeV, they are more symmetric reactions with projectiles like iron, zinc or nickel and targets like bismuth or lead. The compound nucleus undergoes fission or evaporates 1-2 neutrons. Figure 2 shows the nuclear chart of the superheavy elements. The isotopes synthesised in cold fusion reactions are surrounded with the blue dotted line. The ones synthesised in hot fusion reactions are surrounded with a red dotted line and the ones synthesised in the "warm" ^{48}Ca-induced reactions are surrounded by the green dotted line.

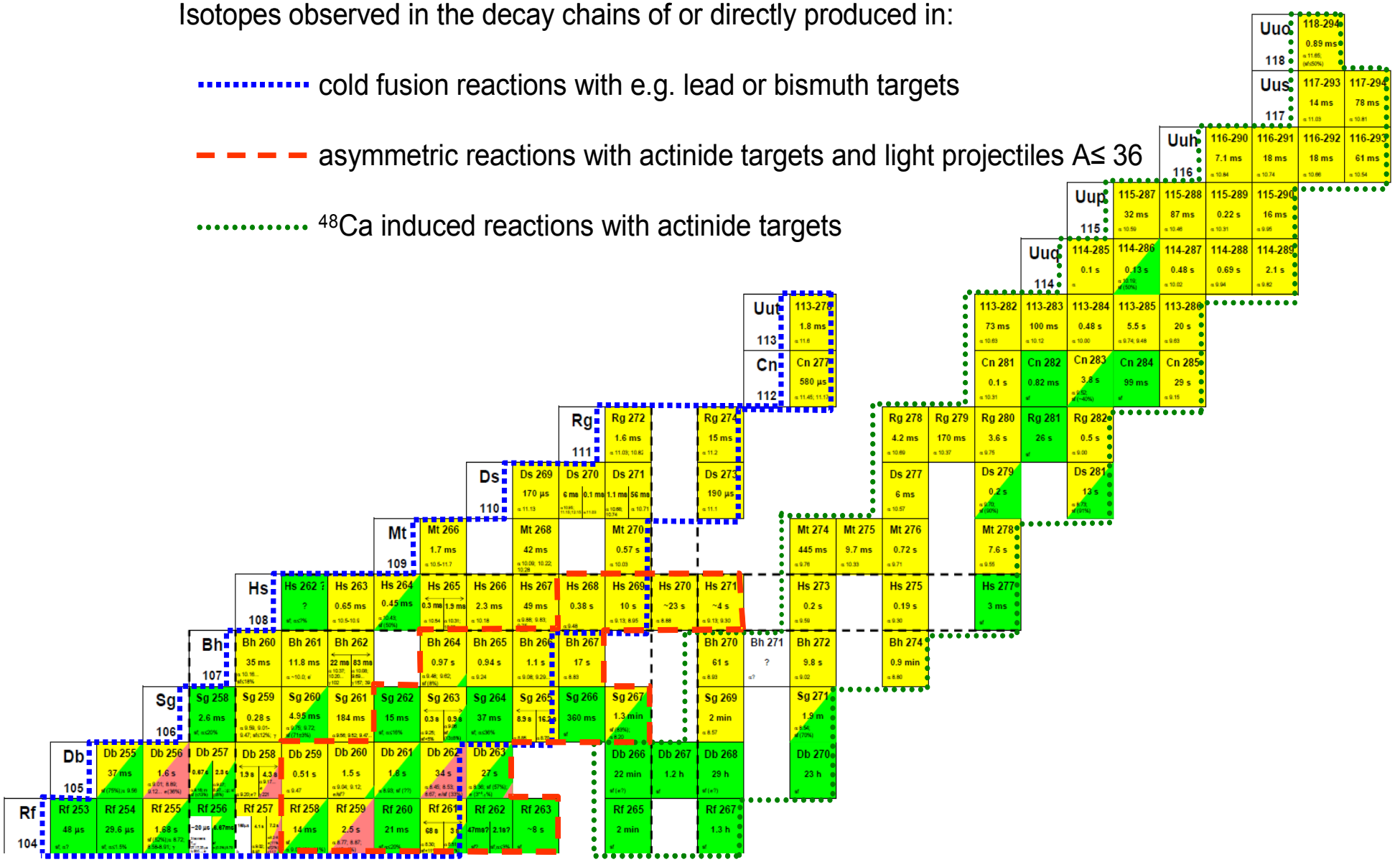

Figure 2: Nuclear chart of the superheavy elements.

The cross section for formation of evaporation residues σ_{EVR} of nuclear fusion reactions can be described with equation (1.1-1). [15], [16], [17]

$$\sigma_{EVR} = \sigma_{capture} \cdot p^{hindrance} \cdot p^{shape} \cdot W^{survival} \tag{1.1-1}$$

$\sigma_{capture}$ is the capture cross section of two nuclei for an unhindered system producing a nonfissioning EVR, $p^{hindrance}$ is the hindrance factor, p^{shape} the shape factor and $W^{survival}$ the survival probability.

The capture cross-section depends on the reduced DeBroglie matter wave length $\lambda\!\!\!^{-}$ and the upper value for the orbital angular momentum l_{limit},[15]

$$\sigma_{capture} = \pi \cdot \lambda\!\!\!^{-2} \cdot l_{limit}^2 \tag{1.1-2}$$

The fused system is very excited, so it has the possibility to de-excite by, e.g., neutron evaporation or fission. $W^{survival}$ is the probability that the system undergoes neutron evaporation instead of fission and the compound nucleus survives. [17]

$$W^{survival} = \prod_{i=1}^{v} \frac{\Gamma_n}{\Gamma_n + \Gamma_f} \approx \frac{1}{1 + \Gamma_n / \Gamma_f} \tag{1.1-3}$$

$W^{survival}$ depends on the partial probabilities Γ_n and Γ_f, representing de-excitation by either neutron evaporation (survival) or by fission (destruction), respectively.

The ratio Γ_n / Γ_f depends on the excitation energie E^*, the temperature T, the neutron evaporation energy B_n, and the fission barrier B_f. [18],[17]

$$\frac{\Gamma_n}{\Gamma_f} = K \cdot \frac{e^{(E^* - B_n)/T}}{e^{(E^* - B_f)/T}} = K \cdot e^{-(B_n - B_f)/T} \tag{1.1-4}$$

K is defined by the nuclear temperature T and the mass number A of the compound system. [15]

$$K = 0.14/MeV \cdot A^{2/3} \cdot T \tag{1.1-5}$$

With only $\sigma_{capture}$ and $W^{survival}$, a correct description of the synthesis of the elements 93-106 in fusion reactions induced by α-particles or light ions on actinide targets was possible. These reaction cross-sections are between 10 nbarn and several 100 nbarn.

The excitation energies in cold fusion reactions are lower. Using the model to predict cross-sections for the production of SHE in symmetric reactions (with $E_x \sim 0$ and $B_f > B_n$) yields cross-sections around 100 mbarn. However, the experiments show that the cross-sections are many orders of magnitude lower. Processes like deep-inelastic reactions and quasi-fission, which compete with fusion, were discovered helping to explain the low cross sections of these fusion reactions. Investigating relatively symmetric reactions of Pb or Bi targets and projectiles with Z=20-30 to produce the elements Z = 102-112 showed that the cross-section decreases exponentially with increasing Z of the projectile. [17]

This can be explained by the huge dynamical hindrance of the transition of the two-body system at the point of nuclear capture towards the formation of a compound nucleus. The fusion hindrance is described with different models. In the diffusion model, the hindrance $P^{hindrance}$ is defined by [19], [20]

$$P^{hindrance} = \frac{1}{2} \cdot \left(1 - erf \sqrt{\frac{\bar{B}}{k_B \cdot T}} \right) \tag{1.1-6}$$

in which $\bar{B}$ is the barrier height averaged over the isotopic distribution induced by the neutron flow.

Armbruster suggested to split the factor in a hindrance and a shape factor. [17] He describes the factor $p^{hindrance}$ by a a fluctuation–dissipation model [17]

$$p^{hindrance} = C \cdot e^{-(0.5/\log e) \cdot (z - z_0)} \tag{1.1-7}$$

z is the distance between the two potential centers of the fused system. z_0 is the the distance, if the nuclei are spherical.[21]. Armburster furthermore introduced the shape factor p^{shape}. This factor describes the dependence of the fission probabilities on the shape of the decaying nuclei. The cross sections of the ^{48}Ca induced reactions to produce the elements Z=112-118 [22], [23] are higher than the exponential extrapolation predicts (see Figure 3). Armbruster [17] explains this with the assumption that these nuclei are oblate deformed resulting in reduced fission probabilities. All

nuclei have to overcome a prolate saddle point to fission. Oblate nuclei also have to pass over a prolate saddle point which leads to a fission hindrance and a gain factor $p^{shape}=10$. Prolate nuclei are less hindered to pass over a prolate saddle point towards fission. For these nuclei, Armburster suggest to set $p^{shape}=1$. [17]

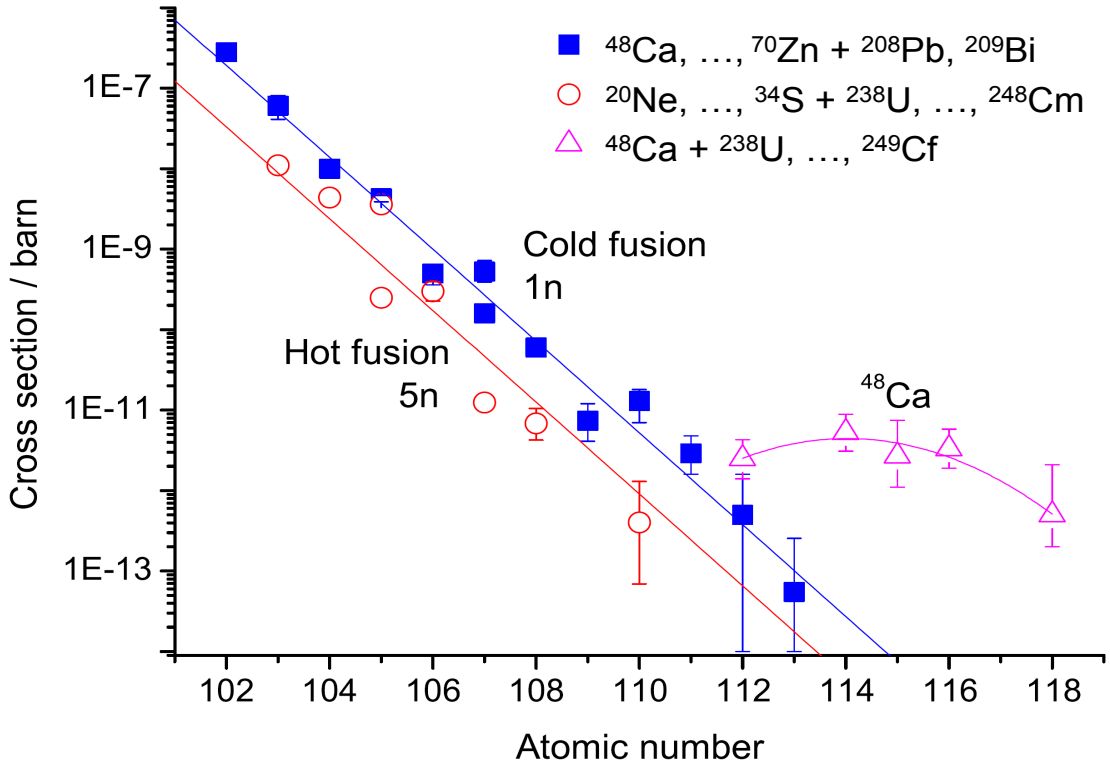

Figure 3:Experimental cross sections for the formation of nuclei with Z ≥102 for the 1n evaporation channel of cold fusion reactions, the 5n channel of hot fusion reactions, and the 4n channel of the fusion reactions with ^{48}Ca + actinide targets. The curves are drawn to guide the eye.[24]

According to the liquid drop model, all elements with Z > 100 would have spontanous fission half-lives of less then one second [25], as the surface tension surface tension is very small or even not existing. However, experimentally measured half-lives are several orders of magnitude higher. This can be explained by nuclear shell effects. [26],[27]. For a spherical nucleus the ground state shows for example an increased binding energy of up to 10 MeV due to shell effects compared to the liquid drop model. The stronger binding energy results in a higher fission barrier.

1.2 Chemistry of superheavy elements and relativistic effects

The transactinides are the elements following the actinides in the periodic table. In the actinide series the 5f-shell is filled. The first transactinides (104 to 112) are supposed to be transition metals, as their chemical behaviour is characterized by filling of the 6d-orbitals. In the following elements 113 to 118, the 7p orbitals are filled. Element 118, as a heavier homologue of radon, should be an inert gas.

With the increasing number of protons in the nuclei of the heavy elements, the attraction of electrons to the core becomes stronger. The electrons move faster and their mass *m* increases

$$m = \frac{m_0}{\sqrt{1-\left(\frac{v}{c}\right)^2}} \qquad (1.2\text{-}1)$$

where m_0 is the rest mass, v is the speed of the electron and c is the speed of light. The effective Bohr radius a_B depends on the mass of the electron.

$$a_B = \frac{\hbar^2}{m \cdot c^2} = a_B^0 \cdot \sqrt{1-\left(\frac{v}{c}\right)^2} \qquad (1.2\text{-}2)$$

where $\hbar$ is the reduced Planck constant and a_B^0 the non-relativistic Bohr radius.

This effect leads to the shrinking and stabilisation of the spherical s and the $p_{1/2}$ orbitals and is called direct relativistic effect. The 7s orbital of dubnium, for example, is 25% relativistically contracted and energetically stabilized. Another example of the direct relativistic effect is visible in group 11; the ground state of gold is (d^9s^1), while the ground state of its heavier homologue element 111 is (d^8s^2) due to the stabilisation of the s orbital. [9], [11], [28]

The second, so-called indirect- relativistic effect is a consequence of the direct relativistic effect: the contraction of the s and $p_{1/2}$ orbitals leads to a stronger shielding of the nuclear charge and leads to a destabilisation and expansion of the $p_{3/2}$, d and f orbitals. The non-radially symmetric orbitals which have no electron density at the core, are energetically destabilized by this shielding and

expand.

The third relativistic effect is the spin-orbit splitting. The levels with a non-zero azimutal quantum number l (the p, d, and f orbitals) split into sublevels with the total angular momentum quantum number $j = l \pm ½$.

The spin-orbit splitting increases with decreasing number of sub shells –i.e. the $np_{1/2} - np_{3/2}$ splitting is larger than the $nd_{3/2}$ - $nd_{5/2}$ splitting, and both are larger than the $nf_{5/2} - nf_{7/2}$ splitting. The magnitude of the spin-orbit splitting in transactinides is comparable to the strength of chemical bonds. [11], [28]

Transactinide chemists try to find hints of these relativistic effects in their studies of these heavy elements and investigate whether the trends in the periodical table are still valid for these elements.

Until now, only very simple chemical systems with the transactinides were studied. The elements rutherfordium, dubnium, and seaborgium were studied in the aqueous phase and in the gas phase. Rutherfordium and dubnium seemed in first experiments to fit into the trends established by the lighter homologues in their groups. However, further studies showed that due to relativistic effects these trends were broken. In group 4 and group 5 inversions of trends were observed when going from the 5d to the 6d element. [9], [10] In experiments studying the fluoride complexation of rutherfordium, rutherfordium showed more similarities with its pseudo-homologue thorium than with its homologous zirconium and hafnium. [29] In gas-phase chemistry experiments, a higher volatility of rutherfordium tetrachloride was observed than compared to the hafnium tetrachloride. This was seen as evidence for relativistic effects. [30] Dubnium showed a none-tantalum like behaviour in chloride complexation studies, and behaved more like protactinium. [31] Furthermore, it could be shown that due to relativistic effects, the $DbBr_5$ is more volatile than the bromide complexes of the lighter homologues. [32] The observed sequence in volatility $DbBr_5 > NbBr_5 > TaBr_5$ is in agreement with theoretical calculations which take the relativistic effects into account. While in group six the extrapolated trends could be proven in the seaborgium chemistry experiments and seaborgium was claimed to be “oddly ordinary”.[33] Seaborgium forms like its lighter homologoues molybdenum and tungsten anionic or neutral complexes in aqueous solution. [34],[35] Furthermore, it was measured in gas-phase chemistry experiments that SgO_2Cl_2 is less volatile than WO_2Cl_2. [36]

Bohrium and hassium only have been studied in the gas phase. BhO_3Cl was synthesized and its adsorption on quartz was studied. A trend of decreasing volatility $TcO_3Cl > ReO_3Cl > BhO_3Cl$ was measured. [37]

In several experiments it could be proven that hassium forms, volatile tetroxide like its lighter homologues ruthenium and osmium. HsO_4 is slightly less volatile than OsO_4. [38] In a different experiment, it was shown that HsO_4 forms the sodium hassate ($Na_2[HsO_4(OH_2)]$) in a reaction with sodium hydroxide (NaOH). [39]

Pitzer predicted that due to the relativistic effects the elements copernicium (112), 114, and 118 might be inert gases. [40] Later on, it could be demonstrated in experiments that copernicium [41] and 114 [42],[43] are volatile metals that interact with a gold surface.

2 Chemistry experiments with single atoms

2.1 General aspects

All transactinide experiments can only be conducted under one-atom-at-a-time conditions due to the low production rates from a few atoms per hours down to a few atoms per week or even month. Furthermore, their half-lives are relatively short. The half-lives of the isotopes suitable for chemistry experiments are in the range of seconds.

In “classical” chemistry experiments, the amount of the species under investigation is in the range of mol (with 1 mol = $6.022 \cdot 10^{23}$). For reversible reactions, the law of mass action gives the ratio K as the chemical activities of products to the chemical activity of educts at the equilibrium of the chemical reaction. The value K should be independent from the amount of reactants. Generally it can be written as

$$K = \prod_{i=1}^{n} a_i^{\nu_i} \qquad (2.1\text{-}1)$$

in which a_i are the chemical activities of the reactants and ν_i are the stoichiometric coefficients, which are negative for educts and positive for products.

However, in case of single atom chemistry, the law of mass action fails. The reactant can only be in the one or in the other phase so, an equilibrium constant K is no longer defined. Guillaumont [44] demonstrated that using the ratio of probabilities to find the reactant in the one or in the other state is a valid substitution to the use of chemical activities. Therefore, it is necessary to perform several experiments to estimate the probabilities to find the species in a specific state. Ideally, the experiments are designed such the atom is exchanged between two phases often enough to obtain statistically significant probabilities. Chromatographic methods are therefore well suited to study superheavy elements.

Due to the short half-lives and low production rates of the transactinides, chemistry experiments

with these elements are a great challenge. Each experiment has to be carefully tested and optimized using the lighter homologues under comparable conditions – this means also the homologues have to be studied under carrier free conditions. The following steps are essential for every online chemistry experiment:

- Production of the element
- Fast transport to the chemistry setup and in some cases, preseparation from unwanted nuclear reaction byproducts
- Transfer into the chemistry setup
- The chemistry experiment itself
- Preparation of samples for decay spectrometry and identification of the element by detection of its nuclear decay.

As the experiment should be as fast as possible, it is preferred to reduce the number of steps by combination of these steps. Ideally, these processes are fully automated.

Production of the elements of interest:

As described in chapter 1.1, the transactinides have to be produced in heavy-ion fusion reactions. The choice of nuclear reaction is a first critical decision, which is based on features such as production rate and half-lives of the isotopes. The cross-sections of hot fusion reactions are in most cases lower than the ones of cold fusion reactions leading to the same element, but the isotopes produced in hot fusion reactions are more neutron rich than those produced in cold fusion reactions, which leads to longer half-lives (see Figure 2 chapter 1.1). In most cases, hot fusion reactions or ^{48}Ca-induced fusion reactions with actinide targets are chosen.

The production of the lighter homologues in tracer amounts for test experiments is a less crucial point. For test experiments with 4d elements, fission products can be used in many cases. These can be delivered by a fission source such as ^{252}Cf - for example Miss Piggy [45] at the university of Bern, or by placing fissile material in a thermal neutron beam, e.g., in an nuclear reactor. This is, e.g., a common technique at the TRIGA Mainz reactor [46]. The choice of the target material depends on which isotopes should be studied. At the TRIGA Mainz reactor, ^{235}U, ^{239}Pu, and ^{249}Cf are available as targets. Figure 4 shows the independent mass yields in the neutron-induced fission of ^{235}U and ^{249}Cf.

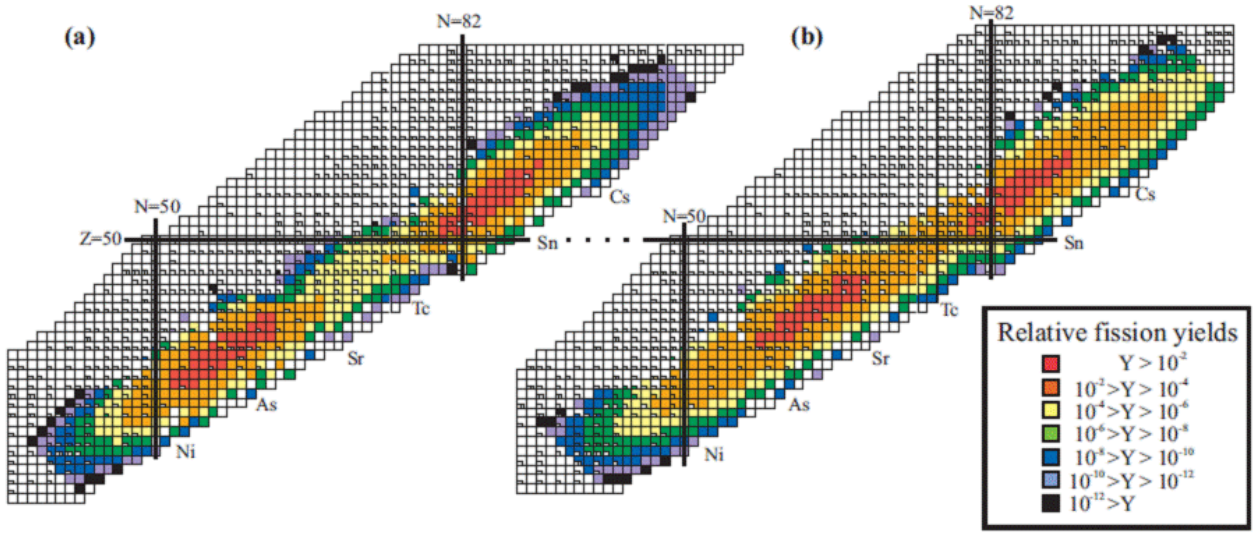

Figure 4: Yields of the thermal neutron induced fission of a) ^{235}U and b) ^{249}Cf. Figure taken from[47].

Furthermore, a radon emitting source can be used to produce lead and bismuth, the lighter homologues of the elements Z=114 and 115. [48] Of course, the lighter homologues can also be synthesized in nuclear fusion reactions.

Fast transport to the chemistry setup and preseparation from unwanted nuclear reaction by-products

An important factor in SHE chemistry experiments is a fast transport of the nuclear reaction products from the target to the chemistry devices. An aerosol particle gas-jet is a well established technique to transport isotopes with half-lives of a few seconds.[49], [50] In this technique, the recoiling ions are thermalized in a gas-filled chamber. The chamber is flushed with a carrier gas seeded with aerosol particles (order of 10^7 particles per cm^3). Common aerosols are, e.g., potassium chloride, carbon, or molybdenum oxide. Non-volatile fusion products attach onto these particles and are transported with the transport gas to the collection site. A drawback of this technique is that unwanted byproducts of the nuclear reaction are not suppressed. For experiments using nuclear fission products of the light-mass branch, the target can be covered with a thin aluminum foil to withhold the heavier fission products with the lower recoil energies, reducing the background enormously.

One further problem in accelerator-based nuclear reaction experiments is the plasma created by the intense projectile beam behind the target, which destroys the aerosol particles. This reduces the

gas jet yield dramatically at high beam intensities. [51]

For selected chemical systems, these drawbacks can be circumvented by working without aerosol particles and instead adding in-situ reactive gas to the carrier gas to produce volatile compounds – like oxygen in the case of OsO_4 or HsO_4 [52] – which can be transported in the gas stream. The technique of the reactive gas mixtures provides a selective, chemical separation from the unwanted byproducts and the transport itself becomes part of the chemistry experiment.

Volatile elements like Rn, Hg, Cn, and element 114 [41],[43],[42] can be transported in a pure inert-gas stream without adding any reactive gas or clusters and separated by the transportation process from the byproducts. However, only elements that are either volatile in their elemental state or form simple inorganic compounds of high thermal stability and volatility, can be studied with this technique. It is not possible in nuclear fusion reactions to introduce organic compounds directly in the recoil chamber and to transport the fusion products as, e.g., organometallic compounds, as these are easily destroyed by the plasma behind the target. [53]

To overcome these problems, nuclear fusion experiments can take advantage of physical preseparation. [54] In a gas-filled recoil separator, the fusion products and the transfer products as well as the main beam can be separated according to their different magnetic rigidities. The group at the Berkeley Gas-filled Separator (BGS) was the first who developed a so-called Recoil Transfer Chamber (RTC) for coupling a physical preseparator and a chemistry setup connected via a gas jet. [55] In the last years, the combination of a physical preseparator and a gas jet system was also established at RIKEN in Wako, Japan, at the GAs-filled Recoil Ion Separator GARIS [56], at the Dubna Gas-Filled Recoil Separator DGFRS at the Flerov Laboratory of Nuclear Reactions in Dubna, Russia [57], and at the TransActinide Separator and Chemistry Apparatus TASCA at GSI. [58] TASCA itself will be described in detail in the following chapter.

Transfer into the chemistry setup, the chemistry experiment itself, preparation of samples for decay spectrometry

In case of liquid phase chemistry, a potassium-chloride gas jet is usually used to transport the nuclear reaction products. The aerosol particles are collected by the impaction technique. The gas-jet expands into a vacuum chamber, where the transport gas is removed by the pump and the heavier aerosol particles impact onto the wall opposite to the gas-jet inlet. Afterwards the potassium chloride

and with it the transported isotopes can be dissolved in an aqueous solution and the chemistry experiments, for example liquid-liquid extraction experiments or ion-exchange chromatography can be performed. Alternatively, the gas-jet can be mixed directly in a degasser with the liquid solution [59], for which, however, relatively large amounts of liquid are necessary. The solvent fractions have to be collected and prepared for radioactive decay spectroscopy.

In case of γ-decaying isotopes of the lighter homologues, the samples can be placed directly in front of a γ-ray detector. In case of a transactinide experiment, samples which are suitable for α-spectroscopy have to be prepared. One approach relies on mixing the effluents with liquid scintillator and detection with a scintillation detection system. The advantage of this method is the speed, however, the low energy resolution requires zero-background conditions. The detection system must be sensitive enough to detect a single event. Another possibility is to evaporate the solution and place the samples in front of a silicon semiconductor α-detector. This method is more time consuming than the liquid scintillation method, but the energy resolution is higher and the background problems are a less crucial factor.

Liquid-phase chemistry experiments have been conducted in manual setups (e.g. [60], [61]). There have also been partially automated setups, e.g., the Automated Rapid Chemistry Apparatus ARCA [62], in which the aerosol separation and ion exchange chromatography is automated, but the sample preparation and transfer to the detection setup are still manual operations. An advanced version of the ARCA is the fully Automated Ion-exchange separation apparatus coupled with the Detection system for Alpha spectroscopy AIDA, in which also the sample preparation and transfer to the detection system is automatized. [63] The liquid-liquid extraction technique has been fully automated with the Short-lived Isotopes Studied by the AKufve technique SISAK. [64] The advantage of SISAK compared to ARCA and AIDA is that it is faster and continuous. The drawback of the SISAK technique is the huge amount of solvent that is needed and with it the upcoming problems for decay spectroscopy. ARCA and AIDA could be used without physical preseparation (see e.g. [34], [65]), but SISAK-experiments with the transactinides require physical preseparation. [66]

In the case of gas-phase experiments, the fastest method is to produce the volatile compound in-situ in the recoil chamber and transport it in a pure gas stream to a collection or chemistry setup. One possiblity is to adsorb the species of interest on a surface. In case of studying physisorption at low temperatures or chemisorption in the cold on metal, the surface can be the detector itself. [67] If

chemisorption on a reactive surface is studied, this surface needs to be placed in front of a detector [39]. In both cases, the chemistry and sample preparation for the decay spectroscopy occurs in one single step.

The method of adsorption on the detector-surface is used in the the Cryo-Thermochromatographic Separator CTS [67] and its following optimized versions Cryo-On-Line Detector COLD [68] and the Cryo Online Multidetector for Physics And Chemistry of the Transactinides COMPACT. [24] The technique of a reactive adsorbing surface in front of α-detectors was realized with the Continuously working Arrangement for cLusterLess transport of InSiTu produced volatile Oxides CALLISTO. [39]

However, this method is not usable for every chemistry system, specifically, if corrosive reagents are needed. If it is not possible to synthesize the compound of interest in the reaction chamber or the compound of interest is not transportable in a gas-stream at room temperature, the recoil ions have to be transported with an aerosol jet. The aerosol particles have to be collected, e.g., on a quartz wool plug and then the reaction agent has to be added and the compound volatilized. If it is not possible to place the adsorbate surface close to a detector, isothermal chromatography technique is used. The volatile compound has to fly through a tube of the adsorbing surface and the molecules of interest, which leave the tube have to be detected. In experiments with the lighter homologues, the compound can easily be trapped on a filter (e.g., charcoal) which is placed in front of a γ-detector. For a transactinide experiment, samples for α-spectrometry are prepared often using the reclustering techniques. [69] After leaving the tube, aerosol clusters are added to the gas steam. The compounds of interest adsorb on the clusters. These clusters can be collected by the impaction technique and the samples can be placed in front of the detector. This procedure has been automatized in the On-Line Gas chemistry Apparatus OLGA[69], which was used for isothermal chromatography.

For every experiment, the goal is to have the highest possible efficiency; this depends on:

- The nuclear reaction
- Preseparation
- The transport the isotopes
- The chemistry experiment itself
- The detection of the nuclear decay .

In this thesis, the possibilities of an electrodeposition experiment for hassium were examined. Electrodepostion has to be conducted from the liquid phase onto a metal surface. The technical advantage of electrodeposition would be that the chemistry procedure is combined with the sample preparation.

The second part of the thesis focuses on the synthesis and studies of volatile metal-carbonyl complexes. The synthesis of these compounds can be conducted in a Recoil Transfer Chamber (RTC). The chemistry and the transport are combined by this method. The carbonyl complexes can be directly adsorbed on a detector surface and are suitable for thermochromatography studies. With carbonyl chemistry, a new compound class of the transactinides is being discovered and it will open the door for organometallic chemistry of the transactinides.

2.2 TASCA – TransActinide Separator and Chemistry Apparatus

The gas-filled separator TASCA [70], [71] was constructed at the GSI Helmholtzzentrum für Schwerionenforschung, Darmstadt (GSI). It is designed for physics experiments as well as for chemistry experiments, which need physical preseparation [54], [53] of nuclear fusion products from transfer products and beam particles. In TASCA, the ions are separated by their physical properties – in this case their magnetic rigidity – before they are guided to the detection or chemistry device. The magnetic configuration is a classical Dipole Quadrupole Quadrupole DQQ configuration. The design of TASCA was optimized for the study of ^{48}Ca-induced fusion reactions with actinide targets.

TASCA, shown in Figure 5, is set up at the X-branch at the UNIversal Linear ACcelerator (UNILAC) at GSI. It can be filled with ~0.30-2.00 mbar He or a He/H_2-mixture. To allow to work with high beam intensities, there is no vacuum window between TASCA and the UNILAC. The pressure difference between TASCA (~1 mbar) and the UNILAC (10^{-7} mbar) is maintained by differential pumping with one roots pump and two turbo pumps. The beam intensity is only limited by the UNILAC itself or by the target.

The beam from the UNILAC passes the differential pumping section of TASCA and impinges on the target wheel. Depending on the target material, there is a choice between three different target wheel sizes. The target wheel rotation is synchronized to the beam macro structure of the UNILAC beam (for main beam users the pulse frequency is 50 Hz, the macropulse length is 5 ms). The advantage of a rotating target wheel compared to a stationary target is a larger area for irradiation and less thermal stress for the target. One beam pulse only irradiates one target segment, so that during this time, the other segments can cool down.

The ions recoiling from the target interact with the filling gas and are brought to an average charge state q_{ave} [72].

$$q_{ave} \propto v \cdot \sqrt[3]{Z} \qquad (2.2\text{-}1)$$

v is the velocity of the recoiling ion, which depends on the beam energy, nuclear reaction, and

target thickness, and Z is the proton number of the ion.

Inside the dipole magnet of TASCA, the fusion products are separated from the primary beam and the transfer products according to their magnetic rigidity. [72]

$$B \cdot \rho = \frac{m \cdot v}{q_{ave} \cdot e_0} \qquad (2.2\text{-}2)$$

where B is the magnetic flux [T] and ρ gyroradius of the ion due to the magnetic field [m], m is the mass of the ion [kg], v is the velocity of the ion [m/s], q_{ave} is the average charge state and e_0 is the elementary charge [C].

The separated products are focused by the two quadrupole magnets into the focal plane. TASCA can be operated in two different ion-optical modes – the High Transmission Mode HTM (magnetic configuration = DQ_hQ_v, where the indices refer to vertical (v) and horizontal (h) focusing) and the Small Image Mode SIM, (DQ_vQ_h) [73]. In the HTM, the transmission through TASCA is higher than in SIM. The advantage of the SIM compared to the HTM is the much smaller image size in the focal plane. Semchenkov [73] simulated for the reaction $^{238}U(^{48}Ca,3n)^{283}112$ an image size of $(2 \cdot 12)$ cm^2 and a transmission for 112 of 54 % in the HTM. For the SIM he calculated an image size of $(3 \cdot 3)$ cm^2 and a transmission of 36 %. The transmission strongly depends on the nuclear reaction and on the target thickness.

In the focal plane, various detector systems can be installed like the focal plane detector for the HTM [74] or TASISpec [75] for the SIM.

For chemistry experiments, a RTC is installed right behind the focal plane as an interface between the preseparator and the chemistry setups. Different types of RTCs exist – one for the SIM and two for the HTM. [58] The evaporation residues pass the RTC window at the end of TASCA and are thermalized in the RTC. From here, the atoms can be transported with a gas jet to chemistry or detection setups.

In order to slow down the recoiling ions, Mylar degrader foils can be installed in front of the RTC window. As window material, Mylar foil was chosen. The thickness of the foil depends on the kinetic energy of the recoil ions and is tailored to the respective range in Mylar. Furthermore, the recoiling ions are slowed down in the RTC window. There are specific requirements on the window material. It has to be thin enough that the ions can pass through but it also hat to withstand the

pressure difference between TASCA and the RTC.

Because of this enormous pressure on the large HTM window, two 1.0-mm wide supporting bars were implemented in the flange. For both types of RTC (SIM and HTM) a grid with a honeycomb structure with 0.3 mm wide spokes and a hole pitch of 2.9 mm is installed to support the window foil. This grid was made from hard Stainless Steel by laser cutting. Its geometrical transparency is 80%. To minimize losses due to non-parallel trajectories of the evaporation residues, the grid has a thickness of only 1 mm. Supported by this grid, Mylar foils with thicknesses larger than ~1.3 µm are able to withstand the pressure difference between TASCA and the RTC. For thinner windows, a 20-µm thick Ni mesh made by electro-etching with square $(0.3 \cdot 0.3)$ mm^2 holes and 20 µm wide spokes can be placed on top of the metal grid. It has a transparency of around 90%.

Depending on the isotope of interest, the HTM or SIM RTC is chosen. For relatively long-lived isotopes, the HTM would be preferred, due to the higher transmission in TASCA. For relatively short-lived isotopes (with half-lives of only a few seconds or less) the SIM RTC would be the RTC of choice, as it can be faster flushed out by the gas stream, which reduces decay losses.

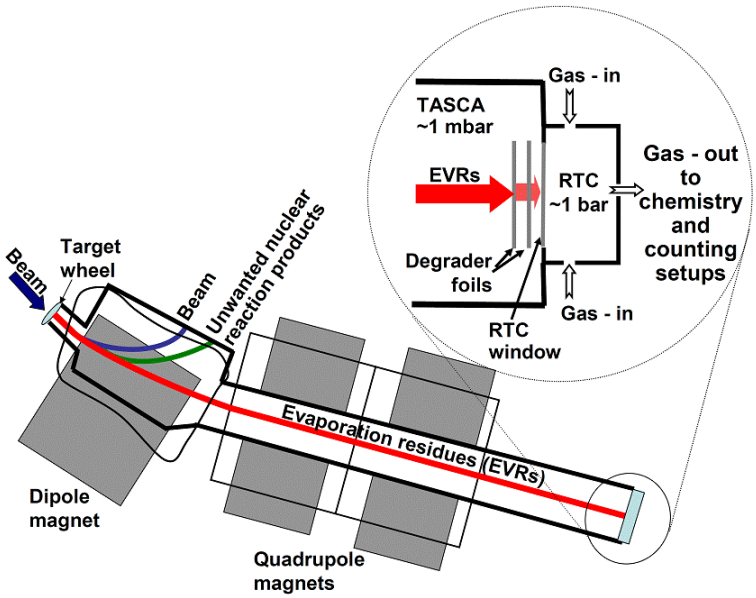

Figure 5: Schematic drawing of TASCA. The beam from the UNILAC passes the differential pumping section of TASCA and impinges on the target wheel. The targets used in TASCA are three or four banana shaped target segments mounted on a rotating target wheel. The target wheel rotation is synchronized to the beam macro structure of the UNILAC beam. TASCA can be filled with a variety of gases, at pressures of ~0.3−2.0 mbar. The evaporation residues leaving the target interact with the gas inside TASCA, thereby attaining an average charge state. Inside the dipole magnet of TASCA, the fusion products are separated from the primary beam and the transfer products according to their magnetic rigidity. The separated products are focused by the two quadrupole magnets into the focal plane. For chemistry experiments, a Recoil Transfer Chamber is installed right at the focal plane as an interface between the preseparator and the chemistry setups. Degrader foils can be inserted in front of the RTC to slow down the evaporation residues if necessary.

3 Underpotential Deposition

Historically, liquid phase chemistry experiments with transactinides have mainly concentrated on the ion-exchange studies (reversed-phase extraction- or ion-exchange chromatography). [76] Electrochemical methods have not been established in transactinide chemistry so far. First tests and developments for the study of the reduction of seaborgium are reported in reference [77]. Therefore, the ARCA was upgraded with a reduction column with an aluminium wire between degasser and ion-exchange column, but the system has not yet been applied to study seaborgium.

Toyoshima et al. [78] developed an electrochemistry apparatus which was successfully applied on a one-atom-at-a-time scale [79] for the heavier actinides. This device combines electrochemistry with ion-exchange chromatography in a flow electrolytic cell. [78]. By this method, the oxidation potential of nobelium (No^{2+}) [79] and the reductions potential of mendelevium (Md^{3+}) [80] were measured. This method requires sample preparation after the chemical studies. In addition it requires several experiments at various potentials. Therefore, is is only suitable for relatively long-lived isotopes with relatively high production rates (several atoms per hour).

Eichler and Kratz [81] suggested to study electrochemistry of the elements 112 up to 116 by underpotential deposition. This would allow electrochemical experiments, which would give information about the reduction potential and the adsorption enthalpy of the studied element on an electrode surface.

The first experimental studies with lighter homologs exploring the possibility of underpotential deposition were performed by Hummrich. [48], [82] He concluded that a minimum half-life of 10 s is needed for efficient electrochemistry studies and suggested to study ^{270}Hs. The half-life of ^{270}Hs of 23 s was estimated by the Q_{α}-values applying a Viola-Seaborg formula. [83] Furthermore, Hummrich suggested a design for an automated electrochemistry apparatus, in which the working electrodes are long metal tapes. These tapes would then be pulled through the electrolytic cell in order to transport the deposited activities in front of α-detectors. [82] In the first experiments with ruthenium and osmium isotopes, it has been demonstrated that it is feasible to deposit trace amounts of these hassium homologues on various electrode materials. [84]

3.1 The phenomenon of underpotential deposition

If a metal electrode is placed in a solution containing ions of the same element, there will be an equilibrium between the oxidized and the reduced states. This leads to an electrode potential E. This potential is described by the Nernst equation

$$E = E^0 + \frac{R \cdot T}{n \cdot F} \cdot \ln \frac{a_{ox}}{a_{rd}} \qquad (3.1\text{-}1)$$

The electrode potential is given by the standard potential E^0 (which is the potential observed under standard conditions – at 293 K, in 1 M solution and atmospheric pressure) plus a second term which includes the ideal gas constant R, the temperature T, the number of transferred charges n, the Faraday constant F and the ratio of the chemical activity of the oxidized species a_{ox} to the chemical activity of the reduced species a_{rd}. As the reduced species is in the described case the electrode, $a_{rd}=1$, and accordingly

$$E = E^0 + \frac{R \cdot T}{n \cdot F} \cdot \ln a_{ox} \qquad (3.1\text{-}2)$$

If a cathodic potential is applied on the electrode, which is lower than the Nernst potential, the ions start to deposit on the electrode surface. The potential at which ions from solution start to deposit on a surface is called critical potential. The critical potential is slightly lower than the Nernst potential, as the Nernst potential does not take into account, e.g., the Nernst diffusion layer and viscosity of the electrolyte solution.

If the electrode is made of a different element (B) than the ions in solution (A^{n+}), the Nernst equation becomes valid as soon as a monolayer of A covers the electrode material B. As predicted by the Nernst equation, the electrode potential is linearly dependent on the logarithm of a_{ox} (the chemical activity of cations in solution) – compare Figure 6. If the concentration of A^{n+} is so low that the electrode is not covered by a complete monolayer of A, the electrode potential is also dependent on the interaction between the electrode material B and the deposited species A. In this case, the potential deviates from the linear dependence of the logarithm of $a_{ox.}$, and the Nernst equation is no longer valid. In case of only a few single ions in solution, the electrode potential becomes independent from the logarithm of the $a_{ox.}$ [81]

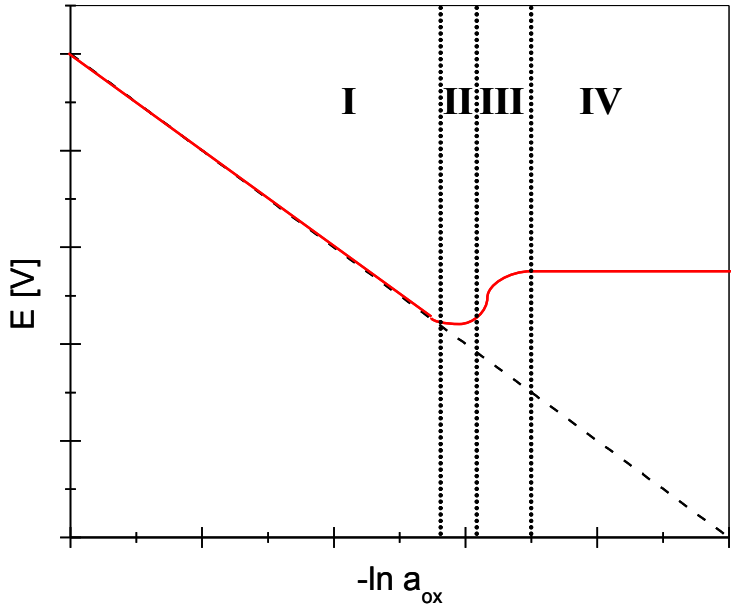

Figure 6: Dependence of the electrode potential on the chemical activity of cations in solution. **I** *represents the case when the Nernst equation is valid and a monolayer of A covers the electrode made of metal B.* **IV** *shows the case of underpotential deposition. For further explanations see the text (after* [81]).

In part II of Figure 6, the electrode potential starts to differ from the predicted trends of the Nernst equation. This occurs when a complete monolayer of A atomes is no longer formed. The deposition behaviour is now dependent on the interaction between atoms of the type A and B as well as the interactions between atoms of the type A and A.

In state III nearly "zero" coverage of atom A is reached. The deposition behaviour is dominated by the interaction of atoms of the type A and B.

Part IV shows that the electrode potential is independent from the chemical activities. This is the case if only few ions are present in the solution. Then the ions do not deposit as "islands" anymore, but only as single atoms. The deposition depends now entirely on the interaction between A and B. [81]

If the deposition of A on B is energetically more favoured than the deposition of A on A, the electrode potential is shifted to higher values (like in Figure 6) and this phenomenon is called underpotential deposition. If the deposition of A on A would be favoured, the potential would be

shifted to lower values (overpotential deposition). [81]

The phenomenon of underpotential deposition can also be observed in experiments with macro amounts of ions in solution. The deposition potential clearly deviates from the Nernst equation until the first monolayer is deposited.

In Ref. [85] a linear correlation between the underpotential shift ΔU and the difference of the working potentials $\Delta\phi$ of the electrode metal and the deposited metal, valid for many electrochemical systems is given by,

$$\Delta U = \frac{1}{2} \cdot \Delta \phi \tag{3.1-3}$$

The correlation between the adsorption enthalpy ΔH_{ads} (of A on B) and the underpotential shift times the electronic charge e_0 were investigated [86], giving

$$-\Delta H_{ads} = e_0 \cdot \Delta U \tag{3.1-4}$$

3.1.1 Thermodynamic description of underpotential deposition

For a more accurate mathematical description of underpotential deposition (only with micro amounts) the Nernst equation has to be modified. One approach is given in reference [87].

If a redox system is in its equilibrium state, the chemical potential of the oxidized form μ_{ox} and the chemical potential of the reduced form μ_{rd} are defined by the following equation [87]

$$\mu_{ox} - \mu_{rd} = n \cdot F \cdot E \qquad (3.1.1\text{-}1)$$

μ_{ox} is defined by the chemical standard potentials μ_{ox}^0, the temperature T and chemical activity a_{ox} as

$$\mu_{ox} = \mu_{ox}^0 + R \cdot T \cdot \ln a_{ox} \qquad (3.1.1\text{-}2)$$

The standard potentials are defined by

$$\mu_{ox}^0 - \mu_{rd}^0 = n \cdot F \cdot E^0 \qquad (3.1.1\text{-}3)$$

The chemical potential of the reduced species is a function of the partial molar enthalpy $\Delta \overline{H}_{rd}$ and the partial molar entropy $\Delta \overline{S}_{rd}$

$$\mu_{rd} = \Delta \overline{H}_{rd} - T \cdot \Delta \overline{S}_{rd} \qquad (3.1.1\text{-}4)$$

Using these equations, the Nernst equation can be rewritten. Equations (3.1.1-2) and (3.1.1-3) are inserted into equation (3.1.1-1), and $\mu_{rd}^0 = 0$, giving

$$E = E^0 + \frac{R \cdot T}{n \cdot F} \ln a_{ox} - \frac{\Delta \overline{H}_{rd}}{n \cdot F} - \frac{T \cdot \Delta \overline{S}_{rd}}{n \cdot F} \qquad (3.1.1\text{-}5)$$

According to references [81],[88] and [89], $\Delta \overline{H}_{rd}$ is equal to the molar net adsorption enthalpy $\Delta \overline{H}_{(A-B)}$. This is the enthalpy needed to deposit one mol of A on an electrode made of metal B under zero-coverage conditions. Furthermore, it is the sum of the partial molar adsorption enthalpy of A on B, $\Delta \overline{H}_{ads}$, and the standard enthalpy of A in the gas-phase, $\Delta H_{A(g)}^0$.

$$\Delta \overline{H}_{(A-B)} = \Delta H_{ads} + \Delta H_{A(g)}^0 \qquad (3.1.1\text{-}6)$$

The equivalent to $\Delta \overline{S}_{rd}$ is the molar net adsorption entropy $\Delta \overline{S}_{(A-B)}$. This is the difference in entropy if one mol of A is deposited on metal B under zero-coverage conditions. The $\Delta \overline{S}_{(A-B)}$ is the summation of the difference in the vibrational entropy of the metallic state and the zero-coverage state, $\Delta \overline{S}_{vib}$, and the growth of the molar configuration entropy, $\overline{S}_{conf}$.

$$\Delta \overline{S}_{(A-B)} = \Delta \overline{S}_{vib} + \overline{S}_{conf} \tag{3.1.1-7}$$

The bonding entropy in this process is negligible. [88] The configuration entropy depends on the degree of coverage X [81], according to,

$$\overline{S}_{conf} = -R \cdot \ln\left(\frac{X}{1-X}\right) \tag{3.1.1-8}$$

The degree of coverage X can be calculated from the amount of deposited metal, $n_{(A)}$, the area that a monolayer of one mol of A , A_m, would cover and the surface area of the electrode, F_E, by,

$$X = \frac{n_{(A)} \cdot A_m}{1000 \cdot F_E} \tag{3.1.1-9}$$

In case of a small degree of coverage X, equation (3.1.1-8) becomes

$$\overline{S}_{conf} = -R \cdot \ln X \tag{3.1.1-10}$$

If equations (3.1.1-10) and (3.1.1-7) are combined with equation (3.1.1-5), the electrode potential can be written as [89],[81]

$$E = E^0 + \frac{R \cdot T}{n \cdot F} \cdot \ln a_{ox} - \frac{\Delta \overline{H}_{(A-B)}}{n \cdot F} + \frac{T \cdot \Delta \overline{S}_{vib}}{n \cdot F} - \frac{R \cdot T}{n \cdot F} \ln X \tag{3.1.1-11}$$

To obtain an equation that is independent from a_{ox}, the potential at which 50% of the ions from solution are deposited on the electrode surface, E_{50}, is introduced. In case of small thermodynamic chemical activities, these can be replaced by concentrations. Therefore, the degree of coverage when 50% of the ions are deposited can be written as

$$X_{50} = \frac{0.5 \cdot c^0_{(A^{n+})} \cdot V \cdot A_M}{1000 \cdot F_E} \tag{3.1.1-12}$$

$c^0_{(A^{n+})}$ is the concentration of ions in solution at the start of the electrolysis. V is the volume of the electrolyte in cm^3.

The E_{50} values [81],[89] can be expressed with

$$E_{50} = E^0 - \frac{R \cdot T}{n \cdot F} \ln 0.5 \cdot c^0 (A^{n+\cdot}) - \frac{\Delta \overline{H}_{(A-B)}}{n \cdot F} + \frac{T \cdot \Delta \overline{S}_{vib}}{n \cdot F} - \frac{R \cdot F}{n \cdot F} \ln \frac{0.5 \cdot c^0_{(A^{n+\cdot})} \cdot V \cdot A_M}{1000 \cdot F_E} \quad (3.1.1\text{-}13)$$

which is equal to

$$E_{50} = E^0 - \frac{\Delta \overline{H}_{(A-B)}}{n \cdot F} + \frac{T \cdot \Delta \overline{S}_{vib}}{n \cdot F} - \frac{R \cdot T}{n \cdot F} \ln \frac{V \cdot A_m}{1000 \cdot F_E} \quad (3.1.1\text{-}14)$$

In the case of a constant ratio of $V/F_E = 1$ the equation can be written as

$$E_{50} = E^0 - \frac{\Delta \overline{H}_{(A-B)}}{n \cdot F} + \frac{T \cdot \Delta \overline{S}_{vib}}{n \cdot F} - \frac{R \cdot T}{n \cdot F} \cdot \ln \frac{A_m}{1000} \quad (3.1.1\text{-}15)$$

The influence of the electrode metal on the deposition can be seen in the underpotential shift ΔE, which is the difference between the Nernst equation and the measured electrode potential. [90]

$$\Delta E = \frac{-\Delta \overline{H}_{(A-B)} + T \cdot \Delta \overline{S}_{vib}}{n \cdot F} \quad (3.1.1\text{-}16)$$

3.1.2 Kinetics of underpotential deposition

One of the most important factors in a transactinide chemistry experiment, is due to the short half-lives of these elements, the speed of the chemical reaction.

The electrodeposition process is a first order kinetics process. If in a chemical reaction of the type

$$A + B \rightarrow C$$

the concentration of B, $c_{(B)}$, is much higher than that of A, $c_{(A)}$, $c_{(B)}$ can be assumed to stay constant. The change of the concentration of A during the reaction is

$$-\frac{dc_{(A)}}{dt} = k \cdot c_{(A)} = k \cdot \left(c^0_{(A)} - c_{(C)} \right) \qquad (3.1.2\text{-}1)$$

where, k is the kinetic constant of the reaction, $c^0_{(A)}$ the initial concentration of A, and $c_{(C)}$ the concentration of C. In the case of underpotential deposition, only a few ions which take part in the deposition process, are in solution. The concentrations must be replaced by the number of atoms. N_{tot} is the total number of atoms (of type A), N_{dep} is the number of deposited atoms.

$$\frac{dN_{dep}}{dt} = k \cdot \left(N_{tot} - N_{dep} \right) \qquad (3.1.2\text{-}2)$$

The kinetic constant depends on the experimental conditions such as stirring of the solution, temperature, the viscosity of the solution and the geometry of the electrolysis cell.

Joliot [91] suggested an extended kinetic equation with two kinetic constants (a and b) based on the results of his studies of the deposition of tracer amounts of polonium,

$$\frac{dN_{dep}}{dt} = a \cdot \left(N_{tot} - N_{dep} \right) - b \cdot N_{dep} \qquad (3.1.2\text{-}3)$$

The constants a and b are dependent on the electrode potential, the stirring of the electrolyte, the volume, and the composition of the electrolyte and the electrode surface. When the maximum deposition N_{max} is reached , $dN_{dep}/dt=0$ and

$$\frac{N_{max}}{N_{tot}} = \frac{a}{a+b} \qquad (3.1.2\text{-}4)$$

Taking this into account and integrating equation (3.1.2-3) leads to

$$a+b=\frac{1}{t}\cdot\ln\frac{N_{max}}{N_{max}-N_{dep}}=-\frac{1}{t}\cdot\ln\left(1-\frac{N_{dep}}{\frac{a}{a+b}\cdot N_{tot}}\right) \qquad (3.1.2\text{-}5)$$

According to this, the ratio of deposited atoms to the total number of atoms can be expressed by

$$\frac{N_{dep}}{N_{tot}}=\frac{a}{a+b}-\frac{a}{a+b}\cdot e^{-\frac{a+b}{t}} \qquad (3.1.2\text{-}6)$$

As Joliot [91] concluded from his experiments, deposition is mainly dependent on the diffusion of the ions in the Nernst diffusion layer. To reflect this, he suggested a second kinetic equation taking into account the diffusion coefficient D, the size of the electrode surface F_E, the thickness of the Nernst diffusion layer δ, the electrolyte volume V and the kinetic constant k (which in these considerations is equal to maximum deposition yield). This expression is given as

$$\frac{dN_{dep}}{dt}=\frac{D\cdot F_E}{\delta\cdot V}\cdot\left(k\cdot N_{tot}-N_{dep}\right) \qquad (3.1.2\text{-}7)$$

with the ratio of the number of deposited atoms to the total number of atoms equal to

$$\frac{N_{dep}}{N_{tot}}=k-k\cdot e^{-\frac{D\cdot F_E}{\delta\cdot V}\cdot t} \qquad (3.1.2\text{-}8)$$

The constant k is dependent on the applied potential. At potentials higher than the critical potential, the maximum deposited amount is very low and the constant k is almost 0. As soon as the potential is lower than the critical potential, the maximum deposited amount rises very quickly until saturation is reached. In this case $k=1$ and the following equation becomes valid

$$\ln\left(1-\frac{N_{dep}}{N_{tot}}\right)=-\frac{D\cdot F_E}{\delta\cdot V}\cdot t \qquad (3.1.2\text{-}9)$$

The diffusion coefficient, D, is defined by the Stokes-Einstein equation

$$D=\frac{k_B\cdot T}{6\cdot\pi\cdot\eta\cdot a} \qquad (3.1.2\text{-}10)$$

where a is the hydrodynamic radius of the ion, η the viscosity, and k_B the Boltzmann constant.

Fahland [92] studied the kinetics of the deposition of tracer amounts. He defined the value t_{50} as the time at which 50% of the ions in solution are deposited on the electrode surface ($N_{dep}/N_{tot} = ½$) . Taking into account the previous equations, t_{50} is

$$t_{50} = \frac{6 \cdot \pi \cdot V \cdot a \cdot \delta \cdot \eta \cdot \ln 2}{F_E \cdot k_B \cdot T} \qquad (3.1.2\text{-}11)$$

According to this equation, it is necessary for the design of a fast electrodeposition experiment, to keep the ratio of electrolyte volume to electrode surface as small as possible. The temperature should also be as high as possible, while remaining below the boiling point of the electrolyte. The viscosity of the electrolyte should be low and the Nernst diffusion layer should be reduced by constant agitation of the solution by vigorous stirring.

3.1.3 Determining the critical potential

First experiments with the deposition of radiotracer amounts of polonium are reported in reference [93]. The deposition yield of polonium was plotted versus the electrode potential and the "break through point" - the potential at which the polonium started to deposit on the surface was identified. Later, Joliot [91] also studied the deposition of polonium. He named the "break through point" critical potential. He investigated the tangent method (see Figure 7) to determine the critical potential (E_{crit}). In this method, the intersection of the tangent of the flat part of the curve (before deposition starts) and of the tangent, which goes through the point of inflection of the gradient part of the curve, defines the E_{crit}.

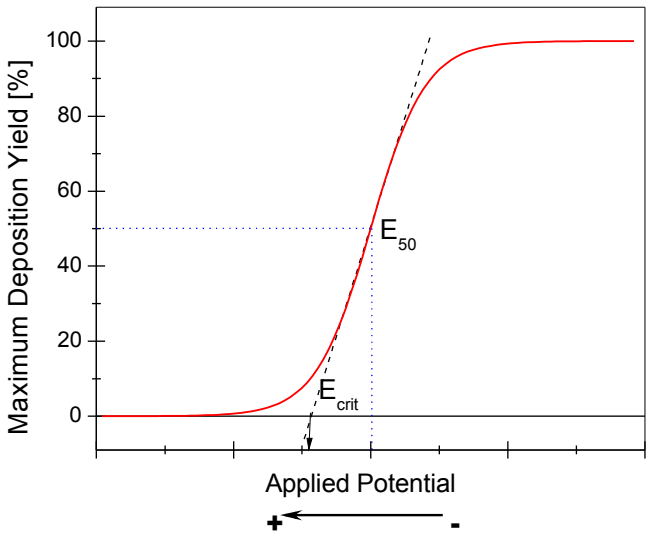

Figure 7: Scheme of an ideal electrodeposition profile. The crossing point of the two tangents (shown in black) determines the E_{crit}. The E_{50} value is the potential, at which 50% of the ions from solution are deposited on the electrode surface.

The measured deposition yields can be fitted by the following function [84]

$$Y = A_1 + \frac{A_2 - A_1}{1 + e^{\frac{E-P}{Q}}} \qquad (3.1.3\text{-}1)$$

Y is the deposition yield (in %) and *E* the applied potential. The constants A_1, A_2, *P* and *Q* will be derived in the following equations. As described in chapter 3.1.1

$$E = E^0 + \frac{R \cdot T}{n \cdot F} \ln a_{ox} - \frac{\Delta \overline{H}_{(A-B)}}{n \cdot F} + \frac{T \cdot \Delta \overline{S}_{vib}}{n \cdot F} - \frac{R \cdot T}{n \cdot F} \cdot \ln X \qquad (3.1.1\text{-}11)$$

The following constants were defined

$$B = E^0 - \frac{\Delta \overline{H}_{(A-V)}}{n \cdot F} + \frac{T \cdot \Delta \overline{S}_{vib}}{n \cdot F} \qquad (3.1.3\text{-}2)$$

$$Q = \frac{R \cdot T}{n \cdot F} \qquad (3.1.3\text{-}4)$$

The degree of coverage *X* as well as the activity of ions in solution, a_{ox}, can be written as a function of the deposition yield *Y*

$$a_{ox} = Z_1 \cdot (100 - Y) \qquad (3.1.3\text{-}5)$$

$$X = Z_2 \cdot Y \qquad (3.1.3\text{-}6)$$

The equation (3.1.1-11) can be rewritten as

$$E = B + Q \cdot \ln\left(Z_1 \cdot (100 - Y)\right) - Q \cdot \ln\left(Z_2 \cdot Y\right) \qquad (3.1.3\text{-}7)$$

and this equation can be converted to

$$\frac{E - B}{Q} = \ln \frac{Z_1 \cdot (100 - Y)}{Z_2 \cdot Y} = \ln \frac{Z_1}{Z_2} + \ln \frac{100 - Y}{Y} \qquad (3.1.3\text{-}8)$$

As next step, the constant *P* is introduced

$$P = B + Q \cdot \ln \frac{Z_1}{Z_2} \qquad (3.1.3\text{-}9)$$

P can be inserted in equation (3.1.3-8)

$$\frac{E-P}{Q}=\ln\frac{100-Y}{Y} \tag{3.1.3-10}$$

From equation (3.1.3-10) we obtain

$$e^{\frac{E-P}{Q}}=\frac{100-Y}{Y} \tag{3.1.3-11}$$

The deposition yield can be written as

$$Y=\frac{100}{1+e^{\frac{E-P}{Q}}} \tag{3.1.3-12}$$

As in most cases, the maximum deposition yield is lower than 100%, the parameter A_1 is defined as the maximum yield. Also at potentials higher than the critical potential, a small amount can be deposited on the surface, therefore the parameter A_2 is defined as the deposition yield at higher potentials.

$$Y=A_1+\frac{A_2-A_1}{1+e^{\frac{E-P}{Q}}} \tag{3.1.3-1}$$

3.2 Underpotential deposition experiments

Hummrich [82] designed an automated electrochemistry apparatus using long palladinated nickel tapes as working electrodes. In reference [84] various electrode materials were tested in electrodeposition experiments with ruthenium and osmium. Tantalum, molybdenum, tungsten and titanium were predicted to show the strongest underpotential shift [89] and, therefore, should be the ideal electrode metals. However, these metals are covered by an oxide layer under "normal" conditions. The test experiments showed that this leads to significant technical problems and these metals are not usable as electrode metals. [84] Furthermore, palladium, nickel, and palladinated nickel were tested as electrode materials. The deposition yields achieved with palladium were highest. However, it was observed that the palladium electrodes partially dissolved in the electrolyte. The palladium re-deposited as palladium black and was even observed as flakes in the electrolyte solution. This phenomenon probably obscures the results. The deposition yields were lower with nickel. Furthermore, it is difficult to keep a pure metallic electrode surface due to oxidation of the nickel.

In the experiments with palladinated nickel electrodes, the palladium dissolved from the surface and a fraction of it was re-deposited. The palladium layer was not homogeneous. The critical potentials determined were in between those measured with nickel and palladium electrodes. [84] Hummrich [82] reported the same – the deposition potential of lead on palladinated nickel was in between the measured values of nickel and palladium electrodes.

While, Hummrich [82] described palladinated nickel as a suitable electrode material, it seems to be problematic to obtain reproducible results. Interpretation of the observed deposition potentials is nearly impossible, as the electrode surface is not well defined. The deposition might be also correlated with the re-deposition of the palladium black flakes on the nickel.

Therefore, it was at least necessary to search for another electrode-metal, which is relatively chemically inert so that its surface stays as a pure metal. Promissing candidates seem to be gold or platinum. In this work, the deposition on gold was studied.

3.2.1 The electrolysis cell

For the tests with gold electrodes, the same electrolysis cell was used as in references [48],[82], and [84] was taken. Figure 8 shows a schematic drawing and photograph of the cell.

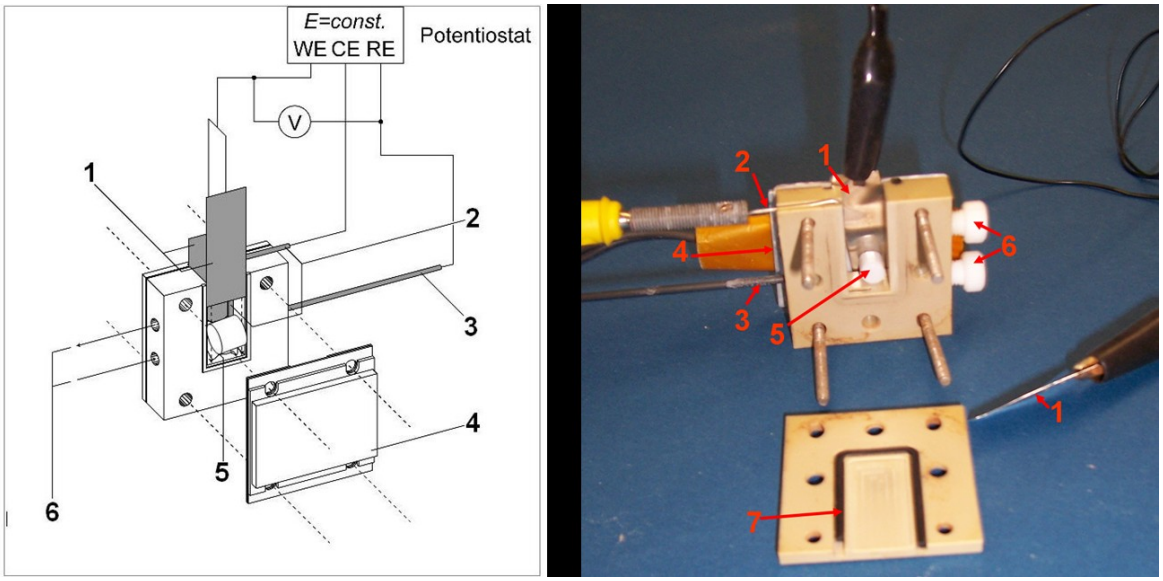

Figure 8: Scheme of the electrolytic cell (left, taken from ref.[48]*) and photograph of the cell (right). 1 denotes the working electrodes, 2 the counter electrode (made of Pt wire), 3 the reference electrode (Ag/AgCl electrode), 4 the PTC-heater, 5 the stir bar, 6 the electrolylte in- and outlet, 7 the viton sealing of the cell.*

The electrolytic cell is made of polyetheretherketone (PEEK). The base area of the inner volume of the cell is (1 cm · 1 cm). Holders for the 1 cm wide working electrodes are situated on two opposing sides of the cells. In the experiments described within this work, the working electrodes were made of 0.05 mm thick gold foil. The counter electrode is a 1-mm diameter platinum wire. Ag/AgCl electrodes were used as references electrodes (Type DRIREF-2, produced by World Precision Instruments). All potentials were measured versus this Ag/AgCl reference electrode made of a silver wire in 3 M KCl solution. The standard potential of this electrode is $E^0=222.3\ mV$. At 50°C the potential of the reference electrode is $E=305.9\ mV$ and at 70°C the potential is $E=311\ mV$ (according to the Nernst equation).

A Positive Temperature Coefficient PTC element (typ HP04, David&Bader) was chosen as heating device. This heating device was separated from the cell by a titanium plate covered with teflon foil. The electrolyte solution was stirred by a cylindrical stir bar (7 mm length, 6 mm width).

3.2.2 Electrodeposition studies of ruthenium

To study the electrodeposition behaviour of ruthenium, the short-lived isotope ^{108}Ru was produced in the neutron-induced fission of ^{249}Cf (^{249}Cf(n,f)^{108}Ru). A target made of 350 µg ^{249}Cf electroplated on a titanium backing and covered with a 15-µm thick aluminum foil was placed in a target chamber at beam port A of the TRIGA Mainz reactor. The neutron flux at this position is $9.8 \cdot 10^{10}$ n·cm^{-2}·s^{-1}. [94]

The target chamber was connected with a gas-jet system [49], [50], [95] to a direct catch setup and to the degasser ALOHA (Automated Liquid Online Heavy Element Apparatus) [96] from which non-volatile fission products were transferred into the electrolysis cell.

The gas jet used was a classical He/KCl jet. Pure helium passed through a tube furnace, which was heated up to 650°C. The oven contained a crucible filled with potassium chloride. At this temperature, KCl sublimates, by cooling it down in the gas stream, it forms aerosol clusters. These clusters were transported with the gas stream to the target chamber.

The pressure inside the target chamber was 2.6 bar. The non-volatile fission products attached to the aerosol clusters and were transported though an 8-m long polyethylene capillary with an inner diameter of 0.8 mm to a gas jet valve. This valve could either direct the jet toward the waste filter or to a second valve. From the second valve, the gas jet was guided through a glass fibre filter (Schleicher&Schüll; No.6) or to the ALOHA.

The direct catch filter was used to monitor the gas jet yield. The aerosol particles and non-volatile fission products were collected on this filter. The collected fission products were measured after a certain collection time with a germanium detector (EG+G Instruments, Model No. LOAX-51450/20-P).

Figure 9 shows a schematic of the experimental setup.

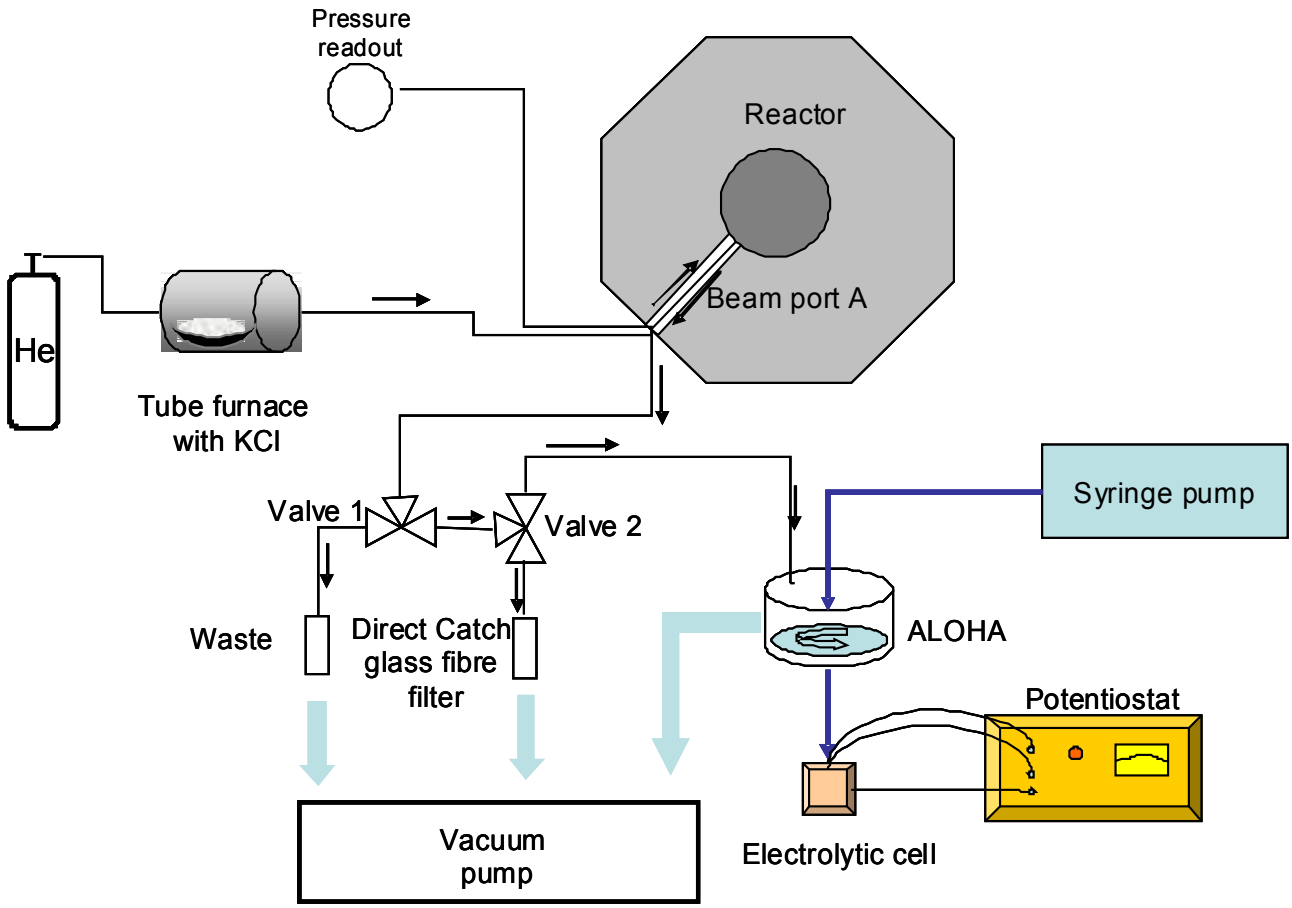

Figure 9: Schematic of the electrochemistry experiment at the TRIGA reactor. The ^{249}Cf target was placed in a target chamber at beam port A. The chamber was flushed with He seeded with KCl-clusters. The non-volatile fission products attach to these clusters and are transported within the gas stream to Valve 1. From there the gas-stream is either guided through the waste filter or to valve 2. From valve 2, the gas stream is either guided trough the direct catch apparatus, where the aerosol particles and fission products are collected on a glass fibre filter, or it is guided to the ALOHA. In the ALOHA, the aerosol particles are collected for dissolution in the electrolyte solution. The fission products are transferred within the solution into the electrolytic cell.

The main part of the ALOHA is a tantalum disk with a diameter of 6.0 cm . Four cavities with volumes of 4.2 µL each with a small hole in the middle are machined into the disk. The disk was rotated by a stepping motor in 90° steps. At the first of the four positions, the gas-jet was forced through a nozzle of 0.3 mm diameter into a chamber evacuated to around 5 mbar. The aerosol particles impacted into the bottom of the cavity and were deposited there. The disc was rotated by 90° after 2 minutes. This put the cavity with the deposited KCl-clusters into the second position. In this position, the potassium chloride and the fission products were dissolved in the electrolyte solution (0.1 molar hydrochloric acid). The activity was transported with the solution through the small hole in the bottom of the cavity into the electrolytic cell. In the third position, the cavity was

cleaned with acetone, and in the fourth position, it was dried by a nitrogen stream.

For the electrodeposition studies of ruthenium, the fission products were collected for 2 min in the ALOHA. Afterwards, the activity was flushed with 1 mL hydrochoric acid into the electrolysis cell, which was heated up to 54°C. 10 s later, the potential, at which deposition should be studied, was applied for 90 s. Afterwards the electrodes were removed from the cell and placed in front of the germanium detector. The time between end of collecting the non-volatile fission products attached at the clusters in the ALOHA and start of the measurement was 2 min. The measuring time was 5 min. Figure 10 shows a typical γ spectrum of the electrodes.

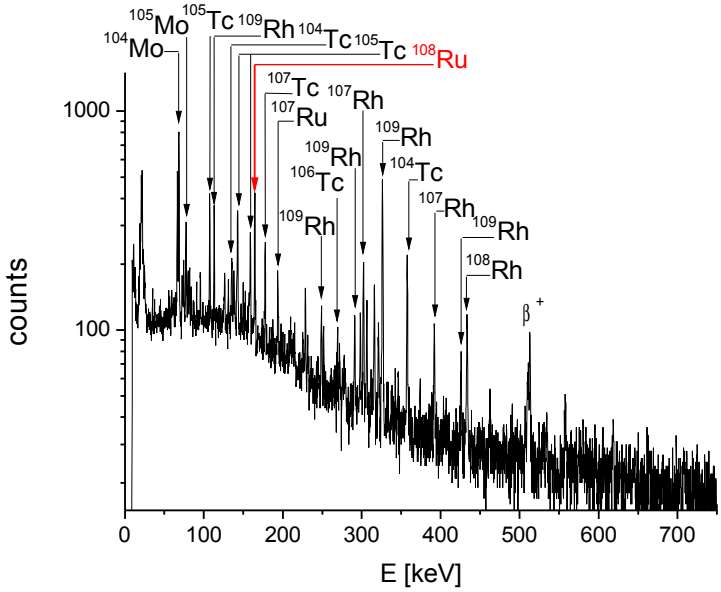

Figure 10: γ-spectrum of the gold electrodes. The activity was collected for 2 min in the ALOHA. Afterwards, the electrolysis was conducted for 90 s at -600 mV (vs. Ag/AgCl). The electrodes were placed in front of the γ-detector 2 min after the end of the collection time in the ALOHA. The activity on the electrodes was measured for 5 min.

The γ line at 165 keV of ^{108}Ru was evaluated for the determination of the ruthenium electrodeposition. ^{108}Ru has a half-life of 4.55 min [97], which is adequate for manual experiments. Over 50% of all ^{108}Ru atoms are produced as a primary fission product. [98] The isobaric precursor ^{108}Tc is relatively short-lived (5.17 s). As a result, the influence of the deposition of ^{108}Tc on the measured deposition yield of ^{108}Ru is negligible.

The measurements were performed at various potentials and the results were normalized to the

gas-jet yield obtained with the ALOHA. Figure 11 shows the dependence of the deposition yield of ^{108}Ru on the applied potential measured vs. Ag/AgCl electrode at 54°C.

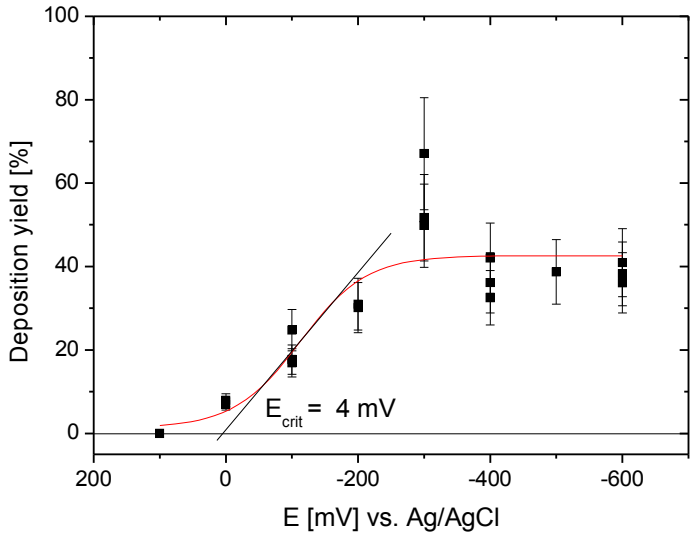

Figure 11: Deposition yield of ^{108}Ru on gold electrodes from 0.1 M HCl dependent on the applied potential at 54 °C.

As the maximum deposition yield was less than 50% in most of the measurements, the E_{50} value could not be determined. The kinetics of the deposition is likely too slow, as it was observed in previous experiments [84] with nickel and palladium electrodes. The maximum deposition yield is similar to that achieved with the palladium electrodes - between 40% and 50%. Under comparable conditions, the nickel electrode had maximum deposition yields of 30%. [84]

The critical potential was determined to (4±50) mV (versus Ag/AgCl at 54°C), which is nearly the same as that reported for the deposition of ruthenium on nickel [84] ((-6±50) mV versus Ag/AgCl at 54°C).

3.2.3 Electrodeposition of osmium on gold

Carrier free osmium for underpotential deposition experiments was produced in the nuclear fusion reaction $^{nat}Ce(^{40}Ar,xn)^{175}Os$. From former electrodeposition experiments with osmium [84], it was known that physical preseparation is needed, so the experiment was set up at TASCA.

The beam energy in the centre of the target was 196 MeV. Three arc shaped Ce_2O_3 targets with an average thickness of 360 µg/cm^2 Ce on 2−µm thick Ti backing were mounted on an ARTESIA target wheel. [99]

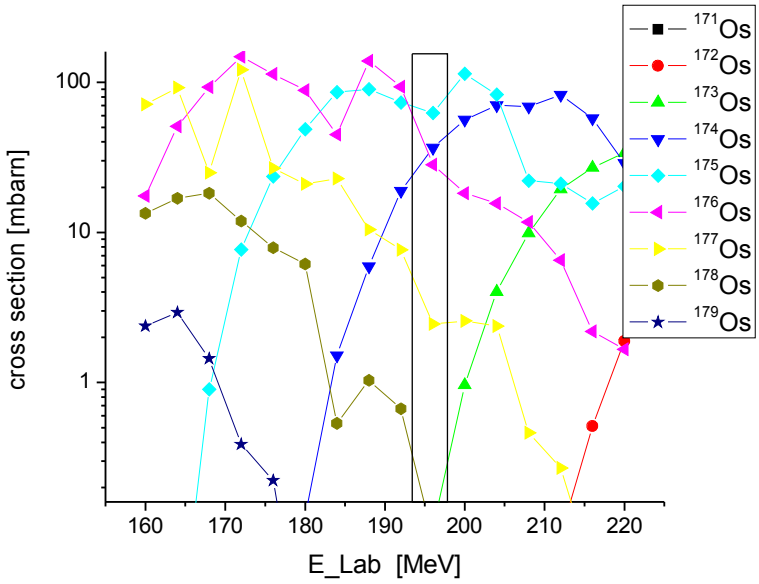

Figure 12: HIVAP[100] *predicted cross-sections for the reaction $^{nat}Ce(^{40}Ar,xn)$. The black frame marks the beam energy in the target during the experiment.*

TASCA was filled with 1.0 mbar helium and operated in the high transmission mode HTM. [73] The dipole was set such that ions with a magnetic rigidity of 1.66 T·m were guided to the center of the focal plane.

In the focal plane of TASCA, the HTM-RTC [58] was attached. The RTC depth was 4 cm and the thickness of the RTC Mylar window was 5.8 µm. The RTC was flushed with a He/KCl jet. The RTC had three gas inlets at the left and three inlets at the right side. The outlet was located in the rear cover plate. A schematic of the experimental setup is shown in Figure 13.

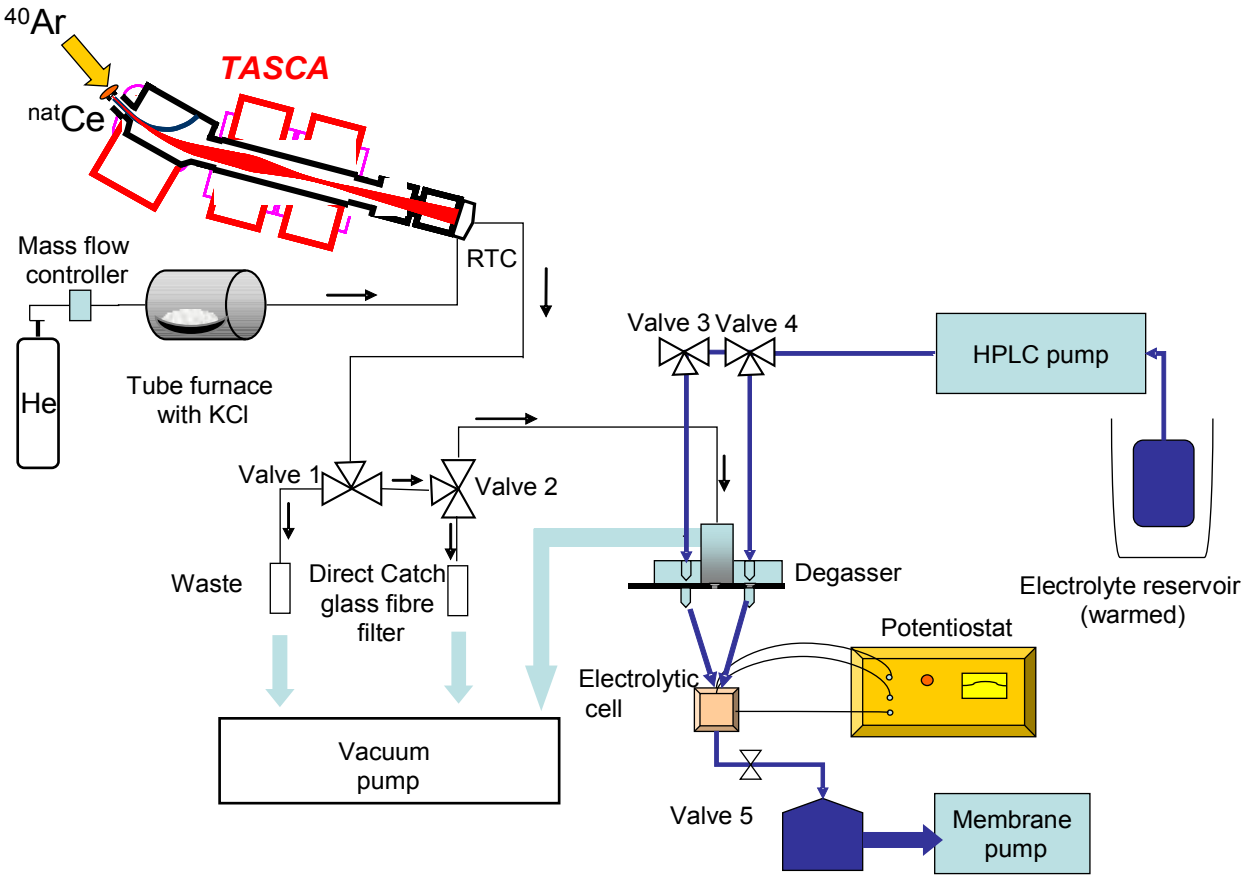

Figure 13: Schematic of the setup of the electrodeposition experiment at TASCA. The evaporation residues were thermalized in the RTC and transported with a He/KCl jet to valve 1 from where they could be directed to the waste filter or to valve 2. Valve 2 directed the gas-jet either to the direct catch filter or the degasser. The aerosol clusters were collected in the degasser and afterwards dissolved in the electrolyte solution and flushed in the electrolytic cell. The cell was emptied by opening valve 5.

The gas jet was operated at a flow rate of 3 L/min. The helium first passed through a 650°C tube furnace containing potassium chloride. The KCl aerosol particles were transported within the gas stream to the RTC, which was kept at a pressure of 1.02 bar. The recoiling ions were thermalized in the RTC and attached to these clusters. The aerosol clusters and the osmium isotopes were transported through a 10 m-long polyethylene capillary to the electrochemistry setup installed in a radiochemical laboratory outside of the irradiation cave. By switching valve 1 and 2, the clusters

were either directed to the waste filter, the direct catch filter (glass fibre filter, Schleicher&Schüll No.6), or to the degasser.

The degasser was an ARCA-type degasser [62] made of Teflon. Figure 14 shows a photograph of the degasser connected to the electrolytic cell.

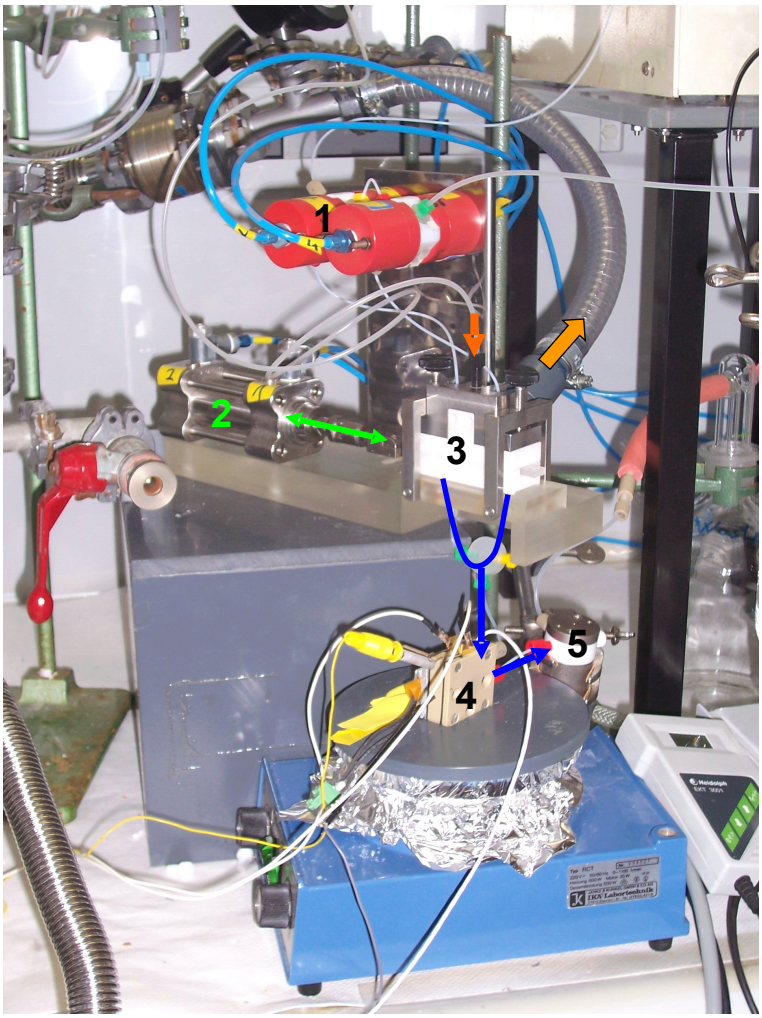

Figure 14: Photograph of the degasser connected with the electrolytic cell. The orange arrows show the directions of the gas flow. The blue arrows symbolize the flow direction of the electrolyte solution. The pneumatic valves **1** *guide the electrolyte solution flow from the HPLC pump to the degasser or waste. The degasser slider is moved with the pneumatic cylinder* **2** *in the directions shown with the green arrow.* **3** *is the main part of the degasser containing the chamber, in which the gas jet is forced onto the slider. From the degasser the transported isotopes are transferred in the electrolysis cell* **4**. *The cell can be emptied by opening valve* **5**.

The main part of this degasser is a slider made of polychlorotrifluoroethylene (Kel-F™). Two cavities (cavity A and cavity B) each with a small hole in the middle are machined into this slider. The slider was moved by a pneumatic cylinder between two positions. At the first positions, cavity A is in a chamber evacuated to 5 mbar. The gas-jet is forced through a nozzle into this chamber. The aerosol particles impact into the bottom of the cavity A and are deposited there. Simultaniously, cavity B is in a position where it can be flushed with the electrolyte solution. After a pre-set time, the slider is moved to the second position. In this position, the deposited potassium chloride and the transported activity in cavity A can be dissolved in the electrolyte solution (0.1 molar hydrochloric acid). Cavity B is then in the evacuated gas jet chamber.

The reservoir containing the electrolyte solution (0.1 molar hydrochloric acid) was warmed in a water bath. From there it was pumped by a HPLC pump to two pneumatic valves, from which the solution was either directed to the cavity A or the cavity B of the slider or to a waste reservoir.

In this experiment, a teflon coated temperature sensor (type PT100) was placed in the electrolysis cell and connected to a temperature controller which regulated the cell heating.

The electrolysis cell could be automatically emptied by opening a magnetic valve. This valve connected the cell with a glass vessel which was kept at low pressure by a membrane pump. After opening the magnetic valve, the electrolyte was sucked out of the cell into the glass vessel in less than a second.

The whole experiment was conducted half-automated and controlled by a computer program written with LabView. The computer communicated with a USB module (National instruments USB 6525) from which TTL signals were given to open or close the magnetic valve to empty the cell or to move the pneumatic cylinder or the pneumatic valves through a valve terminal (Festo type 10 CPV). The time for collecting aerosol clusters in one cavity and the electrolysis time could be pre-set in the labview program. The electrodes had to be moved by hand from the cell to the γ-ray detector after the electrolysis was completed.

In the experiment, the aerosol clusters and the transported isotopes were collected in one cavity of the degasser for 2 minutes. Afterwards, the KCl/osmium deposit was dissolved in 1 mL of the electrolyte solution and flushed into the electrolysis cell within 8 s. Voltage was applied for 1 min. During the electrolyses the temperature varied between 50°C and 70°C, depending on the applied voltage. After one minute, the electrolyte solution was removed and the electrodes were placed in

front of the γ-ray detector. The samples were measured for 3 minutes, with the total time between end of the collection in the degasser and start of the measurement being 90 seconds.

The measurements were performed at various potentials. Figure 15 shows a typical spectrum of the sample deposited on the gold electrodes.

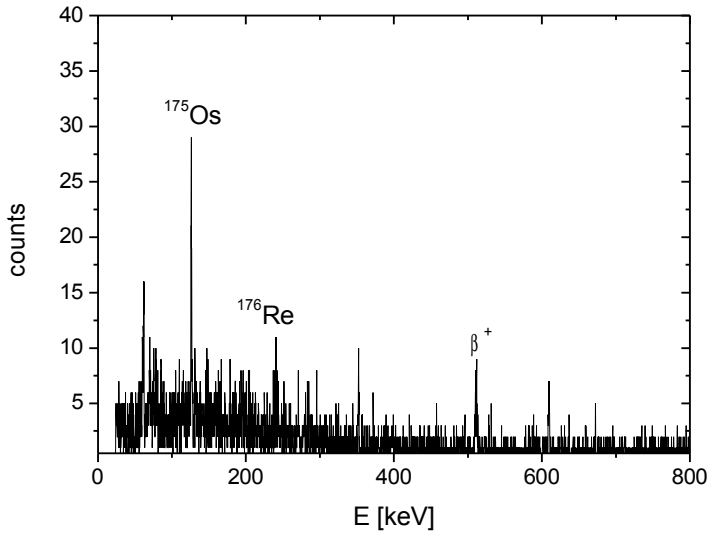

Figure 15: Typical γ-spectrum of the gold electrodes after electrodeposition. The activity was collected for 2 min in the degasser. Afterwards the electrolysis was conducted for 90 s at -200 mV (vs. Ag/AgCl). The electrodes were placed in front of the γ-detector 90 s after the end of the collection time in the degasser. The activity on the electrodes was measured for 3 min.

Unfortunatelly, the beam intensity was low and very unstable during the irradiation. This resulted in very low counting statistics. The 125 keV γ line of ^{175}Os, which has a half-life of 1.4 min, was clearly identified. Because the beam intensity was unstable, the measured values could not simply be normalized by the beam integral.

In the beam log file, the beam integral for every second was written down. The beam integral has to be corrected with the decay of ^{175}Os by the following equation

$$I_{total} = \sum_{t=0}^{t=300} I_t \cdot e^{-\lambda \cdot t} \qquad (3.2.3\text{-}1)$$

I_{total} is the corrected beam integral, t is the time in seconds since the start of ample collection, I_t is the beam integral in the time interval and λ is the decay constant of ^{175}Os. All measurements were

normalized to these corrected integrals.

The measurements were afterwards normalized by the degasser yield. Figure 16 shows the electrodeposition yield as a function of the electrode potential measured versus Ag/AgCl reference electrode.

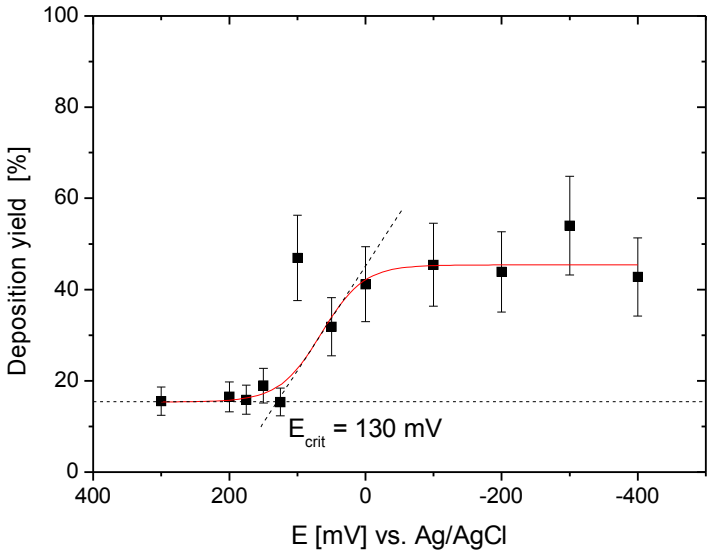

Figure 16: Electrodeposition yields of ^{175}Os on gold electrodes as a function of the electrode potential E. All values were normalized to the corrected beam integral and compared to the degasser yields. The electrolyses were conducted for 90 s in 0.1 M HCl at temperatures between 50°C and 70°C.

The critical potential was observed at (130 ± 80)mV (vs Ag/AgCl at 60°C). As the deposition yield was low (maximum 50%) the E_{50} value could not be determined. Due to the experimental problems (unstable beam and low counting statistics) improved measurements would be desirable.

3.3 The ELectro – CHemistry apparatus ELCH

To perform fast efficient electrolyses coupled with an α-detection system, a tape system was proposed and the basics designed by Hummrich. [82] The electrodes in this device are long tapes pulled through an electrolysis cell in front of arrays of α-PIN-diodes. Furthermore, the electrode surface to electrolyte volume was enlarged to reduce the average deposition time.

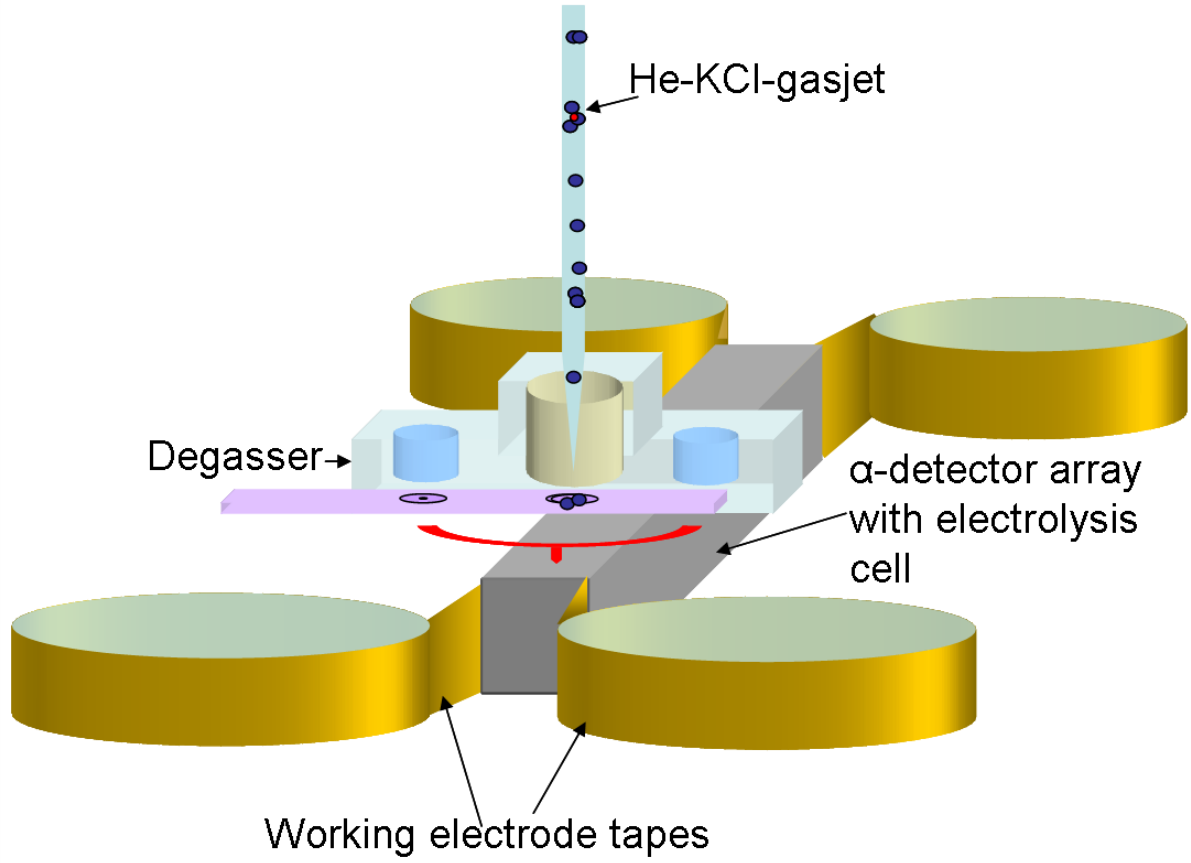

Figure 17: Schematic of the ELectro CHemistry apparatus – ELCH. In this device a degasser is placed directly over the electrolysis cell and connected to the cell by short capillaries (shown in red). The electrolysis cell is closely mounted to an α-detector array. The working electrodes are long metalized tapes.

The degasser unit

It was first planned to combine the ALOHA with the ELCH. However, due to the design of the ALOHA, the connection tube between ALOHA and the electrolytic cell would have been several centimeters long, which enlarged the dead volume between the degasser unit and the cell. Furthermore, leak tight operation of the ALOHA proved very difficult. Also, for experiments with short-lived isotopes it would be very difficult to monitor the gas-jet yield with the degasser.

Taking into account these considerations, a new ARCA-type degasser was constructed. The new degasser also works by impacting KCl clusters into a cavity machined in a slider. This cavity can be moved by two pneumatic cylinders either into a position where it can be flushed by electrolyte solution or in front of an α-PIN diode. Figure 18 shows a photograph of the degasser.

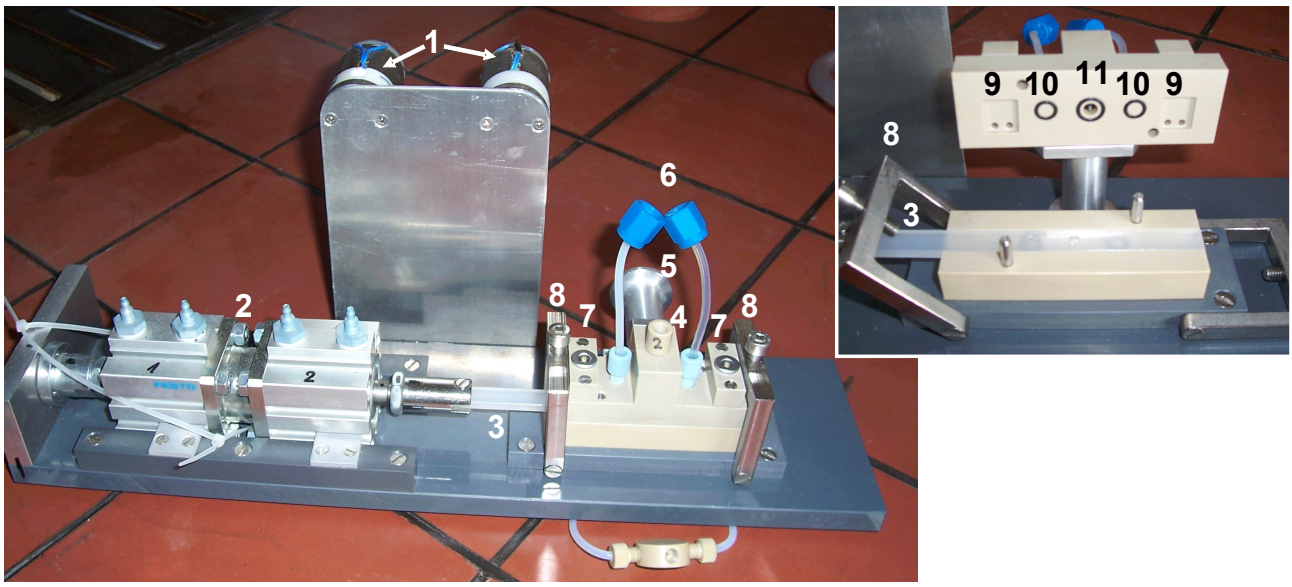

Figure 18: Newly developed ARCA-type degasser. The Kel-F™-slider **3** *can be moved to three different positions by the two pneumatic cylinders* **2**. *The stroke length of each cylinder is 1.5 cm. The distance between the three cavities in the slider is also 1.5 cm. Each cavity has a small hole in the middle. The gas jet enters the degasser through* **4** *and is forced by a nozzle* **11** *onto a cavity in the slider. The He is pumped away through* **5**, *so that the pressure in the degasser is less than 5 mbar. By switching the magnetic valves* **1**, *solution is guided to one of the inlets* **6**. *This way the cavity in front of the drill holes* **10** *can be flushed with solution. The positions* **9** *are the spaces where the α-PIN diodes are placed. These can be connected with the LEMO-connectors* **7** *to preamplifiers. The degasser is sealed by tighting the screws* **8**.

The main part of this degasser is a slider made of polychlorotrifluorethylene Kel-F™. Three cavities (cavity 1, 2 and 3), each with a small hole in the middle are machined into this slider. There

is a distance of 1.5 cm between each cavity. Each cavity has an inner diameter of 3 mm with a 0.3 mm diameter hole in the middle. The slider is moved by two pneumatic cylinders to one of three positions (see Figure 19). The stroke length of each cylinder is 1.5 cm. At the position A, cavity 3 is in a chamber evacuated to 5 mbar. The gas-jet is forced through a nozzle into this chamber. The aerosol particles impact into the bottom of cavity 3 and are deposited there. Cavity 2 is in a position where it can be flushed with the electrolyte solution, and cavity 1 is in front of an α-PIN diode. By moving the slider, the cavities 1 and 3 can be moved to positions where they are placed in front of an α-detector, where they can be flushed with solution, or where they are under the He/KCl jet. Cavity 2 can only be moved between the gas-jet position and the position where it can be flushed with electrolyte.

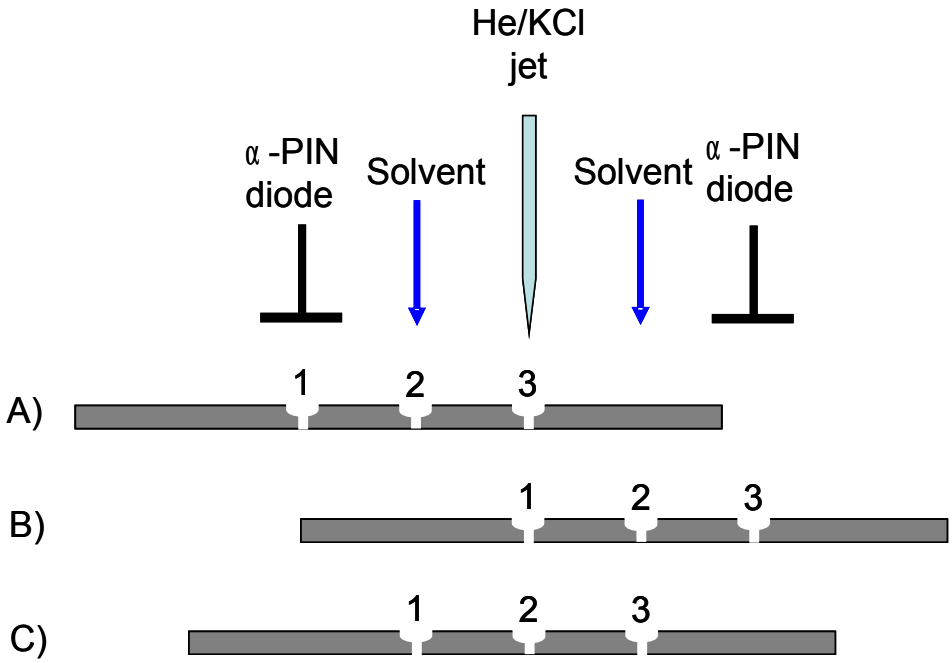

Figure 19: The three possible positions of the Kel-F™-slider. To monitor the gas jet yield the slider is brought into position A). The KCl-clusters and with them the transported nuclides are impacted in the cavity 3. After a preset time, the slider is brought into position B). The cavity 3 is now in front of the α-detector and the aerosol paticles are collected in cavity 1. By moving back the slider into position A), the activity collected in cavity 1 can be measured. To transfer nuclides in solution, the slider is placed in position C); aerosols are impacted into the cavity 2. After a preset time, the slider is moved into position A), now the clusters are collected in cavity 3 and the salt clusters and the nuclides in cavity 2 are dissolved and transferred into the chemistry device by flushing the cavity with solution. Afterwards the slider is moved back into position C), now cavity 3 can be flushed and the clusters are collected in cavity 2.

The degasser is controlled by a USB module (National instruments USB 6525). From this device, TTL signals were given to open or close the magnetic valve to empty the cell or to move the pneumatic cylinders using a valve terminal (Festo type 10 CPV).

The electrodes:

A platinum wire, which does not take up too much space and is relatively chemically inert, is used as counter electrode.

In the test experiment, Ag/AgCl reference electrodes of the type Dri Ref 2 (World Precisions Instruments) were used. These have the advantage that they are relatively small, – but the disadvantage that chloride solution cannot be refilled and they are constructed more for use at ambient temperatures. As an online experiment should run over several days/weeks at temperatures around 50°C, the reference electrode should be replaced by a pseudo-reference electrode. This can, for example, be a silver wire. The potential given by placing a silver wire in HCl solution of known concentration can be calculated by the Nernst equation.

The working electrodes first suggested were palladinated nickel tapes. These have two major disadvantages. First, the tapes can only be handled in lengths up to 10 m, so it is not useful for a long run experiment. The second major disadvantage is that the surface is not a homogeneous metal layer.

As gold has a very stable surface and worked well as deposition electrode, it was decided to use it as a tape electrode material. However, the cost of gold prohibited the use of pure gold tapes. A good alternative proved to be to sputter a gold layer on long Mylar™-foil tapes (20 µm thick, 2 cm wide and length up to 50 m). For covering the Mylar foil by gold, an existing sputter apparatus [101] was modified by T. Lauer. The tape was pulled continuously in front of the sputter head. This way, a homogeneous layer of gold was deposited over the entire Mylar tape.

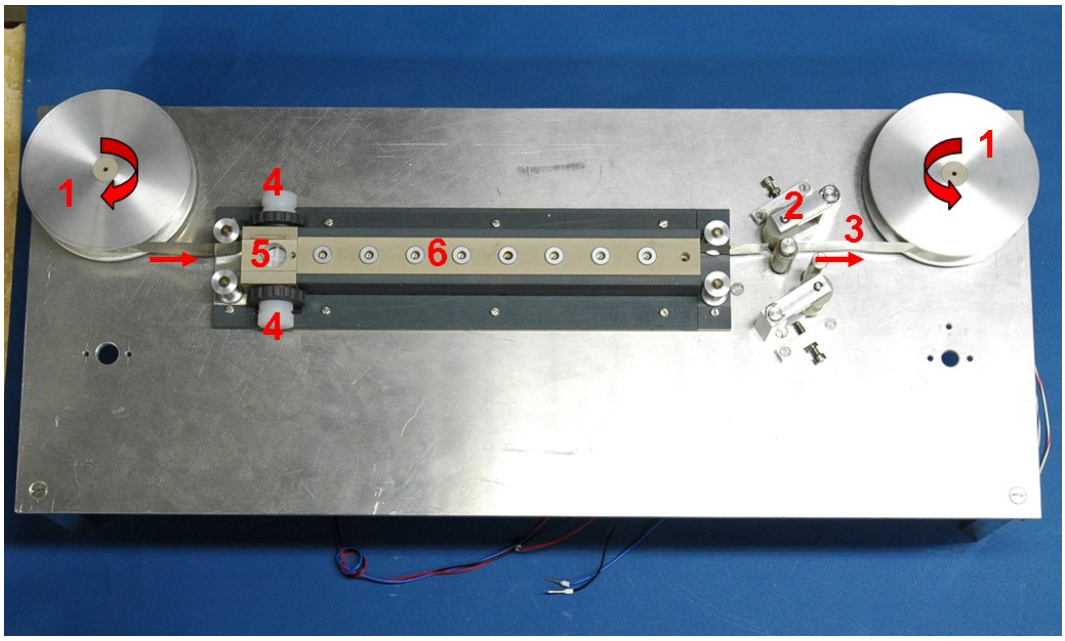

Figure 20: Photograph of the main part of the ELCH. Only one working electrode tape **3** *is mounted in this picture. The tape wheels* **1** *apply tension to the tape by being turned in opposite directions. The tape is moved by turning the silicon covered wheels* **2**. *These are driven by a strong stepping motor. The tape is fixed at the electrolysis cell with the nylon screws* **4**. **5** *is the cell with the magnetic stir bar. In part* **6** *is the α-detector array. The LEMO connectors to connect it to the pre-amplifiers are on the top of the device.*

In the ELCH, the tapes are continuously kept stretched by small motors turning the tape wheels in opposite directions. Small wheels, which are covered with silicon rubber and turned by a stronger stepping motor (Type PD4-N5918L4204 from Nanotec) were used to pull the tape from the electrolysis cell in front of the α-detector array (see Figure 20). The stepping motor was programmed and controlled with a LabView program.

The Electrolysis cell:

The electrolysis cell is directly connected to the α-detector array (see Figure 21). The cell is made of PEEK and has a cylindrical inner form. The used cylindrical magnetic stir bar fills most of the inner volume of the cell. 0.3 mL of electrolyte solution completely filled the cell and covered 2 cm^2 of working electrode surface.

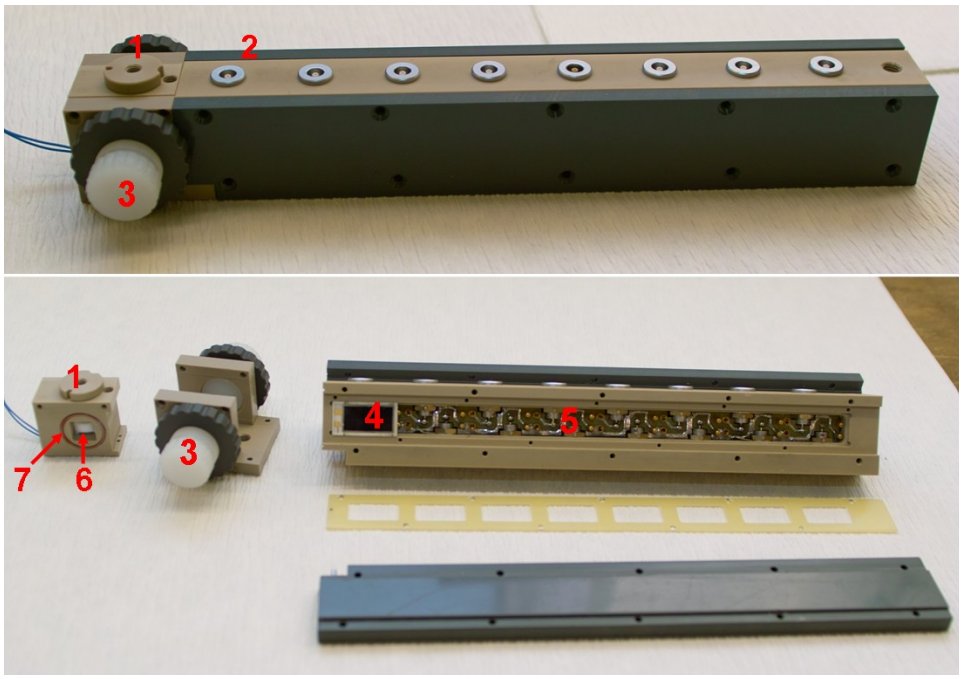

Figure 21: Photographs of the electrolysis cell connected with the α-detection array. The upper photo shows the closed device, the bottom shows the dismounted device. **1** *is the inlet to connect the cell to the degasser. The α-PIN-diodes are mounted on a board* **5** *and are connected by LEMO connectors* **2** *to the preamplifiers. The inner volume of the cell is nearly completely filled by the stir bar* **6**. *The electrode tapes are pressed by the Nylon screws* **3** *onto the FEP-coated sealing ring* **7** *to make the cell leak tight.*

The cell is connected by a tube to the degasser unit. It furthermore has an outlet, which is connected by a tube via a magnetic valve to an evacuated vessel (same as used in the previously mentioned beam time at TASCA). By opening this magnetic valve, the cell can be emptied within less than a second. The temperature in the cell is monitored by a Teflon™-covered PT100 temperature sensor. At the bottom of the electorlysis cell is a small heating device which is regulated by a temperature controller.

Originally, the cell was sealed by tightening the electrode tapes against FEP™ coated o-ring sealing with nylon screws. However, tightening by the screws caused the tape to twist, thus inhibiting its movement by the stepping motor. Therefore, a teflon plug was placed between the screw and the tape. This teflon plug did not turn as the screw was tightened, preventing the twisting of the tape. Unfortunately, the tape could not be moved once the cell was leak tight. The FEP-coated sealing was replaced by various other sealing rings such as viton or teflon. The leaking problem, however, could not be solved.

3.4 Summary and discussion of the electrochemistry experiment

In this work, it has been demonstrated that it is possible to deposit osmium and ruthenium under underpotential deposition conditions onto a gold surface.

The electrodeposition potential of ruthenium on gold from HCl solution was measured to be (4 ± 50) mV vs. Ag/AgCl at 55 °C (311 mV vs. a normal hydrogen electrode). The electrodeposition potential of osmium on gold from HCl solution is (130 ± 50) mV vs. Ag/AgCl at 60 °C (438 mV vs. a normal hydrogen electrode). A correct interpretation of these measured values is difficult.

Osmium and ruthenium are both known in various oxidation states from +8 down to -2. [102] According to ref. [103], the oxidation states of osmium chloride complexes are +2, +3, +4 and +6, the most common of which are +3 and +4.

Various ruthenium complexes are known to be formed in hydrochloric acid solution – the most common complex of ruthenium IV is $[RuCl_6]^{2-}$. Ruthenium (III) probably is in a mixed cationic and anionic complex like $[Ru(H_2O)_2Cl_4]^-$, $[Ru(H_2O)_3Cl_3]$, $[Ru(H_2O)_4Cl_2]^+$ and $[Ru(H_2O)_5Cl]^{2+}$. [103]

All studies presented in ref. [103] have been performed with macro amounts of ruthenium at room temperature. It is not sure that the behaviour of micro amounts is identical. Further investigations are necessary to get more informations about the chemical behaviour of single atoms of ruthenium in solution. This could be done, e.g., in ion-exchange studies at temperatures around 55°C. One could consider an ARCA experiment with anion and cation exchange resin in HCl solution at the TRIGA reactor.

Osmium is well known for forming anionic complexes in aqueous solution (see e.g. [104]). In hydrochloric acid, it is most likely to form anionic chloro or aqua-chloro complexes. The most common oxidation states in aqueous solution are +4 and +6. [103] In reference [105], chromatography studies under one-atom-at-a-time conditions as test experiments for a hassium chemistry studies were performed. These results were interpreted to be mainly due to the $[OsCl_6]^{2-}$ complex. This is likely also the complex studied in the electrodeposition experiments performed in this work, but as these experiments were conducted at temperatures between 50°C and 70°C, further ion-exchange studies in this temperature region should be performed to corroborate this assumption.

In reference [81], the influence of solvation and complexation is not taken into account. It is focused on "naked" ions that are reduced and deposited as neutral atoms. In the work of Hummrich [82], it was also seen that the electrolyte has an influence. But standard potentials of complexed ions usually differ from the potentials of the naked ions. Another problem is that it cannot be verified that the deposited form is the metallic osmium or ruthenium.

For thermodynamical considerations, one should take into account the solvation (as it was done in reference [106]) or complexation of the ions.

The Gibbs energy ΔG is related to the potential E

$$\Delta G = -n \cdot F \cdot E \tag{3.5-1}$$

and in general, the Gibbs enthalpy for a chemical process is

$$\Delta G = \Delta H - T \cdot \Delta S \tag{3.5-2}.$$

Taking into account the enthalpies for decomplexation/desolvation $\Delta G_{complex}$, overcoming the diffusion layers $\Delta G_{diffusion}$, reduction of the metal-ion $\Delta G_{reduction}$, and adsorption of the metal on the surface $\Delta G_{adsorption}$, the Born-Haber-cycle shown in Figure 22 is proposed.

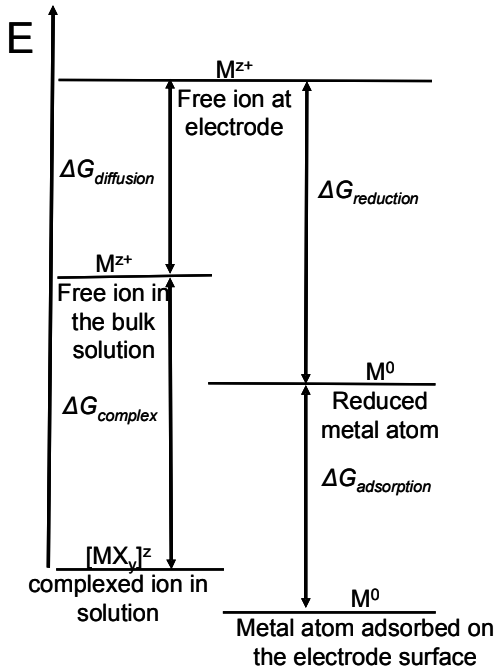

Figure 22: Proposed Born-Haber-Cycle of the deposition process.

Further progress in underpotential deposition studies with group 8 necessitates complexation studies verifying the chemical form in which ruthenium and osmium are present in solution.

According to reference [107], the most stable oxidation states of hassium in solution are +3 and +4. Until now, no experimental studies of hassium in solution have been performed and it is not sure that it would deposit as a pure metal.

Furthermore, several technical problems came up in the development of an automated apparatus. Due to the leaking problems and relatively long tape stepping times, the ELCH does not seem to be well suited for an online experiment. One should think about a new design for an electrolytic cell, e.g., direct deposition on a gold covered detector surface.

Gold seems to be a very promising material as electrode material for long experimental runs. It is relatively inert and the surface can be kept clean. Furthermore, one should think about using a pseudo-reference electrode instead of a reference electrode not designed for higher temperature and long term use.

The degasser developed in this work can be connected to various chemistry devices and was already successfully applied in a MicroSISAK experiment at the TRIGA reactor. [108]

Additional aspects to consider are the half-life of hassium and the cross-section, which are very low. The experiment would have to be performed in combination with physical preseparation,

leading to losses due to the limited transmission of TASCA.

Taking for example the reaction ^{248}Cm(^{26}Mg,5n)^{269}Hs with a cross section of 7 pb. The half-life of ^{269}Hs is 9.7 seconds estimated from the Q_α-values applying a Viola-Seaborg formula. [109] The transmission through TASCA would be around 15%. Estimating a target thickness of 0.5 mg/cm^2 and a stable beam of 800 $nA_{particle}$, a transparency of the RTC window of 80% and a stable jet yield (including the degasser yield) of 60%, 10 sec impaction in the degasser, 10 s time for the electrodeposition, and a detector efficiency of 30% - the average time needed for the detection of a single α-particle from the decay of ^{269}Hs is 20 days (if the experiment runs very stable without any breaks).

For a satisfying statistics one would need at least three or four events at one constant electrode potential. The experiment would have to run for 80 days and afterwards the electrode potential would have to be changed. At least three different electrode potentials should be measured. So the minimum period of beam time needed would be 240 days.

Hummrich suggested to use the ^{270}Hs. The half-life of 22 s was estimated with the Viola-Seaborg formula by measuring the Q_α-values. [110] The cross-section of the reaction ^{248}Cm(^{26}Mg,4n)^{270}Hs is around 3 pb. Taking the same estimates as for the 5n-channel it would take around 79 days to detect one α-particle from the decay of ^{270}Hs. The half-life of ^{270}Hs was recently measured in Dubna in the reaction ^{226}Ra(^{48}Ca,4n)^{270}Hs and found to be $7.6^{+5.3}_{-2.2}$ s [111], so it would be even less efficient.

Due to the estimations of needed beam time, a hassium chemistry experiment is out of reach.

Eichler and Kratz [81] focused in their predictions on the group 12-16 of the period. The nuclear fusion reactions to synthesize these elements have cross-sections of only a few picobarn (see ref. [22]) and their half-lifes are at most a few seconds. With the existing methods and techniques an electrodeposition of these elements cannot currently be performed.

4 Metal-Carbonyl-Complex-Chemistry - Introduction

In the past ten years, gas phase chemical studies using, e.g., thermochromatography have been the workhorse to learn about the chemical behaviour of elements with half-lives less than one minute. Gas phase studies gave the possibility to study the chemical behaviour of bohrium [112], hassium [52], copernicium [41], and element 114 [43],[113], which are out of reach with the established liquid phase chemistry techniques.

In gas-phase chemistry experiments, the elements have to be volatile either in the elemental state or as a quickly synthesized compound. The number of chemical systems that are appropriate for this method is very limited. Only simple, thermally stable, inorganic compounds have been studied so far. In most cases, volatile halides and oxohalides were synthesized, which was a successful method for the elements 104 to 107 (rutherfordium, dubnium, seaborgium, and bohrium). An overview is given in reference [114]. One problem with this method is the handling of the halogenating reagents. Another compound class includes volatile oxides and hydrooxides. Hassium has only been studied as tetroxide adsorbing on inert surfaces such as silicon nitride [52] and on moisturised sodium hydroxide [39]. A significant advantage of the oxide system is that oxygen is a relatively easy to handle reactive gas. This system can be used for thermochromatography detectors without any problems caused by deposition of the reagent on the detector surface. The disadvantage is that only a very limited number of elements of interest form volatile oxides.

Until now, only compounds in which the transactinide is in its highest oxidation state have been synthesized in gas-phase chemistry. Slight evidences of relativistic effects was observed in the studies of these compounds (see e.g. [30],[32]). It may be expected that in compounds of low oxidation states or even oxidation state 0 relativistic effect would be even stronger visible. This effect was already observed in the studies of copernicium [41] and element 114 [43],[113], which are both volatile metals.

Therefore, it is desirable to synthesize compounds with lower oxidation states of the transactinides, in which relativistic effects might be more prominently expressed. In the past, it was

not possible to synthesize metal-organic compounds or complexes with molecular ligands in in-situ chemistry experiments. If a recoil chamber behind a target is flushed with a molecular reagent, the plasma produced by the beam immediately destroys the molecular bonds. Furthermore, the recoil chamber is significantly heated decomposing thermally less stable compounds.

In the last years the method of physical preseparation [115] was established for chemistry experiments and TASCA (see chapter 2) was set up at GSI. At the BGS in Berkeley, it could already be demonstrated that organometallic compounds can be synthesized in an RTC. [116]

To combine the preseparation methods with thermochromatography and nuclear spectroscopy, the transactinide compounds would ideally be volatile at room temperature and below. As such, metal carbonyl complexes seem to be good candidates for this type of experiments.

Metal carbonyl-complexes are characteristic of d-elements and very well known to be volatile. [117] Most metal-carbonyl complexes are typically synthesized at high gas pressures around 300 bar in carbon monoxide atmosphere, which is not feasible in an online chemistry experiment. Furthermore, carbon monoxide is flammable and carbonyl complexes are unstable under some conditions. Therefore, there were initial doubts that carbonyl-complexes are appropriate compounds for studying the chemistry of transactinides. [114], [11] Nevertheless, the question was: is a high carbon-monoxide pressure necessary, if a recoiling atom is thermalized in carbon-monoxide atmosphere.

First test experiments at the TRIGA Mainz reactor reported in the diploma work of Niewisch [118] showed, that the recoiling fission products molybdenum, technetium, ruthenium, and rhodium form volatile carbonyl-complexes, if they are thermalized in a CO-containing atmosphere. The complexes were transported in a gas stream over several meters and separated on a thermochromatography column. [118] This first promising experiment gave the motivation to go on with the studies of carbonyl complexes in online experiments.

4.1 Metal-Carbonyl Complexes

Metal-carbonyl complexes play an important role in inorganic and metal-organic chemistry. They are of great interest as catalysts. Iron pentacarbonyl is produced in kilotons per year for magnetic tapes, nickel tetracarbonyl is the basis for the Mond-process [119] to purify nickel, and many more industrial processes are based on metal-carbonyl complexes. Literature [120] gives an overview of the history and use of carbonyl chemistry. Nowadays, metal-carbonyl complexes are also a focus of interest for radiopharmaceutical research. [121], [122]

The first binary carbonyl-complex, reported in literature in 1890, was nickel tetracarbonyl. Mond and Langer first calcined nickel-containing ores and then treated them with generator gas or water gas at temperatures as low as possible. Finally, the nickel was volatilized as $Ni(CO)_4$ by flushing the reaction chamber with carbon monoxide. The nickel tetracarbonyl was heated to 180°C and pure nickel-metal was obtained. [119]

In 1891, Mond and Langer reported the synthesis of iron pentacarbonyl. [123] Iron pentacarbonyl can be produced by treating pure iron powder with carbon-monoxide at 1 bar. [119] It was later shown, that unpurified iron powder (with an oxide layer) also can be used, if a carbon-monoxide pressure of 300 bar is used.

The development of high pressure techniques led to the discovery of further carbonyl-complexes such as dicobalt octacarbonyl and molybdenum hexacarbonyl. [124] Furthermore, syntheses starting from the metal-salts under high CO pressure were developed to obtain the hexacarbonyls of group 6 elements, and iridium carbonyl and technetium carbonyl compounds. [125], [126], [127]

Table 1 shows all stable, binary metal-carbonyl complexes known from literature. Neutral, binary complexes of Pd, Pt, Cu, Ag, and Au could only be observed in matrix isolation experiments at low temperatures (see e.g. [128], [129]).

Table 1: Stable, neutral, binary metal-carbonyl complexes, list is taken form [130]:

$V(CO)_6$	$Cr(CO)_6$	$Mn_2(CO)_{10}$	$Fe(CO)_5$	$Co_2(CO)_8$	$Ni(CO)_4$
			$Fe_2(CO)_9$	$Co_4(CO)_{12}$	
			$Fe_3(CO)_{12}$	$Co_6(CO)_{16}$	
	$Mo(CO)_6$	$Tc_2(CO)_{10}$	$Ru(CO)_5$	$Rh_2(CO)_8$	
		$Tc_3(CO)_{12}$	$Ru_3(CO)_{12}$	$Rh_4(CO)_{12}$	
				$Rh_6(CO)_{16}$	
	$W(CO)_6$	$Re_2(CO)_{10}$	$Os(CO)_5$	$Ir_4(CO)_{12}$	
			$Os_3(CO)_{12}$	$Ir_6(CO)_{16}$	
			$Os_6(CO)_{18}$	$Ir_6(CO)_{16}$	

Structure and stability of metal-carbonyl-complexes:

The ability of the σ-donor CO ligand to give additional π-backbondings leads to the stability of metal carbonyl complexes with neutral or anionic metal ions. All stable, neutral, binary complexes described in the literature fulfil the 18 valence electron rule with exception of $V(CO)_6$, which has 17 valence electrons. Its octahedral geometry stabilizes this radical molecule and prevents radical-type reactions. (see e.g. [130])

The symmetry of mononuclear transition metal-carbonyl complexes can be explained by the hybridization model of Pauling. Complexes of the type $M(CO)_6$ are octahedral, $M(CO)_5$ are a trigonal bipyramidal and $M(CO)_4$ are tetraedral. (see Figure 23).

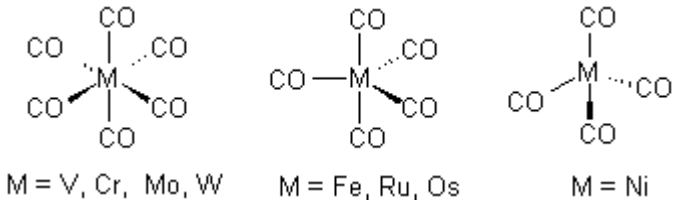

Figure 23: Structure of the stable, binary, mono nuclear transition-metal-carbonyl complexes

Theoretically, metal-carbonyl complexes are one of the most thoroughly investigated classes of transition metal compounds. The CO ligand is a σ-donor and π-acceptor. The dominant interactions in the bonding between the transition metal and the ligand are i) the interaction of the 5σ HOMO (Highest Occupied Molecular Orbital) of the CO molecule with an empty, σ-symmetric atom orbital of the metal (the d_{z^2}-orbital or a p orbital) and ii) the interaction between the 2π* orbital of the CO

and occupied π-type d-orbitals of the metal. [131] Figure 24 shows a scheme of the σ-donation and π-backbonding of the CO ligand to the transition metal. In most cases, the interaction between the 1π-orbital of the CO ligand with an empty, π-type d orbital of the metal (the CO π-donation) is negligible. [130]

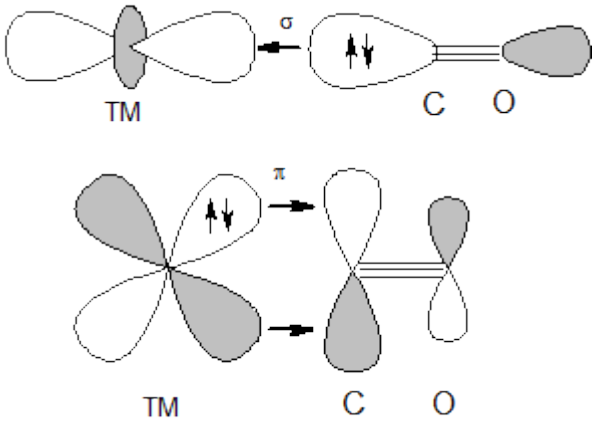

Figure 24: Scheme of the synergistic σ-donation and π-backbonding of the CO ligand with the transition metal (TM), the σ-donation bonding is established between the 5σ HOMO of the CO and the d_{z2}-orbital or a p-orbital of the TM. The π-backbonding is between the 2π orbital of the CO and an occupied π-type d-orbital of the TM.*

The σ-donation interaction leads to a slightly stronger bonding between the C and O, causing the wave number of the CO stretch vibration to increase. The back-donation of electron denisity into the antibinding orbital of the CO (the π-backbonding) leads to a weaker bond between the C and the O causing the wave number of the CO stretch vibration to decrease.

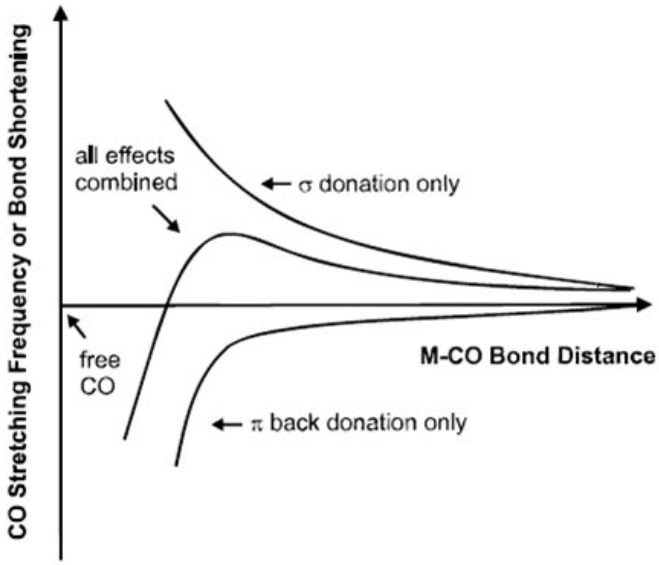

Figure 25: Effect of the σ-donation and π-backbonding on the TM-CO and C-O binding length. [132]

A comparison of isoelectronic 18 valence electron (VE) complexes of the type $[M(CO)_6]^q$ (q = 2-, 1-. 0, 1+, 2+, 3+) with an ionic central metal and a neutral, octahedral CO-cage is shown in Figure 26. With increasing proton number, the σ- donation and the wave number υ_{CO} of the CO stretch vibration increases and the π-backbonding decreases. [132]

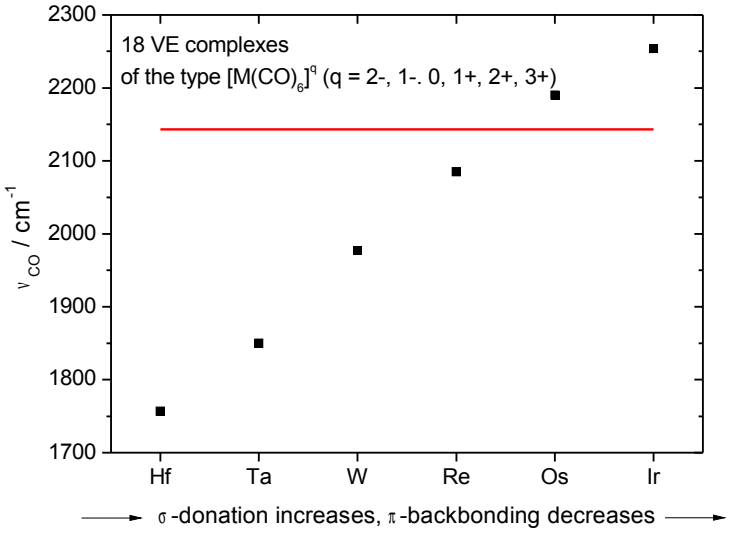

Figure 26: Trends in M-CO binding and wave number of the CO stretch vibration for 18 valence electron (VE) complexes of the type $[M(CO)_6]^q$ (q = 2-, 1-. 0, 1+, 2+, 3+). Data are taken form [132] (experimental data of the T_{1u} vibration mode). The red line shows the wave number of the vibration of free CO ($\upsilon_{CO(free)}$=2143 cm^{-1}).

Nash and Bursten calculated the wave number of the CO vibration for the neutral hexacarbonyl complexes of group 6 elements [133] – the wave numbers all differ only slightly from each other, which can also be seen in the C-O bond length shown in Figure 27. Typical bond lengths in the hexacarbonyl complexes are for the metal-carbon bond around 2 Å and for the carbon-oxygen bond around 1.15 Å.

The experimental wave number for the T_{1u} vibration mode of $Mo(CO)_6$ and $W(CO)_6$ are similar (2003.0 cm^{-1} and 1997.6 cm^{-1}), with a slightly lower vibration frequency measured for $W(CO)_6$. This phenomenon is attributed to relativistic expansion and destabilisation of the 5d shell of tungsten. [133],[134]. This trend is even more visible in the calculated vibrational frequency for $Sg(CO)_6$, which is 1956.1 cm^{-1}. [133] The greater relativistic destabilisation of the Sg 6d orbital compared to the W 5d orbital leads to a stronger π-backbonding between the Sg 6d orbital and the 2π* orbital of the CO. The predicted lower stretching frequencies of $Sg(CO)_6$ are in agreement with the predicted longer C-O bond length compared to the carbonyl complexes of the lighter homologs [133], as shown in Figure 27.

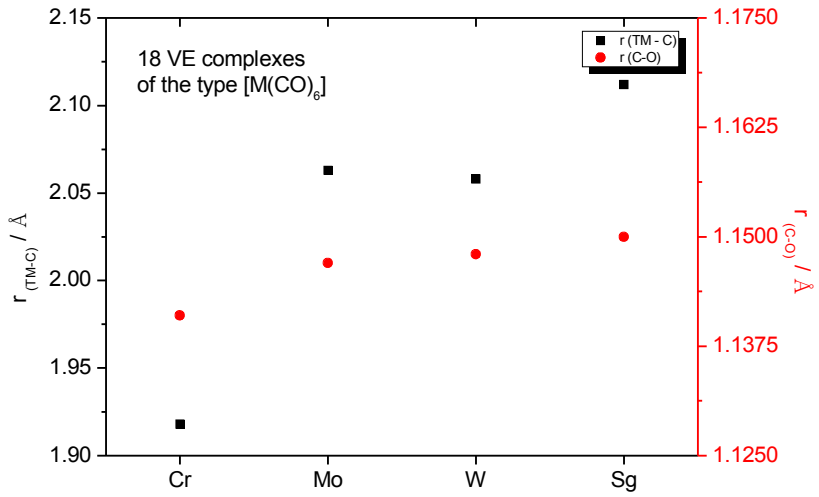

Figure 27: Length of the metal-carbon bond ($r_{(TM-C)}$) and of the carbon-oxygen ($r_{(C-O)}$) in hexacarbonyl complexes of the type [$M(CO)_6$]. The data are taken from [133],[135], the values for chromium, molybdenum, and tungsten are measured in experiments, the values for seaborgium are calculated.

Nash and Bursten predicted that the Sg-C bond is 0.04 Å longer than the W-C bond, which is equal to the difference of the atomic radii of Sg and W. [133] For the octahedral hydrides of the type MH_6, Pyykkö and Declaux calculated that the bond length of Sg-H is 0.06 Å longer than the W-H bond. [136] The smaller difference of the bond length can be explained by the stronger π-backbonding in the $Sg(CO)_6$ complex. [133]

Nash and Bursten predicted a slightly higher value for $Sg(CO)_6$ than for $W(CO)_6$ for the first carbonyl dissociation energies, which is in agreement with the stronger π- backbonding.

One result of Nash and Bursten´s studies is the predictions, that seaborgium forms hexacarbonyl complexes that are comparable to the carbonyl complexes of the other group 6 elements and not like the theoretically-predicted isoelectronic actinide complex $U(CO)_6$. [133]

Actinide carbonyl complexes differ from the transition metal-carbonyl complexes. Uranium hexacarbonyl is extremly unstable and could not be synthesised [133]. However, the cationic carbonyl complexes $[U(CO)_8]^+$ and $[UO_2(CO)_5]^+$ can be analyzed by mass-selected ion infrared spectroscopy in the C-O stretching region. [137] For $[U(CO)_8]^+$ the C-O stretch has a comparable frequency as for the neutral transition-metal complexes, which indicates that the π-backbonding is significant. [137]

Patzschke and Pyykkö also made predictions of darmstadtium monocarbonyl (DsCO) and (PtCO) and compared it with carbon dioxide. [138] These molecules are interesting for theoretical studies as CO is a strong ligand – however, this type of compound probably does not exist. Until now, everything known about transactinide carbonyl complexes are theoretical predictions, no experimental data are available.

Hot atom chemistry of metal-carbonyl complexes:

A remarkable "non-classical" method to synthesize carbonyl-complexes is the use of hot atom chemistry. In the 1960´s and 1970´s, there was significant research activity studying hot atom chemistry. An overview of hot atom chemistry with organometallic compounds, including metal-carbonyl-complexes, is given in the literature [139].

Heck [140] irradiated ^{235}U in carbon dioxide atmosphere. After the irradiation, the reaction vessel was flushed with gas, which was passed through a charcoal filter. ^{99}Mo could be identified in the filter by γ-ray measurements, providing evidence for molybdenum hexacarbonyl formation.

Baumgärtner and his co-workers used Szilard Chalmers type reactions in the solid state to produce $^{99}Mo(CO)_6$. [141] They mixed U_2O_3 with solid $Cr(CO)_6$ and irradiated it with thermal neutrons. Afterwards, the mixture was heated to 90°C in vacuum. The sublimate was collected on a glass wool plug and ^{51}Cr (formed in (n,γ)-reaction) and ^{99}Mo were identified. Further analysis of the sublimate proved that $^{99}Mo(CO)_6$ was formed. It was found that 60% of the ^{99}Mo were formed as the volatile hexacarbonyl and could be sublimated, the rest stayed in the uranium mixture. As only 2 % of ^{99}Mo atoms are formed as primary fission products, it is clear that also the secondary fission products will form molybdenum hexacarbonyl complexes.

Later, this method was optimized and used to discover the fission products ^{104}Mo [142] and ^{105}Mo [143] and their technetium and ruthenium daughter nuclides. As ^{104}Mo and ^{105}Mo are mainly formed as primary fission products, it appears that primary fission products, as well as products from beta decay, form hexacarbonyl complexes using this method.

Similar experiments were performed by Wolf and Fröschen at the cyclotron in Karlsruhe. [144] Chromium, tungsten, and molybdenum were produced in nuclear fusion reactions and the recoiling ions were stopped in chromium hexacarbonyl. The synthesized carbonyl complexes were separated by sublimation and condensation. From their studies, Wolf and Fröschen suggested to perform

carbonyl-chemistry experiments with seaborgium at the UNILAC, which was under development at that time. A scheme for their proposed experiment is shown in Figure 28.

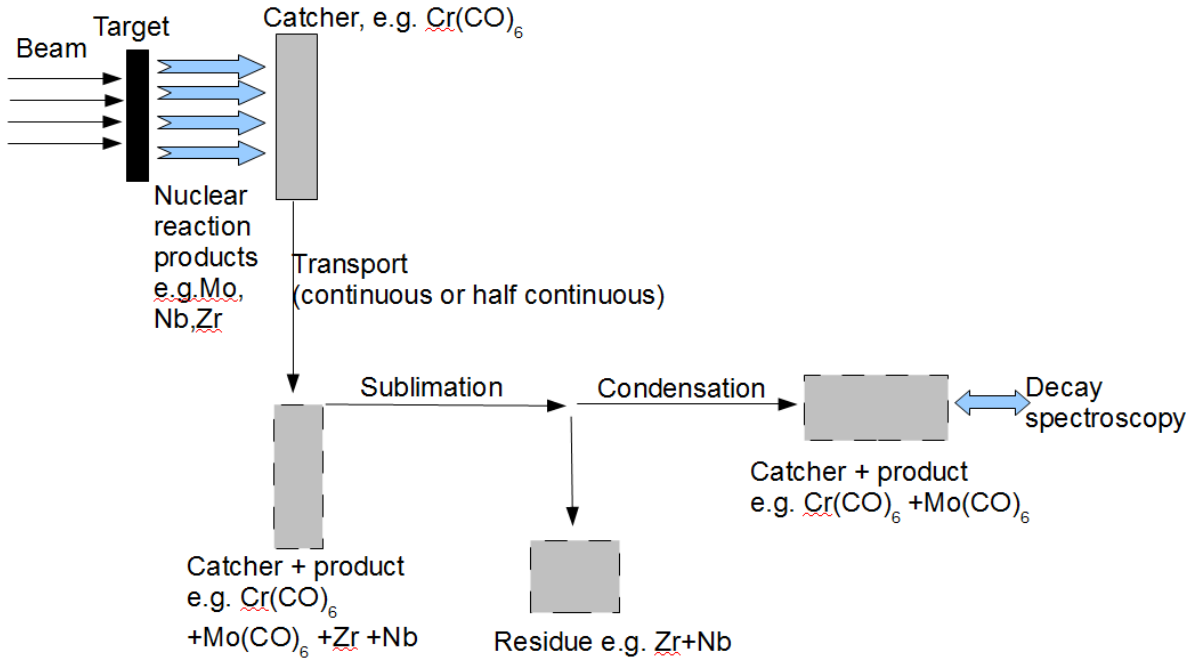

Figure 28: Scheme for an experiment to synthesize group 6 carbonyl-complexes out of heavy ion fusion reaction products suggested by Wolf and Fröschen. Drawing reproduced from literature [144].

In the studies of the β-decay products of $^{99}Mo(CO)_6$ it was observed that the technetium pentacarbonyl radical is formed in THF [145], n-pentane, chloroform, and petroleum ether as well as in the solid state matrix [146]. The highest yields of the technetium pentacarbonyl radical were obtained in the solid state matrix – with over 73%. The pentacarbonyl radicals of manganese and rhenium could be produced in (n,γ)-reactions of dirhenium decacarbonyl [147] (with a yield of 5.1% of $\cdot^{186}Re(CO)_5$ and 5.5% of $\cdot^{188}Re(CO)_5$) and in (n,γ)-reactions of dimanganese decacarbonyl [148] (with a yield of 4.5% $\cdot^{56}Mn(CO)_5$).

4.2 Gas-chromatography

A common technique in transactinide gas-phase chemistry is the chromatography technique. [149], [150] From literature it is known that gas chromatography is a suitable technique to analyze metal carbonyl complexes. [151] As mentioned previously, there are two common experimental gas chromatography techniques used in transactinide chemistry – isothermal chromatography and thermochromatography.

In isothermal chromatography, the chromatography column is kept at a constant temperature. The experiment is repeated several times at different temperatures. At each temperature, the retention time of the compound of interest is determined. In the case of short-lived, radioactive compounds the relative yield of the atoms of interest which reach the end of the column is measured. If 50% of the atoms decay before they reach the end of the column, the time the compound takes to pass through the column is equal to the half-life of the isotope. Thus, the nuclear half-life is taken as an "internal clock" to determine the retention time at $T_{50\%}$. Figure 29 shows the typical curve of an isothermal chromatogram.

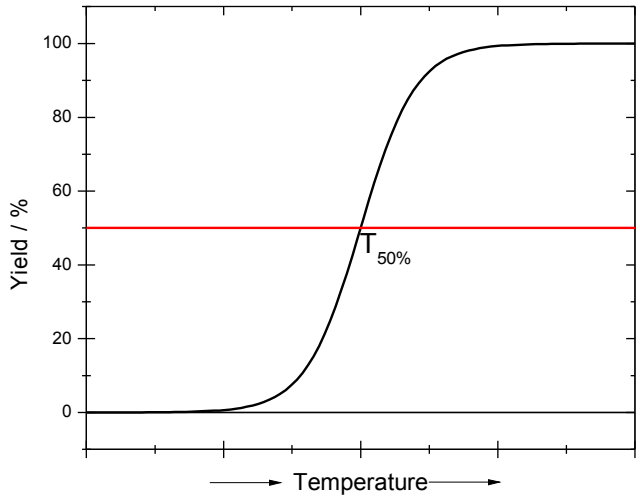

Figure 29: Chromatogram of an isothermal chromatography experiment with a radioactive compound. The experiment itself consists of several experiments at various temperatures. At each temperature, the amount of analyte reaching the end of the column is determined. The amount of time the analyte takes to run through the column at the temperature $T_{50\%}$ is equal to the half-life of the isotope.

In a thermochromatography experiment, a negative temperature gradient is applied along the chromatography column. At the beginning of the column, the temperature is highest while the exit of the column is coldest. During its flight through the column, the analyte interacts with the column surface. The duration the atom or molecule sticks on the surface depends on the local temperature. If the time it sticks on the surface is longer than the life-time of the atom, the decay is observed in this position. A typical chromatogram is shown in Figure 30. In experiments with radioactive analytes, the chromatography peak is detected by decay spectroscopy. This can be done by scanning the column with a γ-detector, or in case of α- or spontaneous fission decaying isotopes, the column itself can be made from α-PIN diodes. [67]

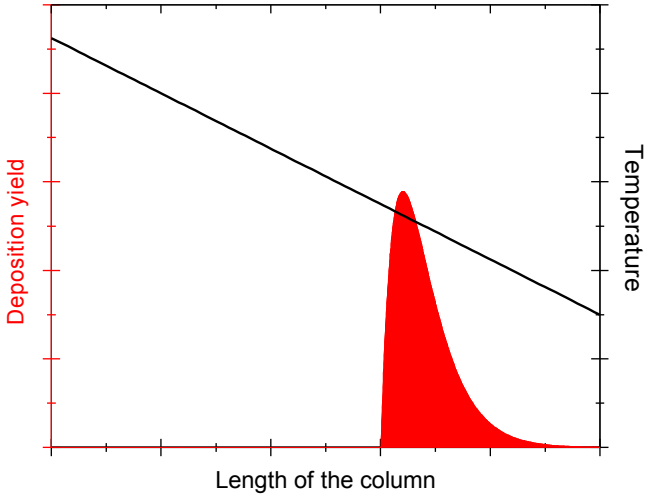

Figure 30: A typical thermochromatogram. The black line shows the temperature gradient over the column and the red curve is the deposition peak of the analyte.

4.2.1 Adsorption

Gas-chromatography yields information about the adsorption mechanism of the analyte on a specific surface. Two types of adsorption exist – physisorption and chemisorption.

Physisorption describes adsorption only due to Van der Waals interactions between adsorbate and adsorbent. This interaction is an electrostatic attraction of the permanent or induced dipole moments of the two species. The dispersion interaction energy $E_{(x)}$ can be describe with the London equation (4.2.1-1) [152],

$$E_{(x)} = -\frac{C_1}{x^6} \qquad (4.2.1\text{-}1)$$

where C_1 is the van der Waals constant between the two systems and x is the interaction distance in centimeters.

In the chemisorption process, a chemical bond is formed between the surface and the adsorbate. In this case, equation (4.2.1-1) cannot be applied. It is also possible that a intermediate situation between physical and chemical adsorption occurs. [114]

Carbonyl complexes are known to physisorb on various surfaces. Several studies about the adsorption of hexacarbonyl complexes on Al_2O_3 and SiO_2 are described in literature [153],[154], [155],and [156]. On Al_2O_3, first physisorption followed by the formation of surface complexes is reported. In reference [153] it is reported that molybdenum hexacarbonyl is first physisorbed on silicon dioxide and under vacuum, it looses some of the carbonyl ligands and forms surface complexes. For chromium and tungsten hexacarbonyl, only physisorption was observed. This is in agreement with the experimental studies of chromium hexacarbonyl on silica reported in reference [156].

Thermodynamics of adsorption

The adsorption enthalpy ΔH_{ads} can be determined in the analysis of gas chromatography experiments, while this is not the case fo the dispersion interaction energy $E_{(x)}$. $E_{(x)}$ is the energy

needed to remove an adsorbed atom or molecule in the frozen state (no translatory or vibrational degrees of freedom) from a surface. If the molecule leaves the surface to the gas-phase, it gets three translatory degrees of freedom (*E=1.5RT*) (see Figure 31). If this molecule adsorbs on the surface, the enthalpy ΔH_{ads} is set free. In case of mobile adsorption, the molecule still has the energy of one vibrational degree of freedom and two translatory degrees of freedom (*E=2RT*) (see Figure 31).

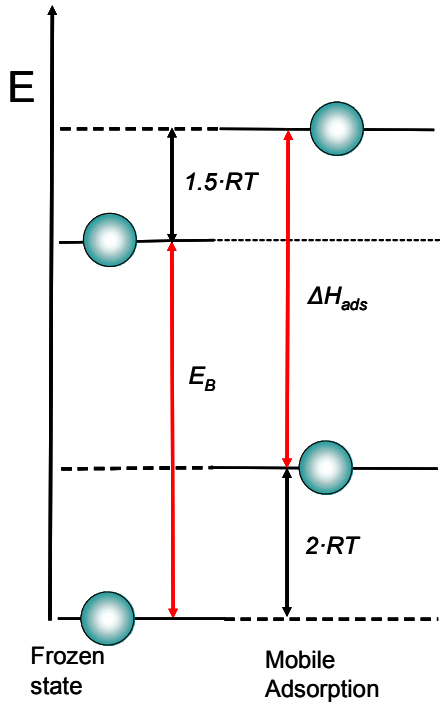

Figure 31: Scheme of the relation between $E_{(x)}$ and ΔH_{ads}., reproduced from reference [157].

The relation between $E_{(x)}$ and ΔH_{ads} is described in equation (4.2.1-2).

$$E_B = -\Delta H_{ads}^{0(T)} + 0.5 \cdot R \cdot T \qquad (4.2.1\text{-}2)$$

For the adsorption process, the fundamental equations

$$\ln K_p = \frac{-\Delta H_{ads}}{R \cdot T} - \frac{\Delta S_{ads}}{R} \qquad (4.2.1\text{-}3)$$

$$\ln K_C = \frac{-\Delta U_{ads}}{R \cdot T} + \frac{\Delta S_{ads}}{R} \qquad (4.2.1\text{-}4)$$

are valid. K_p is the equilibrium constant for partial pressure and K_C is the equilibrium constant for concentrations, ΔU is the change in internal energy, ΔH_{ads} is the change of the enthalpy and ΔS_{ads} is the change of the entropy in the process of adsorption. R is the ideal gas constant and T the temperature. [114]

4.2.2 Monte Carlo Simulation of gas-chromatography experiments

The thermochromatograms presented in this thesis were analysed by comparing them with Monte Carlo Simulation.

Zvara suggested to use Monte Carlo simulations [158] to determine the adsorption enthalpy from the measured thermochromatograms. Türler established this method for analysing isothermal chromatography data [159] and a detailed discussion can be found in reference [114]. First Monte Carlo simulations were developed for chromatography channels with a circular cross section. Problems came up when these Monte Carlo programs were used to analyze experiments with thermochromatography columns made of α-PIN-diodes. [67], [68] In these thermochromatography detectors, the chromatography channel has a rectangular cross section. The existing Monte Carlo simulation programs for circular columns were adapted for the rectangular channel. This was accomplished by dividing the rectangular channel into several virtual circular channels. The radius of the virtual channels was half the height of the rectangular channel. The Monte Carlo simulations were just run for one of these virtual channels. One big problem in this method is that the volume to surface ratio is much smaller than in reality, resulting in the predicted mean free path of an atom until it contacts the wall being too small. In other experiments [83], it was tried to take into account this theoretical-actual mean free path discrepancy. None of the existing simulation programs took into account that the flow profile of a circular channel is significantly different from that of a flat rectangular channel. This mainly influences the height of the theoretical chromatography plates.

The velocity distribution of a laminar flow in a circular tube with the radius r_c is parabolic with the maximum velocities v_{max} in the centre of the tube [160] and equal to,

$$v' = 2 \cdot v_{max} \left(1 - \frac{r^2}{r_c^2}\right) \qquad (4.2.2\text{-}1)$$

The local velocity v' depends on the distance r from the centre. The maximum velocity is twice as high as the mean velocity

The velocity distribution in a rectangular channel strongly depends of the width b to height h ratio.[160]

If $b = h$:

$$v_{max} = 2.1 \cdot v_{mean}$$

If $b >> h$

$$v_{max} = 1.49 \cdot v_{mean}$$

Therefore, it became necessary to write a new simulation program based on the existing codes. Some equations describing general aspects in gas chromatography had to be changed or added to account for the rectangular profile.

In the following pages, the simulation method will be introduced for chromatography columns with rectangular and with circular cross sections.

Diffusion:

Diffusion describes the movement of a molecule in a gas volume without any dynamic flow of the gas. It depends on the mean free path $\lambda_{m,1}$ of a molecule between two collisions with other atoms [158], where

$$\lambda_{m,1} = \frac{1}{\pi \cdot n_2 \cdot \omega_{1,2}^2} \qquad (4.2.2\text{-}2)$$

n_2 is the number of gas atoms. The collision diameter $\omega_{1,2}$ is equal to

$$\omega_{1,2} = \frac{d_{m,1} + d_{m,2}}{2} \qquad (4.2.2\text{-}3)$$

$d_{m,1}$ is the molecular diameter of the tracer and $d_{m,2}$ is the diameter of the gas molecules. The mean free path depends on the number of gas atoms n_2 and, therefore, it is proportional to the gas pressure. Diffusion contributes to the widening of the chromatography peak. The mean squared diffusional displacement z_D^2 is given by the diffusion coefficient $D_{1,2}$ and the time t with [158]

$$z_D^2 = 2 \cdot D_{1,2} \cdot t \qquad (4.2.2\text{-}4)$$

The early Stefan-Maxwell equation describes diffusion in a gas composed of hard sphere molecules and gives the diffusion coefficient by

$$D_{1,2}=\frac{\alpha}{n\cdot\omega_{1,2}^2}\cdot\sqrt{\frac{8\cdot R\cdot T}{\pi}\cdot\left(\frac{1}{M_1}+\frac{1}{M_2}\right)} \qquad (4.2.2\text{-}5)$$

where n is the total number of molecules, α is a coefficient which varies depending on the chromatography system, R is the ideal gas constant, T is the temperature and M_1 and M_2 the atomic masses of the molecules.

More precise semi-empirical equations have been established to describe diffusion processes, such as the Gilliland's equation, Arnold's equation, the Hirschfeld-Bird-Spotz equation, the Chen-Othmer equation, and the Fuller-Schettler-Gilliland equation. A detailed discussion of the equations can be found in reference [161], pages 237-241. While the Gilliland equation is not the most precise equation, more sophisticated equations require molecule parameters that only exist for a limited number of compounds. Therefore, $D_{1,2}$ is calculated in the simulations with the following Gilliland's equation:

$$D_{1,2}=\frac{0.0044\cdot T^{3/2}}{p\cdot\left[\left(\frac{M_1}{\rho_1}\right)^{1/3}+\left(\frac{M_2}{\rho_2}\right)^{1/3}\right]^2}\cdot\sqrt{\frac{1}{M_1}+\frac{1}{M_2}}\left[\frac{cm^2}{s}\right] \qquad (4.2.2\text{-}6)$$

where T is the temperature, p the gas pressure in bar, ρ_1 is the density of the diffusing gas, ρ_2 is the density of the diffusion medium and M_1, M_2 are their respective molecular weights. The diffusion coefficient for heavy molecules in common carrier gases at a pressure around one atmosphere is 0.01 – 0.1 cm^2/s. [114]

Mean jump length

The flight of a molecule through the column can be described by several jumps with ranges on the order of centimetres. The molecule travels in the gas stream until it hits the wall. Adsorption chromatography can be described by the non-equilibrium theory. The overall concentration c is the sum of all local concentrations c_i all over the column. At the equilibrium, all concentrations over the

column would be equal $c^{\S}_{i.}$. If equilibrium were reached, each part of the column would contain the fraction $X^{\S}_{i.}$ [161] with,

$$X_i^{\S} = \frac{c_i^{\S}}{c} \tag{4.2.2-7}$$

The non-equilibrium and equilibrium concentrations are related by the non-equilibrium departure term $\epsilon_{i.}$ with

$$c_i = c_i^{\S}(1+\epsilon_i) \tag{4.2.2-8}$$

The theoretical plate height H of a chromatography channel of any shape is a common factor in chromatograph experiments - it is expressed by ratio of the width σ_z^2 of the chromatography peak to the migration distance z in flow direction. According to reference [161], this is given by

$$H = \frac{\sigma_z^2}{z} = \frac{-2 \cdot \sum X_i^{\S} \cdot \epsilon_i \cdot v_i}{v_{mean} \cdot \frac{\partial \ln c}{\partial z}} \tag{4.2.2-9}$$

v_i is the velocity of a single tracer molecule, v_{mean} is the average velocity of the molecules. The variance σ_z^2 depends on the ratio, *Ro,* of the time the molecule flies in the gas stream, *tf,* to the total time the molecule spends on the surface of the column, *ta*. [161] That is

$$Ro = \frac{tf}{tf + ta} \tag{4.2.2-10}$$

In some cases, the ratio k is used, which is given by

$$k = \frac{ta}{tf + ta} \tag{4.2.2-11}$$

Assuming a simple two phase system such as that in gas-phase chromatography in open columns the local departure term ϵ_M' can be expressed by

$$\nabla^2 \epsilon'_m = \frac{v' - Ro \cdot v_{max}}{D} \cdot \frac{\partial \ln c}{\partial z} \qquad (4.2.2\text{-}12)$$

where v' is the local velocity. The equation of the plate height can be written as

$$H = -\frac{2}{A_m} \cdot \frac{\int \epsilon'_M \cdot v' \, d\, A_M}{v \cdot \partial \ln c / \partial z} \qquad (4.2.2\text{-}13)$$

where A_M is the cross-section of the chromatography channel.

In literature [162] and [161] pages 153-154, this integral is solved, leading to Golay`s equation for the plate height $H°$ of a chromatography column with a circular cross section with a radius r_C

$$H° = \frac{(6\,Ro^2 - 16\,Ro + 11) \cdot r_c^2 \cdot v}{24\,D_{1,2}} \qquad (4.2.2\text{-}14)$$

Gurshka [163] extended this equation through the addition of a diffusion part:

$$H° = \frac{2D_{1,2}}{v} + \frac{(6\,Ro^2 - 16\,Ro + 11) \cdot r_c^2 \cdot v}{24\,D_{1,2}} = \frac{r_c^2 \cdot \pi \cdot D_{1,2}}{Q} + \frac{(6\,Ro^2 - 16\,Ro + 11) \cdot Q}{48 \cdot \pi \cdot D_{1,2}} \qquad (4.2.2\text{-}15)$$

where Q is the mean volumetric velocity in cm^3/s.

For rectangular channels, Golay proposed in reference [164] the following equation to calculate the plate height $H^{\square}$:

$$H^{\square} = \frac{2D_{1,2}}{v} + \frac{4 \cdot (1 + 9\,k + 25.5\,k^2) \cdot v \cdot (0.5 \cdot y)^2}{105 \cdot (k+1)^2 \cdot D_{1,2}} \qquad (4.2.2\text{-}16)$$

where y is the channel height.

As the flow profile depends on the width to heigh ratio, φ, of the channel, Poppe [165] rewrote the Golay equation in more general terms

$$H^{\square} = \frac{2D_{1,2}}{v} + \frac{(f_0 + f_1 k + f_2 k^2) \cdot v \cdot (0.5 \cdot y)^2}{105 \cdot (k+1)^2 \cdot D_{1,2}} \qquad (4.2.2\text{-}17)$$

and determined the coefficients f_i for various values of φ.

For the COMPACT detector:

$\varphi \sim 16$

and according to Poppe [165]

$f_0 = 7.301$, $f_1 = 21.673$ and $f_2 = 31.872$.

This equation (4.2.2-17) was used to determine the mean flight distance of a molecule through the detector channel.

Adsorption:

The mean time a molecule spends on the surface after contacting the wall, $\tau_{a,mean}$, is expressed in the Frenkel equation. [114],[158]

$$\tau_{a,mean} = \tau_0 \cdot e^{\frac{-\Delta H_a}{R \cdot T}} \qquad (4.2.2\text{-}18)$$

where τ_0 is the period of vibration perpendicular to the surface in the adsorbed state. In our case, τ_0 is equal to the reciprocal Debye's phonon frequency of the column surface. [81] The other two factors, that influence the adsorption time, are the local temperature T of the surface and the adsorption enthalpy, ΔH_a.

The total time a molecule spends at the wall in one certain part of the chromatography channel depends on τ_a and the frequency of collisions with the wall. According to Zvara [114] the number of collisions with the wall Z_z over a distance z in gas flow direction is

$$Z_z = \frac{u_m \cdot za_z}{4 \cdot Q} \qquad (4.2.2\text{-}19)$$

where Z_z is a function of the ratio of column surface za_z to volume flow Q and of the mean speed of the molecule u_m. u_m is given by

$$u_m = \sqrt{\frac{8RT}{\pi M}} \tag{4.2.2-20}$$

If z=1, we obtain for a circular channel:

$$Z_z^{\circ} = \frac{r_c}{Q} \cdot \sqrt{\frac{2 \cdot \pi RT}{M}} \tag{4.2.2-21}$$

and for a rectangular channel:

$$Z_z^{\square} = \frac{(x+y)}{Q} \cdot \sqrt{\frac{2RT}{\pi M}} \tag{4.2.2-22}$$

Monte Carlo Simulation:

With these equations, it is possible to write a Monte Carlo Simulation program as suggested in reference [158]. The source codes of the simulation programs used in this work written in Python are given in the appendix A of this thesis.

The form of the chromatography column (rectangular or circular) is described as well as its length z, its radius r_c or its width x and height y. The temperature gradient is entered as a fit function in the program. The constants R, the gas pressure p, the molecular mass of the carrier gas M_1 and of the molecule M_2, the density of the the gas ρ_1 and of the molecule ρ_2, the period of oscillation of the column surface τ_0, the half-life of the isotope $t_{1/2,}$ the volumetric gas flow Q, and the adsorption enthalpy ΔH_a, and the number of molecules to be simulated are inputs into the simulation.

First the diffusion coefficient $D_{1,2}$ is defined with equation (4.2.2-6). The starting point z_i, as well as the time of jump t_f, the processing time of the particle t_t, the time the particle spends at the surface t_a are all set to 0. The parameters Ro (in case of a cylindrical column) and k (in case of the rectangular column) are initially set to 1. The random life time of the nuclide is generated for the first molecule with

$$t_d = \frac{-t_{1/2}}{\ln(2)\cdot\ln(1-random)} \qquad (4.2.2\text{-}23)$$

The adsorption and jump processes are simulated for the molecule as long as t_t is smaller then t_d .

The temperature T_1 at the position z_i of the molecule and the local diffusion coefficient $D_{1,2}$ are calculated.

If t_a is not equal to zero, k or R are calculated according to (4.2.2-11) or (4.2.2-10) for circular and rectangular channels respectively. Afterwards, the mean jump length, which is equal to $H°$ or $H□$, is calculated with equation (4.2.2-15) or (4.2.2-16). Then the random jump length N_i is generated by

$$N_i = -H\cdot\ln(1-random) \qquad (4.2.2\text{-}24)$$

Afterwards the new position z_i is calculated. If it is outside the column, the molecule is counted as decay outside the column and the simulation process for a new molecule is started.

If the new position is inside the column, the temperature of the new position T_2 and the flight time t_f will be calculated according to

$$t_f = \frac{2\cdot x\cdot y\cdot N_i}{\frac{Q\cdot T_1}{273.15}+\frac{Q\cdot T_2}{273.15}} \qquad (4.2.2\text{-}25)$$

The processing time t_t will be increased by t_f. If $t_t > t_d$, the central atom of the complex decays and the position z_i is recorded. The simulation process then starts for the next molecule.

If $t_t < t_d$, the mean time it is adsorbed on the surface, τ_a will be calculated with formula (4.2.2-18) and the mean number of collisions $Z°_z$ or $Z□_z$ will be calculated by equation (4.2.2-21) or (4.2.2-22). Then, the random contact time of the molecule with the surface is generated by

$$t_a = -Z_z\cdot\tau_a\cdot H\cdot\ln(1-random) \qquad (4.2.2\text{-}26)$$

The processing time t_t is increased by t_a. If $t_t < t_d$, the simulation process for the complex goes on, if $t_t > t_d$, the location z_i will be recorded and the simulation will start with a new molecule.

4.2.3 Thermal decomposition of carbonyl-complexes

As mentioned previously, the strength of carbonyl-metal bonding will probably be influenced by relativistic effects. [133] Common method to determine this bond strength is the infrared vibrational spectroscopy (see e.g. [130], [166], [137]). However, this method cannot be applied on a one-atom-at-a-time scale.

In experiments presented in this thesis, thermal decomposition of the carbonyl complexes was studied. This gives a hint of the bonding strength. The decomposition yield as a function of temperature was determined.

The distribution ratio K_{com} of the probabilities that the complex decomposes $p[M]$ to the probability that it stays as a complex $p[M(CO)_x]$ is also dependent on the gas-volume V to hot surface area A.

$$K_{com} = \frac{p[M]}{p[M(CO)_x]} \cdot \frac{V}{A} \qquad [4.2.3\text{-}1]$$

According to Arrhenius

$$K_{com} \propto e^{\frac{-E_A}{R \cdot T}} \qquad [4.2.3\text{-}2]$$

E_A is the activation energy, R the ideal gas constant, and T the surface temperature. The E_A is equal to the free reaction enthalpy $\Delta G^{\ddagger}$, which is a function of the reaction enthalpy $\Delta H^{\ddagger}$ and the reaction entropy times the temperature $T\Delta S^{\ddagger}$.

$$\Delta G^{\ddagger} = \Delta H^{\ddagger} - T \cdot \Delta S^{\ddagger} \qquad [4.2.3\text{-}3]$$

Furthermore, it can be written as a function of $ln\ K_{com}$

$$\Delta G^{\ddagger} = R \cdot T \cdot \ln K_{com} \qquad [4.2.3\text{-}4]$$

ln K_{com} can be expressed as a function of *1/T*

$$\ln K_{com} = \frac{\Delta G^{\ddagger}}{R} \cdot \frac{1}{T} \qquad [4.2.3\text{- }5]$$

As the logarithm of the volume to surface ratio stays constant, it is expressed as constant a ,

$$\ln \frac{p[M]}{p[M(CO)_x]} = a - \frac{\Delta G^{\ddagger}}{R} \cdot \frac{1}{T} \qquad [4.2.3\text{-}6]$$

The ratio of the probabilities that the complex either decomposes *p[M]* or stays as a complex *p[M(CO)$_x$],* is determined in the experiment. The logarithm of this ratio is plotted as a function of the inverse temperature. The slope of the plot is the free reaction enthalpy divided by the ideal gas constant.

4.3 Experimental studies of metal-carbonyl complexes

4.3.1 Carbonyl chemistry experiments at the TRIGA Mainz reactor

As mentioned in chapter 2, the TRIGA reactor in Mainz gives a good opportunity for the first developmental steps of new chemical systems for the transactinides.

Targets and neutron flux:

For the experiments, either a 310 µg ^{235}U target covered with a 13 µm thick aluminum foil or a 350 µg ^{249}Cf target covered with 15 µm thick aluminum foil which was perforated, was placed in the target chamber at beam port A close to the reactor core. The thermal neutron flux at this beam port is 9.8 $\cdot 10^{10}$ neutrons/(cm^2·s) in the continuous mode. Another operation mode is the pulse mode. A 2$ pulse is 30 ms wide (FWHM) and delivers the same neutron dose as 75 s of continuous operation, a 1.5 $ pulse is 40 ms wide (FWHM) and delivers the same neutron dose as 20 s continuous operation. [94]

Figure 32 shows a scheme of the target chamber. The target chamber is connected by Swagelok fittings to the gas jet setup. Gas is flushed around the target from a circlular allocator and leaves through an outlet at the top of the chamber. The chamber is connected with a manometer to monitor the pressure in the chamber.

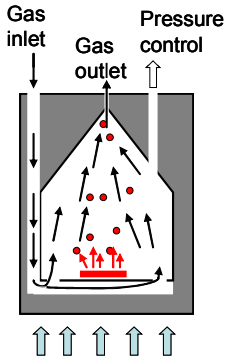

Figure 32: Schematic drawing of the target chamber. The black arrows symbolize the gas flow, the red bar is the target and the red dots symbolize the fission products.The blue arrows symbolize the neutron flux.

Gas

The inert gas used was nitrogen (Westfalengas, purity 4.8) – with a minimum purity of 99.998 % N_2, the maximum amounts of impurities are 5 ppm O_2, 1 ppm C_nH_m and 5 ppm H_2O. Two different purities of carbon-monoxide were chosen for the experiments, Westfalengas, purity 2.0, with a minimum purity of 99% CO and maximum impurities of 1% O_2 + N_2 + Ar + H_2 and Westfalengas 3.7 with a minimum purity of 99.97% CO and maximum impurites of 250 ppm O_2 + N_2 + Ar, 10 ppm H_2 , and 5 ppm H_2O.

Gas jet system

The tube material was chosen depending on the experiment. Polyethylene (PE) is more stable against neutron/radiation damage. Perfluoralkoxyl (PFA) becomes brittle while exposed to the neutron field of the reactor, but it is much more tight and thus more ideal for experiments that require very dry conditions. Two different gas jet setups were used in the experiment – one open system and one loop system.

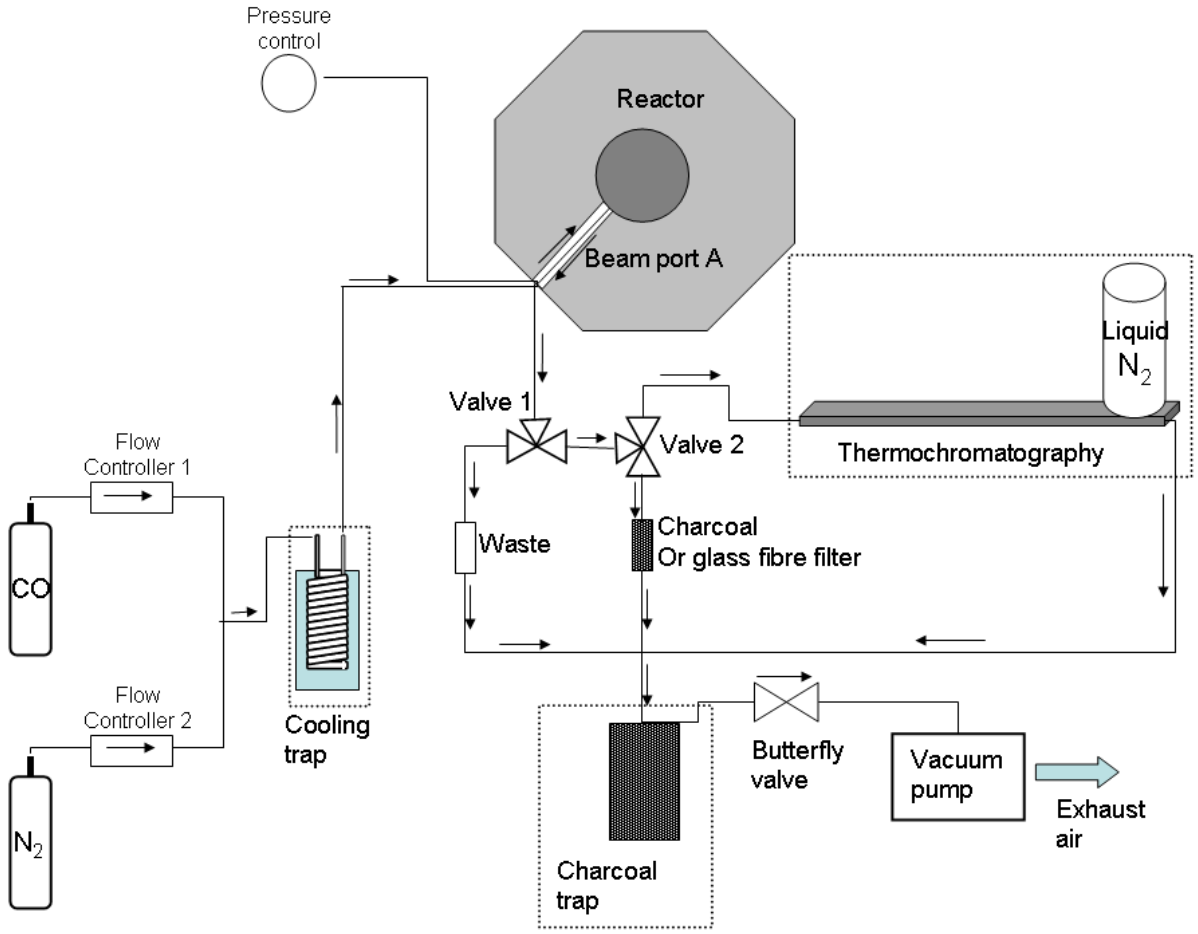

Figure 33: Scheme of the open gas-flow system used at the reactor. The mixing ratio of CO and N_2 as well as the total gas flow is regulated by the mass flow controllers 1 and 2. The cooling trap can be installed optionally to dry the gas. The gas flows through a tube with 7 mm inner diameter into the target chamber. From there, the gas and the volatile compounds leave through a capillary. By switching valve 1 and 2 the gas stream can be guided through a filter (glass fiber filter or charcoal) or through a chemistry device such as a thermochromatography setup, or through a waste filter. Optionally, a charcoal trap can be installed afterwards. At the end of the system is a vacuum pump. A manometer and a pressure gauge are connected to the target chamber to monitor the pressure inside the target chamber. The gauge is connected to a butterfly valve in front of the vacuum pump to control the pressure in the chamber by regulating pumping capacity.

Figure 33 shows the scheme of the open gas flow system at the reactor. The gas flow is regulated by two gas flow controllers (MKS Type 1179AX23CM1BV and MKS Type 1179B52CM1BV). The gas passed through a copper coil placed in a dry ice – ethanol bath to remove moisture. It was then guided through the target chamber. The gas stream was guided with Swagelok three way valves either through a charcoal trap, the chemistry device (e.g., a thermochromatography column) or through the waste filter. The gas was pumped away by a vacuum pump. In front of the vacuum

pump, a butterfly valve (MKS Type 651C-D2S1N) was installed. The pressure inside the target chamber was monitored by a pressure gauge (MKS Type 627D23MBC1B). The baratron and the butterfly valve were connected to the same controller (MKS Type 651C-D2S1N). The butterfly valve regulated the pumping capacity to maintain a set pressure inside the target chamber. The gas-flow controllers, the butterfly valve, and the pressure readout were operated with a LabView program.

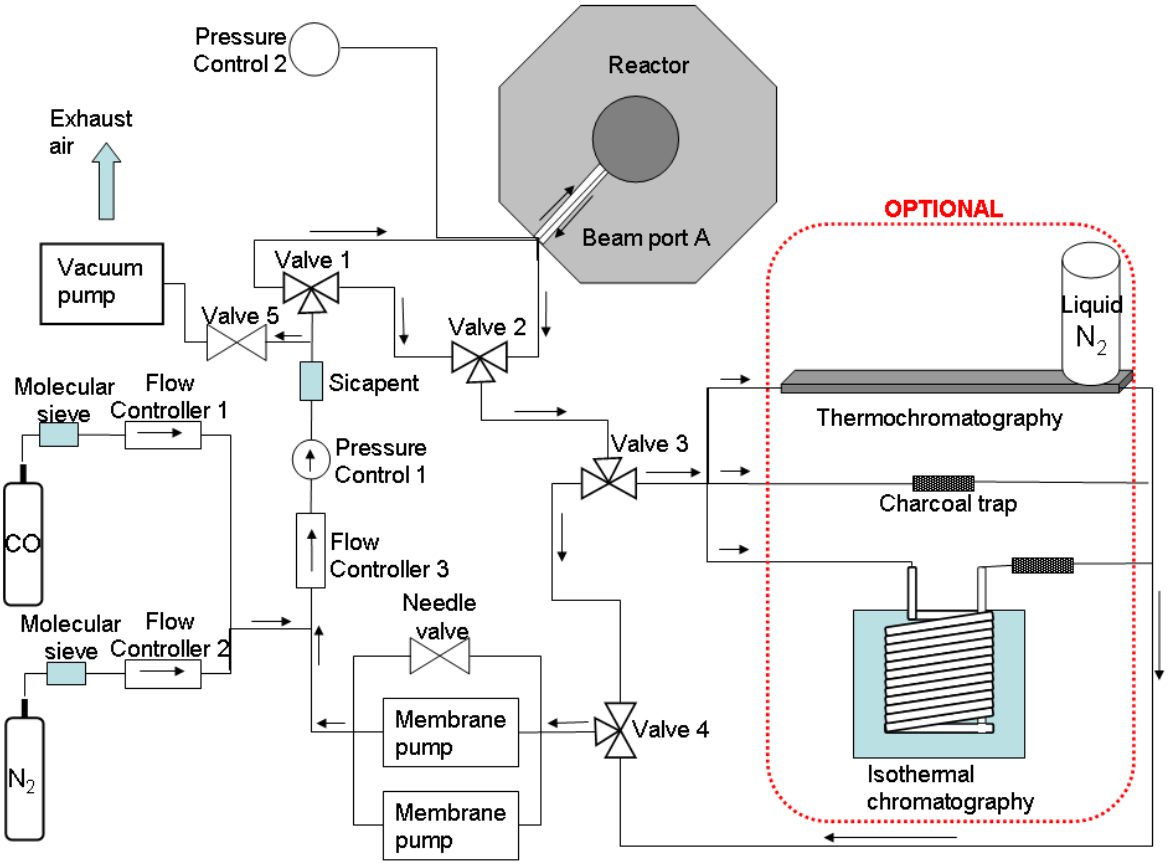

Figure 34: Scheme of the gas-jet loop used at the reactor. The whole loop can be evacuated by opening valve 5. The gas is predried by passing through cartridges filled with a molecular sieve. By opening the flow controllers 1 and 2 the loop is filled with gas. Flow controller 3 regulates the flow rate in the loop. The membrane pumps ensure a constant flow. The gas inside the loop is dried by Sicapent. By switching valves 1 and 2, the gas can be flushed through the target chamber or a bypass. Switching valves 3 and 4 guides the gas through the chemistry or collection device (e.g., a charcoal trap, a thermochromatography column, or an isothermal chromatography column) or through a bypass.

Figure 34 shows the gas jet loop used at the reactor based on the gas jet system constructed by J. Dvorak [109] for experiments with COMPACT.

All tubes were made of PFA or stainless steel. The whole gas-jet loop was connected to a vacuum

pump and by opening valve 5, the loop was evacuated. The gas mixture in the loop is regulated by controllers 1 and 2. Mass-flow controller 3 regulates the gas-flow rate inside the loop. Two membrane pumps were installed to provide a stable flow in the loop. The gas is passed through a cartridge filled with granulated phosphorus pentoxide drying agent (Sicapent from Merck) to remove moisture. The gas was guided either through the target chamber or a bypass by switching valves 1 and 2. The gas was guided either through the chemistry device or a bypass by switching valves 3 and 4. The pressure inside the target chamber was monitored by a manometer. A baratron (pressure control 1), which was connected to the same control device as the flow controllers, was installed in the loop. If the gas pressure went below a set point, the loop was automatically filled with new gas.

The advantage of the gas loop is, that the gas is dried consequently and the dew point in thermochromatography experiments is lowered. Furthermore, the amount of gas waste is reduced.

Activated charcoal-trap:

Traps consisting of PE tubes filled with activated charcoal were connected by Upchurch™ fittings to the gas jet, to adsorb the volatile metal-carbonyl complexes.

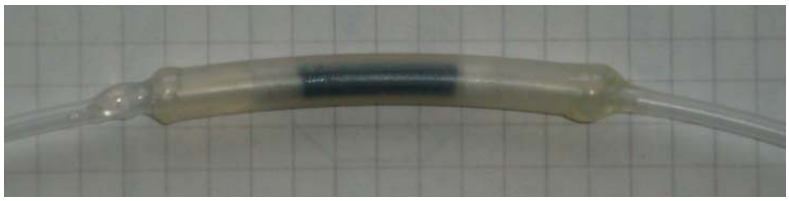

Figure 35: Photo of a charcoal trap. Picture taken from [118]

The traps were made by filling a 5 cm long tube (with 4 mm inner diameter) with ca. 100 mg activated charcoal (20 – 40 mesh). The charcoal was kept in place by quarz wool plugs. PE tubes with an outer diameter of 3 mm were glued with epoxy adhesive into the ends of the traps.

Thermochromatography:

The thermochromatography setup was mainly designed and built in Berkeley and is also described in [116].

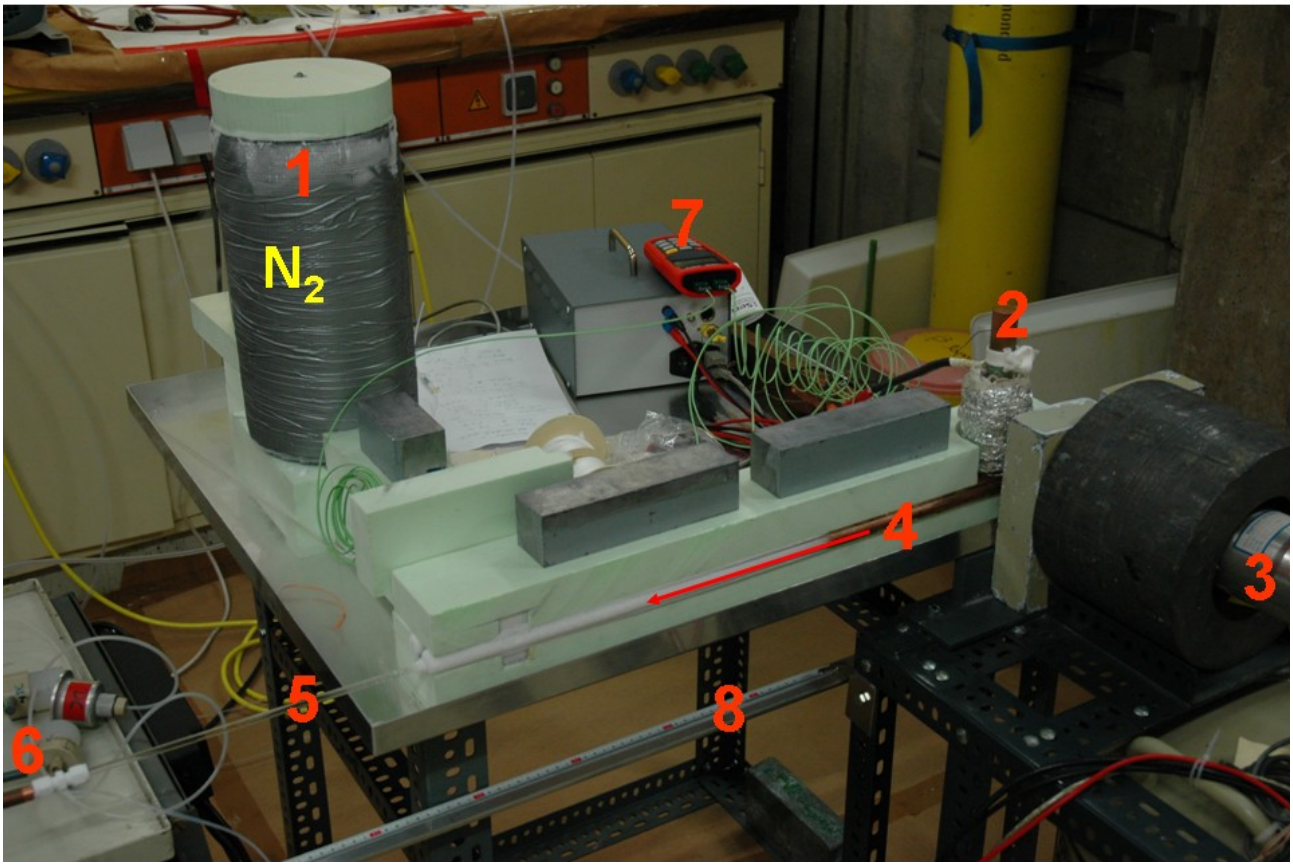

Figure 36 Photograph of the thermochromatography device. The copper sections were insulated with styrofoam. The direction of gas flow through the column is shown by the red arrow. The copper column **4** *was warmed at one end by oven* **2**. *The exit end was cooled by a copper connection to the vessel* **1** *filled with liquid nitrogen. The temperature was measured at three points along the copper column.* **7**. *Inside the copper column was a quartz column* **5**, *which served as thermochromatography column. A charcoal trap* **6** *was at the end of the quartz tube. The chromatography column was scanned with a gamma detector* **3** *whose exact position could be determined by the scale* **8**.

Figure 36 shows a photograph of the thermochromatography setup. A quartz column was placed inside a thin walled copper tube. The length of the copper tube was 70 cm. At one end of the copper tube, an oven was installed. The oven temperature was monitored by a temperature sensor and regulated by a temperature controller. A copper container filled with liquid nitrogen was at the exit side of the chromatography column. By varying the distance of the container to the column the lowest temperature of the column could be varied. The temperature gradient was monitored by three temperature sensors (type K) – one was installed in the middle of the copper tube and the other two at the ends.

The quartz column was connected to the gas-jet system by Swagelok adapters made of Teflon. A charcoal trap, contained in a copper tube, was connected at the exit of the column. The activity

distribution in the column and in the charcoal trap was monitored with a germanium detector. The detector was placed on a slider so that it could be moved parallel to the column.

Isothermal chromatography

In the isothermal chromatography experiments, the gas jet was guided through a helical quartz tube, which was placed in a dry ice-ethanol bath. The quartz tube had an inner diameter of 2 mm and a total length in the cooling bath of 191 cm. The temperature was changed by varying the dry-ice-ethanol ratio.

A charcoal trap was connected behind the quartz column, The trap was placed in front of the germanium detector.

Detector:

In all reactor experiments, a germanium detector type EG&G Ortec GEM- 50195 S with a efficiency of 53.5% was used. The spectra were analysed with the program Genie 2000. The isotopes were identified by the γ-energies published in ref. [97]. The ratio of primary/secondary fission products was calculated using the data given in ref. [98].

4.3.1.1 Experiments with fission products of uranium-235

The carbonyl complex formation of the lighter 4d transition metals (zirconium, niobium, molybdenum) was studied by using a ^{235}U target. In these experiments, the target chamber was flushed either with different carbon monoxide - nitrogen mixtures, pure nitrogen, or a nitrogen-KCl-cluster jet. All the transported compounds were collected on charcoal traps placed in front of the germanium detector and measured. The spectra of the different experiments were compared with each other to learn about the formation and transport of volatile carbonyl complexes.

At the beginning of the beam time, the jet system was connected to a commercial Scanning Mobility Particle Sizer (SMPS). This device is used to count aerosol particles and determine their size. It consists of a Differential Mobility Analyser (TSI Type 3071) and a Condensation Particle Counter (TSI Type 3020). A detailed description is given in references [167] and [47]. The jet system was flushed with 500 mL/min nitrogen. Within 120 s, on average 158.9 aerosol particles with size between 10.7 nm and 504 nm were detected. This is insufficient for an aerosol gas jet transport of fission products.

To confirm that no cluster-contamination of the system falsified the measurements, measurements with KCl-clusters were performed at the end of the beam time, after all experiments with gas mixtures were completed

In order to make sure that the charcoal is sufficient to catch all the carbonyl complexes, a PE tube with an inner diameter of 4 mm was filled over 5 cm with charcoal and connected to the gas jet system. The tube was flushed for 2.5 h with 500 mL/min of the 1:1 carbon monoxide/nitrogen mixture. Three hours after the irradiation, the tube was measured in three sections at a gamma detector. Between the gamma detector and the tube was a 10 cm thick lead collimator with an open slit of 1 cm width. Both ends and the middle of the tube were measured one after another for 1 h. Only in the first section where the gas entered the tube, ^{105}Ru (with a half-life of 4.44 h) could be identified. ^{105}Ru is the daughter of ^{105}Mo and ^{105}Nb which were transported as carbonyl complexes. These measurements show that charcoal is an adequate catcher for carbonyl complexes.

Different measurement cycles were chosen to study the formation of volatile compounds:

- six measurements of 30 s after a 2 $ pulse (30 ms; ~$7.35 \cdot 10^{12}$ neutrons/cm^2),
- three measurements of 120 s after a 2 $ pulse (30 ms; ~$7.35 \cdot 10^{12}$ neutrons/cm^2),
- 10 min flushing the target chamber at 100 kW continuous mode ($9.8 \cdot 10^{10}$ neutrons/($cm^2 \cdot s$)) and after a break of 60 s five measurements of 60 s,
- 30 min flushing of the target chamber at 100 kW ($9.8 \cdot 10^{10}$ neutrons/ ($cm^2 \cdot s$)) and after a 15 min break twelve times 15 min measurements.

In the spectra taken after the 2 $ pulse when the target chamber was flushed with 500 mL/min pure nitrogen, the following isotopes could be identified: ^{90}Kr, ^{91}Kr, ^{92}Kr, ^{91}Rb, ^{140}Xe, ^{139}Xe and ^{84}Se. All these isotopes are volatile in their elemental form.

As soon as CO was added, the activity increased, while the total gas flow was kept constant. The first spectra after the pulse had over 50 % dead time – the following isotopes (which were not observed in the spectra measured with pure nitrogen) could be identified: ^{85}Se, ^{86}Se, ^{87}Se, ^{86}Br, ^{87}Br ^{100}Zr, ^{98}Nb, ^{99}Nb, ^{104}Mo, ^{101}Mo, ^{105}Mo and ^{106}Tc (compare Figure 37).

Comparison of the spectra with cluster jet showed that the following isotopes could only be transported with aerosol clusters and not with a nitrogen-carbon-monoxide jet: ^{93}Sr, ^{94}Sr, ^{95}Sr, ^{94}Y, ^{95}Y, ^{138m}Cs, ^{141}Cs and ^{141}Ba. These measurements also proved that in the case of N_2/CO-jet operation, indeed a chemical transport of volatile species occurred rather than aerosol transport.

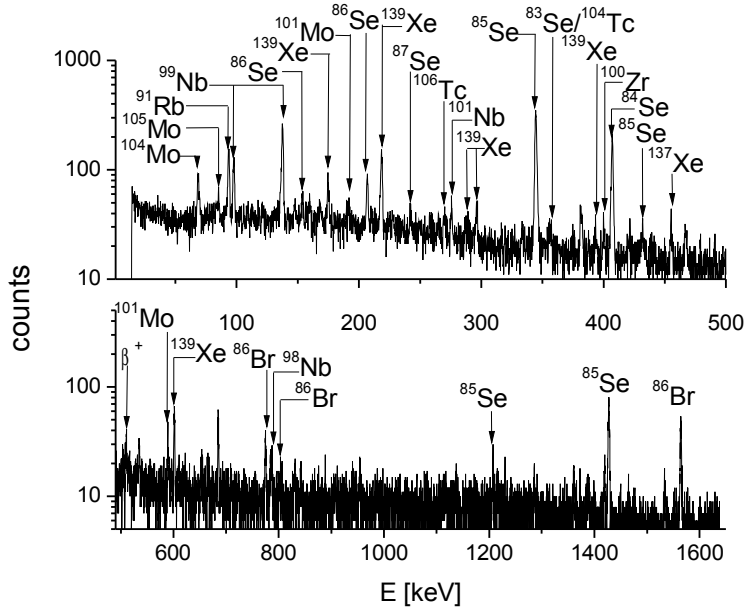

Figure 37: Spectrum of the sample collected in the charcoal-trap after a 2 $ pulse. The transport gas was a mixture of CO (350 mL/min) and N_2 (150 mL/min). The spectrum was measured 30 s after the pulse for 30 s.

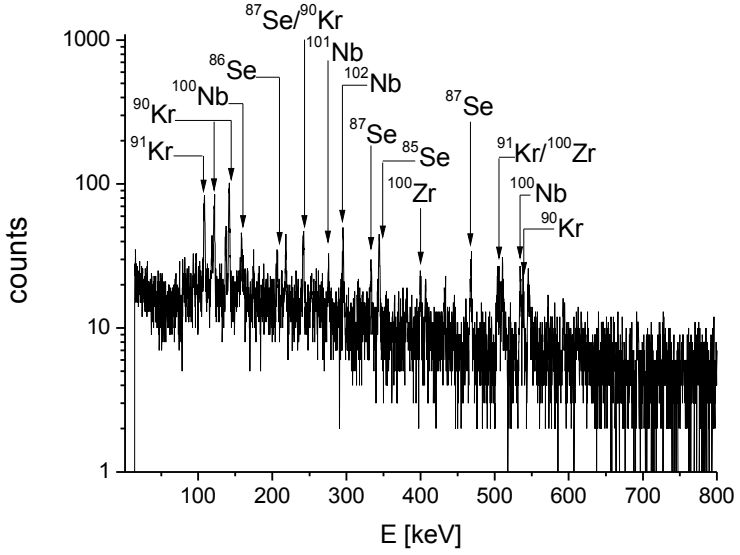

Figure 38: γ-spectrum measured for 10 s after a 1.5 $ pulse. The transport gas was a mixture of CO (250 mL/min) and N_2 (250 mL/min).

Furthermore, the target chamber was flushed with carbon-monoxide-nitrogen mixture (CO/N_2 1/1; 500 mL/min total flow) during a 1.5 $ pulse. Just after the pulse several 10 sec measurements were performed – in the first measurement after the pulse, ^{85}Se, ^{86}Se, ^{87}Se, ^{90}Kr, ^{91}Kr, ^{92}Kr, ^{100}Zr,

^{100}Nb, ^{101}Nb, and ^{102}Nb were identified (see Figure 38).

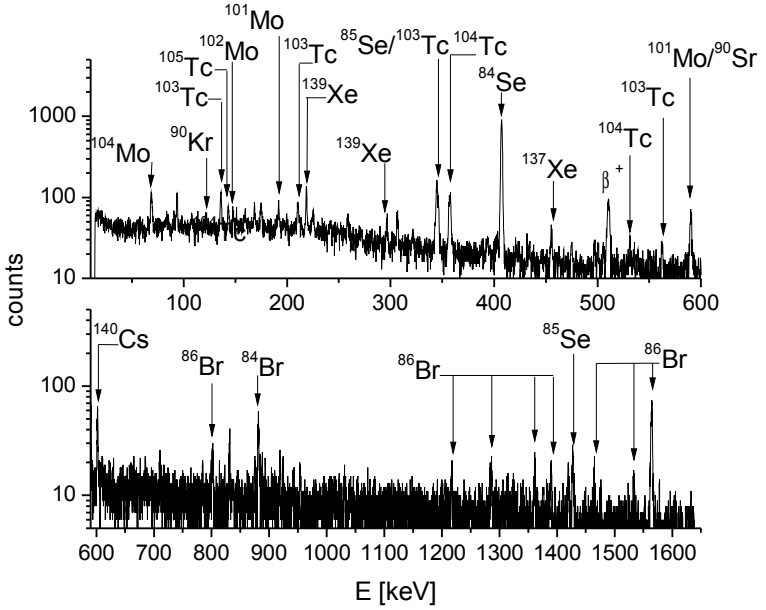

Figure 39: Spectrum measured for 60 s. The reactor was operated at 100 kW. The target chamber was flushed for 10 min with a CO (250 mL/min) and N_2 (250 mL/min). The measurement was started after a 60 s break.

In another measurement cycle, the target chamber was flushed at 100 kW for 10 min. After a 1 min break the sample was measured five times for 60 s. The following isotopes were identified in the first spectra of the samples collected in a pure nitrogen stream: ^{84}Se, ^{85}Se,^{84}Br, ^{86}Br, ^{90}Kr, ^{91}Rb, ^{93}Sr, ^{96}Sr, ^{137}Xe, ^{138}Xe, ^{139}Xe and ^{140}Cs. As soon as CO was added, the amount of selenium increased and the gamma lines of the isotopes ^{102}Mo, ^{104}Mo, ^{103}Tc, ^{104}Tc and ^{105}Tc appeared in the spectra (see Figure 39). With cluster transport, the amount of Sr in the spectra accumulated. ^{94}Sr, ^{95}Sr, ^{138m}Cs, ^{141}Cs and ^{142}Ba were additionally identified in the spectra.

In the long time measurements (30 min irradiating at 100 kW and collecting activity, – after 5 min break 15 min measurement) following isotopes were identified when using carbon monoxide – nitrogen mixture: ^{83}Se, ^{84}Se, ^{84}Br, ^{85m}Kr, ^{87}Kr, ^{92}Sr, ^{93}Sr, ^{97}Nb, ^{101}Mo, ^{102}Mo, ^{101}Tc, $^{102/102m}$Tc, ^{104}Tc, ^{105}Tc, and ^{105}Ru.

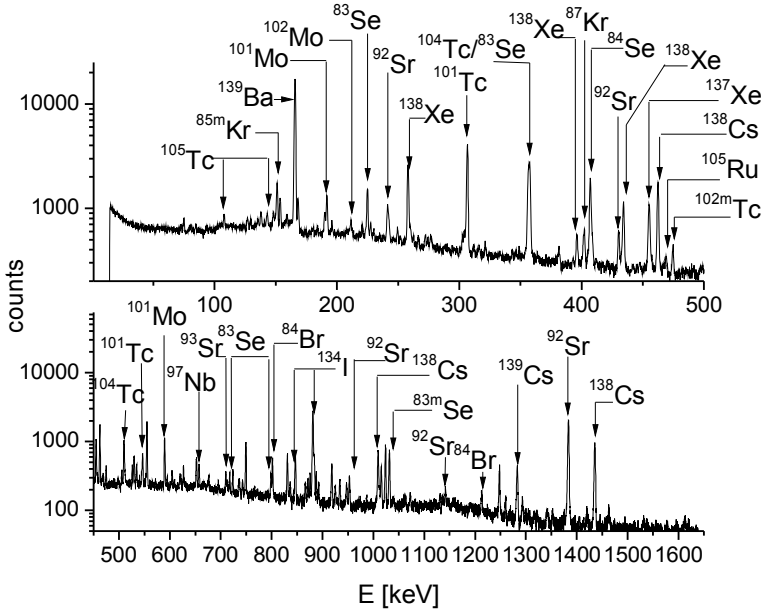

Figure 40: Spectrum of a sample collected for 30 min at 100 kW. The gas mixture was CO (250 mL/min) and N_2 (250 mL/min). The measurement was performed for 15 min, 5 min after the sample was taken.

Selenium is slightly volatile in its elemental state as a single atom and can be transported in a pure nitrogen stream. The volatility increases when CO is added to the gas as it forms volatile SeCO. This phenomenon was already studied in the work reported in references [168] and [169]. The relative transportation yield of ^{84}Se (see Figure 41) was determined by normalzing the peak area of the 407 keV γ-line of ^{84}Se on the life-time of the measurement and the reactor pulse, compared with the samples taken with a KCl clusters.

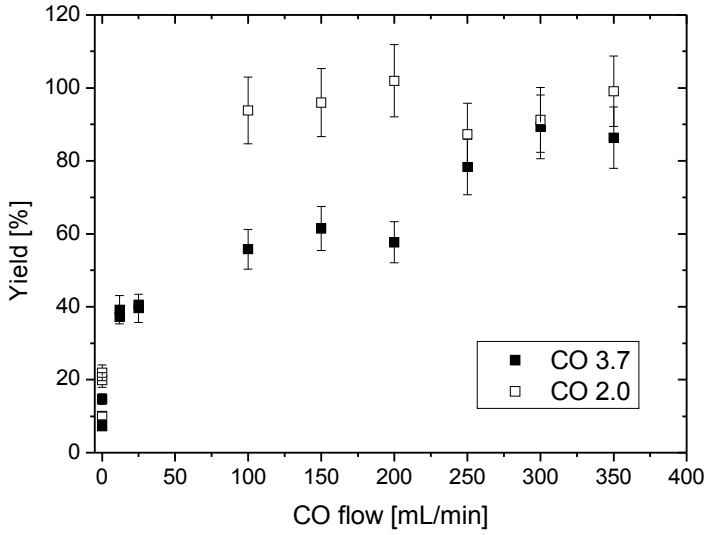

Figure 41: The jet yields of ^{84}Se transported in a N_2/CO gas mixture normalized on a N_2 KCl-cluster jet depending on the amount of CO in the gas stream. The total gas flow was kept at 500 mL/min. Two different CO gas bottles were used – 2.0 and 3.7 purity. The spectra were measured 120 sec after the pulse. The 407 keV γ-line was analysed and normalized to the live time of the measurement and the reactor pulse.

Two different purities of carbon monoxide were tested – 2.0 and 3.7. With the less pure carbon monoxide the jet yield between 100 mL/min and 200 mL/min seems to be higher than with 3.7 carbon monoxide. This difference might be due to some impurities in the gas, which also might form volatile selenium compounds such as SeH_2. As the 2.0 carbon monoxide bottle was empty, it was not possible to repeat the experiment. These results should ideally be verified in a future beamtime.

The 10-s and 30-s spectra showed evidence for the formation of zirconium carbonyl complexes. Only the ^{100}Zr could be identified. 89% of the ^{100}Zr are produced as a primary fission product. Short-lived isotopes of zirconium were clearly seen in the 10 s and in the first 30 s spectrum after the pulse. But due to the high background rate in the spectra after a pulse, it is not possible to analyse the yields of these isotopes quantitatively.

So far, no binary, neutral, mononuclear zirconium carbonyl complexes are known, only binary anionic zirconium hexacarbonyl is known. [170] Reference [171] reports the existence of cationic heptacarbonyls of tantalum and vanadium. A zirconium heptacarbonyl complex would fulfil the 18

valence electron rule and is predicted to be stable. [172] Another possibility is that mixed carbonyl complexes might have been observed, which are formed with impurities (such as hydrogen, water, or oxygen) present in the gas.

Furthermore, ^{99}Nb was identified in the 30 s spectra. This isotope is mainly produced as the daughter of ^{99}Zr. In the 10-s spectra, ^{99}Nb, ^{100}Nb, ^{101}Nb, and ^{102}Nb were observed. ^{99}Nb and ^{100}Nb are mainly from the decay of zirconium. Around 40% of ^{101}Nb and ^{102}Nb are primary fragments formed in the fission process. This would be another evidence for zirconium carbonyl complex formation . An alternative explanation may be that niobium forms (as its lighter homologue vanadium) radical-type hexacarbonyl complexes or mixed carbonyl complexes (e.g, hydro, oxo, or hydroxo -carbonyl complexes) with impurities in the gas.

Jet yields of niobium could only be analysed with the 30 s spectra. Problem is the high dead time after a pulse (at start of the measurement over 50%), therefore the second measurement (30 s after the pulse) was chosen for a quantitative analysis. In Figure 42, the jet yield of ^{99}Nb for different carbon monoxide – nitrogen mixtures normalized to the KCl cluster transport is shown.

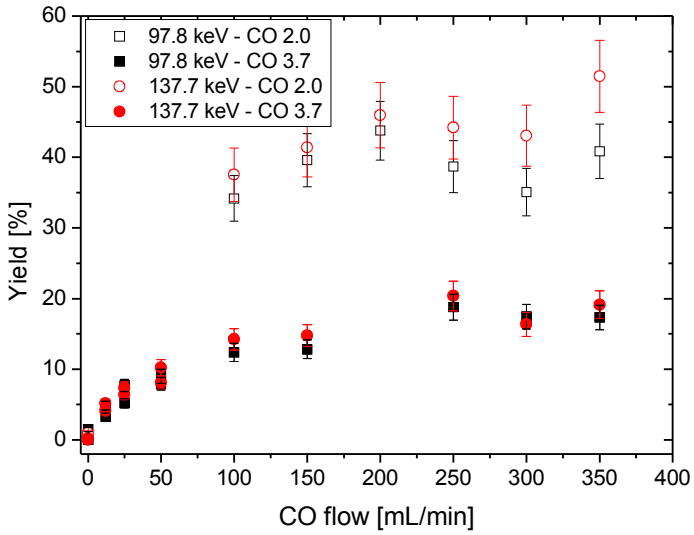

Figure 42: The jet yields of ^{99}Nb transported in a N_2/CO gas mixture normalized to a N_2 KCl-cluster jet depending on the amount of CO in the gas stream. The total gas flow was kept at 500 mL/min. Two different CO gas bottles were used – 2.0 and 3.7 purity. The gamma spectra were measured 30 after a pulse for 30 s For the graph, the two gamma lines 97.8 keV and 137.7 keV were analyzed and normalized to the live time of the measurement and the 2 $-pulse.

The transport yield of ^{99}Nb with carbon-monoxide jet depends strongly on the gas purity. As the ^{99}Nb is mainly a decay product of ^{99}Zr, this is an evidence that the mother nuclide ^{99}Zr forms mixed carbonyl complexes.

The identification of ^{104}Mo (which is formed to 63% as primary fragment in the fission process) and ^{105}Mo (which is to 73% a primary fission product) proofs that $Mo(CO)_6$ is formed. The isotopes ^{101}Mo and ^{102}Mo are also identified which are mainly secondary fission products. The relative yield of the isotopes which are mainly formed as primary fission products is higher than that of the ones mainly formed as secondary fission products. The carbonyl-complex formation takes mainly place, when the ions are thermalized in the gas. The presence of ^{101}Mo and ^{102}Mo seems to be evidence for carbonyl-complex formation with the precursor isotopes of zirconium or niobium.

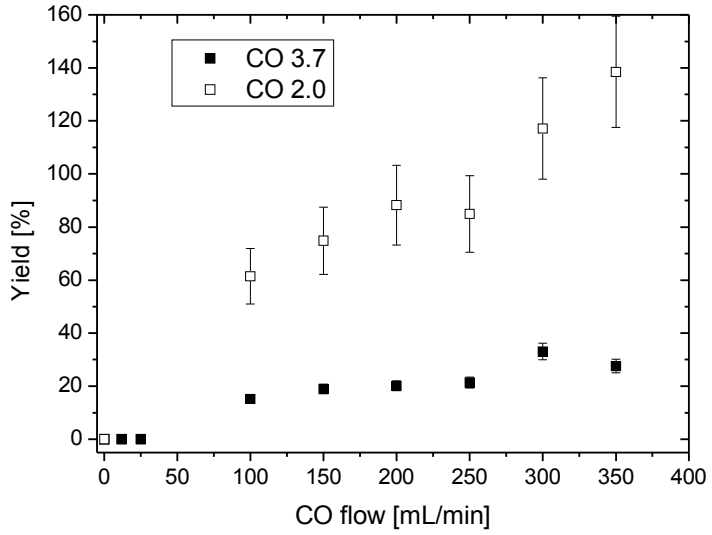

Figure 43: The jet yields of ^{104}Mo transported in a N_2/CO gas mixture normalized on a N_2 KCl-cluster jet depending on the amount of CO in the gas stream. The total gas flow rate was kept at 500 mL/min. CO gas of two different purities was used – 2.0 and 3.7. The spectra were measured 120 sec after the pulse. The 69 keV γ-line was analysed and normalized to the live time of the measurement and the reactor pulse.

The effect that the yield achieved with carbon monoxide 2.0 is higher than with 3.7 was also observed for molybdenum – see Figure 43. This is might hint at the formation of mixed carbonyl complexes of molybdenum or some catalytic effects of the impurities on the carbonyl complex formation. Typical gas impurities are water, hydrogen, oxygen, argon, and nitrogen. Most likely would be the formation of hydro-(or hydroxo)-carbonyl complexes, which are also known to be volatile.

The identified technetium isotopes are mostly formed from the decay of molybdenum – probably they are transported as molybdenum carbonyl complexes, but it also might be possible that the technetium pentacarbonyl-radical complex is formed. These radical-type complexes are known from Szilard-Chalmers reactions. [145] Another possibility is the formation of mixed technetium carbonyl complexes. Hydrogen-carbonyl complexes would be the most likely formed complex type.

4.3.1.2 Experiments with fission products of californium-249

The ^{235}U target was replaced by a ^{249}Cf target to study the carbonyl-complex formation with the 4d transition metals molybdenum, technetium, ruthenium, and rhodium. The target chamber was flushed with a carbon monoxide - nitrogen mixture for 120 s while the reactor was operated continuously at 100 kW. To dry the gas, it was guided through a cooling trap kept on -78°C before entering the chamber. The pressure inside the target chamber was 1400 mbar. The volatile compounds were collected on a charcoal trap and three consecutive γ-spectra were acquired for 120 s each.

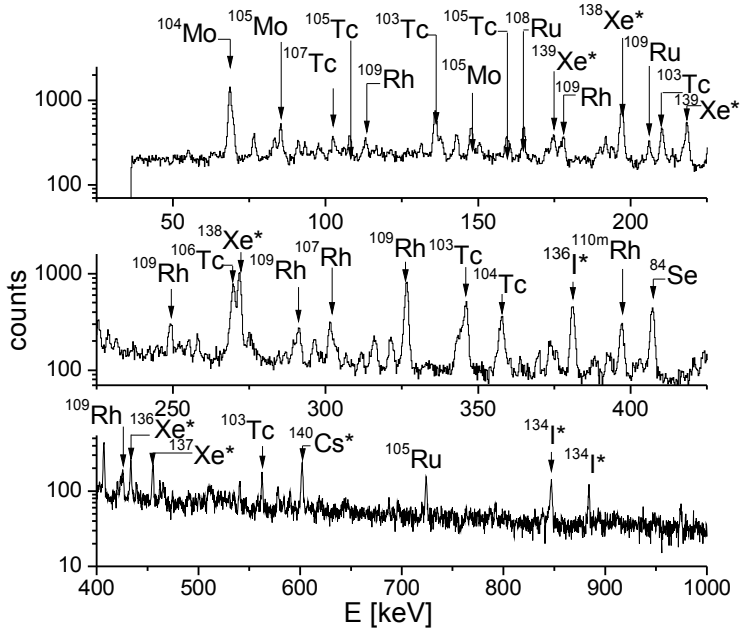

*Figure 44: γ-ray spectrum of the transported fission products (gas mixture of 375 mL/min CO and 125 mL/min N_2) collected for 2 min in a charcoal trap. The sample was measured subsequently for 2 min. Isotopes, which were also visible in spectra of pure N_2 experiments are marked with a star *.*

In pure nitrogen, the following isotopes were transported and identified in the spectra: ^{20}F (which was likely formed by neutron capture of the PFA tubes – ^{19}F(n,γ)^{20}F) ^{84}Se, ^{134}I, ^{134m}I, ^{136}I, ^{135}Xe, ^{136}Xe, ^{137}Xe, ^{138}Xe, ^{139}Xe, ^{139}Cs and ^{140}Cs were identified. When carbon monoxide was added to the

gas jet, the amount of selenium and iodide increased. The following isotopes could be identified: ^{101}Mo, ^{102}Mo, ^{103}Mo, ^{104}Mo, ^{105}Mo, ^{106}Mo, ^{101}Tc, ^{102m}Tc, ^{103}Tc, ^{104}Tc, ^{105}Tc, ^{106}Tc, ^{107}Tc, ^{105}Ru, ^{107}Ru, ^{108}Ru, ^{109}Ru, ^{107}Rh, ^{108}Rh, ^{109}Rh and ^{110m}Rh; Figure 44 shows a typical spectrum subsequently after collecting the sample; not all identified isotopes could be pointed out in this spectrum.

The amount of selenium transported increases with the amount of carbon monoxide in the transport gas. This is in agreement with the previous experiments with the ^{235}U target (chapter 4.3.1) and assigned to the formation of volatile SeCO. The gas purity seems to have a negligible influence on the formation of selenium carbonyl (see Figure 45).

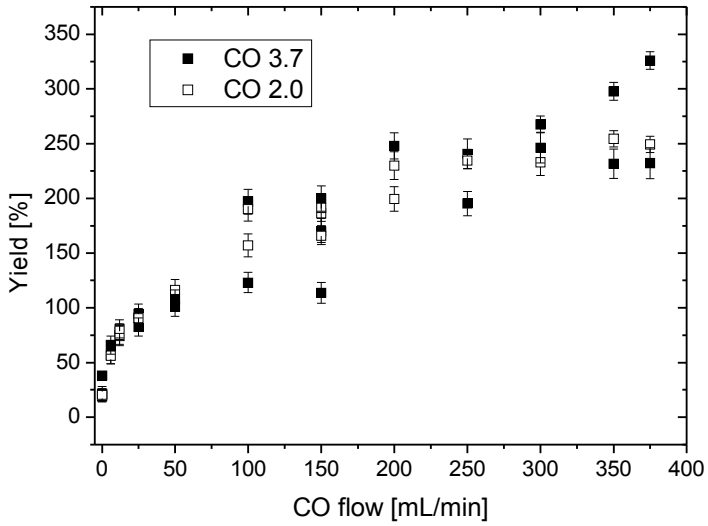

Figure 45: The jet yields of ^{84}Se transported in a N_2/CO gas mixture normalized to a N_2 KCl-cluster jet depending on the fraction of CO in the gas stream. The total gas flow was kept at 500 mL/min. Two different CO purities were tested – 2.0 and 3.7. The volatile compounds were collected for 120 s on the charcoal trap. The spectra were measured 120 sec after collecting the sample.

The formation of molybdenum hexacarbonyl was observed again. In these experiments, the formation seems to be independent from the gas purity (compare Figure 46) - in contrast to the results obtained with the ^{235}U target.

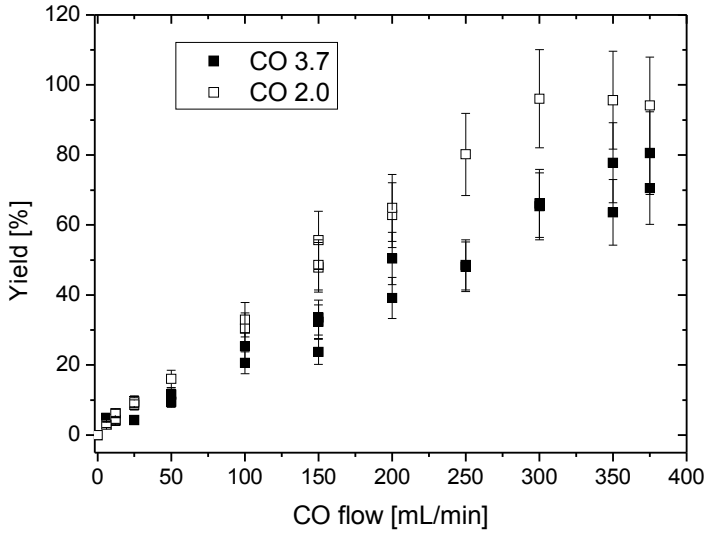

Figure 46: The jet yields of ^{104}Mo transported in a N_2/CO gas mixture normalized to a N_2 KCl-cluster jet depending on the amount of CO in the gas stream. The total gas flow was kept at 500 mL/min. Two different CO gas bottles were used – 2.0 and 3.7 purity. The volatile compounds were collected for 120 s on the charcoal trap. The spectra were measured directly after collecting the sample.

The carbon monoxide 2.0 was contained in two different gas bottles, both delivered from Westfalengas, This might explain the difference in the observed effects of the gas purity on the transportation yield. The influence of the pre-drying of the gas by passing it through a cooling bath seems not to be the critical effect on the formation of the molybdenum hexacarbonyl complex. Removing the cooling bath resulted the same transportation yield (for CO 2.0 and CO 3.7).

No dependence of the transport yield on the gas purity could be observed for the isotopes ^{105}Tc, ^{106}Tc, and ^{107}Tc. ^{103}Tc showed the same slight dependence on the gas purity as ^{104}Mo (compare Figure 46 and Figure 47). Only 7.2% [98] of ^{103}Tc is formed as primary fragments in the fission, it just reflects the transportation yields of molybdenum hexacarbonyl.

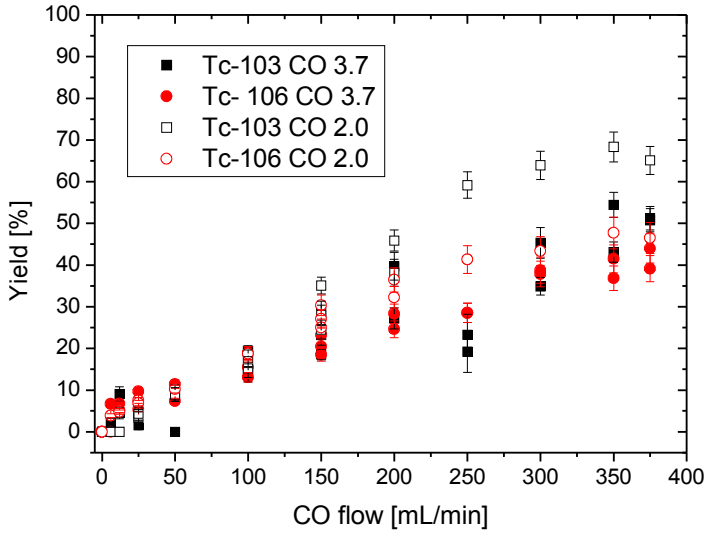

Figure 47: The jet yields of ^{103}Tc and ^{106}Tc transported in a N_2/CO gas mixture normalized to a N_2 KCl-cluster jet depending on the amount of CO in the gas stream. The total gas flow was kept at 500 mL/min. CO of two different purities was used – 2.0 and 3.7. The volatile compounds were collected for 120 s on the charcoal trap. The spectra were measured subsequently after collecting the sample.

Technetium itself seems to form volatile carbonyl complexes. As mentioned previously, a binary, mononuclear technetium complex ($TcCO_5$ radical) is only known from Szilard-Chalmers reactions. [145] Another possible explanation would be the formation of mixed carbonyl complexes with impurities in the gas. Most likely would be the formation of hydro-carbonyl complexes with the hydrogen impurity. Hydroxo- or oxo-carbonyl complexes can also not be excluded.

The transport yield of ruthenium also seems to be independent of the gas purity (Figure 48). Compared to a cluster jet, the yield is significantly lower. From the data obtained it is not possible to distinguish, whether a ruthenium pentacarbonyl complex was formed or whether transport occured in form of a volatile species of the precursor technetium isotopes.

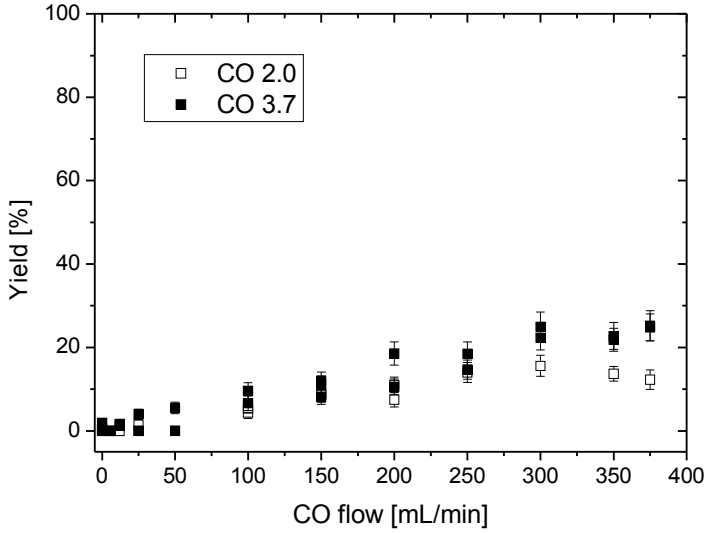

Figure 48: The jet yields of ^{108}Ru in a N_2/CO gas mixture normalized to a N_2 KCl-cluster jet depending on the amount of CO in the gas stream. The total gas flow rate was kept at 500 mL/min. CO of two different purites was used – 2.0 and 3.7. The volatile compounds were collected for 120 s on the charcoal trap. The spectra were measured subsequently after collecting the sample for 120 s.

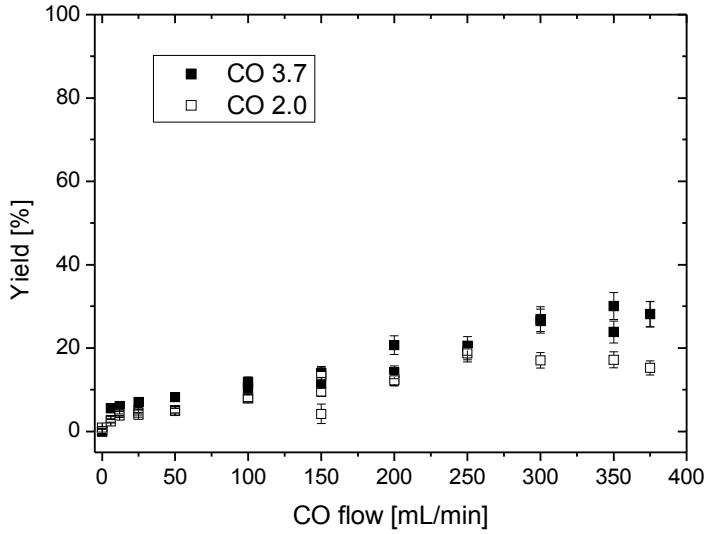

Figure 49: The jet yields of ^{109}Rh in a N_2/CO gas mixture normalized to a N_2 KCl-cluster jet depending on the amount of CO in the gas stream. The total gas flow rate was kept at 500 mL/min. The volatile compounds were collected for 120 s on the charcoal trap. The spectra were measured subsequently after collecting the sample for 120 s.

The yield curve for ^{109}Rh is similar to the curve obtained with ruthenium. As ^{110m}Rh was observed in the spectra, there is evidence that rhodium forms volatile carbonyl complexes, as this isomer is only formed as a primary fission fragment. [98]

Ruthenium is known for forming pentacarbonyl complexes. Binary rhodium carbonyl complexes are not known from literature.

Isothermal chromatography

Gas chromatography methods were used to study the adsorption of the carbonyl complexes. Furthermore, it was hoped to better characterize the complexes and to exclude precursor effects and get a better understandig which are the transported species.

In isothermal chromatography experiments, the adsorption on quartz-glass surface was studied.

Two different modes for the isothermal chromatography were used – in 100 kW reactor mode, the chromatography column was kept at a constant temperature and flushed with the transport gas. The charcoal trap was measured for 15 min. The integrals of the gamma peaks were divided by the live time of the measurement. Afterwards the temperature was changed and after a 15 min break, the trap was measured again.

In the pulse mode, the isothermal column was brought to a certain temperature and flushed with the gas. 10 sec after a pulse the charcoal trap was measured for 10 min. The integrals of the gamma lines were divided by the live time of the measurement and the power of the pulse.

At a flow rate of 600 mL/min, the $T_{50\%}$ values were (-46 ± 10) °C for $^{104}Mo(CO)_6$ ($t_{1/2}$ = 60 s) and (-41 ± 10) °C for $^{105}Mo(CO)_6$ ($t_{1/2}$ = 3.5 s). The adsorption enthalpy of molybdenum hexacarbonyl on quartz was determined to be (−42.5±2.5) kJ/mol. Figure 50 shows the thermochromatogram of ^{105}Mo and ^{104} Mo. The solid lines show the result of the simulation of $-\Delta H_{ads}$=42.5 kJ/mol, the dashed lines depict the error limits of ±2.5 kJ/mol.

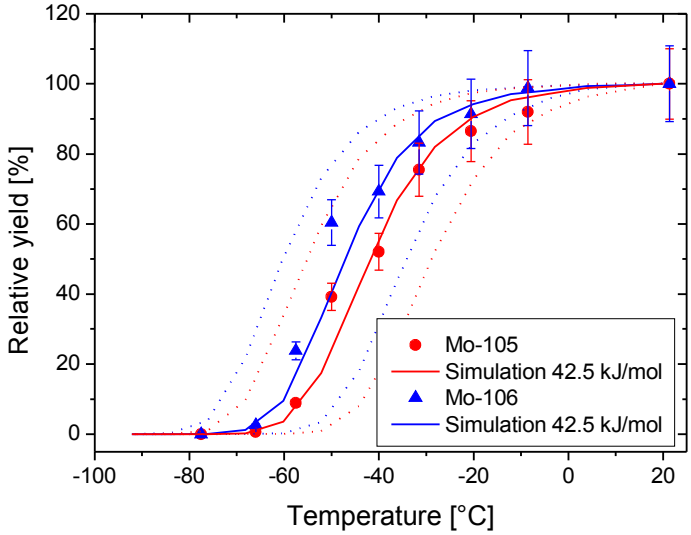

Figure 50: Isothermal chromatogram of ^{104}Mo and ^{105}Mo The dots show the yield obtained in the charcoal trap at a flow rate of 600 mL/min and a pressure of 1315 mbar in the target chamber. The reactor was operated at 100 kW. The values measured at room temperature are the 100% values. The solid lines are the results of the Monte Carlo simulations with $-\Delta H_{ads}$=42.5 kJ/mol. The dashed lines depict the error limits of ±2.5 kJ/mol.

The $T_{50\%}$ values for the different technetium isotope at a gas flow rate of 600 mL/min were (−51 ± 10) °C for ^{103}Tc ($t_{1/2}$ = 54.2 s), (−30 ± 10)°C for ^{106}Tc ($t_{1/2}$ = 35.6 s) and (−17 ± 10) °C for ^{107}Tc ($t_{1/2}$ =21.2 s). The analysis of the measured isothermal chromatograms of ^{103}Tc, ^{106}Tc, and ^{107}Tc is not as straight forward as of the molybdenum isotopes. 93% of the ^{103}Tc are from the decay of ^{103}Mo. The measured yields of ^{103}Tc depending on the column temperature are well described by the Monte Carlo simulations for ^{103}Mo(CO)$_6$. The isotopes ^{106}Tc and ^{107}Tc are around 40% and 17% decay products of molybdenum – with the remainder being formed as primary fission products. Their yields depending on the column temperature also match the Monte Carlo simulations of ^{106}Mo(CO)$_6$ and ^{107}Mo(CO)$_6$.. Furthermore the yields are also in agreement with simulations of technetium pentacarbonyl and an assumed adsorption enthalpy of $-\Delta H_{ads}$=45 kJ/mol for ^{106}Tc(CO)$_5$ and of $-\Delta H_{ads}$=46.5 kJ/mol for ^{107}Tc(CO)$_5$. From these results, it is not possible to distinguish between a transport in the form of a technetium carbonyl complex and a molybdenum hexacarbonyl complex.

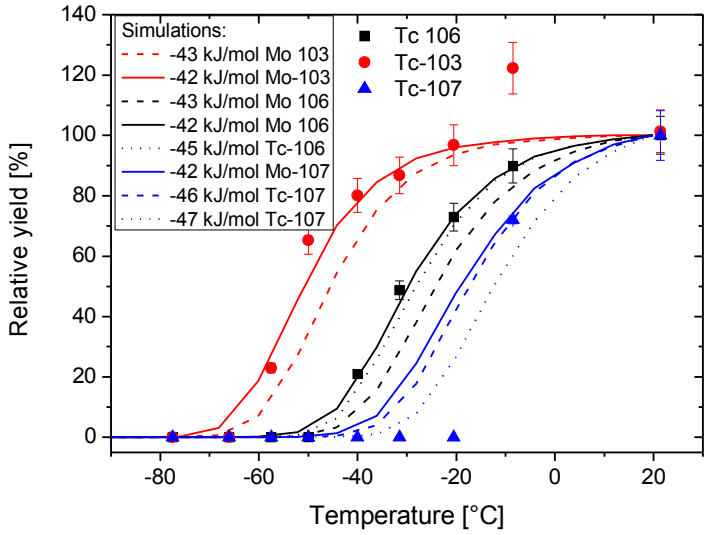

Figure 51: Isothermal chromatogram of ^{103}Tc, ^{106}Tc and ^{107}Tc. The dots show the yield obtained in the charcoal trap by a flow rate of 600 mL/min and a pressure of 1315 mbar in the target chamber. The reactor operated at 100 kW. The values measured at room temperature are the 100% values. The coloured lines are the results of the Monte Carlo simulations. The simulations were run for complexes of the type $Mo(CO)_6$ and $Tc(CO)_5$ with an assumed density of 2 g/cm^3.

The ruthenium isotopes had no appropriate gamma line to analyse quantitatively. The 326.6 keV line of ^{109}Rh could be analyzed. The $T_{50\%}$ temperature of ^{109}Rh ($t_{1/2}$ = 80 s) was (−35 ± 17) °C at a flow rate of 600 mL/min. ^{109}Rh is the daugther of ^{109}Ru, but 25% of ^{109}Rh are also formed as a primary fission product. It is not possible to distinguish from the isothermal chromatogram whether it was transported in the gas stream a $^{109}Ru(CO)_5$ or $^{109}Rh(CO)_4$.

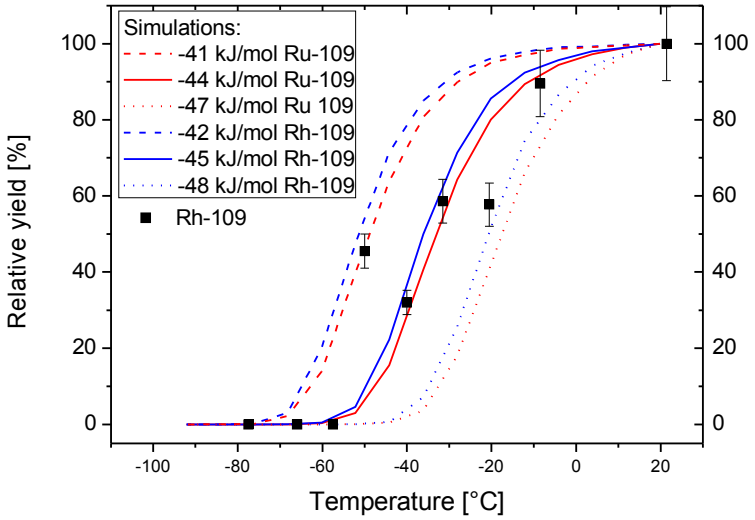

Figure 52: Isothermal chromatogram of ^{109}Rh. The dots show the yield obtained in the charcoal trap by a flow rate of 600 mL/min and a pressure of 1315 mbar in the target chamber. The reactor was operated at 100 kW. The values measured at room temperature are the 100% values. The coloured lines are the results of Monte Carlo simulations. The simulations were run for complexes of the type $Ru(CO)_5$ and $Rh(CO)_4$, both with assumed densities of 2 g/cm^3.

When the gas flow in the jet loop was raised to 1 L/min, the palladium isotopes ^{113}Pd, ^{114}Pd, ^{115}Pd, and ^{116}Pd were identified in the spectra. This measurement was performed in the pulse mode of the reactor. The gamma measurements were started 10 s after each pulse and were run for 10 min. The shortest-lived amoung these isotopes is ^{116}Pd with a half life of 11.8 s. The longest lived isotope is ^{113}Pd with a half life of 1.6 min. The half lives of the precursor isotopes (^{113}Rh, ^{114}Rh, ^{115}Rh, and ^{116}Rh) are in the range of 1 second. As the Pd isotopes were not identified at lower flow rates, it appears that only the short lived mother isotopes of rhodium and ruthenium form volatile carbonyl complexes. Palladium cannot be transported as a carbonyl complex.

Thermochromatography experiments

The second method used to determine the adsorption enthalpies was the thermochromatography. Therefore, the thermochromatography apparatus described in 4.3.1 was used. Different quartz columns were used in the experiments - with 2.7 mm inner diameter and with 4.0 mm inner

diameter. Each quartz column was heated up to 1000°C in a tube furnace while pure oxygen (10 mL/min) passed through the column to clean the quartz surface. The inner surface of one quartz column was covered with gold-covered Mylar foil to study the adsorption on gold.

The results vary from the isothermal chromatography measurements. One of the main problems during the measurement was the low spatial resolution. In the first measurement, a 5 cm thick lead collimator with a slit of 2 cm was placed in front of the gamma detector, but as counting statistics were much too low, the collimator was opened from measurement series to measurement series. At the end the collimator was removed and the distance between thermochromatography column and detector was reduced.

The thermochromatography column was kept on a constant temperature gradient and flushed continuously with the transport gas. The reactor operated at 100 kW so that a stable production rate of fission products was achieved. The detector was moved to different positions of the column. The distance between the measurement positions were 5 cm or 10 cm. Each position was measured for 900 sec. Figure 53 shows the thermochromatogram of ^{104}Mo measured with a 2.3 mm inner diameter column. Most of the ^{104}Mo deposited at a temperature around -92 °C. Compared with the Monte Carlo simulations the adsorption enthalpy of the molybdenum hexacarbonyl on quartz is (−36 ± 8) kJ/mol.

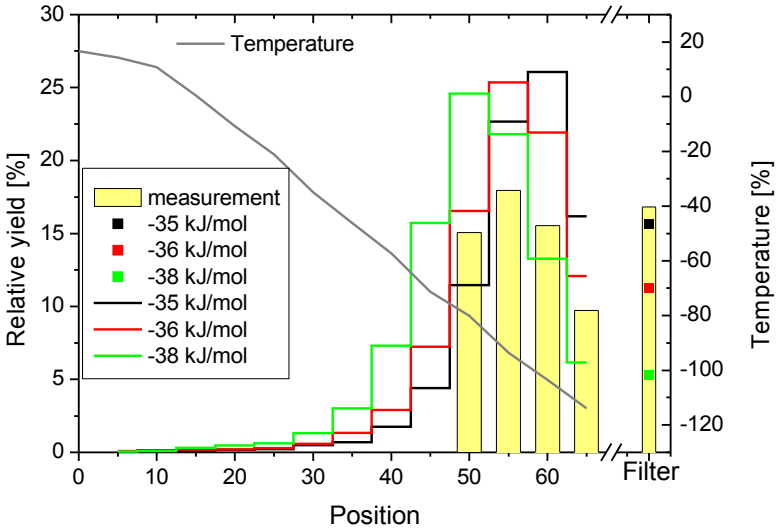

Figure 53: Thermochromatogram of $^{104}Mo(CO)_6$. The gas mixture was a 1:1 mixture of N_2 an CO (purity 2.0). The total gas flow was kept at 230 mL/min and the pressure in the target chamber was 1310 mbar. The inner diameter of the quartz column was 2.7 mm. The resolution of the Monte Carlo simulation was 5 cm. Comparison with the experiments gives $-\Delta H_{ads}=(36 \pm 8)$ kJ/mol.

In another experiment, a gold covered MYLAR foil was inserted into the quartz column (4 mm inner diameter). Most of the ^{104}Mo deposited around -94 °C. The adsorption enthalpy on gold was determined to be (-35 ± 8) kJ/mol. The results are shown in Figure 54. The adsorption behaviour of $Mo(CO)_6$ on gold is the same as on quartz. In both cases, physisorption was observed and within the experimental errors the adsorption enthalpy is the same.

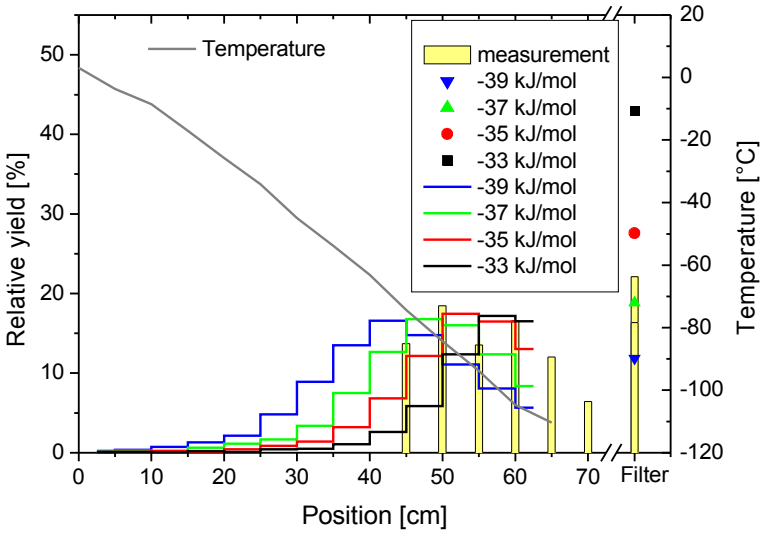

Figure 54: Thermochromatogram of $^{104}Mo(CO)_6$. The inner diameter of the gold coated column was 4 mm. The gas mixture was a 1:1 mixture of N_2 an CO (purity 2.0). The total gas flow was kept on 500 mL/min and the pressure in the target chamber was 1280 mbar. The resolution of the Monte Carlo simulation was 5 cm. Comparison with the experiments gives $-\Delta H_{ads}=(35 \pm 8)$ kJ/mol.

To estimate the adsorption enthalpy of the volatile technetium carbonyl complexes, the gamma line at 102.6 keV of ^{107}Tc was evaluated. ^{107}Tc is mainly formed as a primary fission product. The Tc-carbonyl complexes are adsorbed at the front end of the chromatography column. The evaluated adsorption enthalpy on quartz is (−52 ± 8) kJ/mol (see Figure 56), and on gold is (−45 ± 8) kJ/mol (Figure 55). Within the measurement uncertainties these values are the same. The measurement can be seen as evidence that the adsorption on quartz is stronger than on gold but this needs further investigations.

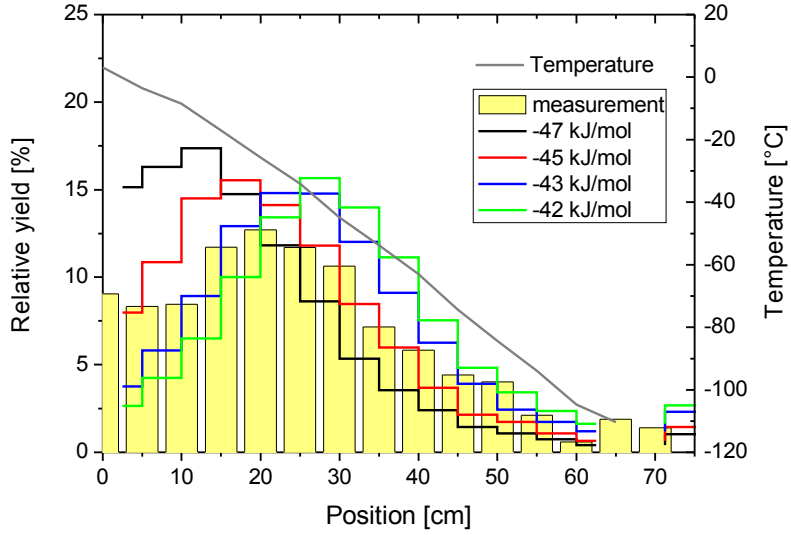

Figure 55: Thermochromatogram of ^{107}Tc. The inner diameter of the gold coated column was 4 mm. The gas mixture was a 1:1 mixture of N_2 an CO (purity 2.0). The total gas flow rate was 500 mL/min and the pressure in the target chamber was 1280 mbar. The resolution of the Monte Carlo simulation was 5 cm and a $Tc(CO)_5$ complex with a specific gravity of 2 g/cm^2 was estimated. From a comparison with the experiments $-\Delta H_{ads}=(45 \pm 8)$ kJ/mol follows.

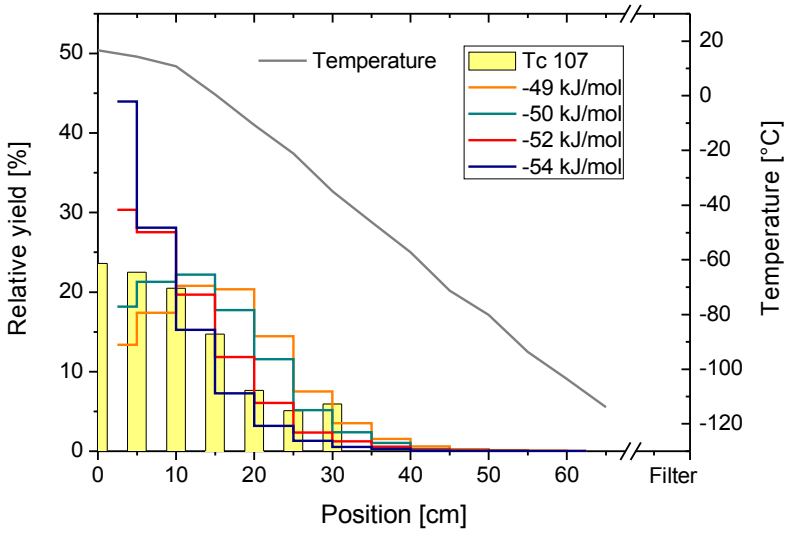

Figure 56: Thermochromatogram of ^{107}Tc on quartz surface. The gas mixture was a 1:1 mixture of N_2 an CO (purity 2.0). The total gas flow rate was 230 mL/min and the pressure in the target chamber was 1310 mbar. The inner diameter of the quartz column was 2.7 mm. The resolution of the Monte Carlo simulation was 5 cm and a $Tc(CO)_5$ complex with a specific gravity of 2 g/cm^2 was estimated. From a comparison with the experiments $-\Delta H_{ads}=(52 \pm 8)$kJ/mol follows.

The adsorption of ruthenium pentacarbonyl could not be studied, because no adequate gamma lines were visible in the spectra. Appropriate rhodium isotopes were ^{111}Rh, ^{110}Rh, and ^{109}Rh. ^{109}Rh is formed to 25% as a primary fission products. More than 50% of the ^{111}Rh and ^{110}Rh are formed as primary fission products. However, it cannot be distinguished whether the transported species was ruthenium pentacarbonyl or a rhodium carbonyl complex.

As shown in Figure 57 and Figure 58, the transported species is adsorbed at the beginning of the columns made of either material, quartz or gold. The adsorption enthalpy evaluated for the quartz surface was (−46 ± 8) kJ/mol and on gold surface (−52± 8) kJ/mol.

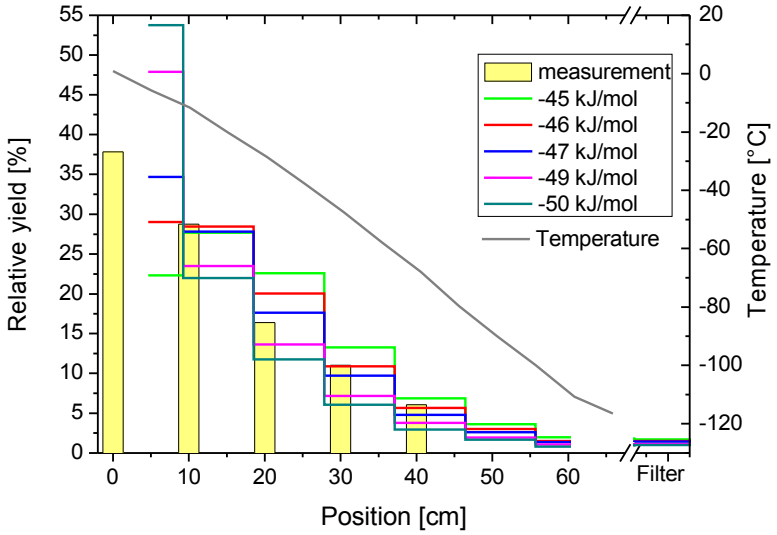

Figure 57: Thermochromatogram of ^{111}Rh carbonyl complex. The inner diameter of the quartz column was 4mm. The gas mixture was a 1:1 mixture of N_2 an CO (purity 3.7). The total gas flow was kept at 500 mL/min and the pressure in the target chamber was 1570 mbar. The resolution of the Monte Carlo simulation was 9.33 cm, $Rh(CO)_4$ with a specific gravity of 2 g/cm^2 was assumed to be the transported species. From a comparison with the experiments $-\Delta H_{ads}=(46 \pm 8)$ kJ/mol follows.

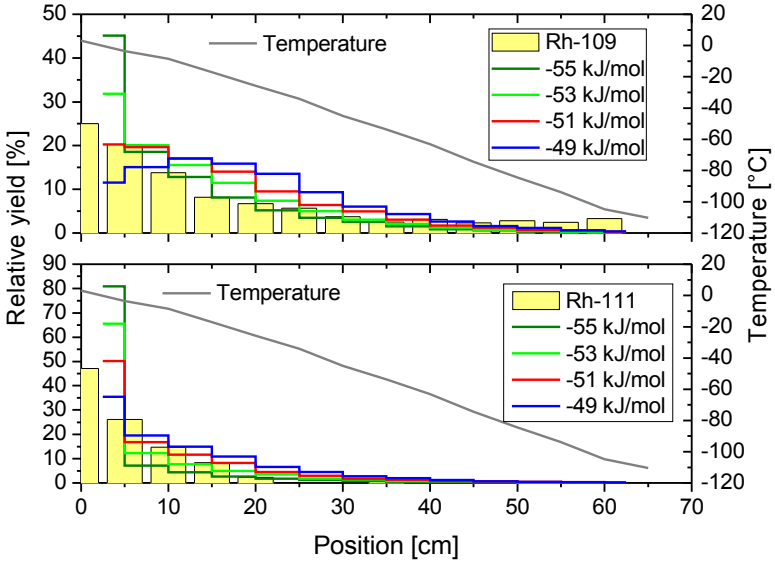

Figure 58: Thermochromatograms of ^{109}Rh (upper picture) and ^{111}Rh (picture at the bottom). The surface of the quatz column was covered with gold. The inner diameter of the column was 4 mm. The gas mixture was a 1:1 mixture of N_2 an CO (purity 2.0). The total gas flow was kept at 500 mL/min and the pressure in the target chamber was 1280 mbar. The resolution of the Monte Carlo simulation was 5 cm and a $Rh(CO)_4$ complex with an specific gravity of 2 g/cm^2 was assumed. From comparison with the experiments $-\Delta H_{ads}=(52 \pm 8)$ kJ/mol follows.

4.3.2 Experiments at Miss Piggy

Further experiments were performed at the ^{252}Cf fission source Miss Piggy at the University of Bern, Switzerland. Here the same isotopes with a little bit different ratio can be produced as with the ^{249}Cf at the TRIGA reactor. Detailed information about Miss Piggy can be found in reference [45].

The target chamber of Miss Piggy was flushed with 1 L/min helium and 0.8 L/min carbon-monoxide. The gas purity, age, and producer was unknown. The gas was purified by passing through a cartridge filled with Sicapent and a second cartridge filled with charcoal. volatile compounds were transported with the gas stream through a quartz tube which was placed in a tube furnace. The compounds, which left the quartz tube were collected in a charcoal trap. The yield of ^{107}Tc and ^{104}Mo observed in the trap as a function of the temperature of the furnace is plotted in Figure 59.

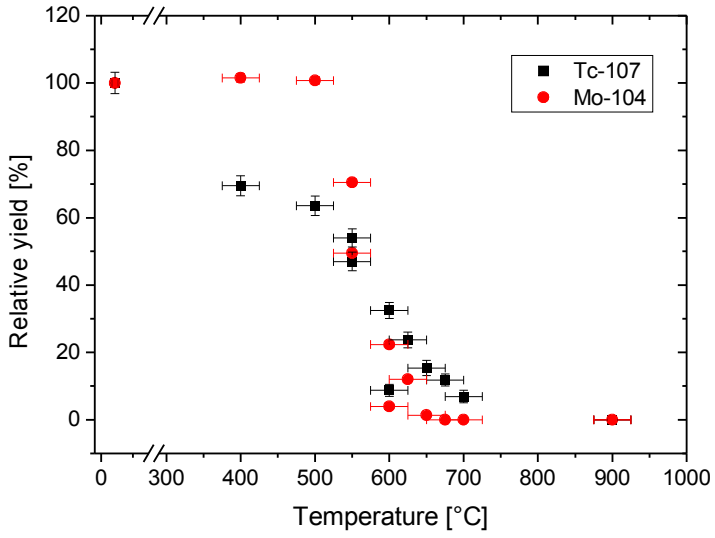

Figure 59: Relative yield observed on the charcoal trap as a function of the temperature of the tube furnace. The yield obtained at 22°C was defined as 100%.

In order to estimate the free enthalpy of the decomposition of the carbonyl-complexes, the logarithm of the ratio of decomposed species to non-decomposed complexes was calculated and plotted as a function of the inverse temperature (see Figure 60 and Figure 61).

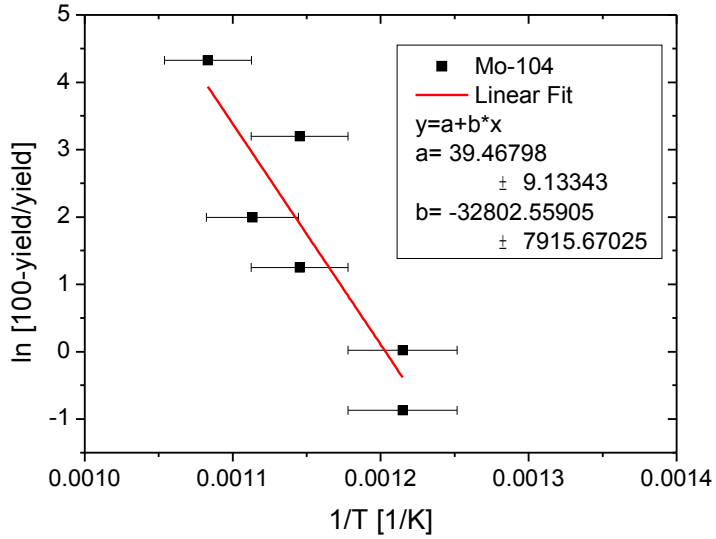

Figure 60: Plot to determine the free enthalpy of the decomposition of $Mo(CO)_6$, $-\Delta G^{\ddagger}$= 272.7±65.8 kJ/mol.

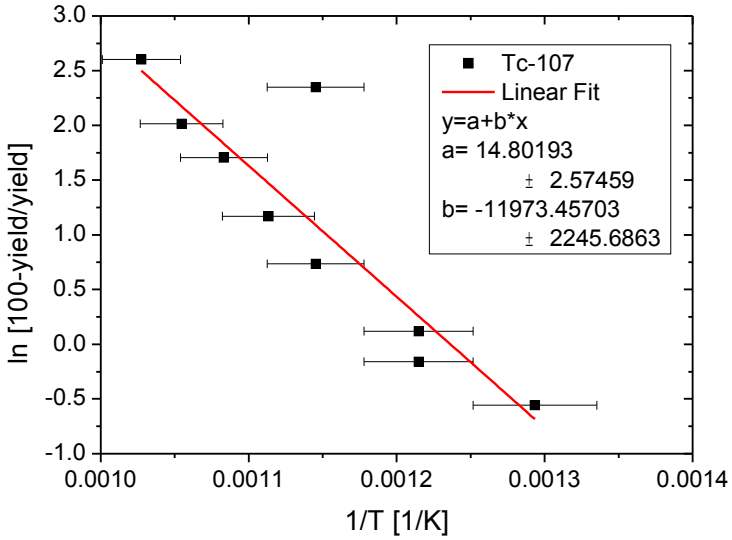

Figure 61: Plot to determine the free enthalpy of the decomposition of $Tc(CO)_x$, $-\Delta G^{\ddagger}$= 99.5±18.7 kJ/mol.

The free enthalpies of the decomposition reaction of these complexes can be estimated by multiplying the slope with the ideal gas constant. For the decomposition of molybdenum hexacarbonyl results $-\Delta G^{\ddagger}$= 272.7±65.8 kJ/mol, for the decomposition of the technetium carbonyl complex $-\Delta G^{\ddagger}$= 99.5±18.7 kJ/mol is determined.

4.3.3 Experiments at TASCA

All the experiments presented in 4.3.1 showed that several 4d elements form very fast volatile compounds, if they are thermalized in a carbon-monoxide containing atmosphere. Their transport in a gas stream is fast, efficient, and comparable with a classical KCl-cluster jet. Nevertheless, it is hard to exclude precursor effects in the experiments with fission products and to interpret all results quantitatively. The transport of the elements of the groups 4, 5, 7, and 9 is not completely understood as no stable binary carbonyl complexes of these elements are known. To overcome precursor effects and get a better understanding of the complex formation, the 5d elements tungsten, osmium, iridium, rhenium, and platinum were synthesised in ^{24}Mg induced fusion reaction populating the xn-channels. These experiments were performed at the gas-filled separator TASCA to avoid heat and plasma in the recoil chamber and to suppress background due to primary beam and transfer-products. In the experiments with tungsten and osmium, α-emitting isotopes were produced which were measured with the COMPACT detector. For the other elements no α-emitting isotopes could be produced and the nuclides were detected by γ-spectroscopy.

Nuclear reactions:

The beam delivered from the UNILAC was $^{24}Mg^{5+}$. The pulse frequency of the beam was 50 Hz and the macro pulse length 5 ms. Two different beam energies were applied during the beam time 6.5 MeV/u and 5.5 MeV/u.

At 6.5 MeV/u, the following nuclear reactions were induced:

^{144}Sm(^{24}Mg,5-4n)$^{163\text{-}164}$W

^{152}Gd(^{24}Mg,6-5n)$^{170\text{-}171}$Os

At 5.5 MeV/u, the following reactions were induced:

^{144}Sm(^{24}Mg,4-3n)$^{164\text{-}165}$W

^{152}Gd(^{24}Mg,4n)^{172}Os

^{159}Tb(^{24}Mg,5-4n)$^{178\text{-}179}$Ir

^{nat}Eu(^{24}Mg,xn)$^{170\text{-}172}$Re

^{164}Dy(^{24}Mg,6n)^{182}Pt

Table 2 gives an overview of the nuclear properties of the isotopes synthesised in the xn-channels of the performed nuclear reactions.

Table 2: Nuclear properties of the nuclear fusion products formed in the xn-channels, data taken from reference[97]

Isotope	$T_{1/2}$ [s]	Decay mode	Branching [%]
^{163}W	2.75	e-capture + β^+	59
		α	41
^{164}W	6	e-capture + β^+	95.6
		α	4.4
^{165}W	5.1	e-capture + β^+	100
		α	<0.2
^{170}Os	7.3	e-capture + β^+	88
		α	12
^{171}Os	8	e-capture + β^+	98.3
		α	1.7
^{172}Os	19.2	e-capture + β^+	99
		α	1
^{178}Ir	12	e-capture + β^+	100
^{179}Ir	79	e-capture + β^+	100
^{170}Re	9.2	e-capture + β^+	100
^{171}Re	15.2	e-capture + β^+	100
^{172}Re	15 / 55	e-capture + β^+	100
^{182}Pt	270	e-capture + β^+	99.969
		α	0.031

In the reactions to synthesise tungsten, osmium, rhenium, and iridium, a target wheel of the type ARTESIA [99] was used. The target material was deposited on thin titanium foil backings held by a banana shaped aluminium frame. Three of these targets were assembled to the target wheel. The target wheel was synchronized to the macropulse structure of the UNILAC. Within one macro pulse length one target segment was irradiated.

For the synthesis of platinium a stationary target was used.

Details according to the target thickeness and isotope composition of the target material will be given later in the sub chapters about every studied element.

TASCA

The experiments took place at the TASCA separator (for a detailed description see chapter 2.2). TASCA is separated from the UNILAC by a differential pumping section. It has a classical DQQ structure – a dipole magnet is placed behind the target followed by two quadrupole magnets. TASCA was operated in the Small Image Mode (SIM) and it was filled with 0.8 mbar helium. By interaction with the helium atoms in the separator, the evaporation residues were brought to an average charge state. The recoiling fusion products were separated in the magnetic field of the dipole magnet from the primary beam and the transfer-products. They were focused by the two quadrupole magnets to the end of TASCA. In the back flange was the window to the recoil transfer chamber (RTC). Two moveable degrader foils, one 1.3 µm and one 0.9 µm thick Mylar foil, were installed in front of the RTC window. The RTC window itself was a 3.3 µm thick Mylar foil supported by a honeycomb grid. The window size was (3x4) cm^2.

Focal plane detector

To optimize the ion optical settings and to get information about the amount of evaporation residues passing the window, a detector chamber was installed behind TASCA. A double sided silicon strip detector (DSSSD) was placed in this chamber 1 cm behind the RTC window. Figure 62 shows a photograph of the detector inside the detector chamber. The detector size was (58 mm·58 mm). It 32 strips in x direction and 32 strips in y direction.

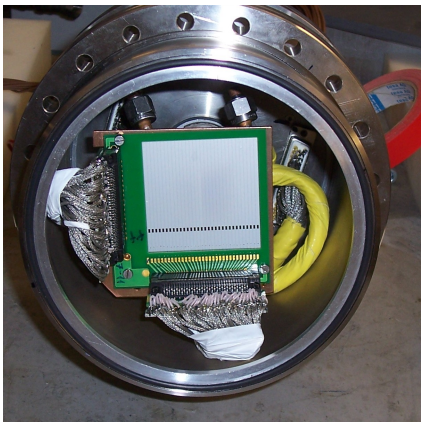

Figure 62: Photograph of the DSSSD inside the detector chamber, which was installed behind TASCA.

The RTC

For the chemistry experiments, the detector chamber was replaced by the RTC. The inner part of the RTC was cylindrical with an inner diameter of 3 cm. The gas entered the RTC at the right and the left side 1 cm behind the RTC window. The rear cover was funnel-shaped with the gas outlet at the back. At the RTC exit was a quarz tube with an inner diameter of 2 mm. The quartz tube was inside an aluminium tube which was wrapped with a heating band connected with a temperature controller. A temperature sensor (type K) was fixed between the heating tape and the aluminum tube, it was connected with the temperature controller of the tape. Figure 63 shows a schematic drawing of the RTC.

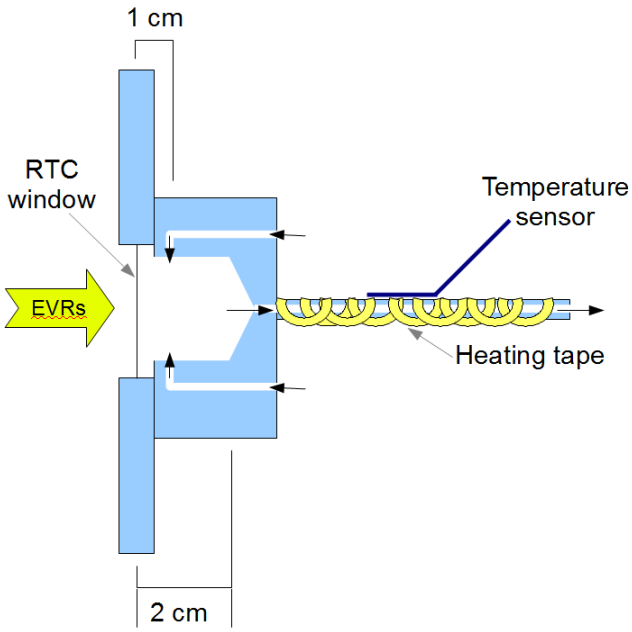

Figure 63: Schematic drawing of the SIM RTC. The evaporation residues (EVRs) enter through the RTC window. The window is rectangular (3·4) cm² The RTC has a circular cross-section (3 cm inner diameter). The gas enters the RTC 1 cm behind the RTC window – result of this is a dead-volume between entrance window and gas stream, which is not flushed effectively. The RTC outlet is a quartz tube which is encased by an aluminum tube wrapped with a heating band. The temperate at was controlled with a temperature sensor placed between the aluminum tube and the heating tape.

Inside the RTC, the evaporation residues were thermalized in gas atmosphere. The RTC was connected to the gas-jet system and was flushed continuously with gas.

Gas jet system

The inert gas used in the experiments was helium, (Linde 6.0= with a purity of minimum 99.9999%, the maximum impurities are according to the deliverer $O_2 \leq 0.5$ ppm, $N_2 \leq 0.5$ ppm, $H_2O \leq 0.5$ ppm, $H_2 \leq 0.5$ ppm, $C_nH_m \leq 0.5$ ppm, CO ≤ 0.1 ppm and $CO_2 \leq 0.1$ ppm. The minimum purity of the carbon monoxide (Linde, 3.0) was 99.9%, the maximum impurities were $N_2 \leq 750$ ppm, $H_2 \leq 250$ ppm, $C_nH_m \leq 50$ ppm and $(O_2 + Ar) \leq 60$ ppm.

The gas jet system was the one constructed for COMPACT by J. Dvorak [109]. It is a loop system to dry the gas continously and reduce the amount of gas needed for the experiment. The scheme of the system is shown in Figure 64.

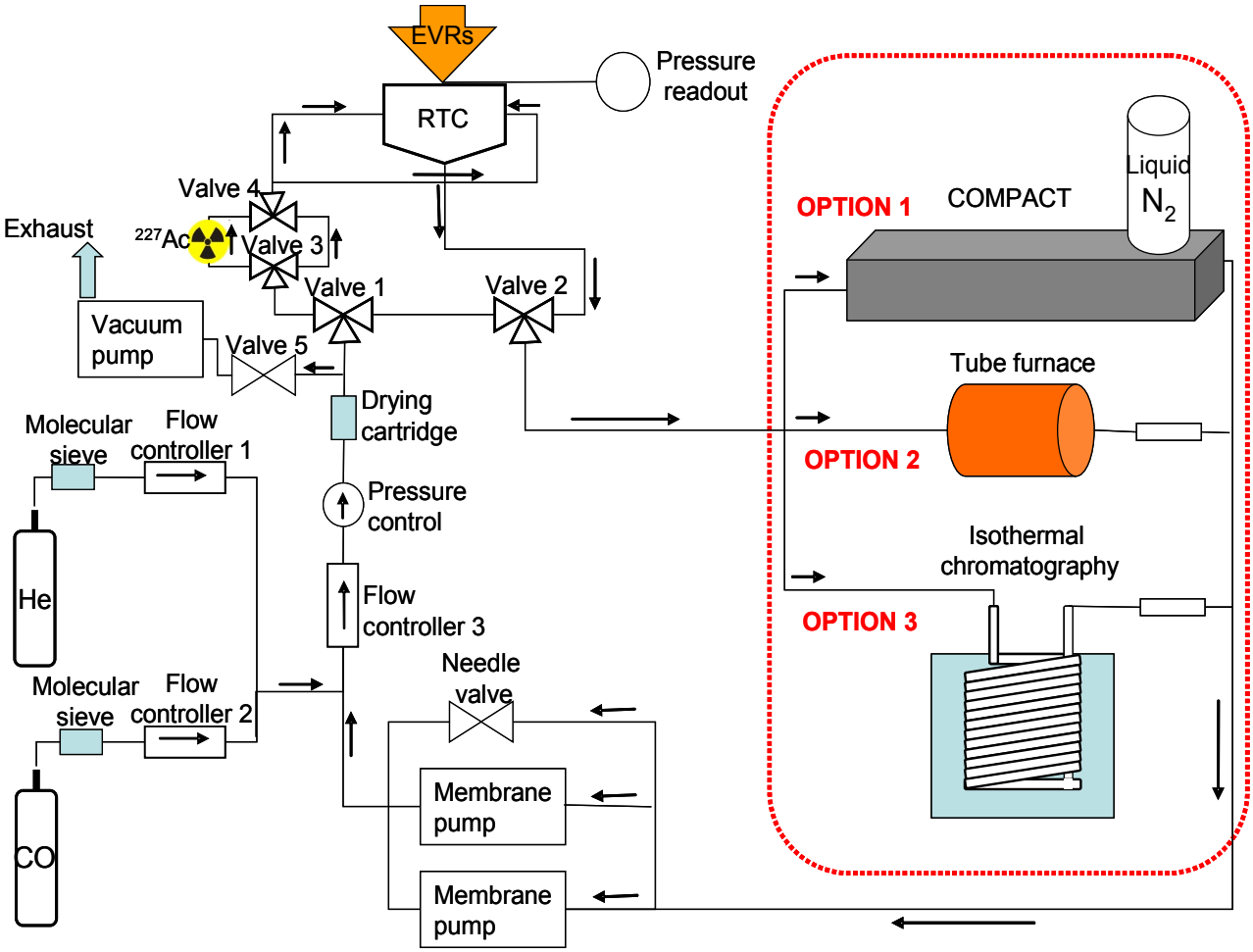

Figure 64:Schematic of the gas loop system at TASCA. The loop system is filled by opening flow controllers 1 and 2. The loop can be evacuated by opening valve 5. To provide a stable gas-flow, two membrane pumps were installed in the loop. The gas flow rate in the loop was regulated by flow controller 3. By switching valves 1 and 2, the gas stream was guided either through the RTC or through a bypass. Depending on the measurement, COMPACT, an isothermal chromatography setup, or a decomposition setup could be installed in the gas loop.

Before entering the loop, the gases were pre-dried by passing a cartridge filled with molecular sieve. The gas-loop was filled and the gas mixture was regulated by the flow controllers 1 and 2. The whole gas jet loop was connected to a vacuum pump. By opening valve 5 the loop was evacuated. By mass-flow controller 3 the flow rate inside the loop was regulated. To provide a stable flow inside the loop, two membrane pumps were installed. To dry the gas in the loop, a cooling trap filled with molecular sieve placed in liquid nitrogen was installed in the experiments with the COMPACT. In the isothermal chromatography experiments and decomposition experiment, this cooling trap was replaced by a cartridge filled with Sicapent (from Merck). A pressure gauge (pressure control) was installed in the loop which was connected to the same control

device as the flow controllers. In case the gas pressure dropped below a set point, the loop was automatically filled with new gas by flow controller 1 and 2.

By switching valves 1 and 2, the gas was guided through the RTC or a bypass. These valves were automated. If the pressure (measured by pressure control) was outside the pre-set limits, these valves switched to bypass. The pressure inside the RTC chamber was monitored by pressure readout.

The tubes were made of stainless steel or PFA. In the experiments with COMPACT, the connection between valve 2 and COMPACT was a 1.5-m long PFA capillary with an inner diameter of 4 mm. To monitor the transport and calibrate the COMPACT detector array, the gas stream could be guided through a ^{227}Ac emanation source by switching valves 3 and 4. One of the decay products of ^{227}Ac is ^{219}Rn ($t_{1/2}$ = 3.19 s), which can be transported within the gas-stream and its α-decaying daughter nuclide ^{211}Po and ^{211}Bi are deposited in the COMPACT detector array.

For the isothermal chromatography and decomposition experiments, the gas loop was extended. Valve 2 and the chemistry device were connected via a 10 m long PTFE capillary with an inner diameter of 2 mm.

COMPACT

The experiments with α-emitting isotopes were performed with the COMPACT detector array. Two different COMPACT detector arrays were used during the beamtime – one (COMPACT I) with quartz (SiO_2) surface the other one (COMPACT II) with a gold surface.

A detailed description and technical details of COMPACT are given in references [24] and [109].

Each COMPACT consists of two Invar™ panels (see Figure 65). On each panel, 32 α-PIN (Positive Intrinsic Negative) diodes of (1·1) cm^2 are glued. Two pannels are assembled that the α-PIN diodes face to each other. In between the pin diodes is a 0.6 mm wide gap with a width of 1 cm (definded by the PIN diode size). The gas stream is passing this channel and the volatile compound might be adsorbed on the detector surfaces. The active detection surface of each pin diode in COMPACT I is (9.3·9.3) mm^2. In COMPACT II, the active detection surface of the pin diodes is (9.7·9.9) mm^2 or (9.7·9.7) mm^2. With this detector assembly, a detection efficiency near 4π is reached.

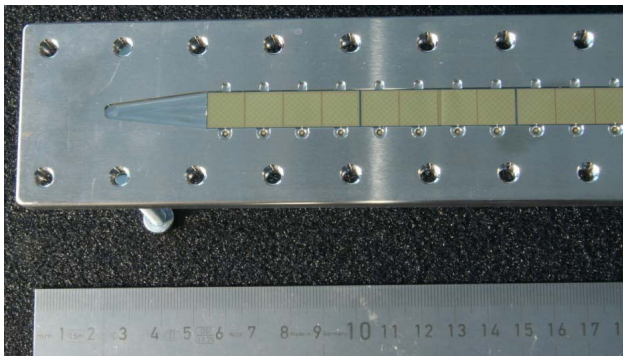

Figure 65: Photography of the Invar panel with the implemented gold-coverd pin detectors. Photo taken from ref. [24].

The “Invar panel sandwich” is placed in a vacuum box made of steel covered with nickel to reduce the influence of electromagnetic fields onto the PIN diodes. One end of the detector panel is contacted by a copper cold finger, which is cooled down with liquid nitrogen. This way, a temperature gradient is kept stable over the duration of the beam time. The gas enters from the warm side of the detector channel and leaves at the cooled end. The temperature is monitored with type K temperature sensors. At the COMPACT I detector array, four temperature sensors are mounted equally distant to each other – one sensor at each end of the array and two in the middle. At the COMPACT II detector array are only three sensors mounted, one at each end of the array and one in the middle.

The isothermal chromatography

For the isothermal chromatography experiments, the helical quartz column was used. It was placed in an ethanol filled thermostat, which could be cooled down to -80 °C. The inner diameter of the column was 2 mm. The total length which was placed in the cool bath was 191 cm. The volatile compounds leaving the column were collected in a charcoal trap which was placed in front of a germanium detector.

Decomposition setup

To get information about the stability of the carbonyl complexes, the gas stream was guided through a quartz tube with an inner diameter of 4 mm, which was surrounded by a tube furnace. In

the middle of the tube was a quartz wool plug to enlarge the contact surface. Behind the quartz tube was an activated charcoal trap placed in front of a germanium detector. Figure 66 shows a photo of the quartz tube in the tube furnace.

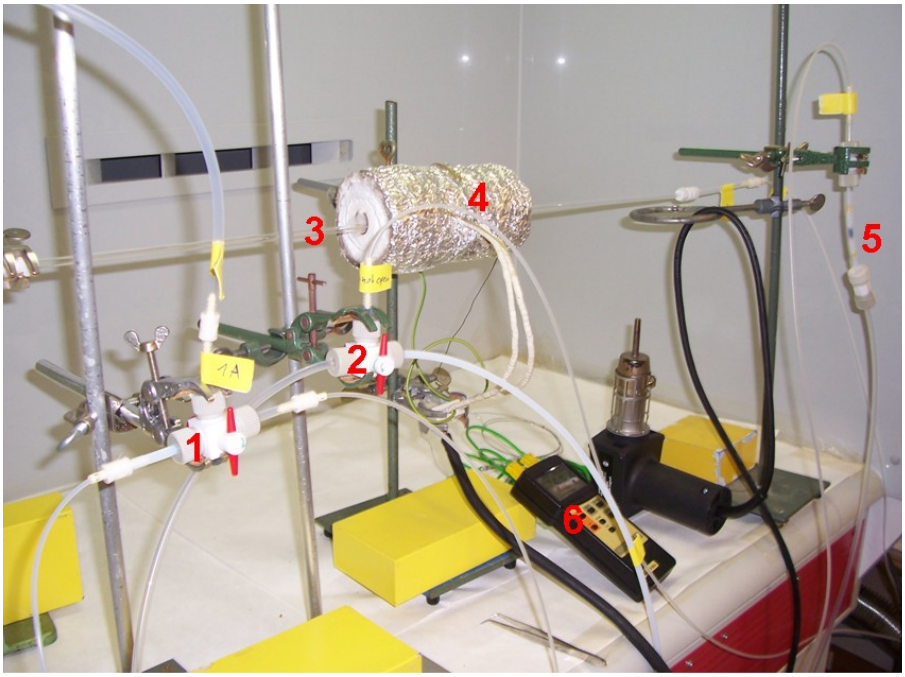

Figure 66: Photo of the decomposition setup. With the valves **1** *and* **2** *the gas could either be guided through the quartz column* **3** *or a bypass. The quartz column contained a quartz-wool plug, which was placed in the centre of the tube furnace* **4**. *The temperature of the oven was monitored by the thermocontroller* **6**. *The activity was collected in the charcoal trap* **5**.

4.3.3.1 Experiments with tungsten

Production of tungsten

Carrier free tungsten was produced in the reaction $^{144}Sm(^{24}Mg,xn)^{168-x}W$. The target wheel used was of the type ARTESIA [99]. The three targets were metallic samarium on 2 µm thick titanium backing foil. The target segments had an average thickness of 380 µg/cm^2 samarium. The ^{144}Sm was enriched to 88.6%.

In Figure 67, the results of HIVAP calculations [100] are shown for the xn- and the pxn-channels.

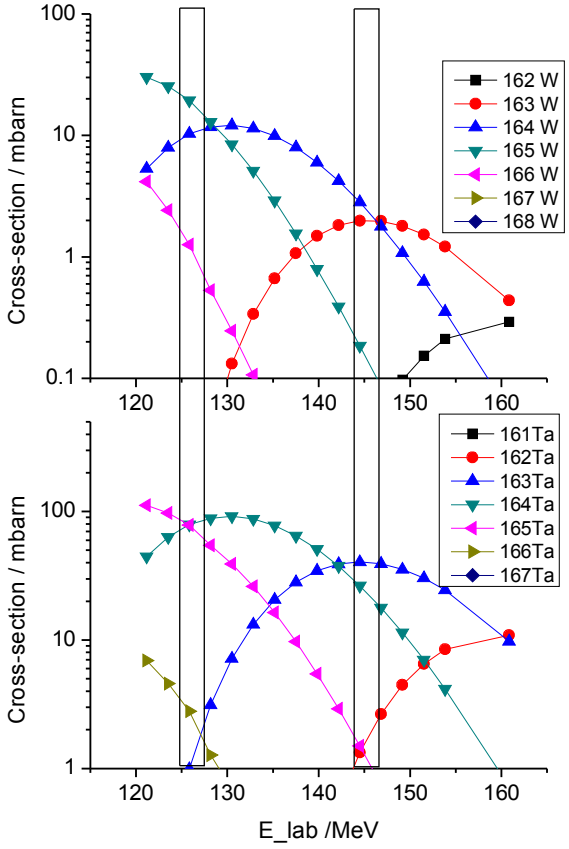

Figure 67: With HIVAP calculated cross sections depending on the beam energy in the target for the reaction $^{144}Sm(^{24}Mg,xn)$ and $^{144}Sm(^{24}Mg,pxn)$.The black frames mark the beam energies covered inside the target.

In the beam time, two different beam energies were chosen – 150 MeV and 132 MeV. At a beam energy from the UNILAC of 150 MeV, the beam energy in the middle of the target was 145 MeV

(calculated with SRIM [173]) and the evaporation residue ^{163}W had an energy of 5.9 MeV at the end of TASCA after passing the 3.3 µm thick Mylar window of the RTC. At a beam energy of 132 MeV from the UNILAC, an energy of 126 MeV in the centre of the target is calculated with SRIM.

For the measurements, none of the degrader foils were placed in front of the RTC window. At a beam energy of 150 MeV, the measurements were performed with the dipole set to 415 A (corresponding $B{\cdot}\rho$ = 1.588 T·m), quadrupole 1 set to 304 A and quadrupole 2 set to 351 A. For these measurements, COMPACT I (with a SiO_2 surface) was used. The measurements performed with COMPACT II (with a gold coated detector-surface) were performed at the beam energy 132 MeV, the dipole was set to 420 A (corresponding $B{\cdot}\rho$ = 1.604 T·m), quadrupole 1 was set to 309 A and quadrupole 2 was set to 357 A.

Measurements with COMPACT 1 - adsorption studies on SiO_2 surface

At the beginning of the experiment, the counting statistics in the COMPACT 1 detector array were rather poor, but during the first hours the statistics increased. Later it was realized that the molecular sieve was a trap for carbon monoxide – and in first measurements the carbon-monoxide concentration was too low. Afterwards, the molecular sieve was saturated with carbon monoxide. The carbon-monoxide could be filled by a defined ratio into the loop and tungsten was transported a a volatile carbonyl complex to the detector channel. Figure 68 shows a typical sum spectrum of the top detectors. Two different tungsten isotopes could be identified - the 2.75-s ^{163}W and the 6.0-s ^{164}W. The α-branch of ^{163}Ta which is produced in the pxn-channel has only an abundance of 0.2% and the α-energy is 4633 keV, so this could not be identified in the spectra.

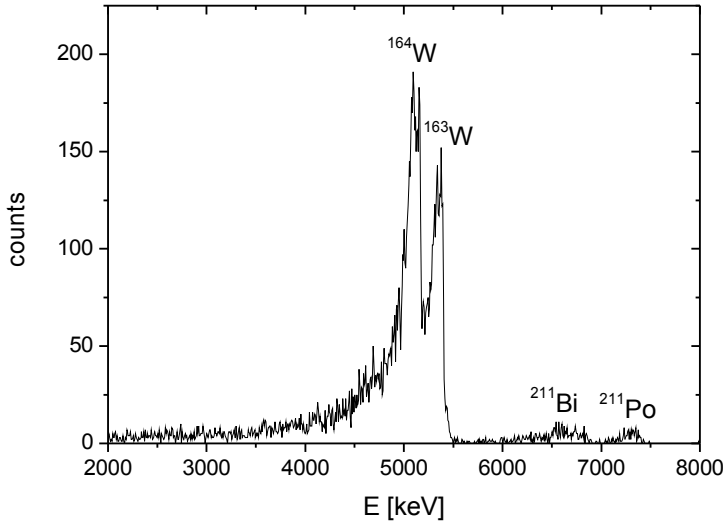

Figure 68: Sum spectrum of the top detectors. The measurement was performed at a gas flow of 850 mL/min and a pressure of 800 mbar inside the RTC. The beam integral was $2.48 \cdot 10^{15}$. ^{164}W and ^{163}W can be clearly identified as well as the ^{211}Bi and ^{211}Po – the daughters of ^{227}Ac.

Various settings were tested. The thermochromatograms were analysed by choosing three different energy windows – from 4000 keV up to 5500 keV to get all the events from ^{163}W and ^{164}W. The second energy gate chosen was from 5250 keV to 5500 keV to take only ^{163}W into account. The third gate was the energy from 4000 keV to 5200 keV to analyse mainly the ^{164}W (although there was a contribution from the low-energy tail of ^{163}W present in this energy region). For each energy window, the total count number over the detector array was set as 100%. The relative yields for each detector pair (the 2 α-PIN diodes facing each other) are determined. Figure 69, Figure 71, and Figure 73 show the thermochromatograms for the different energy windows. The results were compared with Monte Carlo Simulations. For every Monte Carlo Simulation the square number of deviations from the measurement was calculated for each detector pair. All 32 square numbers of deviations were summed to *sum* χ^2. The summed values of the square number of deviations were plotted against $-\Delta H_{ads}$ values used in the different Monte Carlo Simulations (see Figure 70, Figure 72, Figure 74). The better the simulations agree with the measurement the lower is *sum* χ^2 value and $-\Delta H_{ads}$ can be determined. To determine the one σ-area, the measured chromatography peak was fitted by a gaussian peak function and the one σ-area in which the peak-maximum might be shifted is marked in the chromatograms with dashed lines (Figure 69, Figure 71, and Figure 73).

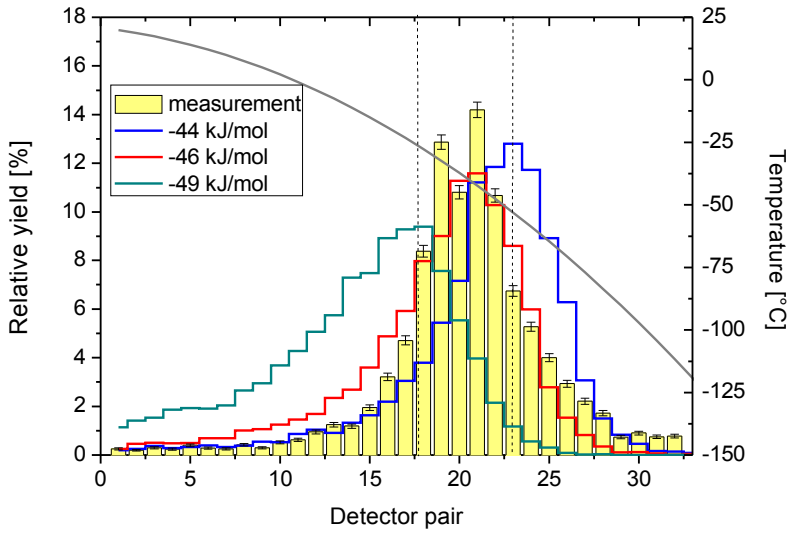

Figure 69: Thermochromatogram of $^{163}W(CO)_6$. The bar plot shows the number of detected α-particles in each detector pair with an energy between 5250 keV and 5500 keV. The grey curve is the temperature profile of the column, and the coloured curves are the simulated chromatograms with $-\Delta H_{ads} = 46^{+3}_{-2}$ kJ/mol. The gas-mixture was 50% He and 50% CO. The total gas-flow was 0.85 L/min, the pressure in the RTC was 0.80 bar. The dashed lines mark the one σ-area in which the peak-maximum might be shifted.

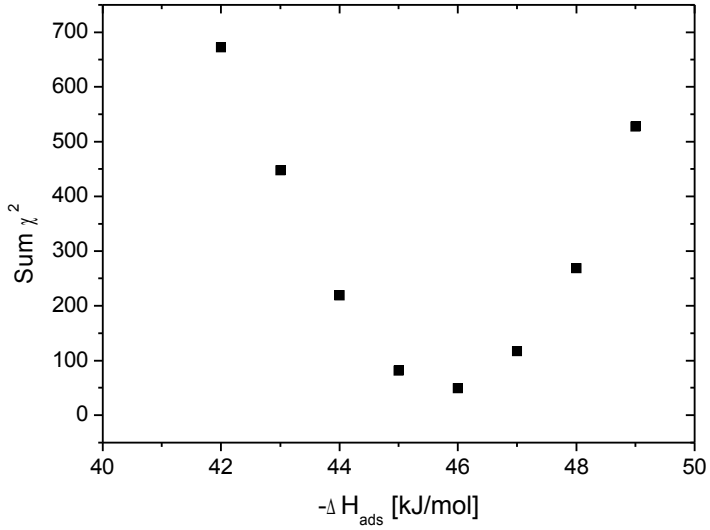

Figure 70: Summed values of the square number of deviations (sum χ^2) of the measurement shown in Figure 69 from values from the simulated thermochromatorgrams. The simulation with $-\Delta H_{ads} = 46$ kJ/mol agrees best with the measured thermochromatogram.

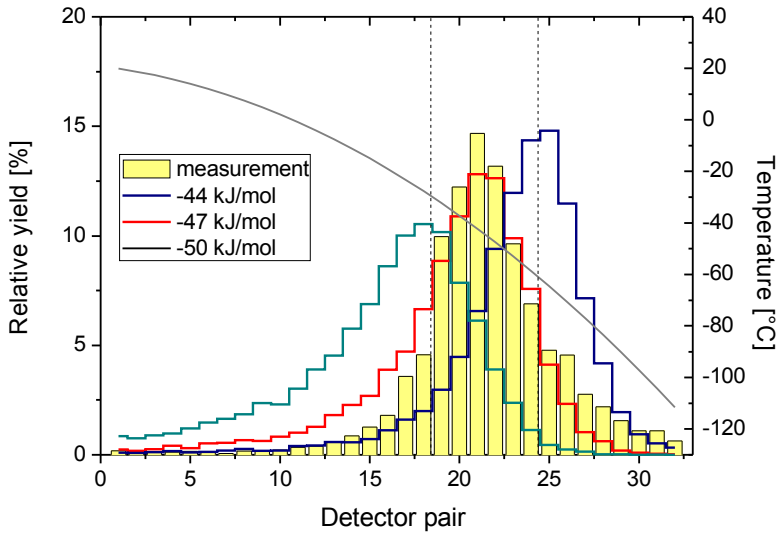

Figure 71: The thermochromatogram measured for $^{164}W(CO)_6$. The bar plot shows the number of detected α-particles in each detector pair with an energy between 4000 keV and 5200 keV. The grey curve is the temperature profile of the column, and the coloured curves are the simulated chromatograms with $-\Delta H_{ads}$= (47±3) kJ/mol. The dashed lines mark the one σ-area in which the peak-maximum might be shifted. The experimental settings are the same as in Figure 69.

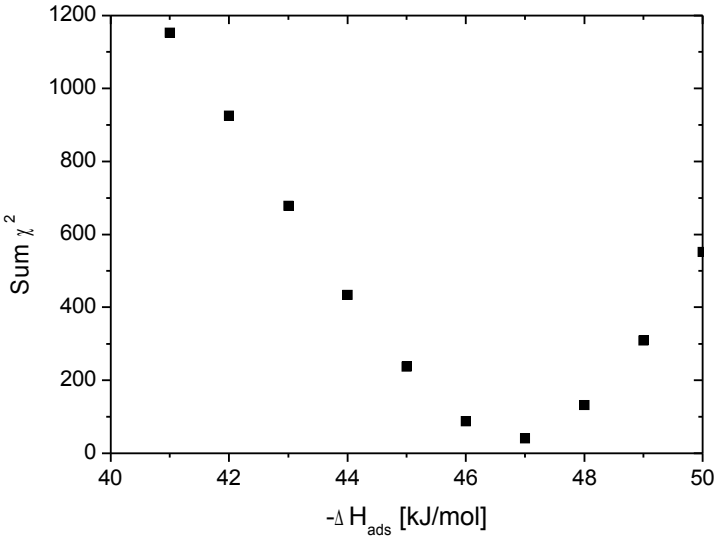

Figure 72: Summed values of the square number of deviations (Sum χ^2) of the measurements shown in Figure 71 from the simulated thermochromatorgrams. The simulation with $-\Delta H_{ads}$= 47 kJ/mol agrees best with the measured thermochromatogram.

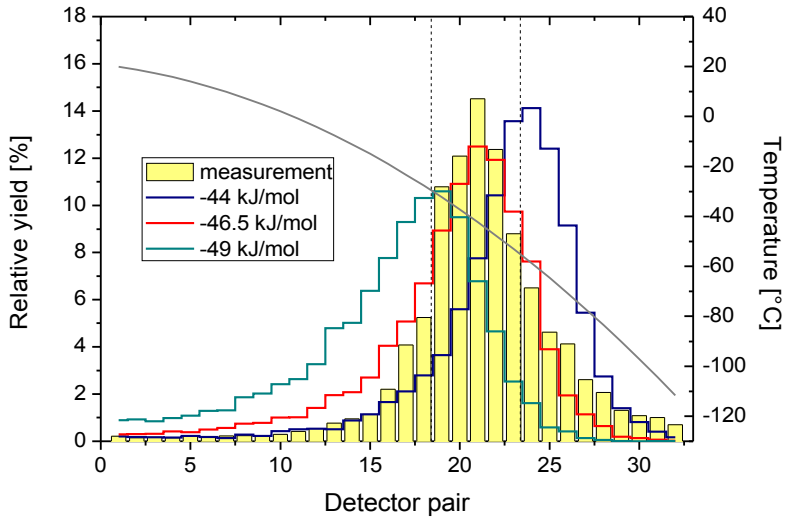

Figure 73: The thermochromatogram measured for $^{163}W(CO)_6$ and $^{164}W(CO)_6$. The bar plot shows the number of detected α-particles in each detector pair with an energy between 4000 keV and 5500 keV. The grey line is the temperature along the column. The experimental settings are the same as in Figure 69. The dashed line show the one σ-area in which the peak-maximum might be shifted. The coloured lines are the simulations: $-\Delta H_{ads}$= (46.5±2.5) kJ/mol. For the simulation a half-life of 4.4 s was estimated.

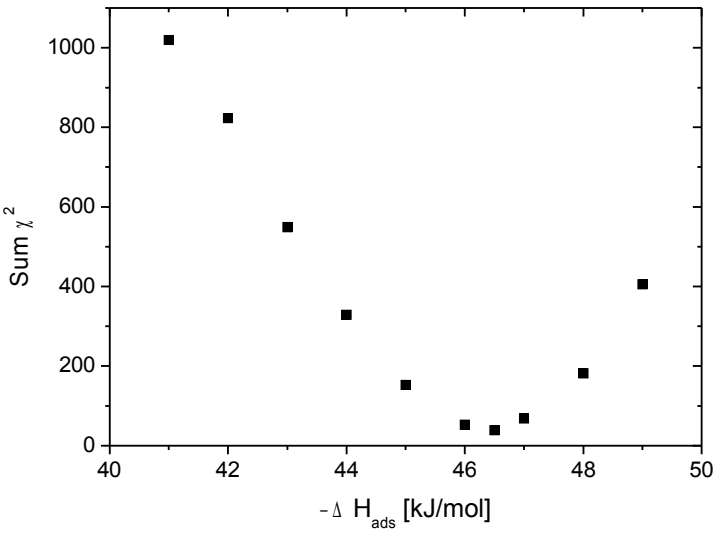

Figure 74: Summed values of the square number of deviations (Sum χ^2) of the measurement shown in Figure 73 from the simulations. The simulation with $-\Delta H_{ads}$= 46.5 kJ/mol agrees best to the measured thermochromatogram.

Furthermore, thermochromatograms were measured at a lower carbon-monoxide concentration. Figure 75 shows a thermochromatogram of a helium/carbon monoxide ratio of 80/20. The adsorption enthalpy of -46^{+2}_{-1} kJ/mol is in good agreement with the measurements at higher carbon-monoxide concentrations.

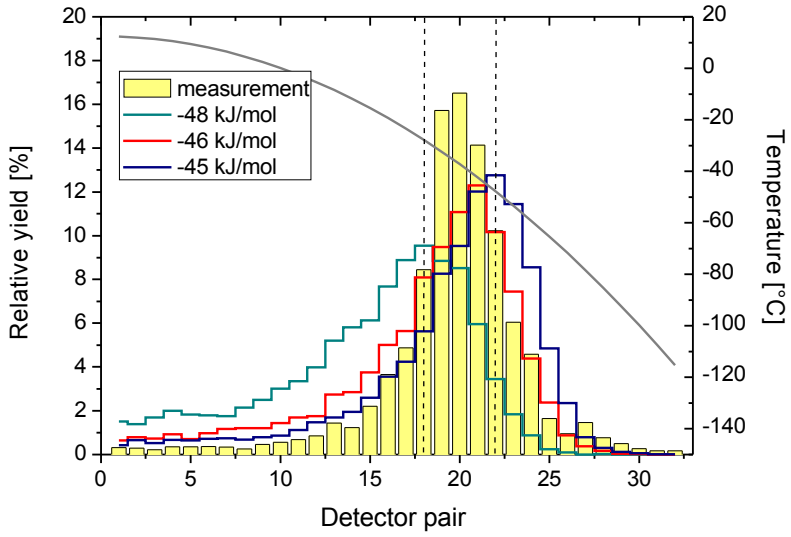

Figure 75: The thermochromatogram measured for $^{163}W(CO)_6$. The bar plot shows the number of detected α-particles in each detector pair with an energy between 5250 keV and 5500 keV. The grey curve is the temperature profile of the column, and the coloured curves are the simulated chromatograms for the different values of $-\Delta H_{ads} = 46^{+2}_{-1}$ kJ/mol. The dashed lines mark the one σ-area, in which the peak-maximum might be shifted. The gas-mixture was 80% He and 20% CO. The total gas-flow was 0.82 L/min, the pressure in the RTC was 0.8 bar and the beam integral was $2.23 \cdot 10^{15}$.

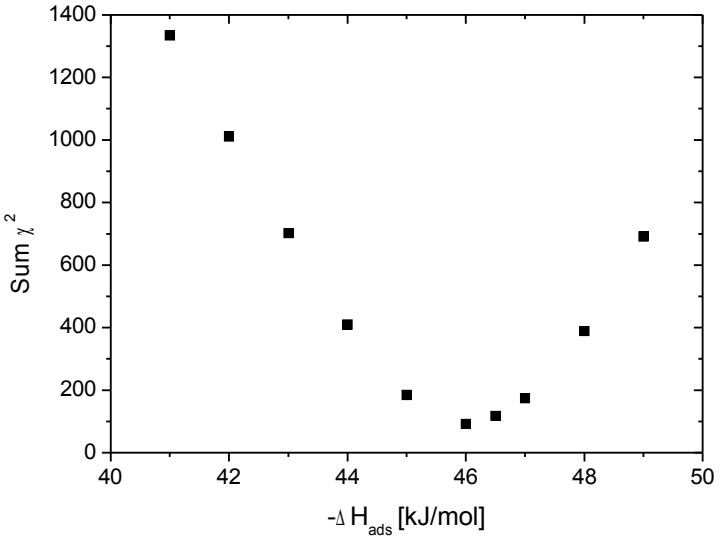

Figure 76: Summed values of the square number of deviations (Sum χ^2) of measured values from the simulated thermo-chromatogram curves shown in Figure 75. The simulation with $-\Delta H_{ads}$=46 kJ/mol agrees best with the measured thermochromatogram.

The results of these measurements are all consistent with each other within the error due to the counting statistics. From the measurements, an adsorption enthalpy of (−46 ± 2.5) kJ/mol for $W(CO)_6$ on SiO_2 surface is determined. This is a typical value for physisorption.

Measurements with COMPACT II – adsorption studies on gold

As mentioned before, the measurements with COMPACT II (which has a gold-covered detector-surface) were done at a lower beam energy. In the spectra, mainly 6-s ^{164}W, with an α-energy of 5149.8 keV, could be identified (see Figure 77).

The trap with the molecular sieve was still connected to the gas-jet system, however, it was saturated with carbon-monoxide at that point in the experiment series.

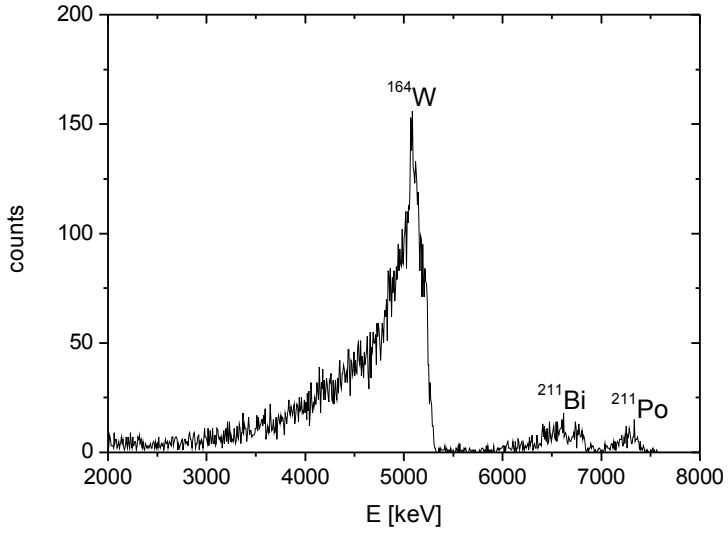

Figure 77: Sum spectrum of the top detector taken at a gas flow rate of 730 mL/min and a pressure of 780 mbar inside the RTC. The beam integral was $3.65 \cdot 10^{15}$.

Data were taken at different flow settings. As an example, the thermochromatogram measured at a 50:50 ratio of helium and carbon-monoxide is shown in Figure 78 and a thermochromatogram measured with a helium to carbon-monoxide ratio oft 90:10 is shown in Figure 80.The data were analysed the same way as described for the measurements with COMPACT I. The relative yield for each detector pair was measured and the thermochromatograms were compared with Monte Carlo simulations. Figure 79 and Figure 81 show the sum of the standard deviations of the measurements from the Monte Carlo Simulations using various values for the adsorption enthalpies.

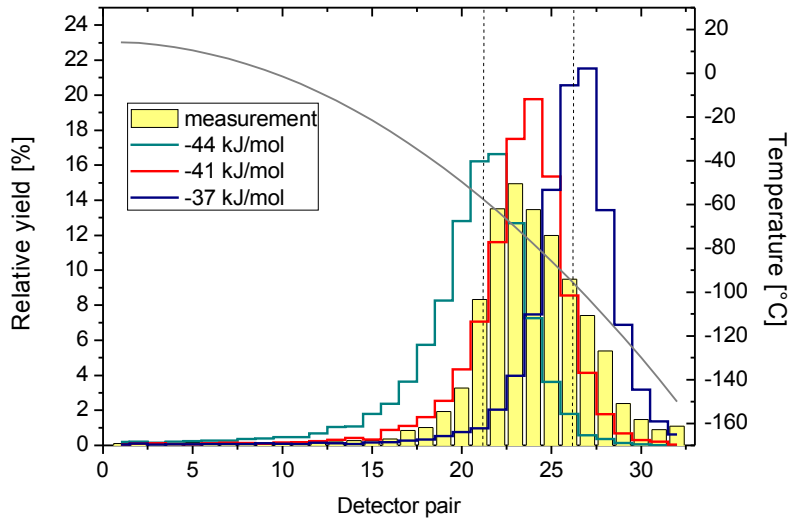

Figure 78: The thermochromatogram measured with $^{164}W(CO)_6$. The bar plot shows the number of detected α-particles in each detector pair with an energy between 4000 keV and 5350 keV. The grey curve is the temperature profile of the column. The coloured lines are the simulated chromatograms with $-\Delta H_{ads} = (41^{+3}_{-4})\,kJ/mol$. The dashed lines mark the one σ-area of the peak-maximum. The gas-mixture was 50% He and 50% CO. The total gas-flow was 0.73 L/min, the pressure in the RTC was 0.80 bar, the beam integral was $2.88 \cdot 10^{15}$

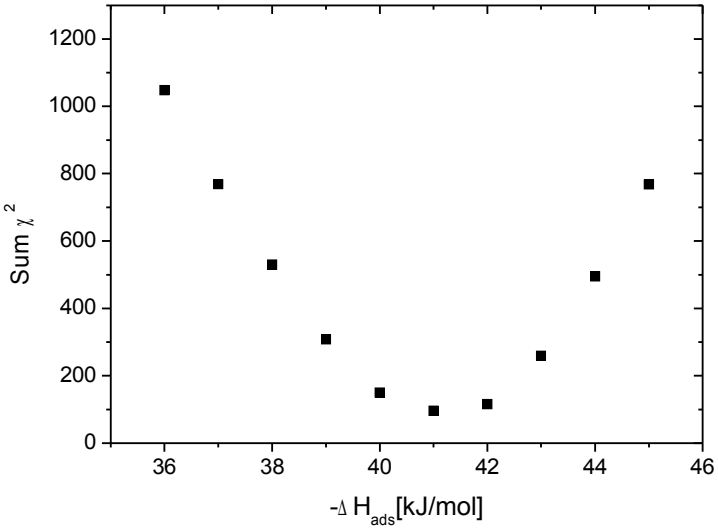

Figure 79: Summed values of the square number of deviations of measured values shown in Figure 78 from the simulated thermochromatorgram curves for different values of $-\Delta H_{ads}$ The simulation with $-\Delta H_{ads}$=41 kJ/mol agrees best with the measured thermochromatogram.

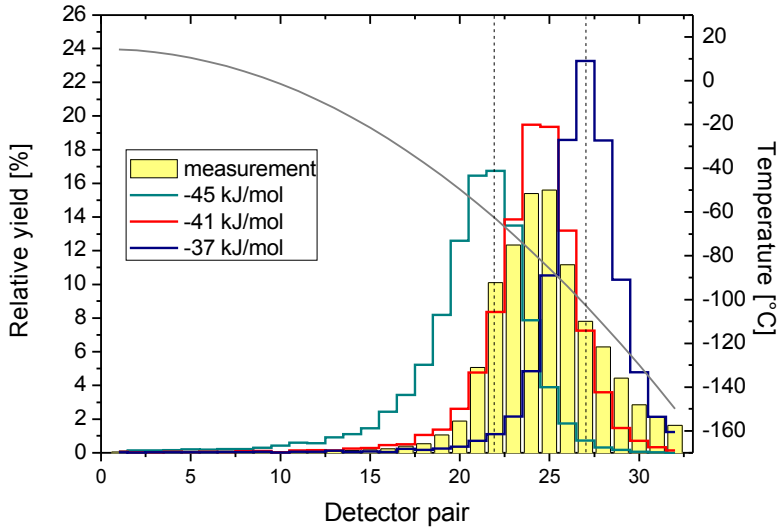

Figure 80: The thermochromatogram measured for $^{164}W(CO)_6$. The bar plot shows the number of detected α-particles in each detector pair with an energy between 4000 keV and 5350 keV. The grey curve is the temperature profile of the column, and the coloured curves are the simulated chromatograms for the different values of ΔH_{ads}. The gas-mixture was 90% He and 10% CO. The total gas-flow was 1.26 L/min, the pressure in the RTC was 0.73 bar and the beam integral was $2.56 \cdot 10^{15}$. The dashed lines show the one σ-area in which the peak-maximum might be shifted. Comparsion with the simulations gives $-\Delta H_{ads} = (41 \pm 4)$ kJ/mol.

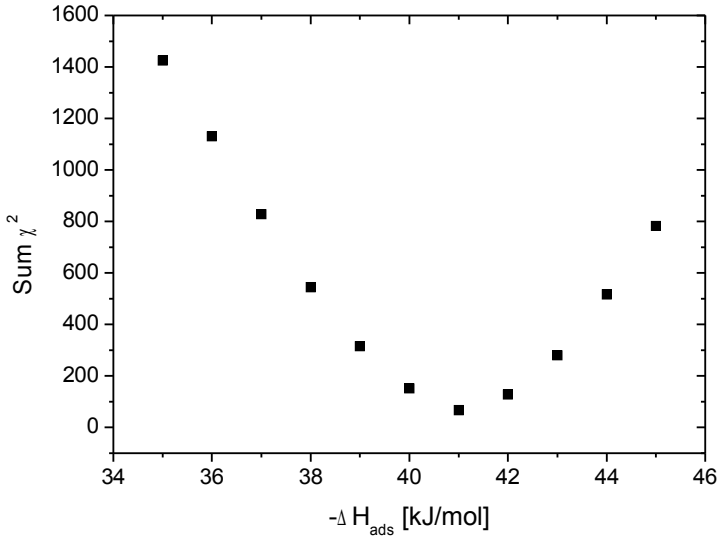

Figure 82: Summed values of the square number of deviations of measured values shown in Figure 80 from the simulated thermochromatogram curves with different values for $-\Delta H_{ads}$. The simulation with $-\Delta H_{ads}$=41 kJ/mol agrees best with the measured thermochromatogram.

The measured adsorption enthalpy of ($-\Delta H_{ads} = 41^{+3}_{-4}$ kJ/mol) is slightly lower than the one determined in the measurement with COMPACT I of ($-\Delta H_{ads}$ = 46.5±2.5 kJ/mol). However, within the statistical errors, the values are comparable. Both values obtained for the adsorption enthalpy of tungsten hexacarbonyl on gold ($-\Delta H_{ads} = 41^{+3}_{-4}$ kJ/mol) and on silicon dioxide ($-\Delta H_{ads}$ = 46.5±2.5 kJ/mol) are typical values for physisorption. It is surprising that the adsorption on gold is weaker than on quartz. One would expect that the adsorption on a metallic surface is stronger than on an inert surface as SiO_2. One reason might be that gold forms surface carbonyl complexes in a carbon-monoxide atmosphere [174], however in the simulations only a pure metallic gold surface was taken into account. The surface compelexes of course change the chemical behaviour of the surface and are probably more inert than gold.

4.3.3.2 Experiments with Osmium

Production of Osmium

Osmium was produced in the reaction ^{152}Gd(^{24}Mg,xn)$^{176-x}$Os. The targets were electroplated as Gd_2O_3 on 1.9 µm thick titanium backing foil. The targets had a thickness of 300 µg/cm^2, 260 µg/cm^2, and 364 µg/cm^2 gadolinium. The isotopic composition of the gadolinium was ^{152}Gd 39.3%, ^{154}Gd 5.9%, ^{155}Gd 16.7%, ^{156}Gd 13.8%, ^{157}Gd 7.7%, ^{158}Gd 10% and ^{160}Gd 6.6%. The cross-sections predicted with HIVAP for the four main Gd-isotopes are shown in Figure 83.

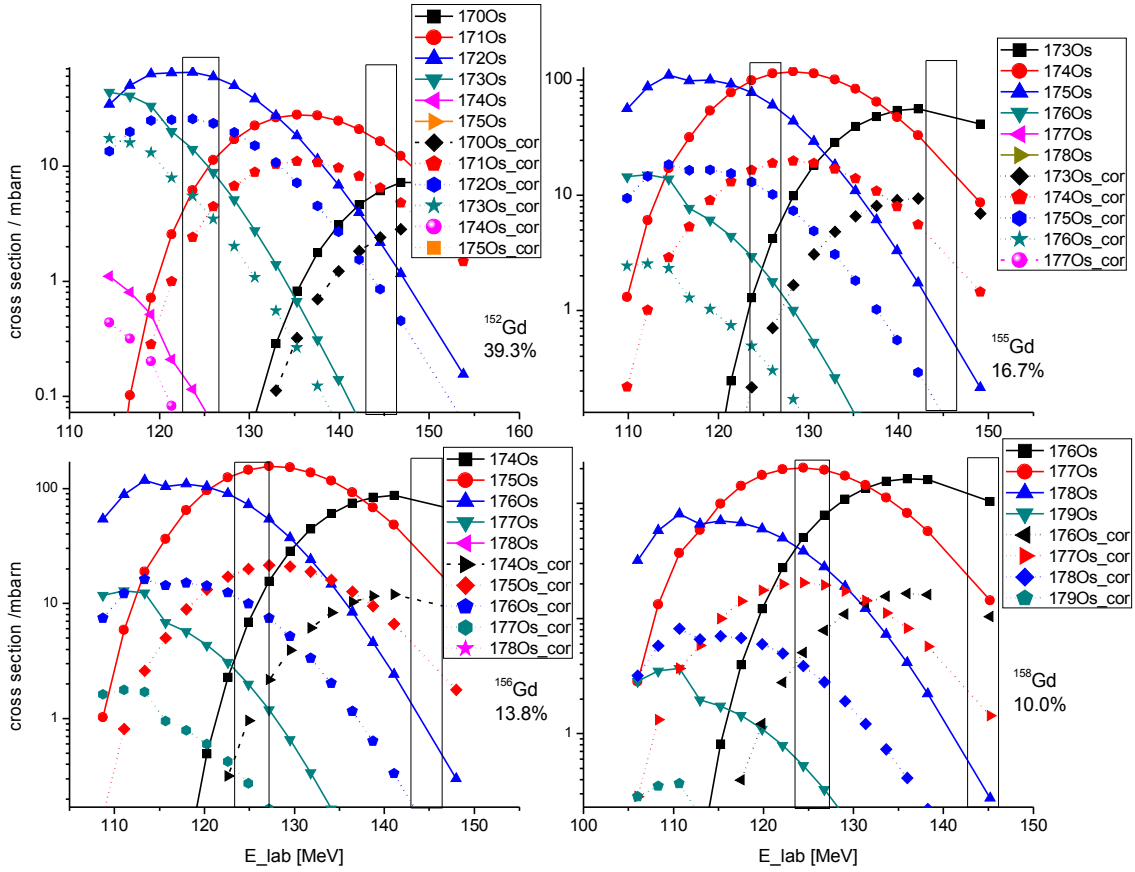

Figure 83: With HIVAP calculated cross sections of the reaction Gd(^{24}Mg,xn) depending on the beam energy in the target for the four main Gd isotopes. The cross sections normalized to the abundance of the isotope are shown with the dashed lines (Os_cor). The black frames mark the beam energies used during the beam time.

Two different beam energies were chosen. For the experiments with COMPACT I (SiO_2 detector-surface), the beam energy was 150 MeV from the UNILAC, corresponding to an energy of 144 MeV in the centre of the target. For the experiments with COMPACT II (gold-covered detector-surface), the beam energy from the UNILAC was changed to 132 MeV, resulting in an energy of 125 MeV in the middle of the target.

For the measurements with COMPACT I, the dipole magnet was set to 416 A corresponding to $B{\cdot}\rho$=1.591 T·m, the quadrupole 1 was set to 316 A and the quadrupole 2 was set to 389 A. According to SRIM simulations, the energy of ^{170,171}Os entering the RTC through the 3.3 µm thick Mylar window was about 5.3 MeV. For the measurements with COMPACT II, the dipole magnet was set to 416 A ($B{\cdot}\rho$=1.591 T·m), the quadrupole 1 to 315 A and the quadrupole 2 was set to 365 A. With SRIM a kinetic energy of 4.2 MeV is predicted for the ^{172}Os after passing the RTC window.

Measurements with COMPACT I – adsorption studies on SiO_2

Figure 84 shows a sum spectrum of the top detector of COMPACT I. ^{170}Os and ^{171}Os could not be separated in the spectra. ^{170}Os has an half-life of 7.3 s, the α-energy is 5402 keV; ^{171}Os has a half-life of 8.0 s, the α-energy is 5254 keV. This indicates the formation and transport of volatile $Os(CO)_5$.

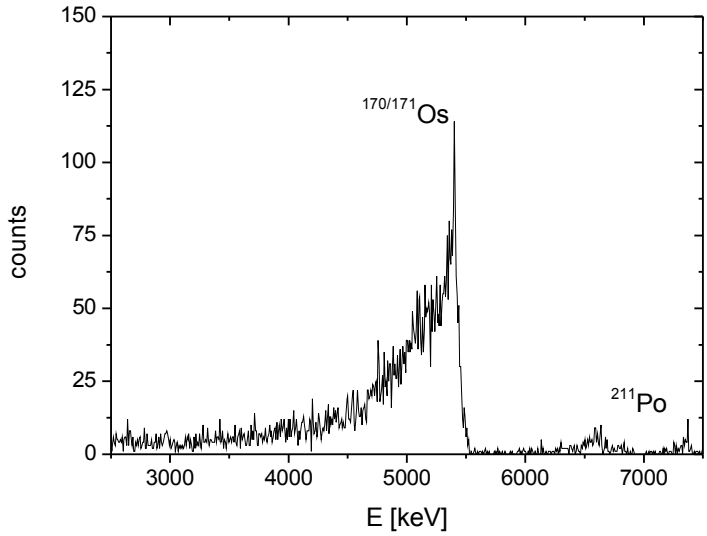

Figure 84: Sum spectrum of the top detector. The measurement was performed at a gas flow rate of 1090 mL/min and a pressure of 730 mbar inside the RTC. The beam integral was $2.18 \cdot 10^{15}$. ^{170}Os and ^{171}Os could not be separated in the spectrum. ^{211}Bi and ^{211}Po , the daughters of ^{227}Ac, can be clearly identified

The measurements were analyzed the same way as the ones performed with the tungsten isotopes. The relative yield for each detector pair was determined and the thermochromatograms were compared with Monte Carlo simulations assuming different adsorption enthalpies. Typical thermochromatograms for different flow rates are shown in Figure 85 and Figure 87. One problem to simulate the thermochromatograms was that no data of the physical density of osmium pentacarbonyl are available. For some measurements, simulations were run with an estimated density of 2.5 and 3.0 g/cm^3; both simulations lead to nearly the same result. In Figure 86, the sum of the error squares are compared and it is seen that the effect of the error in the estimated density is negligible.

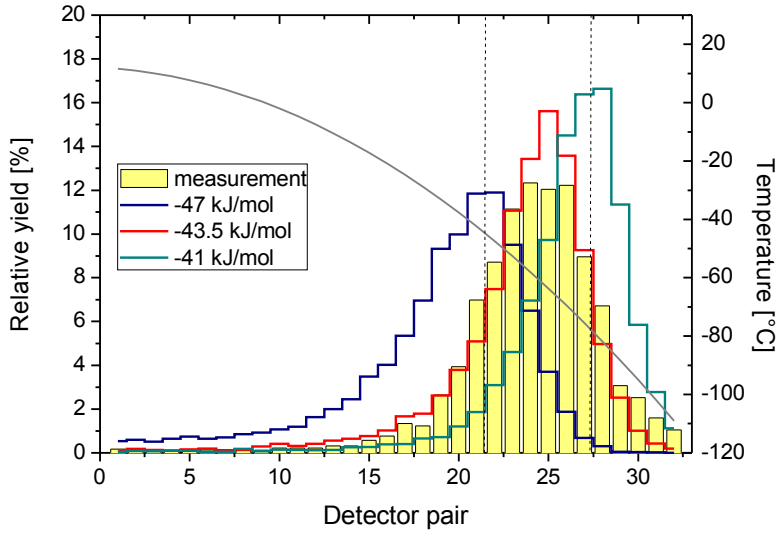

Figure 85: The thermochromatogram measured with $^{170}Os(CO)_5$. The bar plot shows the number of detected α-particles in each detector pair with an energy between 4000 keV and 5650 keV. The grey curve is the temperature profile of the column, and the coloured curves are the simulated chromatograms for $-\Delta H_{ads} = 43.5^{+3.5}_{-2.5} kJ/mol$ The dashed line marks the one σ-area of the peak. The gas-mixture was 50% He and 50% CO. The total gas-flow rate was 0.73 L/min, the pressure in the RTC was 0.75 bar. The beam integral was $2.48 \cdot 10^{15}$.

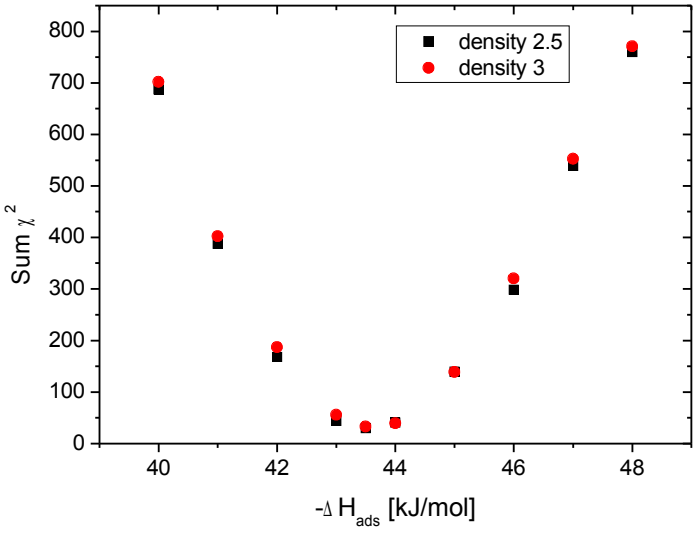

Figure 86: Summed values of error square of measured values compared with the simulated thermochromatorgram curves shown in Figure 85. The simulation was run with estimated densities of osmium pentacarbonyl of 2.5 g/cm² and 3.0 g/cm². Both simulations agree best with the measurements with $-\Delta H_{ads}$=43.5 kJ/mol.

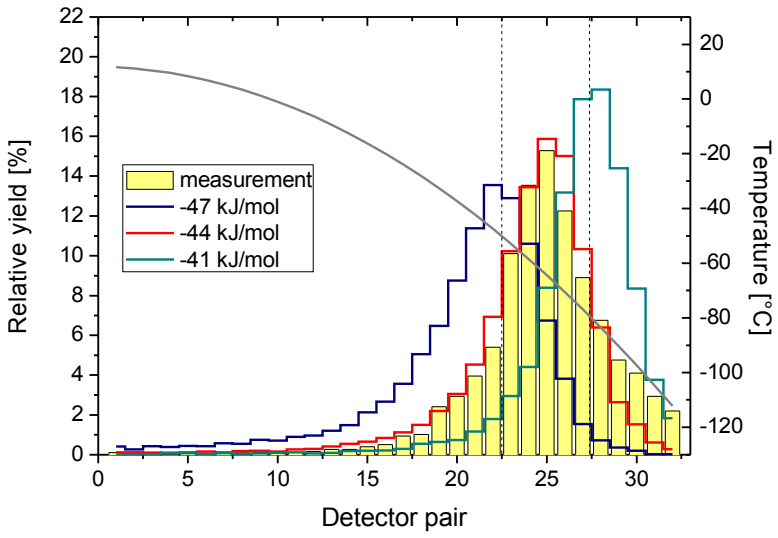

Figure 87: The thermochromatogram measured with $^{170}Os(CO)_5$. The bar plot shows the number of detected α-particles in each detector pair with an energy between 4000 keV and 5650 keV. The grey curve is the temperature profile of the column, and the coloured curves are the simulated chromatograms with $-\Delta H_{ads}$= (44 ±3) kJ/mol. The dashed lines mark the one σ-area in which the peak maximum might be shifted. The gas-mixture was 80% He and 20% CO. The total gas-flow was 1.09 L/min, the pressure in the RTC was 0.73 bar and the beam integral was $2.18 \cdot 10^{15}$.

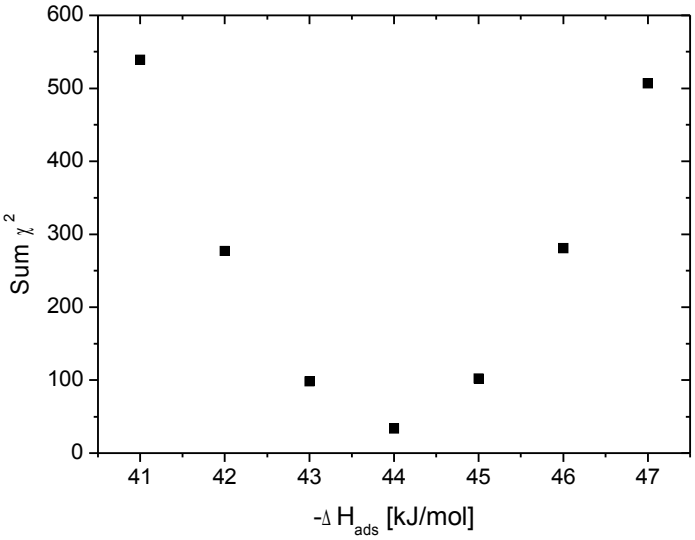

Figure 88: Summed values of the square number of deviations of measured values compared with the simulated thermochromatorgram curves shown in Figure 87. The simulations with $-\Delta H_{ads}$=44 kJ/mol agree best with the measurements.

The adsorption enthalpies determined in the different measurements are within the uncertainties the same. A value of $-\Delta H_{ads}$= *(44 ±3)* kJ/mol indicates the physisorption of osmium pentacarbonyl on a silicon dioxide surface.

Measurements with COMPACT II – adsorption studies on gold

As mentioned before, the measurements with COMPACT II were run at a lower beam energy. The isotope ^{172}Os with a half-life of 19.2 s was mainly produced and formed volatile $Os(CO)_5$ in the RTC. In Figure 89 a typical sum spectrum of the top detector array is shown.

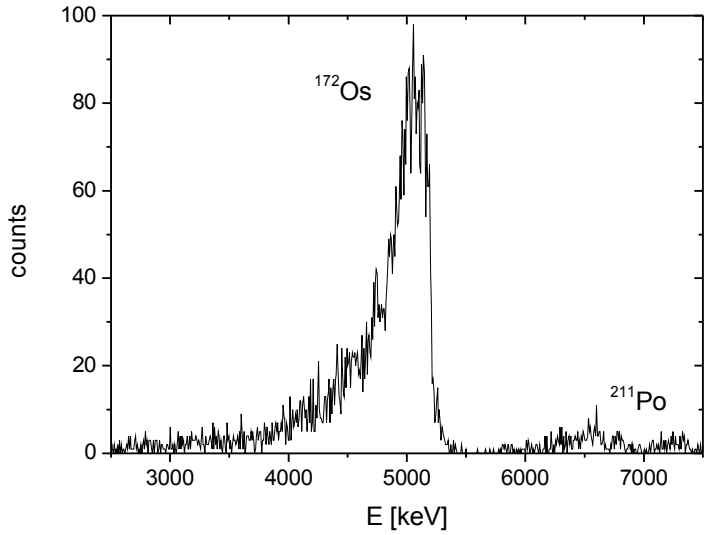

Figure 89: Sum spectrum of the top detector. The measurement was performed at a gas flow of 730 mL/min and a pressure of 800 mbar inside the RTC. The beam integral was $2.53 \cdot 10^{15}$. ^{172}Os as well as ^{211}Bi and ^{211}Po, the daughters of ^{227}Ac, can be clearly identified

Various measurements were done. Typical thermochromatograms are shown in Figure 90, Figure 92, and Figure 94. The relative yield for each detector-pair was determined and the results were compared with Monte Carlo Simulations for different adsorption enthalpies. The adsorption enthalpies were determined by the minimum deviation of the simulations from the measurement (see Figure 91, Figure 93 and Figure 95).

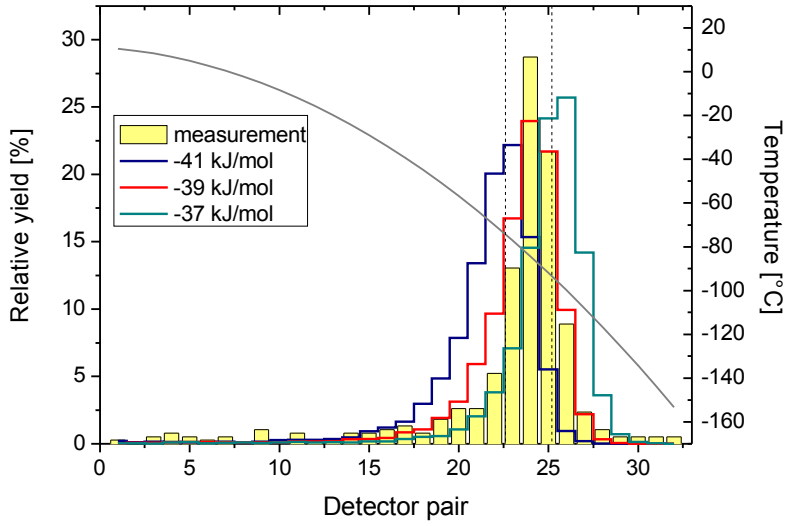

Figure 90: The thermochromatogram measured with ^{172}Os. The bar plot shows the number of detected α-particles in each detector pair with an energy between 4000 keV and 5400 keV. The grey curve is the temperature profile of the column, and the coloured lines are the simulated chromatograms with *$-\Delta H_{ads}$= (39 ± 2) kJ/mol. The dashed line show the one σ-area in which the peak maximum might be shifted. The gas-mixture was 50% He and 50% CO. The total gas-flow was 0.24 L/min, the pressure in the RTC was 0.94 bar and the beam integral was 2.47·10^{15}.*

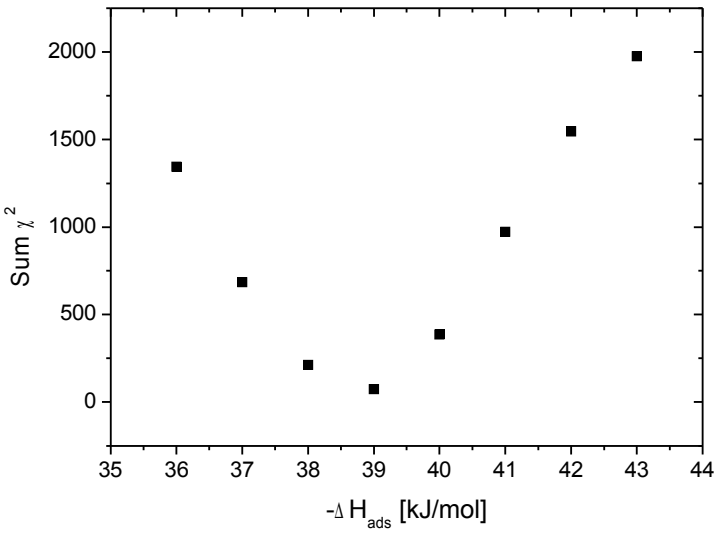

Figure 91: Summed values of the square number of the deviations of measured values compared with the simulated thermochromatography curves shown in Figure 90. From the simulations , $-\Delta H_{ads}$=39 kJ/mol can be deduced.

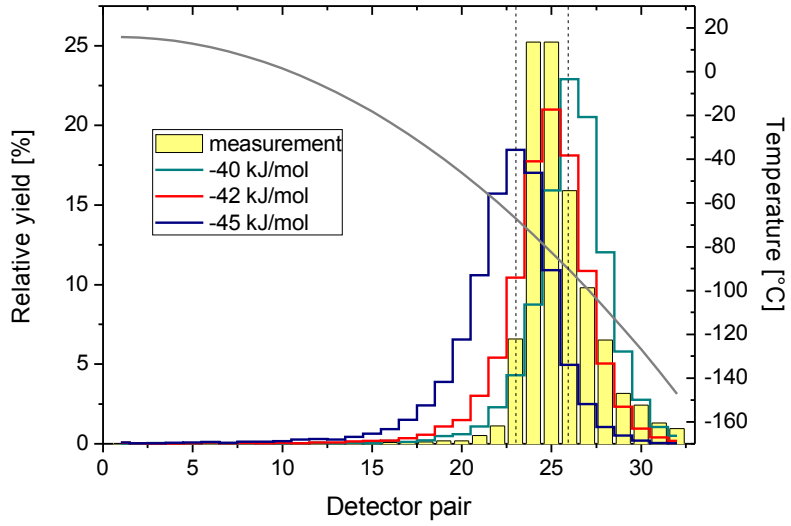

Figure 92: The thermochromatogram measured with ^{172}Os. The bar plot shows the number of detected α-particles in each detector pair with an energy between 4000 keV and 5400 keV. The grey curve is the temperature profile of the column, and the coloured curves are the simulated chromatograms for the different ΔH_{ads}. The gas-mixture was 80% He and 20% CO. The total gas-flow was 0.82 L/min, the pressure in the RTC was 0.8 bar and the beam integral was $2.50 \cdot 10^{15}$. The dashed lines show the one σ-area in which the peak-maximum might be shifted. Comparison with the simulations gives $-\Delta H_{ads} = (42^{+3}_{-2})$ kJ/mol.

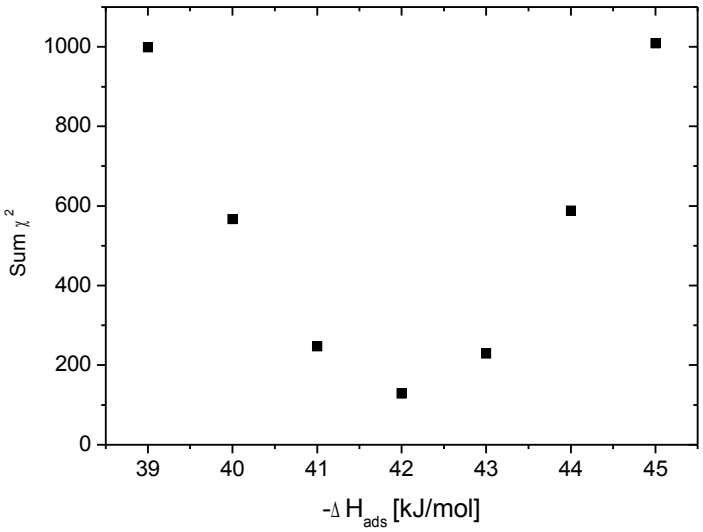

Figure 93: Summed values of the square number of deviations of measured values compared with the simulated thermochromatorgraphy curves shown in Figure 92. From the simualtions, $-\Delta H_{ads}$=42 kJ/mol can be deduced.

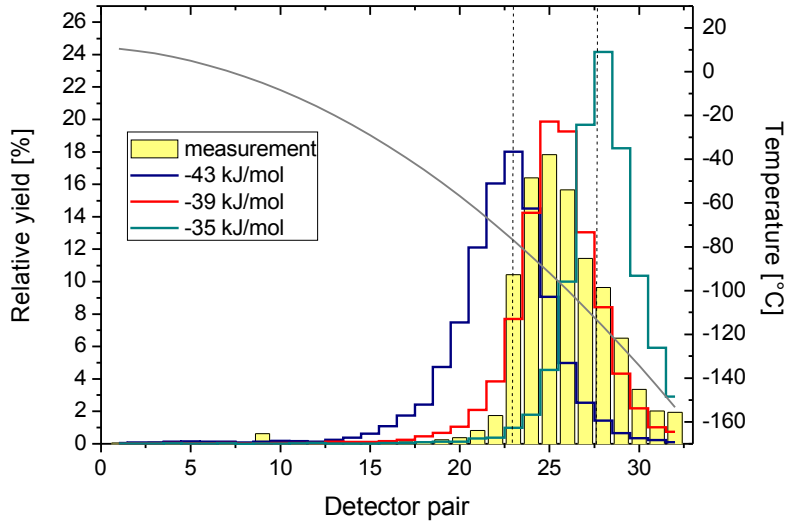

Figure 94: The thermochromatogram measured with ^{172}Os. The bar plot shows the number of detected α-particles in each detector pair with an energy between 4000 keV and 5400 keV. The grey curve is the temperature profile of the column, and the coloured curves are the simulated chromatograms for the different ΔH_{ads}. The gas-mixture was 50% He and 50% CO. The total gas-flow was 0.73 L/min, the pressure in the RTC was 0.8 bar and the beam integral was $2.32 \cdot 10^{15}$. The dashed lines show the one σ-area in which the peak-maximum might be shifted. Comparsion with the simulations gives $-\Delta H_{ads} = (39 \pm 4)$ kJ/mol.

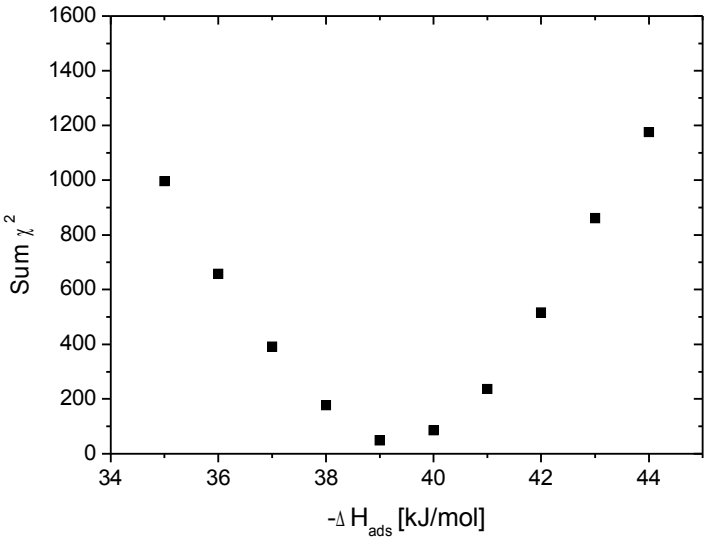

Figure 95: Summed values of the square number of deviations of measured values compared with the simulated thermochromatograms shown in Figure 94. From the simulations $-\Delta H_{ads} = 39$ kJ/mol can be deduced.

Within the statistical errors, the determined adsorption enthalpies are the same – the difference between the results comes from the uncertainties in the gas mixture. During the experiments, the molecular sieve was still connected to the gas loop, which made it difficult to guarantee a certain helium to carbon monoxide ratio. With the ratio, the average molecular mass, the average density and with it the gas flow regulated with a mass flow controller changes. The accurate adsorption enthalpy is probably between the measured values $-(39\pm 4)$kJ/mol and $-(42^{+3}_{-2})$ kJ/mol.

The measured adsorption enthalpies are typical for physisorption. The same phenomenon as in the experiments with tungsten hexacarbonyl was observed. The adsorption of osmium pentacarbonyl on gold is slightly weaker than on the quartz surface. Probably, gold carbonyl surface complexes were formed in the carbon-monoxide atmosphere. However in the simulations only a pure gold surface was taken into account.

4.3.3.3 Experiments with Iridium

Production of iridium

Iridium was produced in the reaction ^{nat}Tb(^{24}Mg,xn)$^{183-x}$Ir. Terbium itself is mono-isotopic (^{159}Tb). The targets were made of Tb_2O_3 sputterd on a 2.2 µm thick titanium backing – the target thicknesses were 650 µg/cm^2, 310 µg/cm^2, and 310 µg/cm^2 terbium, respectively.

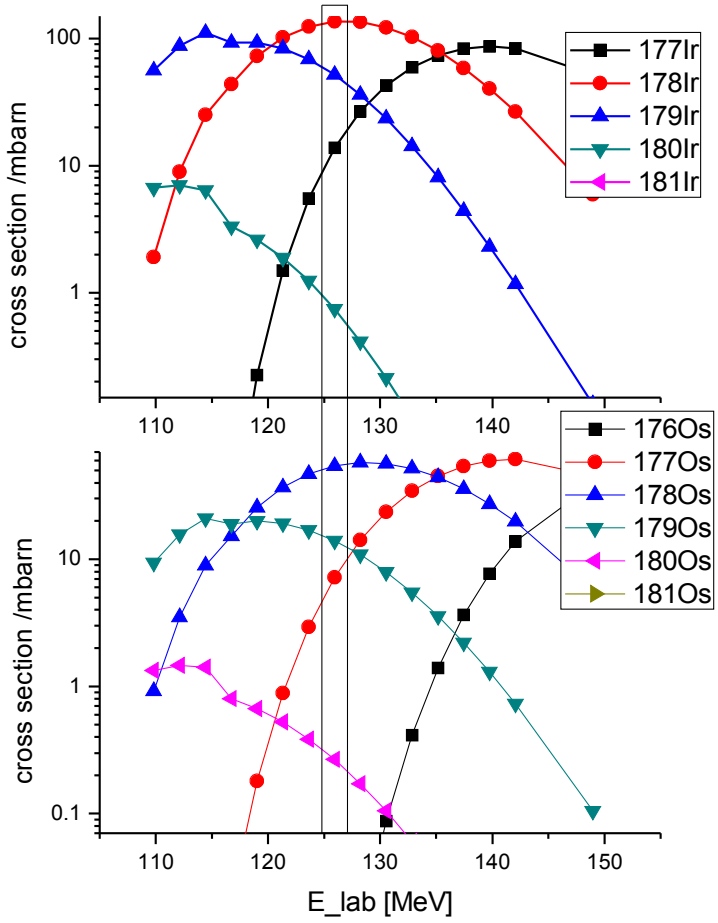

Figure 96: Excitation functions calculated with HIVAP for the reaction ^{159}Tb(^{24}Mg,xn)(top) and ^{159}Tb(^{24}Mg,pxn) (bottom).The black frame marks the beam energy applied during the beam time.

The beam energy was 132 MeV from the UNILAC. An average beam energy of 126 MeV in the middle of the target was calculated with SRIM. The energy of ^{178}Ir after passing the RTC window was estimated to be 3.9 MeV (according to SRIM the range in 1 bar helium would be 1 cm). TASCA magnets were set to the following values: dipole 445 A (corresponding $B{\cdot}\rho$ = 1.684 T·m), quadrupole 1 335 A and quadrupole 2 387 A.

Isothermal chromatography

To get information about the adsorption behaviour of the iridium carbonyl complexes, the isothermal chromatography setup was used. The target chamber was flushed for 30 min with a mixture of 80% helium and 20% carbon-monoxide with a total flow rate of 0.54 L/min. The pressure inside the RTC was 1 bar. From the RTC, the gas was guided through the isothermal chromatography column (which was kept at a constant temperature) followed by a charcoal trap. The charcoal was placed in front of the germanium detector and was measured during the flushing time.

With every new measurement, the temperature of the column was varied. Two of the measured spectra are shown in Figure 97 - the upper one was taken when the chromatography column was kept at −90 °C, the one at the bottom was taken when the column was at room temperature (25 °C). The 12-s isotope ^{178}Ir and the 79-s isotope ^{179}Ir could be identified in the spectrum when the column was at room temperature. When the column was at −90 °C no gamma line of iridium was visible in the spectrum. Only the longer-lived daughter nuclides were identified. The activity of the daughter was accumulated from measurement to measurement as the charcoal trap was not changed in between.

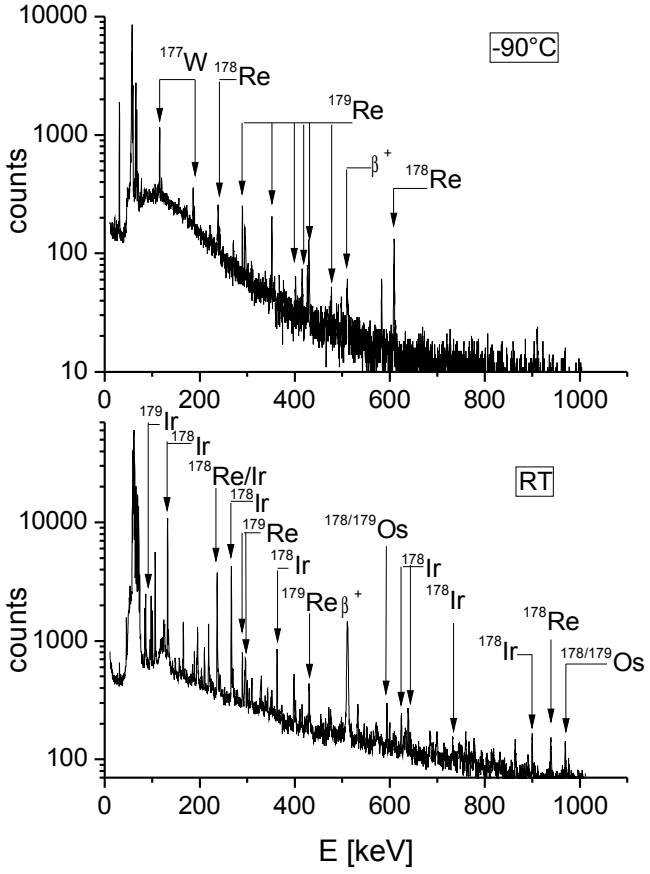

Figure 97: Spectra of the isothermal chromatography experiments. The bottom spectrum was measured when the thermochromatography column was kept at room temperature (25 °C). The short lived isotopes ^{178}Ir and ^{179}Ir could be clearly identified. The upper spectrum was taken when the column was kept at -90 °C. No Ir isotopes were identified. The Ir isotopes decayed in the column. The isotopes identified were only the long-lived daughters of Ir – ^{178}Re, ^{179}Re and ^{177}W. As the charcoal trap was used for several measurements, the activities of the daughter nuclides were accumulated.

All gamma spectra were normalized to the beam integral and live time of the measurement. The spectrum measured at 25 °C was taken as 100%.

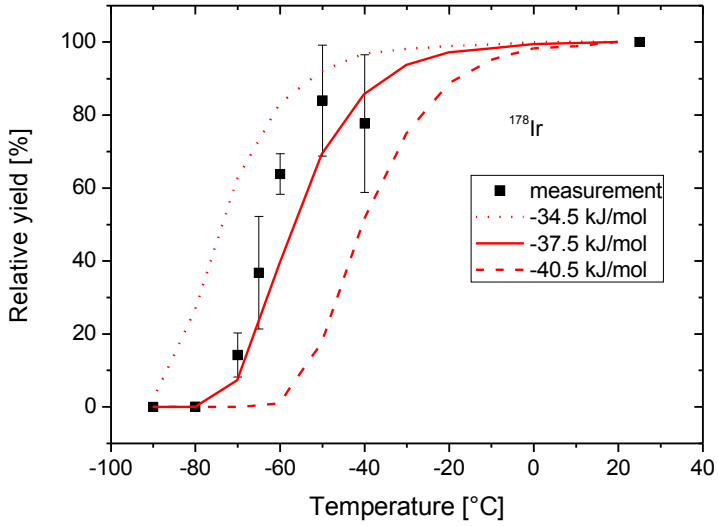

Figure 98: Isothermal chromatogram of ^{178}Ir. The black dots are the mean values of the yields determined with the gamma lines at 131.6 keV, 266.1 keV, 363.1 keV, 624.4 keV, 638.8 keV, 732.2 keV and 899.7 keV – the error bars are the standard deviation. The red lines are the results of the Monte Carlo simulations with $-\Delta H_{ads}$=37.5±3.0 kJ/mol. It was estimated that the chemical compound is $Ir(CO)_4$ with an estimated density of 3 g/cm^2.

The result of the measurement with ^{178}Ir and the Monte Carlo simulations are shown in Figure 98. The yield obtained at room temperature was defined as 100%. Binary, mono-nuclear iridium carbonyl complexes are not known from literature. In single-atom chemistry - as it is performed in this experiment- it is almost inconceivable that poly-nuclear iridium complexes are formed. One explanation might be the formation of mixed carbonyl complexes – most probably hydro-carbonyl complexes, as hydrogen is a common impurity in gases. Otherwise, radical, mono-nuclear iridium tetracarbonyl complex would have to be assumed. As it could not have been proven which was the transported species, the iridium tetracarbonyl complex with a density of 3 g/cm^3 was assumed in the simulation of the isothermal chromatograms. The adsorption enthalpy of the iridium carbonyl complex is based on the measured values compared with the simulations (-37.5±3.0 kJ/mol). It points to physisorption on the silicon oxide surface.

Thermal stability of the iridium carbonyl complex

The decomposition setup was used to get information about the stability of the iridium complex. The RTC and the decomposition setup were flushed with gas a mixture of 80% helium and 20% carbon-monoxide at a total flow rate of 0.54 L/min and pressure inside the RTC around 1050 mbar. The charcoal trap, which was behind the decomposition setup, was monitored by a gamma detector during each experiment.

All spectra were normalized to the beam integral and the live time of the measurement. The spectrum measured at 52 °C was set as the 100% value. In Figure 99 the depenence of the yield collected in the charcoal trap on the oven temperature is shown.

At around 200°C the complexes start to decompose.

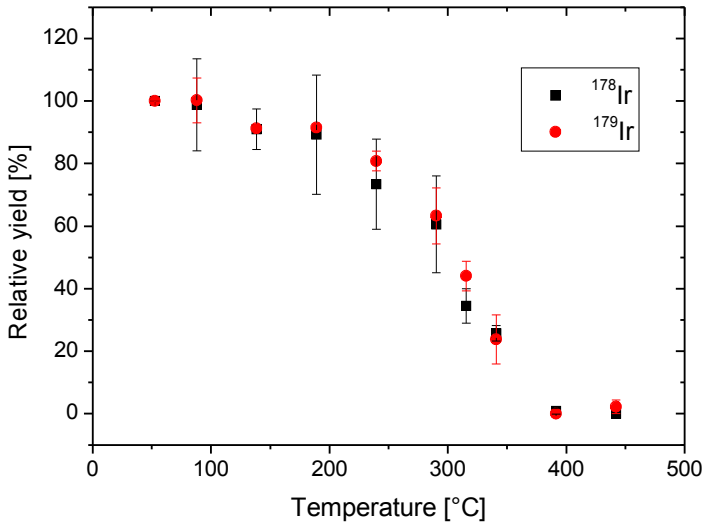

Figure 99: Yield measured in the charcoal trap depending on the temperature of the quartz wool plug in the decomposition setup. The black squares show the yield of ^{178}Ir (determined with the gamma lines at 131.6 keV, 266.1 keV, 363.1 keV, 624.4 keV, 638.8 keV, 732.2 keV and 899.7 keV), the red dots show the yield of ^{179}Ir (determined with the gamma line at 86.3 keV and 97.5 keV). At 300 °C 50% of the $Ir(CO)_x$ is destroyed – at 390 °C all $Ir(CO)_4$ is decomposed.

Based on the ^{178}Ir data, an Arrhenius plot was created (see Figure 100). The value for the free reaction enthalpy $\Delta G^{\ddagger}=(-43 \pm 8)$ kJ/mol was obtained.

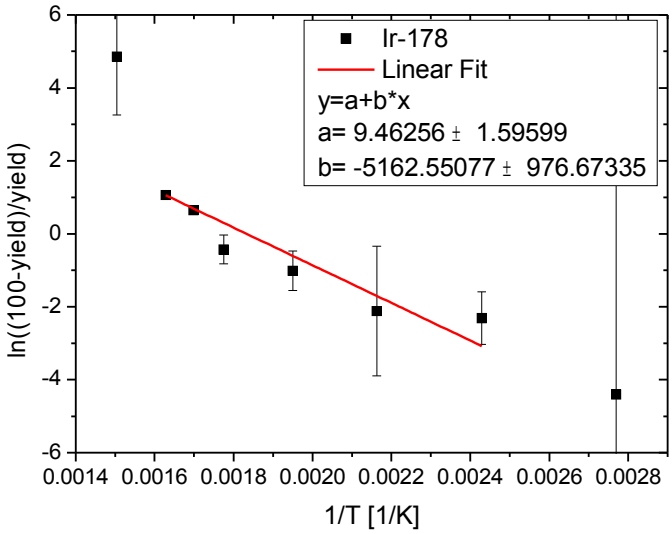

Figure 100: Arrhenius plot of the thermal decomposition of $^{178}Ir(CO)_x$. $\Delta G^{\ddagger} = -43 \pm 8$ kJ/mol

4.3.3.4 Experiments with Rhenium

Production of rhenium

Rhenium was produced in the reaction $^{nat}Eu(^{24}Mg,xn)^{170-172}Re$. Natural europium consists of the two isotopes ^{151}Eu (47.81% abundance) and ^{153}Eu (52.19% abundance). The cross-sections predicted by HIVAP are shown in Figure 101. The targets were made of 450 µg/cm^2 europium, sputtered as Eu_2O_3 on 2.2-µm thick titanium backing foil.

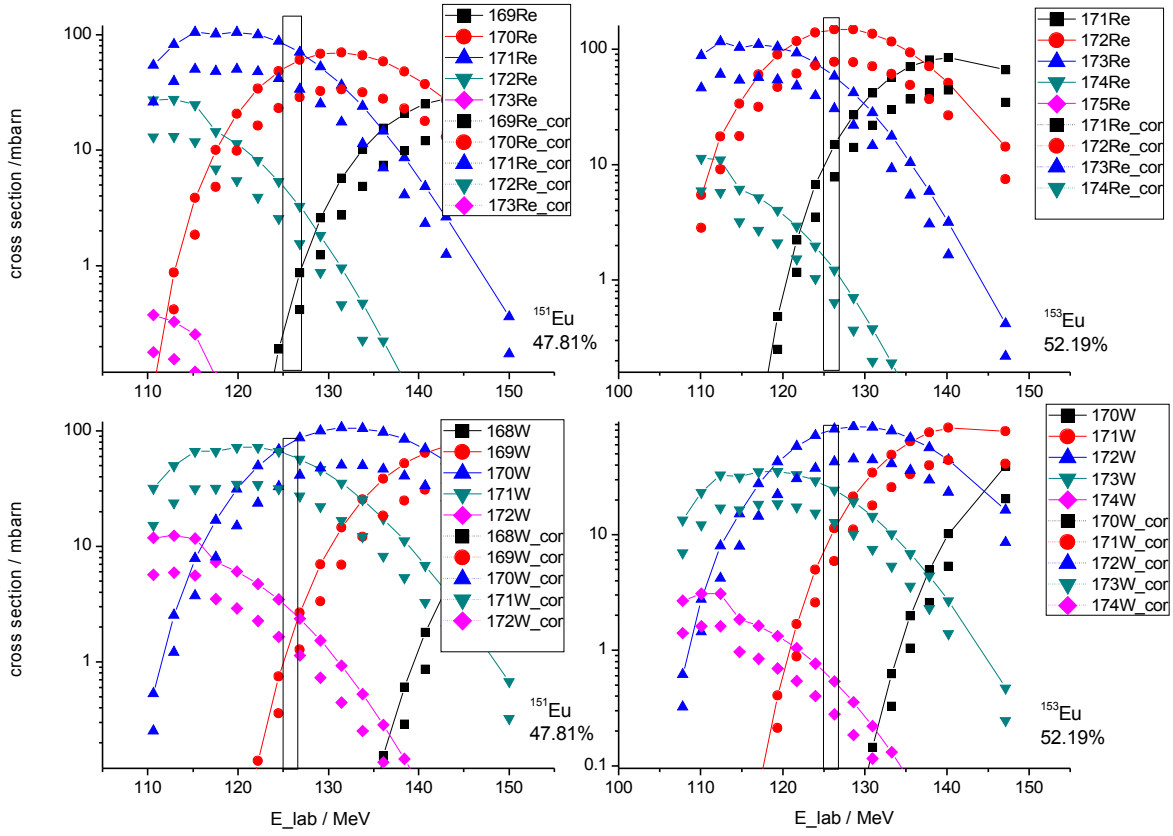

Figure 101: Excitation functions calculated with HIVAP for the reaction $^{151}Eu(^{24}Mg,xn)^{175-x}Re$ and $^{153}Eu(^{24}Mg,xn)^{177-x}Re$ (top diagrams) and for the reactions $^{151}Eu(^{24}Mg,pxn)^{174-x}W$ and $^{153}Eu(^{24}Mg,pxn)^{176-x}W$ (bottom diagrams). The cross sections normalized to the abundance of the isotope are shown with the dashed lines (Re_cor and W_cor) . The black frame marks the beam energy in the middle of the target.

The beam energy from the UNILAC was 132 MeV. In the middle of the target, the beam energy was estimated to be 126 MeV [173]. The calculated energy of the evaporation residues after passing the RTC window is 4.0 MeV up to 4.1 MeV. The dipole magnet of TASCA was set to 444 A (corresponding $B{\cdot}\rho$ = 1.681 T·m), the quadrupole 1 was set to 325 A and quadrupole 2 to 376 A.

Isothermal chromatography

The adsorption behaviour of the rhenium carbonyl complexes was studied with isothermal chromatography. The target chamber was flushed for 30 min with a mixture of 80% helium and 20% carbon-monoxide with a flow rate of 0.54 L/min. The pressure inside the RTC was 1 bar. From the RTC, the gas was guided through the isothermal chromatography column (which was kept ar a constant temperature) followed by a charcoal trap. The charcoal was placed in front of the germanium detector and was measured during the flushing time.

With every new measurement, the temperature of the column was varied. Two of the measured spectra are shown in Figure 102, the upper one was taken with the chromatography column was kept at −70 °C, the one at the bottom was taken when the column was at room temperature (20 °C). In the spectrum taken at 20 °C the isotopes ^{170}Re ($t_{1/2}$=9.2 s), ^{171}Re ($t_{1/2}$=15.2 s), and $^{172/172m}$Re ($t_{1/2}$=15 s / 55 s) could be identified. When the column was at −70 °C no gamma line of rhenium was visible in the spectrum. Only the long-lived daughter nuclides of hafnium and tantalum were identified. The activity of the daughters was accumulated from measurement to measurement as the charcoal trap was not changed in between. Hence, the daughter isotopes were still identified in the spectrum measured at −70 °C.

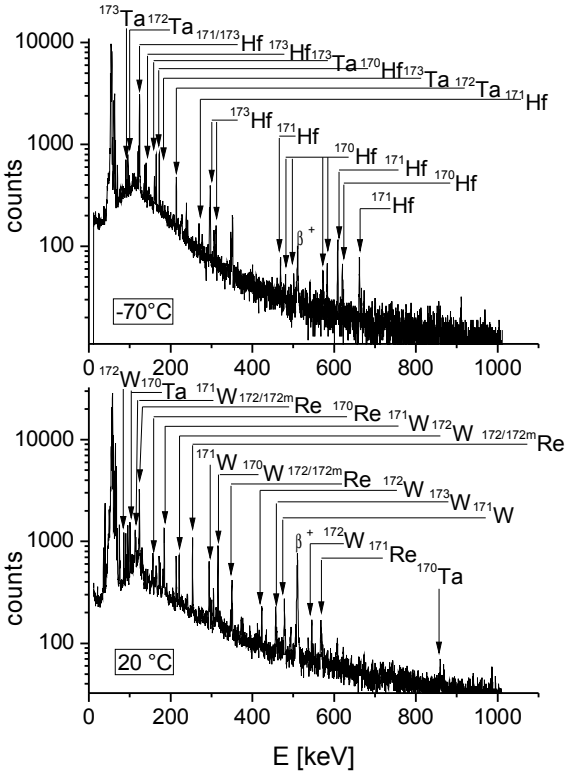

Figure 102: Spectra of the samples collected in the charcoal trap. The lower spectrum was measured when the chromatography column was kept at 20 °C – the isotopes ^{170}Re, ^{171}Re and $^{172/172m}$Re can be identified. The upper spectrum was measured when the column was kept at −70 °C. Here, only the long-lived daughter isotopes were identified in the spectrum.

For rhenium, no stable mononuclear, binary carbonyl-complexes are known. Only Szilard Chalmers reaction studies gave the evidence that rhenium can form radical-type pentacarbonyl complexes.[147]

However, it seems to be more likely that the recoiling rhenium ions formed mixed carbonyl complexes with impurities in the gas. According to the Linde company which produced the carbon monoxide, up to 250 ppm hydrogen are in the carbon-monoxide. Therefore the formation of hydrocarbonyl rhenium complexes might be possible. As it could not be verified which is the transported species, a volatile rhenium pentacarbonyl complex with a density of 2.5 g/cm^2 was assumed in the Monte Carlo simulations.

In Figure 103, the isothermal chromatogram of ^{170}Re and the results of the Monte Carlo simulations are shown. As the 100% yield, the spectrum, which was measured when the column temperature was at 20 °C, was taken. All spectra were normalized to the live time and the beam integral.

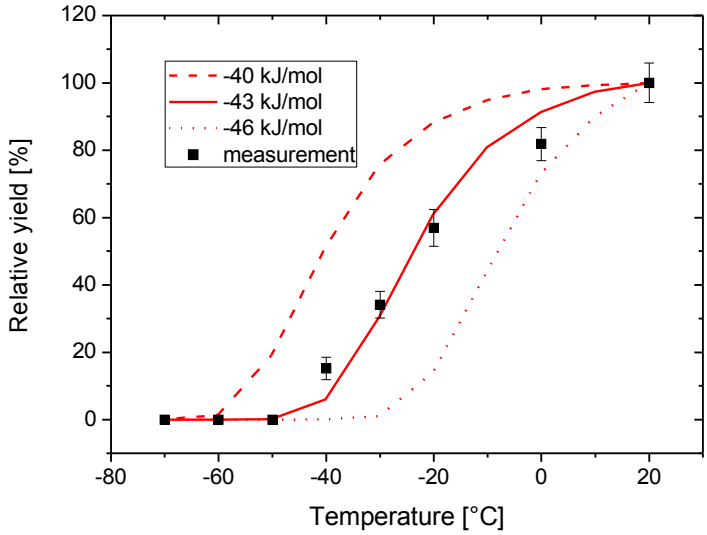

Figure 103: Isothermal chromatogram of ^{170}Re. The black dots are the measured yield determined from the gamma line at 156.9 keV– the error bars represent the statistical error of the gamma measurement. The red lines are the results of the Monte Carlo simulations with $-\Delta H_{ads}=43\pm3$ kJ/mol. It was assumed that the chemical compound is $Re(CO)_5$ with an assumed density of 2.5 g/cm^2.

Thermal stability of the rhenium carbonyl complex

The decomposition setup was used to study the thermal stability of the rhenium complex. The RTC and the decomposition setup was flushed with a gas mixture of 80% helium and 20% carbon-monoxide at a flow rate of 0.54 L/min and a pressure inside the RTC around 1050 mbar. The charcoal trap which was behind the decomposition setup was monitored by a gamma detector during each experiment.

All spectra were normalized to the beam integral and the life time of the measurement. The spectrum measured at 38 °C was taken as the 100% value. The yield measured in the charcoal trap as a function of the temperature in the quartz tube is shown in Figure 104. At temperatures in excess of 300 °C, the complexes start to decompose.

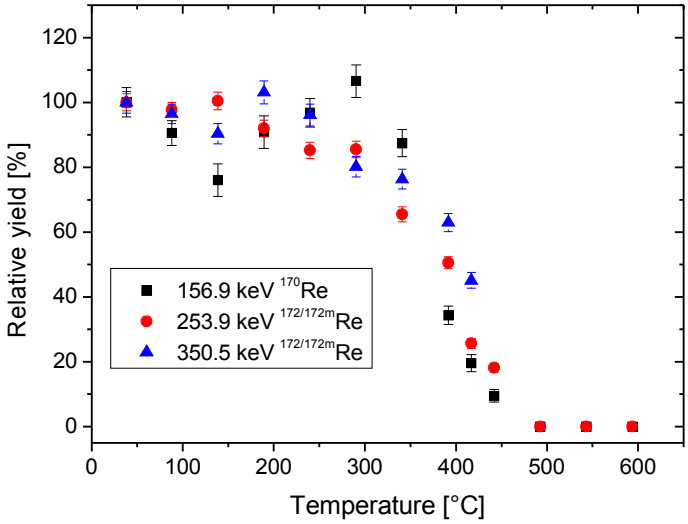

Figure 104: Yield measured in the charcoal trap depending on the temperature of the quartz wool plug in the decomposition setup. The black squares show the yield of ^{170}Re (determined with the gamma lines at 156.9 keV), the red dots show the yield of $^{172/172m}$Re (determined with the gamma line at 253.9 keV) as well as the blue triangles (determined with the gamma line at 350.5 keV . At 390 °C 50% of the Re(CO)$_x$ is decomposed – at 490 °C all Re(CO)$_x$ is decomposed.

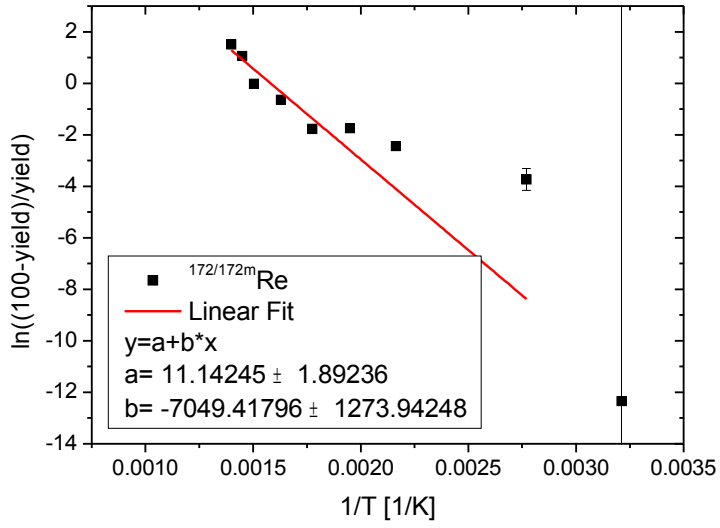

Figure 105: Arrhenius plot of the thermal decomposition of $^{172/172m}$Re(CO)$_x$. $\Delta G^{\ddagger} = -59 \pm 11$kJ/mol

The logarithm of the ratio of decomposed complex to stable complex was plotted as a function of the inverse temperature (see Figure 105). From this a free reaction enthalpy $\Delta G^{\ddagger}=(-59 \pm 11)$ kJ/mol was obtained.

4.3.3.5 Experiments with Platinum

Platinum was produced in the reaction ^{164}Dy(^{24}Mg,6n)^{182}Pt.

The target was a stationary target of ^{164}Dy on a carbon backing foil. The beam energy was 132 MeV from the UNILAC. TASCA was filled with 0.8 mbar helium. The dipole was set at 435 A (corresponding $B{\cdot}\rho$ = 1.652 T·m), quadrupole 1 was set to 355 A and quadrupole 2 was set to 390 A.

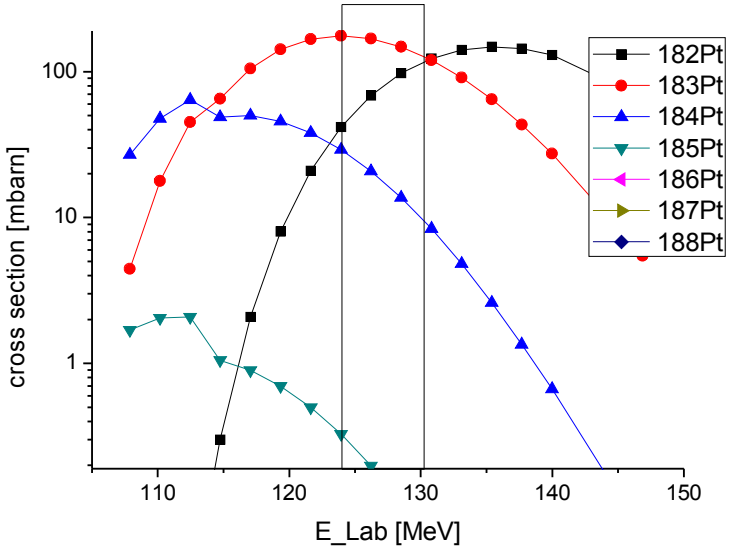

Figure 106: Excitation fundtions calculated with HIVAP for the reaction ^{164}Dy(^{24}Mg,xn)$^{188-x}$Pt depending on the projectile energy. The black frame marks the beam energy in the target.

To test if the TASCA settings are correct, an aluminum catcher foil was placed 1 cm behind the RTC window. It was irradiated for 15 min with a beam current of 50 $nA_{particle}$. Within 90 s after the end of irradiation, the catcher foil was placed in front of the gamma detector. It was measured for 1000 s and ^{182}Pt and ^{182}Ir were identified (see Figure 107, upper spectrum).

Subsequently, the RTC was flushed with a mixture of helium (80%) and carbon monoxide (20%) at a gas-flow of 0.54 L/min. The gas was guided through a charcoal trap which was placed in front of the germanium detector. The amount of platinum that could be identified compared to that in the

aluminum catcher foil was very small. The spectrum, that was measured while the charcaol trap was flushed with the helium / carbon monoxide mixture to monitor the transport, looked the same as the background spectrum. Also in the spectrum measured after the charcoal trap was flushed for 15 min no platinum could be identified (see Figure 107, bottom spectrum).

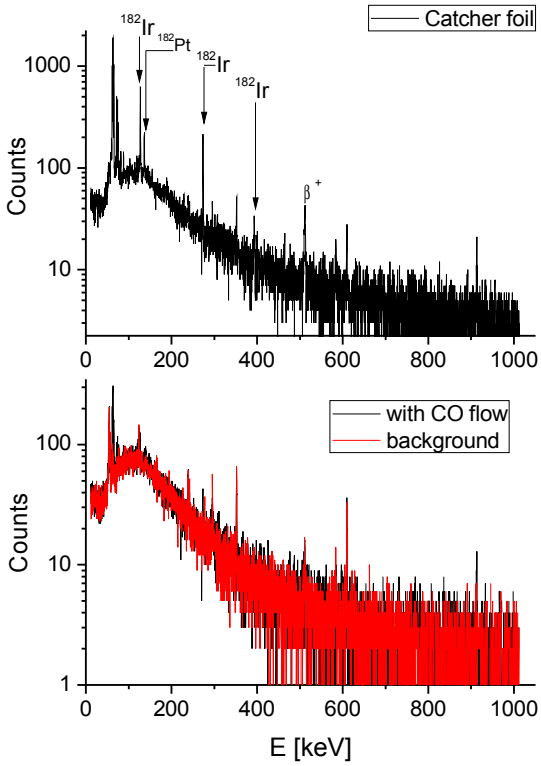

Figure 107: The upper part shows the spectrum of the aluminum catcher foil, which was placed in the RTC, irradiated for 15 min and measured 1000 s with the germanium detector. ^{182}Pt and ^{182}Ir could be clearly identified. The spectrum at the bottom is from the charcoal trap. The red curve shows the background of the trap, the black line is the spectrum measured when the charcoal trap was flushed with the gas stream.

The conclusion is that platinum does not form volatile carbonyl-complexes, like already concluded for its lighter homologue palladium from the experiments with the ^{249}Cf-target at the TRIGA reactor. Matrix isolation[129] seems to be the only way to obtain mononuclear binary carbonyl complexes of platinum and palladium.

4.4 Summary and discussion of the experimental studies of transitionmetal-carbonyl complexes

With CO transported elements:

In the presented experiments it was possible to synthesize carbonyl complexes of various transition metals plus selenium carbonyl.

Selenium carbonyl was already produced in a similar way and publicated. [168], [169]

Group 4:

Zirconium isotopes were produced in the fission of ^{235}U. ^{100}Zr was identified as transported isotope, which is mainly a primary fission product. In reference [172] zirconium heptacarbonyl (which would fulfil the 18 valence electron rule) is predicted, but no experiments demonstrated the existence of the complex. Literature [170] reports of anionic zirconium hexacarbonyl complexes. As the dependence of yield on the purity of carbon-monoxide was clearly seen for ^{99}Nb (which is the daughter of ^{99}Zr), the transported zirconium compound is probably a mixed carbonyl complex. Common impurities in technical gases is hydrogen, water and oxygen. So one option might be the formation of hydro-, hydroxo-, or oxo-carbonyl complexes. Furthermore, hydrocarbon molecules are possible impurities. Volatile, organometallic compounds with carbonyl ligands are well known for zirconium.[170]

Group 5:

Niobium isotopes were studied in the experiments at the TRIGA reactor with ^{235}U target. For niobium, it is hard to say whether it was only detected as the daughter of zirconium, or if it also forms carbonyl-complexes. However, the detection of ^{101}Nb and ^{102}Nb gives a strong evidence that also niobium forms carbonyl complexes. The latter isotopes are formed 40% as primary fission products. The precursor ^{101}Zr and ^{102}Zr have half-lives of 2.3 s and 2.9 s, so that they mainly decay during the transport time. For niobium, no binary mononuclear carbonyl-complexes are known from literature. Niobium formed either radical-type hexacarbonyl complexes as its lighter homolog

vanadium or mixed carbonyl complexes with impurities of, e.g., hydrogen, oxygen or hydrocarbon in the system.

Group 6:

Molybdenum was clearly identified in the spectra of fission products obtained by ^{235}U, ^{249}Cf, and ^{252}Cf fission. Molybdenum hexacarbonyl complexes are very well studied. In the experiments with the ^{235}U target, the influence of gas purity on the yield of molybdenum transport was very clear – in the ^{249}Cf fission experiments this effect was not visible. This phenomenon might be due to the different carbon-monoxide bottles.

Tungsten was synthesized as the xn-product from a nuclear fusion reaction, i.e., there were no precursor effects to be taken into account. It is very likely that the tungsten-hexacarbonyl complex was formed.

Group 7:

In the evaluation of technetium, precursor effects have to be taken into account. For the isotopes ^{105}Tc, ^{106}Tc, and ^{107}Tc no dependence of the transport on the gas purity could be observed. The analysis of the measured isothermal chromatograms of ^{103}Tc, ^{106}Tc, and ^{107}Tc is not as straight forward as in the case of the molybdenum isotopes. ^{107}Tc is only to 17% decay product of molybdenum –the major fraction is a primary fission product. This is evidence that also technetium carbonyl complexes are formed. From literature [145], the formation of technetium pentacarbonyl radical in Szilardt Chalmers reactions is known. For its lighter homolog manganese, even chemical studies of the pentacarbonyl radical are reported [175]. “Common” technetium carbonyl complexes are $Tc_2(CO)_{10}$ or $Tc(CO)_5X$ (X= halogen) [176]. Probably, mixed technetium carbonyl complexes (such as hydro or hydrocarbon carbonyl complexes) were formed, but also the formation of pentacarbonyl radical-type complexes cannot be excluded.

The heavier homolog of technetium - rhenium was studied at TASCA. No precursor phenomenon disturbs its chemical investigation. Rhenium either formed rhenium pentacarbonyl complexes or mixed carbonyl complexes with some impurities in the gas. Radical type complexes are not common, however their existence was reported in Szilard Chalmers type experiments leading to the formation of radical-type rhenium-pentacarbonyl complexes. [147] However, most likely seems that

rhenium formed hydro or hydrocarbon carbonyl complexes.

Group 8:

Group 8 is know to form stable, volatile pentacarbonyl complexes. Ruthenium was only studied as a fission product. For the ruthenium isotopes identified, it is hard to say, whether they were transported due to precursor effects or whether they were transported as the ruthenium pentacarbonyl complex.

The transport of the heavier homologue osmium was investigated at TASCA, so precursor effects can be excluded and most likely the osmium pentacarbonyl complex was formed.

Group 9:

Rhodium was produced in the fission of ^{249}Cf and ^{252}Cf. Different isotopes of rhodium were detected. For the lighter ones it is hard to say, if ruthenium or rhodium was the transported species. At higher flow rate of 1 L/min ^{113}Pd ($t_{1/2}$=1.64 min), ^{114}Pd($t_{1/2}$= 2.48 min), ^{115}Pd ($t_{1/2}$= 47 s), and ^{116}Pd ($t_{1/2}$= 12.7 s) were identified in the spectra. These palladium isotopes are formed as primary fission products and as daughter nuclides of rhodium. As their half-lives are relatively long, they should also have been observed in the spectra taken at lower gas flow rate, if they had formed volatile carbonyl complexes, but this was not the case. Their mother isotopes ^{113}Rh ($t_{1/2}$= 2.7 s), ^{114}Rh ($t_{1/2}$=1.8 s), ^{115}Rh ($t_{1/2}$= 0.99 s), and ^{116}Rh ($t_{1/2}$=1.7 s), are short lived. This is a strong evidence that rhodium forms rapidly carbonyl complexes. These are either mixed carbonyl complexes (with e.g. hydrogen or hydrocarbon ligands) – or radical-type tetracarbonyl complexes. These complexes are not reported in literature. However, the lighter homolog cobalt is known to from radicalic cobalt tetracarbonyl if dicobalt octacarbonyl is heated up. [177]

Iridium was synthesized at TASCA and could be transported in the gas stream. Prescursor effects can be excluded and it is verified that it forms volatile complexes with the carbon-monoxide. It might be a radical-type tetracarbonyle complex, or a mixed carbonyl complex (with, e.g., hydrogen or hydrocarbon ligands).

Group 10:

The only stable volatile complexes of group 10 are known for nickel. Nevertheless, it was tried to synthesize platinum carbonyl complexes at TASCA – but without success. Furthermore, in the fission spectra, no evidence of the formation of palladium carbonyl complexes was found. Darling et al. [129] found that palladium tetracarbonyl can be synthesized in matrix isolation experiments at low temperatures and that it is only stable up to 80 K - these are not suitable experimental conditions for one-atom-at-a-time experiments.

The results of this work are summarized graphically in the periodic table shown in Figure 108. Elements, for which the formation of volatile carbonyl complexes have unambiguously been demonstrated and understood, are shown in dark green. Carbonyl complex formation of the elements shown in light green was obviously observed, but are not quite understood. The elements shown in yellow are uncertain candidates for carbonyl-complex formation, because β^--decay precursor effects cannot be excluded. The transactinides rutherfordium through meitnerium are potential candidates for future carbonyl chemistry experiments.

1												13	14	15	16	17	18
1 H	2																2 He
3 Li	4 Be											5 B	6 C	7 N	8 O	9 F	10 Ne
11 Na	12 Mg	3	4	5	6	7	8	9	10	11	12	13 Al	14 Si	15 P	16 S	17 Cl	18 Ar
19 K	20 Ca	21 Sc	22 Ti	23 V	24 Cr	25 Mn	26 Fe	27 Co	28 Ni	29 Cu	30 Zn	31 Ga	32 Ge	33 As	34 Se	35 Br	36 Kr
37 Rb	38 Sr	39 Y	40 Zr	41 Nb	42 Mo	43 Tc	44 Ru	45 Rh	46 Pd	47 Ag	48 Cd	49 In	50 Sn	51 Sb	52 Te	53 I	54 Xe
55 Cs	56 Ba	57+* La	72 Hf	73 Ta	74 W	75 Re	76 Os	77 Ir	78 Pt	79 Au	80 Hg	81 Tl	82 Pb	83 Bi	84 Po	85 At	86 Rn
87 Fr	88 Ra	89+" Ac	104 Rf	105 Db	106 Sg	107 Bh	108 Hs	109 Mt	110 Ds	111 Rg	112 Cn	113 ---	114 ---	115 ---	116 ---	117 ---	118 ---

*	58 Ce	59 Pr	60 Nd	61 Pm	62 Sm	63 Eu	64 Gd	65 Tb	66 Dy	67 Ho	68 Er	69 Tm	70 Yb	71 Lu
"	90 Th	91 Pa	92 U	93 Np	94 Pu	95 Am	96 Cm	97 Bk	98 Cf	99 Es	100 Fm	101 Md	102 No	103 Lr

Figure 108: Overview of the studied carbonyl-compound formations. The elements shown in dark green were observed to form carbonyl-compounds and the formation is understood. The complex formation of the elements shown in light green was observed, but is not completely understood. The elements shown in yellow formed volatile carbonyl-complexes, but precursor effects disturbed the studies. The elements shown in red could be proven not to form volatile carbonyl complexes. The elements shown in light blue are the transactinides, which are candidates that could be studied by carbonyl chemistry.

Formation of the volatile complexes of nuclear reaction products:

The direct formation of molybdenum hexacarbonyl from fission products was first described by Baumgärtner et al. They mixed ^{235}U with $Cr(CO)_6$ [141] and bombarded it with neutrons. Baumgärtner et al. mainly found secondary fission products such as ^{99}Mo. [141] They first interpreted this result such that mainly the beta decay descendants form the carbonyl complexes. Later his group discovered with the same method the isotopes ^{105}Mo and ^{104}Mo. [143],[142] As these two isotopes are mainly formed as primary fission products [98], the statement of Baumgärtner's previous publication, that the hexacarbonyl complex is mainly formed by beta decay products, needs to be revised.

In the experiments performed in this thesis, the formation of carbonyl complexes was achieved in the gas phase by in-situ reactions of nuclear reaction products in their thermalization process. The experiments were conducted in a continuous mode. The transportation yields (compared with those of a cluster gas jet) of ^{104}Mo were higher than for ^{101}Mo. This needs to be interpreted such that the formation of carbonyl-complexes with primary fission products is favoured.

The average kinetic energy of the single primary fission fragments with masses around 105 is around 100 MeV in the thermal-neutron induced fission of ^{235}U. In the spontaneous fission of ^{252}Cf the average kinetic energy of a single primary fission fragments with masses around 105 is around 108 MeV. [178] For the neutron-induced fission of ^{249}Cf no literature data were found; the kinetic energies of interest are also probably between 100 MeV and 110 MeV.

These energies are high enough for the fission products to pass through the target into the gas atmosphere. For the evaporation residues produced at TASCA, SRIM [179] predicts kinetic energies between 4 MeV and 6 MeV after passing through the RTC window. With energies in the range of MeV, the ions are too “hot” to form chemical bonds with the CO - as the common dissociation energies are in the range of a few eV (see, e.g., [133], where the first dissociation energies calculated for hexacarbonyl complexes are around 50 kcal/mol = 2.18 eV). During the thermalization of the recoil ions, their charge state decreases. The charge state distribution and charge changing cross sections of ions with high energies penetrating through gases are well studied. [180] However, for the changing of the charge states in the thermalization process no data and theories are available.

From the fact that the carbonyl complexes were transported in the gas stream over several meters, they are most likely neutral. The neutralisation of the ions and the formations of metal-carbonyl bonds are probably a subsequent processes. The formation of the bond to the first carbonyl groups is probably a very fast process as soon as the ion is cooled down. In [181] and [182] it is reported that iron and cobalt ions in a buffer gas cell even formed up to two carbonyl bonds with carbon monoxide impurities (which were in the range of ppm) present in the buffer gas. No other molecule formation with any other impurity in the buffer gas was observed.

Thermal stability of the complexes

Only a few studies were conducted to get information about the thermal stability of the complexes. One conclusion was, that high temperatures (over 300°C) should be avoided in the recoil chamber.

The free reaction enthalpy of the decomposition of iridium and rhenium carbonyl complexes determined in this work were $\Delta G^{\ddagger}=-43 \pm 8$ kJ/mol and $\Delta G^{\ddagger}=-59 \pm 11$ kJ/mol.

The studies on the stability of technetium and molybdenum carbonyl complexes should be repeated as the temperature was not measured directly in the quartz tube that the complexes passed. Best known from literature are the first dissociation energies of group 6 (see, e.g., [135]). Therefore, more systematic studies of short lived chromium, molybdenum, and tungsten isotopes need to be performed.

Adsorption of the carbonyl complexes on a surface

All values for the adsorption enthalpies of transition-metal carbonyl complexes measured in this work were between -35 kJ/mol and -52 kJ/mol (compare Table 3). These are typical enthalpies for physisorption processes and are comparable to the value associated with adsorption of group 8 tetroxides on silicon nitride. [157]

Table 3: $-\Delta H_{ads}$ of the assumed transition-metal-carbonyl complexes as evaluated from the different chromatography methods (IC – isothermal chromatography, TC – thermochromatography at the reactor, COMPACT – thermochromatography in a detector channel) and different adsorbing surfaces. In the measurements of Tc and Rh precursor effects can not be excluded.

	IC SiO_2	TC SiO_2	COMPACT SiO_2	TC Au	COMPACT Au
$Mo(CO)_6$	42.5 ± 2.5	36 ± 8		35 ± 8	
$W(CO)_6$			$46\ ^{+3}_{-2}$ 47 ± 3 46.5 ± 2.5		$41\ ^{+3}_{-4}$
$Tc(CO)_5$	46.5 ± 3	52 ± 8			
$Re(CO)_5$	43.0 ± 3				
$Os(CO)_5$			44 ± 3 $43.5\ ^{+3.5}_{-2.5}$		39 ± 2 $42\ ^{+3}_{-2}$
$Rh(CO)_4$	44 ± 3	46 ± 8		52 ± 8	
$Ir(CO)_4$	37.5 ± 3				

Several studies about the adsorption of hexacarbonyl complexes on Al_2O_3 and SiO_2 are described in literature [153],[154],[155], and [156]. On Al_2O_3, first physisorption followed by the formation of surface complexes is reported. In reference [153], it is reported that molybdenum hexacarbonyl is first physisorbed on silicon dioxide; under vacuum, it looses some of the carbonyl ligands and forms surface complexes. For chromium and tungsten hexacarbonyl, only physisorption was observed. This is in agreement with the experimental studies of chromium hexacarbonyl on silica reported in reference [156]. In the measurements presented in this work, physisorption is probably the common adsorption process.

As mentioned previously the adsorption enthalpy can be calculated with equation

$$E_{(x)} = -\Delta H_{ads} + 0.5 \cdot R \cdot T \qquad (4.2.1\text{-}2)$$

For physisorption, the London equation (4.2.1-1) is valid, which predicts the binding energy

$$E_{(x)} = -\frac{C_1}{x^6} \qquad (4.2.1\text{-}1)$$

The adsorption of a molecule on a two dimensional surface can be extended by a summation over all molecule-molecule interactions. Alternatively, the summation can be replaced by a triple integration of (4.2.1-1) which leads to

$$E_{(x)} = -\left(\frac{\pi}{6}\right) \cdot N \cdot C_1 \frac{1}{x^3} \qquad (4.4\text{-}1)$$

N is the number of atoms per one cubic centimeter.

The van der Waals constant C_1 can be expressed as [183]

$$C_1 = \frac{3}{2} \cdot \alpha_A \cdot \alpha_B \cdot \frac{E_A \cdot E_B}{E_A + E_B} \qquad (4.4\text{-}2)$$

where α_A and α_B are the polarizabilities of the adsorbed molecule A and the surface B. E_A and E_B are the average dipole transition energies. According to [184] and [24], the average dipole energies are equal to the ionization potentials *IP*. In reference [185], the average dipole energies were replaced by $1.57 \cdot IP$ – which delivered more accurate results for noble gases.

The physisorption energy can thus be written as

$$E_{(x)} = -\frac{\pi}{4} \cdot N \cdot \frac{1}{r^3} \cdot \frac{\alpha_A \cdot \alpha_B}{\frac{1}{IP_A} + \frac{1}{IP_B}} \qquad (4.4\text{-}3)$$

or

$$E_{(x)} = -\frac{\pi}{4} \cdot N \cdot \frac{1}{x^3} \cdot \frac{\alpha_A \cdot \alpha_B}{\frac{1}{1.57 \cdot IP_A} + \frac{1}{1.57 \cdot IP_B}} \qquad (4.4\text{-}4)$$

If no data of the polarizability of the surface B are available, it can be calculated with [186]

$$\alpha_B = \frac{3}{4 \cdot \pi \cdot N} \cdot \frac{(\epsilon - 1)}{(\epsilon + 2]} \tag{4.4-5}$$

where ϵ is the dielectrical constant of the surface material.

For the calculation of the adsorption energy on a silicon-oxide surface, the following equations were used

$$E_{(x)} = \frac{-3}{16} \cdot \left(\frac{\varepsilon - 1}{\varepsilon + 2}\right) \cdot \frac{\alpha_A}{\left(\frac{1}{IP_A} + \frac{1}{IP_B}\right) \cdot x^3} \tag{4.4-6}$$

and

$$E_{(x)} = \frac{-3}{16} \cdot \left(\frac{\varepsilon - 1}{\varepsilon + 2}\right) \cdot \frac{\alpha_a}{\left(\frac{1}{1.57 \cdot IP_A} + \frac{1}{1.57 \cdot IP_B}\right) \cdot x^3} \tag{4.4-7}$$

The dielectrical constant of silicon oxide is 3.81 and the ionization potential is 11.7 eV. [157]

For the hexacarbonyl complexes, the $E_{(x)}$ and ΔH_{ads} were calculated - the used data for this and the results are given in Table 4

Table 4: Data from literature taken for the calculation of the binding energy between a SiO_2 surface and the hexacarbonyl complexes of group 6 together with the calculated values.

	[a)]IP [eV]	[b)]α [cm^3]	[c)]r_{VdW} [Å]	[d)]E(x) [kJ/mol]	[d)]$-\Delta H_{ads}$ [kJ/mol]	[e)]E(x) [kJ/mol]	[e)]$-\Delta H_{ads}$ [kJ/mol]
$Cr(CO)_6$	8.03	$223.011 \cdot 10^{-25}$	3.161	29.42	28.29	46.19	45.06
$Mo(CO)_6$	8.12	$257.045 \cdot 10^{-25}$	3.244	31.58	30.45	49.59	48.45
$W(CO)_6$	8.18	$273.643 \cdot 10^{-25}$	3.2295	34.23	33.09	53.73	52.6

a) taken from Lit [187] (E73-E79); b) Lit [188]; c) estimated from the crystal structures [189], [190], [191] which are orthorombic, the r_{vdw} should be around half of the shortest distance between two metal atoms (rhomboder-width c in the cristal structure); d) calculated according to eq. (4.4.-6); e) calculated according to [157], [185] – equation (4.4-7)

Compared to the experiments, the values obtained with equation (4.4-7) fit best. The empirical ansatz taking *1.57·IP* seems to be necessary for calculating the adsorption enthalpies. The trend that the adsorption enthalpy of $Mo(CO)_6$ is lower than that of $W(CO)_6$ is seen in the experimental results as well as in the calculations,

For the calculation of the adsorption enthalpies on gold, equations (4.4-6) and (4.4-7) were used. The ionization potential of gold is 9.2 eV [192] and the polarizabilty is $5.8 \cdot 10^{-24}$ cm [192].

Table 5: Data from literature taken for the calculation of the binding energy between a gold surface and the hexacarbonyl complexes of group 6 together with calculated values.

	[a)]IP [eV]	[b)]α [cm^3]	[c)]r_{VdW} [Å]	[d)]E(x) [kJ/mol]	[d)]$-\Delta H_{ads}$ [kJ/mol]	[e)]E(x) [kJ/mol]	[e)]$-\Delta H_{ads}$ [kJ/mol]
$Cr(CO)_6$	8.03	$223.011 \cdot 10^{-25}$	3.161	37.44	38.57	58.78	59.91
$Mo(CO)_6$	8.12	$257.045 \cdot 10^{-25}$	3.244	40.16	41.3	63.05	64.19
$W(CO)_6$	8.18	$273.643 \cdot 10^{-25}$	3.2295	43.5	44.64	68.3	69.43

a) taken from Lit [187] E73-E79; b) Lit [188]; c) estimated from the crystal structures [189], [190], [191] which are orthorombic, the r_{vdw} should be around half of the shortest distance between to metal atoms (rhomboder-width c in the cristal structure); d) calculated according to eq. (4.4.-6); e) calculated according to [157], [185] – equation (4.4-7).

The results are in disagreement with the measurement. The adsorption enthalpy on gold is predicted by the calculation to be lower than the values predicted for silicon oxide. But in the measurement, the adsorption enthalpy, e.g., for $W(CO)_6$ on silicon oxide was determined to be -46.5 kJ/mol while the one on gold was determined to be -41 kJ/mol. Within the error bars these values are nearly the same. But taking a closer look at the chromatograms, e.g, Figure 71 and Figure 78, the maximum deposition of $^{164}W(CO)_6$ on quartz is at (-42 ± 10)°C and under comparable conditions on gold at $\left(-70^{+10}_{-20}\right)$ °C. This shows a trend that the adsorption on silicon dioxide is stronger than that on gold. One explanation might be that the carbon monoxide is chemisorbed on the gold surface as reported in reference [174]. In this case, surface complexes are formed and instead of studying the adsorption on gold, the adsorption of carbonyl complexes on gold-carbonyl complexes is investigated.

4.5 Outlook and perspectives of transactinide-carbonyl chemistry and applications in nuclear physics

The in-situ carbonyl chemistry seems to be a promising method to study the transactinides rutherfordium, dubnium, seaborgium, bohrium, hassium, and meitnerium. In Table 6, a list of adequate nuclides for a carbonyl-chemistry experiments plus the nuclear fusion reactions to synthesize these isotopes is given.

Table 6: Overview of the adequate isotopes for transactinide carbonyl complex chemistry experiments

Isotope	$T_{1/2}$ [s]	Reaction	σ [pb]	Reference
^{257}Rf	3.8±0.8	^{249}Cf(^{12}C,4n)	2000±400	[193]
^{259}Rf	$2.5^{+0.4}_{-0.3}$	^{238}U(^{26}Mg,5n)	1520±350	[194]
^{261a}Rf ,^{261b}Rf	68±3 and	^{238}U(^{26}Mg,3n)	28^{+92}_{-26}	[194]
	1.9±0.4	^{244}Pu(^{22}Ne,5n)	1800^{+800}_{-400} for^{261b}Rf with a production ratio of ^{261a}Rf/^{261b}Rf = 2.5	[195]
		^{248}Cm(^{18}O,5n)	11000±200 for^{261b}Rf; with a production ratio of ^{261a}Rf/^{261b}Rf = 1.1±0.2)	[196]
^{262}Db	34±4	^{248}Cm(^{19}F,5n)	1300±400	[197]
		^{249}Bk(^{18}O,5n)	5300±2800	[198]
^{263}Db	27^{+10}_{-7}	^{249}Bk(^{18}O,4n)	1600±1000	[198]
^{265a}Sg, ^{265b}Sg	$8.9^{+2.7}_{-1.9}$	^{248}Cm(^{22}Ne,5n)	180^{+80}_{-60} For ^{265a}Sg	[199], [200]
	$16.2^{+4.7}_{-3.5}$		200^{+60}_{-50} For ^{265b}Sg	
^{267}Bh	17^{+14}_{-6}	^{249}Bk(^{22}Ne,4n)	96^{+55}_{-25}	[201]
^{269}Hs	~9.7	^{226}Ra(^{48}Ca,5n)	≤ 5	[111]
		^{248}Cm(^{26}Mg,5n)	~7	[83]
^{270}Hs	$7.7^{+4.9}_{-2.2}$	^{226}Ra(^{48}Ca,4n)	$8.3^{+6.7}_{-3.7}$	[111]
		^{248}Cm(^{26}Mg,4n)	~3	[83]

But as it is not completely understood, why elements of groups 4, 5, 7, and 9 could be transported in the gas-stream with carbon-monoxide, further test experiments are needed. For example, the influence of impurities like hydrogen, halogens, oxygen, water or nitrogen monoxide or hydrocarbons (e.g., methane, ethylene, and ethane) should be studied in detail. Furthermore, activated charcoal could be used to filter organic impurities out of the gas and test if this has an influence on the formation of the carbonyl complexes.

Nevertheless, metal carbonyl chemistry holds huge promises for the discovery of a new compound class of transactinides. This would be the first step of crossing the border from simple inorganic chemistry to metallorganic chemistry in the superheavy element region.

Next step for group 6 would be to study the seaborgium hexacarbonyl. This experiment could be done at TASCA in combination with COMPACT. The nuclear reaction of choice would be $^{248}Cm(^{22}Ne,5n)^{265}Sg$. The cross-section of this reaction is a few hundred picobarn. ^{265}Sg has two different isomeric states, one with ~16 s and the other one with ~6 s half-life. [199] According to reference [200], the total cross section for both isomers is ~380 pb, estimating an average beam current of 1 $\mu A_{particle}$, an average target thickness of 500 $\mu g/cm^2$ ^{248}Cm, a transmission through TASCA of 7%, a RTC window transparency of 80%, and an overall efficiency of the gas-jet COMPACT system of 50%, the decay of ~7 Sg atoms per day would be detected in COMPACT. Within a few days of beamtime, statistics should be high enough to study the formation of $Sg(CO)_6$ and its adsorption behaviour on silicon oxide.

As mentioned in chapter 4.1, the relativistic effects in $Sg(CO)_6$ should be visible according to Nash [133]. As the 6d orbitals of seaborgium are delocalised due to relativistic effects, the overlapping of the d-orbitals with with LUMO of the CO ligand (the anti-binding π-orbital) becomes bigger, the metal-carbon bond becomes stronger, and the carbon - oxygen bond becomes weaker. In chemistry with macro-amounts, infrared adsorption spectroscopy would be the method of choice to study the bond strength. In case of small amounts, infrared dissociation spectroscopy is used (see, e.g., [137], [171]). Anyhow, these techniques cannot be applied on a one-atom-at-a-time scale. The obvious way to study transactinide carbonyl complexes would be a thermal dissociation experiment. This could be realized by placing an improved decomposition setup directly at the RTC exit followed by the COMPACT detector. By varying the temperature of the decomposition setup, information on the strength of the metal-carbon bond can be obtained. Under constant conditions (gas-flow, gas mixture, pressure etc.), seaborgium can be studied in comparison to chromium, ruthenium, and tungsten. For chromium and ruthenium, the COMPACT detector would have to be

replaced by a charcoal trap which is monitored by a gamma detector, as no α-emitting isotopes of the elements are available.

For the hexacarbonyl complexes of chromium, molybdenum, and tungsten, the first dissociation energies are known from literature (see, e.g., [135], [202]) For $Cr(CO)_6$, the first dissociation energy is 36.8 kcal/mol, for $Mo(CO)_6$ it is 40.5 kcal/mol and for $W(CO)_6$ it is 46.0 kcal/mol according to ref. [202]. Due to the relativistic effects the trend of the increasing of the first dissociation energy would be broken. According to ref. [133], the first dissociation energy of $Sg(CO)_6$ should nearly be the same as for $W(CO)_6$. This can be correlated to the free reaction enthalpies obtained in the online studies. If this method turns out to be adequate and sufficiently accurate, the dissociation energy of $Sg(CO)_6$ could be estimated from experiments.

A highlight experiment would also be to study the chemistry of meitnerium. So far only decay studies have been performed with meitnerium, so it would be the first chemistry experiment with meitnerium. All former studies trying to find a suitable chemical system for meitnerium failed. Experiments with volatile chlorides and oxides of rhodium lead to the conclusion that these compounds are not adequate for online experiments. [203]

Nevertheless, it is now demonstrated that carbonyl chemistry is a suitable method to study group 9 elements. The results of the experiments with rhodium and iridium - the lighter homologs- performed in this work are very promising – although they are not fully understood until know. So further studies are necessary.

^{278}Mt has a half-life of 7.6 s which would be adequate for chemical studies, however, this isotope was only observed in the decay chain of ^{294}117. This has been produced in the reaction ^{249}Bk(^{48}Ca,3n)^{294}117 with a cross-section of 0.5 pb. [23] But this data bases on one observed decay chain, the target material is short-lived and very rare, and for a chemistry experiment, direct production of the isotope would be preferred.

The second meitnerium isotope which is claimed to have an adequate half-life of 0.56 s is ^{270}Mt. However, this is based on two events with significantly different life times observed in the decay chain of ^{278}113, produced in the reaction ^{209}Bi(^{70}Zn,1n)^{278}113 with a cross section of 31 fb. [204] This cross-section is much too low for a chemistry experiment and as mentioned previously, a direct production of Mt would be favoured to exclude precursor effects.

The most promising way seems to be the direct synthesis of ^{270}Mt and/or ^{271}Mt (which have not been discovered so far). ^{271}Mt has a closed neutron shell with N=162 and the half-life can be estimated to be in the range of a second. From extrapolations of the cross-sections for reactions of

the type ^{248}Cm(Y,5n), a cross-section of ~1 pb can be estimated for ^{248}Cm(^{27}Al,5n)^{270}Mt (see Figure 109).

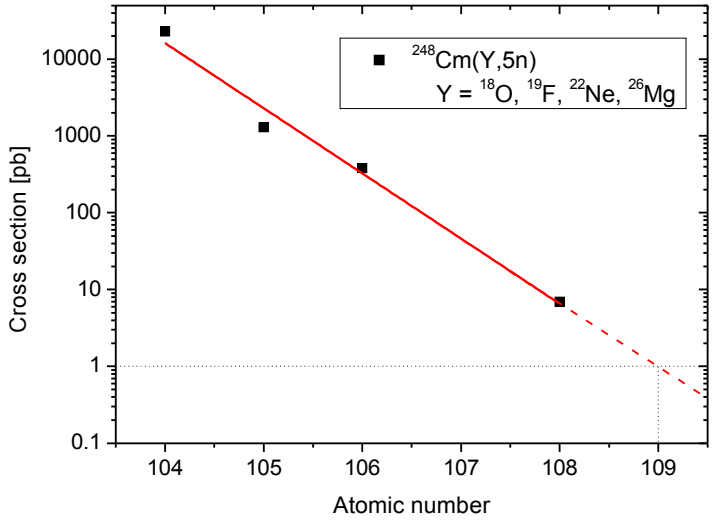

Figure 109: Experimentally determined cross-sections (black dots) of the reactions ^{248}Cm(^{18}O,5n)^{261}Rf [196], *^{248}Cm(^{19}F,5n)^{262}Db* [197], *^{248}Cm(^{22}Ne,5n)^{265}Sg* [200] *and ^{248}Cm(^{26}Mg,5n)^{269}Hs* [83]. *By extrapolation of the cross sections (red line), a cross-section of 1 pb is estimated for the reaction ^{248}Cm(^{27}Al,5n)^{270}Mt (black dotted lines).*

This reaction first has to be studied in an experiment at TASCA with a focal plane detector. Estimating a target thickness of 500 µg/cm^2 ^{248}Cm and a beam current of 1 µA$_{particle}$, within 6 weeks 4 decay chains of ^{270}Mt could be observed in the focal plane, if the estimated cross section of 1 pb is correct. For a chemistry experiment, 3 month of beam time would be needed. For this type of experiment, the COMPACT setup used in the 114-chemistry experiment [113] should be chosen. This has the big advantage that the RTC made of Teflon has the same size as the SIM-RTC window and is directly connected with the thermochromatography detector channel.

Another interesting research field which could make use of transactinide carbonyl-chemistry, is nuclear spectroscopy. In the first seaborgium experiments, the two isomers of ^{265}Sg were assigned to be two different isotopes, ^{265}Sg and ^{266}Sg. Reanalysis [199] of the experimental data available from literature led to the result that ^{265}Sg has two isomeric states and that the assigments to ^{266}Sg were wrong interperations of the experiment results. Figure 110 shows the decay scheme of ^{269}Hs,

including the two isomeric states of ^{265}Sg and ^{261}Rf. It also includes the nuclear fusion reactions to synthesize ^{265}Sg and ^{261}Rf. Until now, the two isomeric states of ^{265}Sg are not understood by theory. None of the theoretical calculations predicts an isomeric state long-lived enough to decay by α-emission into ^{261}Rf. Furthermore, it is not understood which of the two isomers of ^{265}Sg is the ground state. [199]

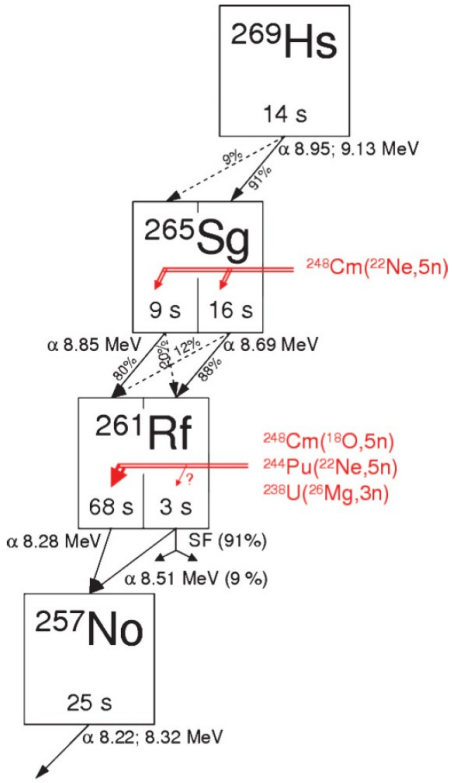

Figure 110: Decay scheme of ^{269}Hs and the nuclear fusion reactions to synthesize ^{265}Sg and ^{261}Rf. Taken from [199].

The isomeric states of ^{261}Rf have been observed in different reactions, e.g., ^{244}Pu(^{22}Ne,5n)^{261a,b}Rf [195] and ^{248}Cm(^{18}O,5n)^{261a,b}Rf [196]. Recently also the two isomeric states of ^{265}Sg have been confirmed in the reaction ^{248}Cm(^{22}Ne,5n)^{265a,b}Sg [200], but only the emitted α-particles were detected. To get a better understanding of the isomeric states, it would be helpful to do correlation spectroscopy. Yakushev suggested the design of a new isothermal chromatography detector – AlBeGa [205], which is shown in Figure 111. The chromatography channel is a meander formed by two pixelized detectors for α- and spontaneous fission detection. These detector panels are cooled with ethanol or liquid nitrogen. They are surrounded by two detector panels sensitive to β- particles for the detection of conversion electrons. The outer sphere of this detector "sandwich" consists of

two germanium clover detectors for X-ray and γ-measurement. With this device, radioactive compounds, which are volatile at room temperature and synthesized under conditions adequate for the TASCA-RTC system, can be studied. $Sg(CO)_6$ would be an interesting and promissing candidate for this type of experiments as the two isomeric states of ^{265}Sg in combination with its chemistry could be studied.

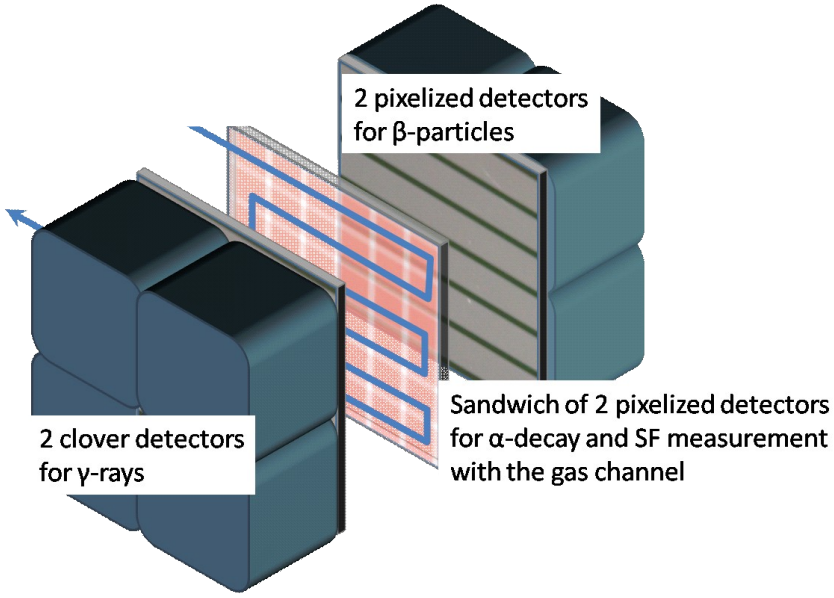

Figure 111: Schematic drawing of the AlBeGa detector. The chromatography channel is made of pixelized detectors for α and SF measurement. This detector plate is cooled by liquid nitrogen. The α detectors are in between a "sandwich" of two pixelized β-detectors. The outer shell consists of two clover detectors for γ and X-ray measurement.[205]

Furthermore, $Hs(CO)_5$ would be adequate for AlBeGa-experiments. Alternatively, the HsO_4 would be a good candidate for chemistry and spectroscopy studies with AlBeGa. The interesting isotopes are ^{269}Hs, ^{270}Hs, and ^{271}Hs. The decay chain of ^{269}Hs provides information about the isomeric states of ^{265}Sg and ^{261}Rf. ^{270}Hs is claimed to be a doubly magic nucleus with a closed neutron shell (N=162). [83] There are two possible nuclear reactions to synthesize these hassium isotopes, $^{248}Cm(^{26}Mg,3\text{-}5n)^{269\text{-}271}Hs$ [83], [206] and $^{226}Ra(^{48}Ca,3\text{-}4n)^{269\text{-}270}Hs$ [111]. The cross-section for $^{238}U(^{36}S,3\text{-}4n)^{269\text{-}270}Hs$ is significantly lower than in the ones of the other two reactions. [207] In case of $^{248}Cm(^{26}Mg,3\text{-}5n)^{269\text{-}271}Hs$, the HsO_4 is the adequate system as no physical preseparator would be needed. Due to the limited transmission through TASCA, the losses would be over 90%. As the oxide system is a good chemical separation system with high chemical yields, this would be

preferred. For the carbonyl system, problems would be expected in a experiment without preseparation, due to the plasma and the heat in the target chamber. For ^{226}Ra(^{48}Ca,3-4n)$^{269-270}$Hs, TASCA or any other separator would be needed as ^{226}Ra is an emanating target, which decays into ^{222}Rn. This would lead to background problems in an experiment, if the volatile compounds are directly synthesized in the recoil chamber behind the target. The noble gas radon would be transported to the detector. In an experiment behind a separator, the carbonyl system would be the chemical system of choice. Carbonyl complexes cannot be synthesized without a preseparator due to the fact that the heat and the plasma behind the target probably destroy the carbon monoxide molecules as well as the complexes. Behind a separator, the carbonyl chemistry would be easier to handle than the tetroxide chemistry. The carbonyl complex formation takes place at room temperature, a heating of the RTC is not needed and the kinetics is very fast. The oxide system would require a heating of the RTC.

Furthermore, the nuclear spectroscopy studies of dubnium and bohrium are of great interest. As these elements have an odd proton number, the chance is high to observe isomeric states. The isotope ^{262}Db can be formed in the reaction ^{249}Bk(^{18}O,5n) and ^{263}Db could be produced in ^{249}Bk(^{18}O,4n). The preferred reaction to produce ^{267}Bh would be ^{249}Bk(^{22}Ne,4n). The nuclear properties of the products of these very asymmetric reactions are hard to study in the focal plane of any physical separator. The target-like transfer products would lead to significant background problems in the focal plane detector or the high rate might even destroy the detector. Carbonyl-chemistry in combination with AlBeGa would allow low background studies of these nuclei with a high α-β^--γ-correlation efficiency.

5 Résumé

Within this thesis, methods for on-line chemistry experiments in combination with physical preseparation were developed. This included liquid phase chemistry of single-atoms as well as in-situ gas-phase chemistry.

The underpotential deposition of ruthenium and osmium as tests for a hassium experiments, (see chapter 3) were studied. It has been demonstrated in online experiments at the TRIGA Mainz reactor and at the UNILAC behind TASCA that tracer amounts of ruthenium (chapter 3.2.2) and osmium (chapter 3.2.3) can be deposited on gold electrodes in experiments coupled to an gas-jet system. Nevertheless, the attempts to automatize the electrodeposition experiments lead to several technical problems (chapter 3.3). For further investigations, gold-covered detectors should be developed, which could be used as working electrodes. Furthermore, the half-lives of the transactinides, which would be suitable for electrodeposition studies, are too short and the cross sections of the nuclear fusion reactions too low (see chapter 3.4). This requires developments of ion beams of higher intensities and of targets, which are stable at high beam currents.

In the second part of this thesis, methods for in-situ synthesis of new transactinide compound classes were explored. Until now, only thermally stable, simple, inorganic compounds have been synthesised in transactinide gas-phase chemistry. Making use of physical preseparation allows now also the synthesis of thermally less stable compounds. The RTC of TASCA can be filled with molecular, gaseous reagents. As the primary beam is deflected in TASCA, no plasma is created in the RTC and the gas in the RTC stays at ambient temperature. This allows the synthesis of thermally-less stable compounds with molecular ligands.

As first steps in the direction metal-organic chemistry, carbonyl complexes were chosen. It was demonstrated that isotopes of the 4d transition metals zirconium, niobium, molybdenum, technetium, ruthenium, and rhodium produced in the fission of uranium-235 and californium-249 form volatile carbonyl-complexes, if they are thermalized in a carbon-monoxide containing recoil chamber (chapter 4.3.1). Furthermore, short-lived isotopes of the 5d elements tungsten, rhenium, osmium, and iridium were synthesised in nuclear fusion reactions at TASCA (chapter 4.3.2). These isotopes formed volatile carbonyl complexes by stopping these isotopes in a carbon-monoxide

containing atmosphere in the RTC. These complexes were transported in a carrier gas-stream.

All experiments showed that in-situ carbonyl chemistry is a very effective and fast method. Short-lived isotopes can be transported this way fast and with high yields. Additionally carbonyl chemistry can be combined with gas-chromatography. The adsorption studies of several carbonyl complexes on silicon dioxide or gold surfaces showed that these complexes physisorb at temperatures below -40°C. This allows studies with thermochromatography detectors like COMPACT. Additionally, the thermal stabilities of some complexes were determined and it was shown that they decompose at temperature around 300°C. All these experiments were conducted under conditions compatible with a transactinide experiment. Carbonyl chemistry appears to be a suitable method for the transactinide elements rutherfordium, dubnium, seaborgium, bohrium, and meitnerium.

Based on the results obtained in this thesis, it is possible within a few days of beam time to study the formation and adsorption of seaborgium hexacarbonyl. This would be the first volatile transactinide complex with the oxidation state zero. It is predicted that relativistic effects influence the seaborgium carbonyl bond [133], and these might become visible in decomposition experiments with the hexacarbonyl complexes of group 6.

Another milestone in superheavy element chemistry is now in reach. Until now, no adequate chemistry system for meitnerium was found. The carbonyl-chemistry studies with rhodium and iridium showed, that experiments with meitnerium would also be promising.

Additionally, nuclear spectroscopy can make use of carbonyl complexes. Carbonyl-complexes would allow the chemical preparation of spectroscopy samples by their deposition on a cold α-detector surface. If the detector array would be built in a sandwich type structure, with the α-detectors in the middle surrounded by detectors sensitive for β^--particles and the outer sphere would consist of germanium clover detectors, a high α-β^--γ- correlation efficiency under low background conditions could be reached.

Bibliography

[1] D. C. Hoffman, F. O. Lawrence, J. L. Mewherter, and F. M. Rourke, *Nature* **234,** 132 (1971).

[2] E. McMillan and P. H. Abelson, *Phys. Rev.* **57,** *12,* 1185 (1940).

[3] G. T. Seaborg, E. M. McMillan, J. W. Kennedy, and A. C. Wahl, *Phys. Rev.* **69,** *7-8,* 366 (1946).

[4] G. T. Seaborg, R. A. James, and A. Ghiorso, *Metallurgical Laboratory Report CS-2135, University of Chicago* **1944,** *p15,* 26.

[5] G. T. Seaborg, R. A. James, L. O. Morgan, and A. Ghiorso, *Metallurgical Laboratory Report CS-2741, University of Chicago* **1949,** *pp3-4,* 9 pp.

[6] G. T. Seaborg, *Chem. Eng. News* **23,** 2190–2193 (1945).

[7] G. T. Seaborg, *J. Chem. Educ.* **46,** *10,* 626 (1969).

[8] G. T. Seaborg, *J. Chem. Soc., Dalton Trans., 20,* 3899–3907 (1996).

[9] J. V. Kratz, *Chemistry of transactinides* in *Handbook of Nuclear Chemistry, 2nd ed.,* edited by A. Vértes et al. , Vol 2, 925 (Springer Dodrecht, 2011).

[10] M. Schädel, *Angew. Chem. Intl. Ed.* **45,** 368–401 (2006).

[11] M. Schädel, *The chemistry of superheavy elements* (Kluwer Academic Publishers, Dordrecht, The Netherlands, 2003).

[12] Y. T. Oganessian, *J. Alloy. Compd.* **213,** 50–60 (1994).

[13] V. Zagrebaev and W. Greiner, *Phys. Rev. C* **78,** *3,* 34610 (2008).

[14] S. Hofmann, *Radiochim. Acta* **99,** *7-8,* 405–428 (2011).

[15] P. Armbruster, *Annu. Rev. Nucl. Part. Sci.* **50,** 411–479 (2000).

[16] P. Armbruster, *C. R. Physique* **4,** 571–594 (2003).

[17] P. Armbruster, *Eur. Phys. J. A* **37,** *2,* 159–167 (2008).

[18] T. Sikkeland, J. Maly, and D. F. Lebeck, *Phys. Rev.* **169,** *4,* 1000–1006 (1968).

[19] W. J. Swiatecki, K. Siwek-Wilczynska, and J. Wilczynski, *Phys. Rev. C* **71,** *1,* 14602 (2005).

[20] Z.H. Liu and J.-D. Bao, *Phys. Rev. C* **80,** 54608 (2009).

[21] Y. Aritomo and M. Ohta, *Nucl. Phys. A* **764,** *0,* 149–159 (2006).

[22] Y. Oganessian, *J. Phys. G: Nucl. Part. Phys.* **34,** R165-R242 (2007).

[23] Y. T. Oganessian, F. S. Abdullin, P. D. Bailey, D. E. Benker, M. E. Bennett, S. N. Dmitriev, J. G. Ezold, J. H. Hamilton, R. A. Henderson, M. G. Itkis, Y. V. Lobanov, A. N. Mezentsev, K. J. Moody, S. L. Nelson, A. N. Polyakov, C. E. Porter, A. V. Ramayya, F. D. Riley, J. B. Roberto, M. A. Ryabinin, K. P. Rykaczewski, R. N. Sagaidak, D. A. Shaughnessy, I. V. Shirokovsky, M. A. Stoyer, V. G. Subbotin, and R. Sudowe, *Phys. Rev. Lett.* **104,** *14,* 142502 (2010).

[24] A. Yakushev, *Chemical charaterization of element 108, hassium and synthesis of new hassium isotopes,* Habilitation thesis, Technical University Munich, (2009).

[25] N. Bohr and J. A. Wheeler, *Phys. Rev.* **56,** 426 (1939).

[26] S.G. Nilsson, J.R. Nix, A. Sobiczewski, Z. Szymanski, S. Wycech, C. Gustafson, and P. Möller, *Nucl. Phys. A* **115,** 545–562 (1968).

[27] S. V. Strutinsky, *Nucl. Phys. A* **95,** *2,* 420–442 (1967).

[28] V. Pershina, *Radiochim. Acta* **99,** *7-8,* 459–476 (2011).

[29] A. Kronenberg, K. Eberhardt, J. V. Kratz, P. K. Mohapatra, A. Nähler, P. Thörle, W. Brüchle, M. Schädel, and A. Türler, *Radiochim. Acta* **92,** *7,* 379–386 (2004).

[30] A. Türler, G. V. Buklanov, B. Eichler, H. W. Gäggeler, M. Grantz, S. Hüberner, D. T. Jost, V. Y. Lebedev, D. Piguet, S. N. Timokhin, A. Yakushev, and I. Zvara, *J. Alloy. Compd.* **271-273,** 287–291 (1998).

[31] W. Paulus, J. V. Kratz, E. Strub, S. Zauner, W. Brüchle, V. Pershina, M. Schädel, B. Schausten, J. L. Adams, K. E. Gregorich, D. C. Hoffman, M. R. Lane, C. Laue, D. M. Lee, C. A. McGrath, D. K. Shaughnessy, D. A. Strellis, and E. R. Sylwester, *Radiochim. Acta* **84,** 69–77 (1999).

[32] Z. Qin, M. S. Lin, F. L. Fan, W. X. Huang, X. L. Yan, J. Bai, X. L. Wu, F. A. Lei, H. J. Ding, F. Ma, G. S. Li, H. B. Zhou, and J. S. Guo, *Radiochim. Acta* **2011**.

[33] R. Lougheed, *Nature* **388,** *6637,* 21–22 (1997).

[34] M. Schädel, *J. Alloy. Compd.* **271,** 312–315 (1998).

[35] M. Schädel, W. Brüchle, E. Jäger, B. Schausten, G. Wirth, W. Paulus, R. Günther, K. Eberhardt, J. V. Kratz, A. Seibert, E. Strub, P. Thörle, N. Trautmann, A. Waldek, S. Zauner, D. Schumann, U. Kirbach, B. Kubica, R. Misiak, Y. Nagame, and K. E. Gregorich, *Radiochim. Acta* **83,** 163–165 (1998).

[36] A. Türler, W. Brüchle, R. Dressler, B. Eichler, R. Eichler, H. W. Gäggeler, M. Gärtner, J. P. Glatz, K. E. Gregorich, S. Hübener, D. T. Jost, V. Y. Lebedev, V. G. Pershina, M. Schädel, S. Taut, S. N. Timokhin, N. Trautmann, A. Vahle, and A. B. Yakushev, *Angew. Chem. Int. Ed.* **38,** *15,* 2212 (1999).

[37] R. Eichler, B. Eichler, H. W. Gäggeler, D. T. Jost, D. Piguet, and A. Türler, *Radiochim. Acta* **88,** 87–93 (2000).

[38] Ch. E. Düllmann, R. Dressler, B. Eichler, H. W. Gäggeler, F. Glaus, D. T. Jost, D. Piguet, S. Soverna, A. Türler, W. Brüchle, R. Eichler, E. Jäger, V. Pershina, M. Schädel, B. Schausten, E. Schimpf, H. J. Schött, G. Wirth, K. Eberhardt, P. Thörle, N. Trautmann, T. Ginter, K. Gregorich, D. C. Hoffman, U. W. Kirbach, D. M. Lee, H. Nitsche, J. B. Patin, R. Sudowe, P. M. Zielinski, S. N. Timokhin, A. Yakushev, A. Vahle, and Z. Qin, *Czech. J. Phys.* **53,** A291 (2003).

[39] A. von Zweidorf, R. Angert, W. Brüchle, S. Bürger, K. Eberhardt, R. Eichler, H. Hummrich, E. Jäger, H. O. Kling, J. V. Kratz, B. Kuczewski, G. Langrock, M. Mendel, U. Rieth, M. Schädel, B. Schausten, E. Schimpf, P. Thörle, N. Trautmann, K. Tsukada, N. Wiehl, and G. Wirth, *Radiochim. Acta* **92,** 855–861 (2004).

[40] K. S. Pitzer, *J. Chem. Phys.* **63,** *2,* 1032–1033 (1975).

[41] R. Eichler, N. V. Aksenov, A. V. Belozerov, G. A. Bozhikov, V. I. Chepigin, S. N. Dmitriev, R. Dressler, H. W. Gäggeler, V. A. Gorshkov, F. Haenssler, M. G. Itkis, A. Laube, V. Y. Lebedev, O. N. Malyshev, Y. T. Oganessian, O. V. Petrushkin, D. Piguet, P. Rasmussen, S. V. Shishkin, A. V. Shutov, A. I. Svirikhin, E. E. Tereshatov, G. K. Vostokin, M. Wegrzecki, and A. Yeremin, *Nature* **447,** *7140,* 72–75 (2007).

[42] A. Yakushev, *Research activities on SHE with TASCA at GSI* (PacificChem, Honululu, Hawaii, 2010).

[43] R. Eichler, N. V. Aksenov, Y. V. Albin, A. V. Belozerov, G. A. Bozhikov, V. I. Chepigin, S. N. Dmitriev, R. Dressler, H. W. Gäggeler, V. A. Gorshkov, R. A. Henderson, A. M. Johnsen, J. M. Kenneally, V. Y. Lebedev, O. N. Malyshev, K. J. Moody, Y. T. Oganessian, O. V. Petrushkin, D. Piguet, A. G. Popeko, P. Rasmussen, A. A. Serov, D. A. Shaughnessy, S. V. Shishkin, A. V. Shutov, M. A. Stoyer, N. J. Stoyer, A. I. Svirikhin, E. E. Tereshatov, G. K. Vostokin, M. Wegrzecki, P. A. Wilk, D. Wittwer, and A. V. Yeremin, *Radiochim. Acta* **98,** 133–139 (2010).

[44] R. Guillaumont and A. Peneloux, *J. Radioanal. Nucl. Chem.* **143,** *2,* 275–286 (1990).

[45] Ch. E. Düllmann, B. Eichler, R. Eichler, H. W. Gäggeler, D. T. Jost, U. Kindler, D. Piguet, S. Soverna, P. Thörle, N. Trautmann, and A. Türler, *Nucl. Instrum. Methods Phys. Res. Sect. A* **512,** 595–605 (2003).

[46] G. Hampel, K. Eberhardt, and N. Trautmann, *ATW-International Journal For Nuclear Power* **51,** *5,* 328 (2006).

[47] M. Eibach, *Characterization of a carbon aerosol generator in a helium gas-jet for the extraction of fission products from the research reactor TRIGA Mainz,* Diploma thesis, Johannes Gutenberg - Universität Mainz, (2009).

[48] H. Hummrich, N. L. Banik, M. Breckheimer, W. Brüchle, R. Buda, Feist. F., E. Jäger, J. V. Kratz, B. Kuczewski, D. Liebe, Niewisch. L, M. Schädel, B. Schausten, E. Schimpf, and N. Wiehl, *Radiochim. Acta* **96,** 73–83 (2008).

[49] H. Wollnik, H. G. Wilhelm, G. Röbig, and H. Jungclas, *Nucl. Instrum. Methods* **127,** 539–545 (1975).

[50] H. Wollnik, *Nucl. Instrum. Methods* **139,** 311–318 (1976).

[51] H. Haba, H. Kikunaga, D. Kaji, T. Akiyama, K. Morimoto, K. Morita, T. Nanri, K. Ooe, N. Sato, A. Shinohara, D. Suzuki, T. Takabe, I. Yamazaki, A. Yokoyama, and A. Yoneda, *J. Nucl. Radiochem. Sci.* **9,** *1,* 27–31 (2008).

[52] Ch. E. Düllmann, W. Brüchle, R. Dressler, K. Eberhardt, B. Eichler, R. Eichler, H. W. Gäggeler, T. N. Ginter, F. Glaus, K. E. Gregorich, D. C. Hoffman, E. Jäger, D. T. Jost, U. W. Kirbach, D. M. Lee, H. Nitsche, J. B. Patin, V. Pershina, D. Piguet, Z. Qin, M. Schädel, B. Schausten, E. Schimpf, H. J. Schött, S. Soverna, R. Sudowe, P. Thörle, S. N. Timokhin, N. Trautmann, A. Türler, A. Vahle, G. Wirth, A. B. Yakushev, and P. M. Zielinski, *Nature* **418,** *6900,* 859–862 (2002).

[53] Ch. E. Düllmann, *Eur. Phys. J. D* **45,** 75–80 (2007).

[54] Ch. E. Düllmann, *Czech. J. Phys.* **56, Suppl. D,** D333-D338 (2006).

[55] U. W. Kirbach, K. Gregorich, V. Ninov, D. M. Lee, J. B. Patin, D. A. Shaughnessy, D. A. Strellis, P. A. Wilk, D. C. Hoffman, H. Nitsche, *The Recoil product Transfer Chamber (RTC): A new interface for heavy element chemistry studies at the Berkeley Gas-filled Separator*, Nuclear Science Division Annual Report 1999, Lawrence Berkeley National Laboratory, (1999).

[56] H. Haba, D. Kaji, H. Kikunaga, T. Akiyama, N. Sato, K. Morimoto, A. Yoneda, K. Morita, T. Takabe, and A. Shinohara, *J. Nucl. Radiochem. Sci.* **8,** *2,* 55–58 (2007).

[57] D. Wittwer, F.Sh. Abdullin, N.V. Aksenov, Yu.V. Albin, G.A. Bozhikov, S.N. Dmitriev, R. Dressler, R. Eichler, H.W. Gäggeler, R.A. Henderson, S. Hübener, J.M. Kenneally, V.Ya. Lebedev, Yu.V. Lobanov, K.J. Moody, Yu.Ts. Oganessian, O.V. Petrushkin, A.N. Polyakov, D. Piguet, P. Rasmussen, R.N. Sagaidak, A. Serov, I.V. Shirokovsky, D.A. Shaughnessy, S.V. Shishkin, A.M. Sukhov, M.A. Stoyer, E.E. Tereshatov, Yu.S. Tsyganov, V.K. Utyonkov, G.K. Vostokin, M. Wegrzecki, and P.A. Wilk, *Nucl. Instrum. Meth. Phys. Res. Sect. B* **268,** 28–35 (2009).

[58] J. Even, J. Ballof, W. Brüchle, R. A. Buda, C. E. Düllmann, K. Eberhardt, A. Gorshkov, E. Gromm, D. Hild, E. Jäger, J. Khuyagbaatar, J. V. Kratz, J. Krier, D. Liebe, M. Mendel, D. Nayak, K. Opel, J. P. Omtvedt, P. Reichert, J. Runke, A. Sabelnikov, F. Samadani, M. Schädel, B. Schausten, N. Scheid, E. Schimpf, A. Semchenkov, P. Thörle-Pospiech, A. Toyoshima, A. Türler, V. Vicente Vilas, N. Wiehl, T. Wunderlich, and A. Yakushev, *Nucl. Instrum. Meth. Phys. Res. Sect. A* **638,** *1,* 157–164 (2011).

[59] N. Trautmann, P. O. Aronsson, T. Björnstad, N. Kaffrell, E. Kvåle, M. Skarestad, G. Skarnemark, and E. Stender, *Inorg. Nucl. Chemi. Let.* **11,** 729–735 (1975).

[60] J. M. Gates, R. Sudowe, M. N. Ali, M. G. Calvert, I. Dragojević, P. A. Ellison, M. A. Garcia, N. Gharibyan, K. E. Gregorich, S. L. Nelson, S. H. Neumann, T. Parsons-Moss, L. Stavsetra, and H. Nitsche, *Radiochim. Acta* **97,** 167–172 (2009).

[61] J. M. Gates, L. Stavsetra, R. Sudowe, M. N. Ali, M. G. Calvert, I. Dragojević, J. Dvorak, Z. Dvorakova, P. A. Ellison, M. A. Garcia, K. E. Gregorich, S. L. Nelson, T. Parsons-Moss, and H. Nitsche, *Radiochim. Acta* **97,** 173–176 (2009).

[62] M. Schädel, W. Brüchle, E. Jäger, E. Schimpf, J. V. Kratz, U. W. Scherer, and H. P. Zimmermann, *Radiochim. Acta* **48,** 179-176 (1989).

[63] Y. Nagame, H. Haba, K. Tsukada, M. Asai, A. Toyoshima, S. Goto, K. Akiyama, T. Kaneko, M. Sakama, and M. Hirata, *Nucl. Phys. A* **734,** 124–135 (2004).

[64] J. P. Omtvedt, J. Alstad, K. Eberhardt, K. Fure, R. Malmbeck, M. Mendel, A. Nähler, G. Skarnemark, N. Trautmann, N. Wiehl, and B. Wierczinski, *J. Alloy. Compd. Vol.* **271-273,** 303–306 (1998).

[65] A. Toyoshima, H. Haba, K. Tsukada, M. Asai, K. Asiyama, S. Goto, Y. Ishii, I. Nishinaka, T. K. Sato, Y. Nagame, W. Sato, Y. Tani, H. Hasegawa, K. Matsuo, D. Saika, Y. Kitamoto, A. Shinohara, M. Ito, J. Saito, H. Kudo, A. Yokoyama, M. Sakama, K. Sueki, Y. Oura, H. Nakahara, M. Schädel, W. Brüchle, and J. V. Kratz, *Radiochim. Acta* **96,** 125–134 (2008).

[66] J. P. Omtvedt, J. Alstad, H. Breivik, J. E. Dyve, K. Eberhardt, C. M. Folden III, T. Ginter, K. Gregorich, E. A. Hult, M. Johansson, U. W. Kirbach, D. M. Lee, M. Mendel, A. Nähler, V. Ninov, L. A. Omtvedt, J. B. Patin, G. Skarnemark, L. Stavsetra, R. Sudowe, N. Wiehl, B. Wierczinski, P. A. Wilk, P. M. Zielinski, J. V. Kratz, N. Trautmann, H. Nitsche, and D. C. Hoffman, *J.Nucl. Radiochem. Sci.* **3,** *1,* 121–124 (2002).

[67] U. W. Kirbach, C. M. Folden III, T. N. Ginter, K. E. Gregorich, D. M. Lee, V. Ninov, J. P. Omtvedt, J. B. Patin, N. K. Seward, and D. A. Strellis, *Nucl. Instrum. Meth. Phys. Res. Sect. A* **484,** *1-3,* 587–594 (2002).

[68] Ch. E. Düllmann, B. Eichler, R. Eichler, H. W. Gäggeler, D. T. Jost, D. Piguet, and A. Türler, *Nucl. Instrum. Meth. Phys. Res. Sect. A* **479,** *2-3,* 631–639 (2002).

[69] H. W. Gäggeler, D. T. Jost, U. Baltensperger, A. Weber, A. Kovacs, D. Vermeulen, and A. Türler, *Nucl. Instrum. Meth. Phys. Res. Sect. A* **309,** 201–208 (1991).

[70] M. Schädel, D. Ackermann, L. L. Andersson, J. Ballof, M. Block, R. A. Buda, W. Brüchle, I. Dragojević, Ch. E. Düllmann, J. Dvorak, K. Eberhardt, J. Even, J. M. Gates, J. Gerl, A. Gorshkov, P. Golubev, R. Graeger, K. E. Gregorich, E. Gromm, W. Hartmann, F. P. Heßberger, H. Hild, R. Hoischen, A. Hübner, J. Jäger, J. Khuyagbaatar, B. Kindler, I. Kojouharov, J. V. Kratz, J. Krier, N. Kurz, S. Lahiri, D. Liebe, B. Lommel, M. Maiti, M. Mendel, E. Merchan, D. Nayak, J. Nilssen, J. P. Omtvedt, K. Opel, P. Reichert, D. Rudolph, A. Sabelnikov, F. Samadani, H. Schaffner, B. Schausten, R. Schuber, E. Schimpf, A. Semchenkov, L. Stavsetra, J. Steiner, J. Szerypo, P. Thörle-Pospiech, A. Toyoshima, A. Türler, J. Uusitalo, N. Wiehl, H. Wollersheim, T. Wunderlich, A. Yakushev, *TASCA commissioning completed*, Scientific Report 2008, GSI Helmholtzzentrum für Schwerionenforschung, (2009).

[71] M. Schädel, *Eur. Phys. J. D* **45,** 67–74 (2007).

[72] A. Ghiorso, S. Yashita, M. E. Leino, L. Frank, J. Kalnins, P. Armbruster, J. P. Dufour, and P. K. Lemmertz, *Nucl. Instrum. Meth. Phys. Res. Sect. A* **269,** *1,* 192–201 (1988).

[73] A. Semchenkov, W. Brüchle, E. Jäger, E. Schimpf, M. Schädel, C. Mühle, F. Klos, A. Türler, A. Yakushev, A. Belov, T. Beyakova, M. Kaparkova, V. Kukhtin, E. Lamzin, and S. Sytchevsky, *Nucl. Instrum. Meth. Phys. Res. Sect. B* **266,** 4153–4161 (2008).

[74] A. Gorshkov*, A new focal plane detector for the gas filled separator TASCA*, Doctoral thesis, Technical University Munich, (2010).

[75] L. L. Andersson, D. Rudolph, P. Golubev, R. D. Herzberg, R. Hoischen, E. Merchan, D.

Ackermann, C. E. Düllmann, K. Eberhardt, J. Even, J. Gerl, F. P. Heßberger, E. Jäger, J. Khuyagbaatar, I. Kojouharov, J. V. Kratz, J. Krier, N. Kurz, W. Prokopowicz, M. Schädel, H. Schaffner, B. Schausten, E. Schimpf, A. Semchenkov, A. Türler, H. J. Wollersheim, A. Yakushev, P. Thörle-Pospiech, W. Hartmann, A. Hübner, B. Lommel, B. Kindler, and J. Steiner, *Nucl. Instrum. Meth. Phys. Res. Sect. A* **622,** *1,* 164–170 (2010).

[76] J. V. Kratz, *Radiochim. Acta* **99,** *7-8,* 477–502 (2011).

[77] E. Strub, *Zu den chemischen Eigenschaften von Rutherfordium, Dubnium und Seaborgium,* Doctoral thesis, Johannes Gutenberg - Universität Mainz, (2000).

[78] A. Toyoshima, Y. Kasamatsu, Y. Kitatsuji, K. Tsukada, H. Haba, A. Shinohara, and Y. Nagame, *Radiochim. Acta* **96,** 323–326 (2008).

[79] A. Toyoshima, Y. Kasamatsu, K. Tsukada, M. Asai, Y. Kitatsuji, Y. Ishii, H. Toume, I. Nishinaka, H. Haba, K. Ooe, W. Sato, A. Shinohara, K. Akiyama, and Y. Nagame, *J. Am.Chem. Soc.* **131,** *26,* 9180–9181 (2009).

[80] A. Toyoshima, K. Tsukada, M. Asai, T. K. Sato, Z. J. Li, N. Sato, T. Kikuchi, Y. Kitatsuji, Y. Nagame, K. Ooe, Y. Kasamatsu, A. Shinohara, H. Haba, J. Even, *Reduction of menedelevium using an elechrochemistry apparatus*, JAEA-Tokai Tandem Annual Report 2009, April 1 2009 - March 31, 2010; JAEA-Tokai, Department of Research Reactor and Tandem Accelerator, (2010).

[81] B. Eichler and J. V. Kratz, *Radiochim. Acta* **88,** *8_2000,* 475 (2000).

[82] H. Hummrich, *Der Einsatz elektrochemischer Methoden für die Untersuchung superschwere Elemente,* Doctoral thesis, Johannes Gutenberg - Universität Mainz, (2006).

[83] J. Dvorak, W. Brüchle, M. Chelnokov, R. Dressler, Ch. E. Düllmann, K. Eberhardt, V. Gorshkov, E. Jäger, R. Krücken, A. Kuznetsov, Y. Nagame, F. Nebel, Z. Novackova, Z. Qin, M. Schädel, B. Schausten, E. Schimpf, A. Semchenkov, P. Thörle, A. Türler, M. Wegrzecki, B. Wierczinski, A. Yakushev, and A. Yeremin, *Phys.Rev. Lett.* **97,** *24,* 242501 (2006).

[84] J. Even, *Unterpotentialabscheidung von Ruthenium und Osmium,* Diploma thesis, Philipps Universität Marburg, (2008).

[85] H. Gerischer, D. M. Kolb, and M. Przasnyski, *Surface Science* **43,** *2,* 662–666 (1974).

[86] D. M. Kolb and H. Gerischer, *Surface Science* **51,** *1,* 323–327 (1975).

[87] J. T. Byrne and L. B. Rogers, *J. Electrochem. Soc.* **98,** *11,* 457–463 (1951).

[88] B. Eichler and H. Rossbach, *Absortion von Metallen auf metallischen Oberflächen und ihre*

Anwendung in der Kernchemie. Report 12-83-718 JINR Dubna. Report 12-83-718 JINR Dubna, Übersetzung von C.Riedel, Darmstadt (1989),

[89] B. Eichler, *Metallchemie der Transaktinoide*. PSI Berich Nr 00-09. PSI Berich Nr 00-09, 2000.

[90] B. Eichler, *Influence of electrode metal on the electrochemical deposition potential of the transactinides. Poster contribution 3rd International conference on the chemistry and physics of the transactinide elements* (3rd International conference on the chemistry and physics of the transactinide elements, TAN07, Davos, 2007).

[91] F. Joliot, *J. Chim. Phys.* **27,** 119–162 (1930).

[92] J. Fahland, *Die elektrolytische Abscheidung von Metallen bei geringen Konzentrationen,* Doctoral thesis, Johannes Gutenberg - Universität Mainz, (1960).

[93] G. v. Hevesy and F. Paneth, *Monatshefte für Chemie / Chemical Monthly* **36,** *1,* 45–49 (1915).

[94] Johannes Gutenberg-Universität Mainz, Institut für Kernchemie, *Technische Unterlagen für die Bestrahlung am TRIGA Mainz* (1989).

[95] E. Stender, N. Trautmann, and G. Herrmann, *Radiochem. Radioanal. Lett.* **1980,** *4-5,* 291–296 (42).

[96] A. Kronenberg, *Entwicklung einer online-Chromatographie für Element 106 (Seaborgium),* Doctoral thesis, Johannes Gutenberg - Universität Mainz, (2001).

[97] S. Y. F. Chu, L. P . Ekström and R. B. Firestone, *The Lund/LBNL Nuclear Data Search Version 2.0* (1999).

[98] T. R. England and B. F. Rider, *Thermal Neutron Induced Fission,* LA-UR-94-3106; ENDF-349 (1993).

[99] K. Eberhardt, W. Brüchle, Ch.E. Düllmann, K.E. Gregorich, W. Hartmann, A. Hübner, E. Jäger, B. Kindler, J.V. Kratz, D. Liebe, B. Lommel, H.-J. Maier, M. Schädel, B. Schausten, E. Schimpf, A. Semchenkov, J. Steiner, J. Szerypo, P. Thörle, A. Türler, and A. Yakushev, *Nucl. Instrum. Meth. Phys. Res. Sect. A* **590,** 134–140 (2008).

[100] W. Reisdorf and M. Schädel, *Z. Phys. A Hadron. Nucl.* **343,** *1,* 47–57 (1992).

[101] M. Meister, *Aufbau eines Sputterlabors und Herstellung von Leitern ultrakalter Neutronen,* Diploma thesis, Johannes Gutenberg - Universität Mainz, (2009).

[102] A. F. Holleman, E. Wiberg, and N. Wiberg, *Lehrbuch der anorganischen Chemie* (de Gruyter, Berlin, 1995).

[103] T. M. Buslaeva and S. A. Simanova, *Russian Journal of Coordination Chemistry* **26,** *6,* 379–387 (2000).

[104] J. V. Kratz, J. O. Liljenzin, and G. T. Seaborg, *Inorg. Nucl.Chem. Lett.* **10,** *10,* 951–957 (1974).

[105] L. I. Guseva, Z. Szeglowski, D. T. Lien, B. Kubica, G. S. Tikhomirova, and S. N. Timokhin, *J. Radioanal. Nucl. Chem.* **260,** *2,* 357–362 (2004).

[106] V. Sudha and M. V. Sangaranarayanan, *J. Phys. Chem. B* **106,** *10,* 2699–2707 (2002).

[107] M. Schädel, *J. Radioanal. Nucl. Chem.* **3,** *1,* 113–120 (2002).

[108] D. Hild, *MikroSISAK für die Chemie der schwersten Elemente,* Doctoral thesis, Johannes Gutenberg - Universität Mainz, (2012).

[109] J. Dvorak, *Decay properties of nuclei close to Z =108 and N = 162,* Doctoral thesis, Technical University Munich, July / 2007.

[110] J. Dvorak, W. Brüchle, M. Chelnokov, R. Dressler, C. E. Düllmann, Z. Dvorakova, K. Eberhardt, E. Jäger, R. Krücken, A. Kuznetsov, Y. Nagame, F. Nebel, K. Nishio, R. Perego, Z. Qin, M. Schädel, B. Schausten, E. Schimpf, R. Schuber, A. Semchenkov, P. Thörle, A. Türler, M. Wegrzecki, B. Wierczinski, A. Yakushev, and A. Yeremin, *Phys.Rev. Lett.* **100,** *13,* 132503 (2008).

[111] R. Graeger, *Reaction studies about the Q-value in uence on the production of superheavy elements,* Doctoral thesis, Technical University Munich, 2010.

[112] R. Eichler, W. Brüchle, R. Buda, S. Bürger, R. Dressler, C. E. Düllmann, J. Dvorak, K. Eberhardt, B. Eichler, C. M. Folden III, H. W. Gäggeler, K. E. Gregorich, F. Haenssler, D. C. Hoffman, H. Hummrich, E. Jäger, E. Schimpf, A. Semchenov, S. Soverna, R. Sudowe, N. Trautmann, P. Thörle, A. Türler, B. Wierczinski, N. Wiehl, P. A. Wilk, G. Wirth, A. Yakushev, and A. von Zweidorf, *Radiochim. Acta* **94,** 181–191 (2006).

[113] A. Yakushev, J.M. Gates, A. Gorshkov, R. Graeger, A. Türler, D. Ackermann, M. Block, W. Brüchle, Ch.E. Düllmann, H.G. Essel, F.P. Heßberger, A. Hübner, E. Jäger, J. Khuyagbaatar, B. Kindler, J. Krier, N. Kurz, B. Lommel, M. Schädel, B. Schausten, E. Schimpf, K. Eberhardt, M. Eibach, J. Even, D. Hild, J.V. Kratz, L.J. Niewisch, J. Runke, P. Töhrle-Pospiech, N. Wiehl, J. Dvorak, H. Nitsche, J.P Omtvedt, A. Semchenkov, U. Forsberg, D. Rudolph, J. Uusitalo, L.-L. Andersson, R.-D. Herzberg, E. Parr, Z. Qin, and M. Wegrzecki, *To be submitted to Nature* (2011).

[114] Ivo Zvara, *The Inorganic Radiochemistry of Heavy Elements. Methods for Studying*

Gaseous Compounds (Springer, 2008).

[115] Ch. E. Düllmann, *Nucl. Instrum. Meth. Phys. Res. Sect. B* **266,** 4123–4130 (2008).

[116] Ch.E. Düllmann, K.E. Gregorich, G.K. Pang, I. Dragojević, R. Eichler, C.M. Folden III, M.A. Garcia, J.M. Gates, D.C. Hoffman, S.L. Nelson, R. Sudowe, and H. Nitsche, *Radiochim. Acta* **97,** *8,* 403–418 (2009).

[117] A. A. Blanchard, *Chem.Rev.* **21,** *1,* 3–38 (1937).

[118] Niewisch. L, *Neuartige Verbindungsklassen der Transactiniden am Beispiel der Carbonyle und Metallocene der leichteren Homologen,* Diploma thesis, Johannes Gutenberg - Universität Mainz, (2010).

[119] L. Mond, C. Langer, and F. Quincke, *J. Chem. Soc., Trans.* **57,** 749–753 (1890).

[120] W. A. Herrmann, *J. Organomet. Chem.* **383,** *1-3,* 21–44 (1990).

[121] A. E. Miroslavov, N. I. Gorshkov, A. L. Lumpov, A. N. Yalfimov, D. N. Suglobov, B. L. Ellis, R. Braddock, A.-M. Smith, M. C. Prescott, R. S. Lawson, and H. L. Sharma, *Nucl. Med. Biol.* **36,** *1,* 73–79 (2009).

[122] M. A. Terán, E. Martínez, A. L. Reyes, A. Paolino, M. Vital, P. Esperón, J. P. Pacheco, and E. Savio, *Nucl. Med. Biol.* **38,** *2,* 279–285 (2011).

[123] L. Mond and C. Langer, *J. Chem. Soc., Trans.* **59,** 1090–1093 (1891).

[124] L. Mond, H. Hirtz, and M. D. Cowap, *Z. Anorg. Chem.* **68,** *1,* 207–219 (1910).

[125] W. Hieber and E. Romberg, *Z. Anorg. Allg. Chem.* **221,** *4,* 321–331 (1935).

[126] W. Hieber and H. Lagally, *Z. Anorg. Allg. Chem.* **245,** *3,* 321–333 (1940).

[127] W. Manchot and W. J. Manchot, *Z. Anorg. Allg. Chem.* **226,** *4,* 385–415 (1936).

[128] D. McIntosh and G. A. Ozin, *Inorg. Chem.* **16,** *1,* 51–59 (1977).

[129] J. H. Darling and J. S. Ogden, *J. Chem. Soc., Dalton Trans., 10,* 1079–1085 (1973).

[130] C. Elschenbroich, *Organometallchemie* (Teubner, Stuttgart, 2003).

[131] G. Frenking and N. Frohlich, *Chem. Rev.* **100,** *2,* 717–774 (2000).

[132] R. K. Szilagyi and G. Frenking, *Organometallics* **16,** *22,* 4807–4815 (1997).

[133] C. S. Nash and B. E. Bursten, *J. Am. Chem. Soc.* **121,** *46,* 10830–10831 (1999).

[134] J. Li, G. Schreckenbach, and T. Ziegler, *J. Phys. Chem.* **98,** *18,* 4838–4841 (1994).

[135] A. W. Ehlers and G. Frenking, *J. Am. Chem. Soc.* **116,** *4,* 1514–1520 (1994).

[136] P. Pyykkö and J. P. Desclaux, *Chem. Phys.* **34,** *2,* 261–280 (1978).

[137] A. M. Ricks, L. Gagliardi, and M. A. Duncan, *J. Am. Chem. Soc.* **132,** *45,* 15905–15907 (2010).

[138] M. Patzschke and P. Pyykkö, *Chem. Comm.,* 1982 (2004).

[139] D. R. Wiles and Baumgärtner F., *Fortschr. Chem. Forsch.* **32,** 63–108 (1972).

[140] U. Heck, *Über die Reaktionen von Spaltrückstoßatomen mit Kohlenstoffdioxid, Sauerstoff und Wasserstoff,* Diploma thesis, Johannes Gutenberg - Universität Mainz, 1964.

[141] Baumgärtner F. and Reichold P., *Z. für Naturforschung* **169,** 945–948 (1961).

[142] P. Kienle, B. Weckermann, Baumgärtner F., and Zahn U., *Naturwissenschaften* **49,** *13,* 294–295 (1962).

[143] P. Kienle, B. Weckermann, Baumgärtner F., and Zahn U., *Naturwissenschaften* **49,** *13,* 295–296 (1962).

[144] G. K. Wolf and W. Fröschen, *Trenn- und Identifzierungsmethoden für kurzlebige Elemente, Targetentwicklung für den Schwerionenbeschleuniger UNILAC*, Experimente am Karlsruher Zyklotron im Jahre 1972, *KFK 1783,* Kernforschungszentrum Karlsruhe, Zyklotron-Laboratorium, (1973).

[145] I. G. de Jong and D. R. Wiles, *Inorg. Chem.* **12,** *11,* 2519–2522 (1973).

[146] T. Muto and H. Ebihara, J. *Inorg. Nucl. Chem.* **43,** *11,* 2617–2621 (1981).

[147] I. Webber and D. R. Wiles, J. *Inorg. Nucl. Chem.* **38,** *6,* 1103–1107 (1976).

[148] I. G. de Jong, S. C. Srinivasan, and D. R. Wiles, *J. Organomet. Chemi.* **26,** *1,* 119–124 (1971).

[149] I. Zvara, *Isotopenpraxis* **26,** *6,* 251–258 (1990).

[150] A. Türler, *J. Nucl. Radiochem. Scie.* **5,** *2,* R19-R25 (2004).

[151] C. Pommier and G. Guichon, *J. Chromatogr. Sci., 8,* 486–487 (1970).

[152] F. London, *Zeitschrift für Physik* **63,** *3,* 245–279 (1930).

[153] R. F. Howe, *Inorg. Chem.* **15,** *2,* 486–488 (1976).

[154] K. P. Reddy and T. L. Brown, *J. Am. Chem. Soc.* **117,** *10,* 2845–2854 (1995).

[155] S. Myllyoja, M. Suvanto, M. Kurhinen, P. Hirva, and T. A. Pakkanen, *Surf. Sci.* **441,** *2-3,* 454–460 (1999).

[156] S. Myllyoja and T. A. Pakkanen, *J. Mol. Catal. A Chem.* **156,** *1-2,* 195–203 (2000).

[157] Ch. E. Düllmann, B. Eichler, R. Eichler, H. W. Gäggler, and A. Türler, *J. Phys. Chem. B* **106,** 6679–6684 (2002).

[158] I. Zvara, *Radiochim. Acta* **38,** 95–101 (1985).

[159] A. Türler, *Gas Phase Chemistry of the Transactinide Elements Rutherfordium, Dubnium and Seaborgium,*Habilitation thesis, Universität Bern, (1999).

[160] Wibel W., *Untersuchungen zu laminaren, transitioneller und turbulenter Strömung in rechteckigen Mikrokanälen,* Doctoral thesis, Technische Universität Dortmund, 2009.

[161] J. C. Giddings, *Dynamics of Chromatography. Part 1, Principles and Theory* (Marcel Dekker, New York, USA, 1965).

[162] J. C. Giddings, *J. Chromatogr. A* **5,** 46–60 (1961).

[163] E. Grushka and V. Maynard, *J. Chem. Educ.* **49,** *8,* 565-567 (1972).

[164] D. H. Desty and Koninklijke Nederlandse Chemische Vereniging, *Gas chromatography, 1958* (Butterworth's, 1958).

[165] H. Poppe, *J. Chromatogr. A* **948,** *1-2,* 3–17 (2002).

[166] J. Velasquez and M. A. Duncan, *Chem. Phys. Lett.* **461,** *1-3,* 28–32 (2008).

[167] R. A. Günther, *Optimierung eine He(KCl)-Gasjet-Transportsystems und Untersuchung der Elemente 104, 105 and 106,* Doctoral thesis, Johannes Gutenberg - Universität Mainz, (1997).

[168] M. Wachsmuth, B. Eichler, L. Tobler, D. T. Jost, H. W. Gäggeler, and M. Ammann, *Radiochim. Acta* **88,** 873–877 (2000).

[169] M. Wachsmuth, B. Eichler, L. Tobler, F. Hänssler, H. Gäggeler, and M. Ammann, *J. Radioanal. Nucl. Chem.* **254,** *1,* 201–208 (2002).

[170] D. M. Antonelli, E. B. Tjaden, and J. M. Stryker, *Organometallics* **13,** *3,* 763–765 (1994).

[171] A. M. Ricks, Z. D. Reed, and M. A. Duncan, *J. Am. Chem. Soc.* **131,** *26,* 9176–9177 (2009).

[172] Q. Luo, Q.-S. Li, Z. H. Yu, Y. Xie, R. B. King, and H. F. Schaefer, *J. Am. Chem. Soc.* **130,** *24,* 7756–7765 (2008).

[173] J. F. Ziegler, *Nucl. Instrum. Meth. Phys. Res. Sec. B.* **219-220,** 1027–1036 (2004).

[174] G. C. Bond, C. Louis, and D. T. Thompson, *Catalysis by gold* (Imperial College Press [u.a.], London, 2006), Vol. 6.

[175] R. Chellappa and D. Chandra, *J. Chem. Thermodyn.* **37,** *4,* 377–387 (2005).

[176] J. C. Hileman, D. K. Huggins, and H. D. Kaesz, *J. Am. Chem. Soc.* **83,** *13,* 2953–2954 (1961).

[177] M. Garner, D. Chandra, and K. Lau, *J. Phase Equilib.* **16,** *1,* 24–29 (1995).

[178] H. W. Schmitt, J. H. Neiler, and F. J. Walter, *Phys. Rev.* **141,** *3,* 1146 (1966).

[179] J. F. Ziegler, M. D. Ziegler, and J. P. Biersack, *Nucl. Instrum. Meth. Phys. Res. Sec. B.* **268,** *11-12,* 1818–1823 (2010).

[180] H. D. Betz, *Rev. Mod. Phys.* **44,** *3,* 465 (1972).

[181] M. Block, C. Bachelet, G. Bollen, M. Facina, C. M. Folden, C. Guénaut, A.A. Kwiatkowski, D. J. Morrissey, G. K. Pang, A. Prinke, R. Ringle, J. Savory, P. Schury, and S. Schwarz, *Phys. Rev. Lett.* **100,** *13,* 132501 (2008).

[182] R. Ferrer, M. Block, C. Bachelet, B. R. Barquest, G. Bollen, C. M. Campbell, M. Facina, C. M. Folden, C. Guénaut, A. A. Kwiatkowski, D. L. Lincoln, D. J. Morrissey, G. K. Pang, A. M. Prinke, R. Ringle, J. Savory, P. Schury, and S. Schwarz, *Phys. Rev. C* **81,** *4,* 44318 (2010).

[183] D. R. Lide, *CRC handbook of chemistry and physics. A ready-reference book of chemical and physical data* (CRC Press, Boca Raton, 2003).

[184] V. Pershina, *Radiochim. Acta* **93,** *3,* 125–131 (2005).

[185] L. Pauling and M. Simonetta, *J. Chem. Phys.* **20,** *1,* 29–34 (1952).

[186] V. Pershina, T. Bastug, B. Fricke, and S. Varga, *J. Chem. Phys.* **115,** *2,* 792 (2001).

[187] R. C. Weast, ed., *Handbook of chemistry and physics* (CRC Press, Cleveland, Ohio, 1974).

[188] G. Nagarajan, *Bull. Soc. Chim. Belges* **90,** *11,* 1077–1092 (1981).

[189] A. Whitaker and J. W. Jeffery, *Acta Cryst.* **23,** *6,* 977–984 (1967).

[190] T. C. W. Mak, *Z. Kristallogr.* **166,** *3-4,* 277–281 (1984).

[191] F. Heinemann, H. Schmidt, K. Peters, and D. Thiery, *Z. Kristallogr.* **198,** *1-2,* 123–124 (1992).

[192] R. Eichler and M. Schädel, *J. Phys. Chem. B* **106,** 5413–5420 (2002).

[193] L. P. Somerville, M. J. Nurmia, J. M. Nitschke, A. Ghiorso, E. K. Hulet, and R. W. Lougheed, *Phys. Rev. C* **31,** *5,* 1801–1815 (1985).

[194] J. M. Gates, M. A. Garcia, K. E. Gregorich, C. E. Düllmann, I. Dragojević, J. Dvorak, R. Eichler, C. M. Folden III, W. Loveland, S. L. Nelson, G. K. Pang, L. Stavsetra, R. Sudowe, A. Türler, and H. Nitsche, *Phys. Rev. C* **77,** 34603 (2008).

[195] A. Gorshkov, A. Yakushev, A. Türler, Ch. E. Düllmann, M. Schädel, J. Khuyagbaatar, K. Eberhardt, J. V. Kratz, D. Liebe, D. Ackermann, W. Brüchle, J. Ballof, M. Block, I. Dragojevic, J. Even, J. M. Gates, R. Graeger, F. P. Heßberger, E. Jäger, J. Krier, J. P. Omtvedt, H. Nitsche, D. Rudolph, A. Sabelnikov, F. Samdani, B. Schausten, E. Schimpf, A. Semchenkov, L. Stavsetra, P. Thörle-Pospiech, A. Toyoshima and J. Uusitalo*, Study of the $^{22}Ne + ^{244}Pu$ fusion-evaporation reaction in TASCA commissioning experiment*, to be submitted 2011.

[196] H. Haba, D. Kaji, H. Kikunaga, Y. Kudou, K. Morimoto, K. Morita, K. Ozeki, T. Sumita, A. Yoneda, Y. Kasamatsu, Y. Komori, K. Ooe, and A. Shinohara, *Phys. Rev. C* **83,** *3,* 34602 (2011).

[197] Y. Nagame, M. Asai, H. Haba, S. Goto, K. Tsukada, I. Nishinaka, K. Nishio, S. Ichikawa, A. Toyoshima, K. Akiyama, H. Nakahara, M. Sakama, M. Schädel, J. V. Kratz, H. W. Gäggeler, and A. Türler, *J. Nucl. Radiochem. Sci.* **3,** *1,* 85–88 (2002).

[198] J. V. Kratz, M. K. Gober, H. P. Zimmermann, M. Schädel, W. Brüchle, E. Schimpf, K. E. Gregorich, A. Türler, N. J. Hannink, K. R. Czerwinski, B. Kadkhodayan, D. M. Lee, M. J. Nurmia, D. C. Hoffman, H. Gäggeler, D. Jost, J. Kovacs, U. W. Scherer, and A. Weber, *Phys. Rev. C* **45,** *3,* 1064 (1992).

[199] Ch. E. Düllmann and A. Türler, *Phys. Rev. C (Nuclear Physics)* **77,** *6,* 64320 (2008).

[200] H. Haba, D. Kaji, Y. Kudou, K. Morimoto, K. Morita, K. Ozeki, R. Sakai, T. Sumita, A. Yoneda, Y. Kasamatsu, Y. Komori, A. Shinohara, H. Kikunaga, H. Kudo, K. Ooe, N. Sato, and K. Tsukada, *Production of Sg-265 for chemical studies using the gas-jet transport system coupled to the RIKEN gas-filled recoil ion separator* (4th International conference on the chemistry and physics of the transactinide elements, TAN 11; Sochi, 2011).

[201] P. A. Wilk, K. E. Gregorich, A. Türler, C. A. Laue, R. Eichler, V. Ninov, J. L. Adams, U. W. Kirbach, M. R. Lane, D. M. Lee, J. B. Patin, D. A. Shaughnessy, D. A. Strellis, H. Nitsche, and D. C. Hoffman, *Phys. Rev. Lett.* **85,** *13,* 2697 (2000).

[202] K. E. Lewis, D. M. Golden, and G. P. Smith, *J. Am. Chem. Soc.* **106,** *14,* 3905–3912 (1984).

[203] F. Haenssler, *Thermochromatographische Untersuchungen von inaktivem und radioaktivem Rhodium (Rh-107) mit verschiedenen Trägergasen,* Diploma thesis, Universität Bern, (2001).

[204] K. Morita, K. Morimoto, D. Kaji, K. Akiyama, S. Goto, H. Haba, E. Ideguchi, K. Katori, H. Koura, H. Kudo, T. Ohnishi, A. Ozawa, T. Suda, K. Sueki, F. Tokanai, H. Yamaguchi, A. Yoneda, and A. Yoshida, *Journal of the Physical Society of Japan* **76,** *4,* 43201 (2007).

[205] A. Yakushev, *Hassium spectroscopy experiments at TASCA* (TASCA 08, 7th Workshop on Recoil Separator for Superheavy Element Chemistry, GSI Darmstadt, 2008).

[206] J. Dvorak, W. Brüchle, Ch.E. Düllmann, Z. Dvorakova, K. Eberhardt, R. Eichler, E. Jäger, Y. Nagame, Z. Qin, M. Schädel, B. Schausten, E. Schimpf, R. Schuber, A. Semchenkov, P. Thörle, A. Türler, M. Wegrzecki, and A. Yakushev, *Phys. Rev. C* **79,** *3,* 37602 (2009).

[207] R. Graeger, D. Ackermann, M. Chelnokov, V. Chepigin, Ch. E.Düllmann, J. Dvorak, J. Even, A. Gorshkov, F. P. Heßberger, D. Hild, A. Hübner, E. Jäger, J. Khuyagbaatar, B. Kindler, J. V. Kratz, J. Krier, A. Kuznetsov, B. Lommel, K. Nishio, H. Nitsche, J. P. Omtvedt, O. Petrushkin, D. Rudolph, J. Runke, F. Samadani, M. Schädel, B. Schausten, A. Türler, A. Yakushev, and Q. Zhi, *Phys. Rev. C* **81,** *6,* 61601 (2010).

Appendix

A) Source codes of the Monte Carlo Simulations

1) For Isothermal Chromatography

```
# Monte Carlo simulation of thermotography using a
# microscopic model proposed by. I. Zvara. in
# Simulation of Thermochromatographic Process by the Monte Carlo Method),
# Radiochimica Acta 38, 95-101 (1985)
#
# Original BASIC program made by A. Tuerler from 10/05/94
# rewritten J.Even for PYTHON 2.6
#
#################################################################################
#Some definitions

from numpy import *
from random import random
from math import *
from math import *
from string import *
import sys

def sqr(x):
  """Function returning square."""
  return x*x



class progressBar:
     def __init__(self, minValue = 0, maxValue = 10, totalWidth=12):
          self.progBar = "[]"     # This holds the progress bar string
```

```
        self.min = minValue
        self.max = maxValue
        self.span = maxValue - minValue
        self.width = totalWidth
        self.amount = 0        # When amount == max, we are 100%
done
        self.updateAmount(0)  # Build progress bar string
    def updateAmount(self, newAmount = 0):
        if newAmount < self.min: newAmount = self.min
        if newAmount > self.max: newAmount = self.max
        self.amount = newAmount

        # Figure out the new percent done, round to an integer
        diffFromMin = float(self.amount - self.min)
        percentDone = (diffFromMin / float(self.span)) * 100.0
        percentDone = round(percentDone)
        percentDone = int(percentDone)

        # Figure out how many hash bars the percentage should be
        allFull = self.width - 2
        numHashes = (percentDone / 100.0) * allFull
        numHashes = int(round(numHashes))

        # build a progress bar with hashes and spaces
        self.progBar = "[" + '#'*numHashes + ' '*(allFull-
numHashes) + "]"

        # figure out where to put the percentage, roughly
centered
        percentPlace = (len(self.progBar) / 2) -
len(str(percentDone))
        percentString = str(percentDone) + "%"

        # slice the percentage into the bar
        self.progBar = self.progBar[0:percentPlace] +
percentString + self.progBar[percentPlace+len(percentString):]
    #def __str__(self):

            #return str(self.progBar)
```

```
          #def __str__(self):
          #return str(self.progBar)


#Asking for parameters
def get_param(message="Enter value: ", default=0, int_or_float="f",
repeat=3, warning="Wrong value! "):
  """Function asking for parameters


  Asks for parameter, checks if OK and returns.
  """
  while 1:
    r_param = raw_input(message)
    try:
      if int_or_float == "i" :
          param = int(r_param)
      elif int_or_float == "f" :
          param = float(r_param)
      else : raise IOError, 'Not integer or float.'
      return param
      break
    except ValueError:
      if r_param == "":
        param = default
        return param
        break
      else:
        print warning
        repeat = repeat - 1
        if repeat < 0:
          raise IOError, 'Wrong value entered as an answer. '



#Main body


M2 = get_param("Mass of gas in amu (CO = 28): ", 28)
```

```
d2 = get_param("Density of gas in g/cm3: ", 1.25)
P  = get_param("Pressure of gas in bar: ", 1.3)
p0 = get_param("Period of oscillation in 10e-12 s (0.2): ", 0.2)
particles  = get_param("Number of particles : ", 10000,'i')
Q  = get_param("The STP flow rate of gas through column (cm3/s): ",
25)
halflife = get_param("Half-life of the nuclide in s: ", 15)
M1 = get_param("Molecular weight of the substance: ", 333)
d1 = get_param("Density of the substance in g/cm3: ", 2)
dHa1 = get_param("The adsorption enthalpy to start with: ", -50)
length = get_param("Length of column in cm: ",191)
radius = get_param("Radius of column in cm (0.1): ",0.1)
T1  =  get_param("Temperature  of  the  column  to  start  with  in  K:
",293,'i')
T2  =  get_param("Temperature  of  the  column  to  stop  with  in  K:
",183,'i')
dTstep = get_param("How many steps in temperature : ",14,'i')


R =  8.31432e+7 #Universal gas constant cgs


prog = progressBar(0, particles, 77) #Initialise progress bar
oldprog = str(prog)


print
"-----------------------------------------------------------------
-----"


#Calculate some values
hist_steps = 2
cross_section = pi*sqr(radius)
mean_path=radius



D298 = 0.0044 * pow(298.15,1.5) * sqrt(1.0/float(M1)+1.0/float(M2))
/
(float(P)*sqr(pow(float(M1)/float(d1),1.0/3)+pow(float(M2)/float(d2
),1.0/3)))   #   Calculate   diffusion   coefficient   using   proper
Gilliland's formula


#T0 = temp_numpy(0) #Temperature at the entry of the column
```

```
#TE = temp_numpy(length) #Temperature at the end of the column
#print "T0: ", T0-273.15, "TE: ", TE-273.15


#Prepare array of results
results=[]
hist=[]
for k in range(hist_steps+1):
    hist.append(0)

#Simulation
for j in range(dTstep+1):
  dT = T1+(T2-T1)/dTstep*j

  for k in range(hist_steps+1): # Setting hist to zero
    hist[k] = 0
  print ""
  print "Calculating temperature",dT,": "


  for n in range(particles): # For all particles
    #print "New particle"
    prog.updateAmount(n) #make progress bar
    if oldprog != str(prog):
        print prog, "\r",
        oldprog=str(prog)

    xi = float(0) # Starting at zero
    tf = float(0) # Time of jump
    tt = float(0) # Processing time of particle
    ta = float(0) # Time the particle spends staying on the surface
    td = -halflife / log(2)*log(1-random()) # Generate random life
time for nuclide
    #print "\nParticle #",n,"Half-life je ",td
    Ro = float(1)
    while tt < td :
      #T1 = temp_numpy(xi) # Calculate temperature in xi
```

```
          Dcoff = D298*pow(dT/298.15,1.5) # Calculate Diffusion
coeficient at the T(xi)
      if tf <> 0 :
        Ro = tf / (tf + ta) # Calculate Ro - ratio of the velocity
of the carrier gas to the  mean migration velocity of the zone


      # Particle jumps
          Nm = cross_section * Dcoff / (Q*dT/273.15) + (11 -
16*Ro+6*sqr(Ro)) * ((Q*dT/273.15)/(48*pi*Dcoff)) # Calculate mean
jump length
      Ni = - Nm * log(1-random()) # Generate random jump length
      xi = xi + Ni # Calculate new position
        if xi > length : break # If particle flies through the
column, we will find it in the filter
      tf = 2 * cross_section * Ni / ((Q*dT/273.15)+(Q*dT/273.15)) #
Calculate flight time (assume that flight time was Ni/Velocity;
Velocity= Qi/cross_section
      tt = tt + tf # Processing time of particle increases
      if tt > td:  break # particle decays


      # Particle stays on the surface for some time
      tm = p0 * (1e-12) * exp((-dHa1*(1e10))/(R*dT)) # Mean time to
stay on surface
        vi = mean_path /(Q*dT/273.15) * sqrt(2*pi*R*dT/M1) #Mean
number of collisions
       ta = -vi * tm * Nm * log(1-random()) # Generate random time
the particle spends staying on the surface
      tt = tt + ta #  Processing time of particle increases
       #print "Dcoff: ", Dcoff, "Colisions:",vi, "Mean stay: ",tm,
"Mean jump :",Nm, "Time of stay: ", ta


     if xi > length : # If particle flies through the column, we
will find it in the filter
      k = 2
      hist[k] = hist[k] + 1
    else :
      k=1
      hist[k] = hist[k] + 1
  results.append(map(int,hist)) # Save results for this enthalpy in
the array of results
```

```
#Results
#print results
print D298
print dHa1
part_ord = int(0.5+log10(particles))
devider = "+"+8*"-"+"+"+("-"*4+"+")*hist_steps+7*"-"+"+"
print devider
print "|Temp."+"|",
for k in range(hist_steps):
  print "%3d|" %(k+1),
print "Filter|"
print devider

for j in range(dTstep+1):
  dT = T1+(T2-T1)/dTstep*j
  line = results[j]
  print "|%8.1f" %(dT),
  for k in range(hist_steps):
    print "%3d" %(line[k]),
  print "%6d" %(line[k+1])
#  print "Enthalpy:",dHa,":",results[j]
print devider
```

2) For thermochromatography experiments using a column with a circular cross-section

```
# Monte Carlo simulation of thermochromatography using a
# microscopic model proposed by. I. Zvara. in
# Simulation of Thermochromatographic Process by the Monte Carlo Method),
# Radiochimica Acta 38, 95-101 (1985)
#
# Original BASIC program made by A. Tuerler from 10/05/94
# rewritten by J. Dvorak in Python 30/05/2005
#
# Changed by J.Even 2010/2011  -
# ONLY for circular TC-channel
# fit function for the temperature gradient was defined with origin,
# has to be changed in the program for any new gradient
##########################################################################
#Some definitions

from numpy import *
from random import random
from math import *
from string import *
import sys

def sqr(x):
  """Make x^2. """
  return x*x



#Asking for parameters
def get_param(message="Enter value: ", default=0, int_or_float="f", repeat=3, warning="Wrong value! "):
  """Function asking for parameters

  Asks for parameter, checks if OK and returns.
```

```
  """
  while 1:
    r_param = raw_input(message)
    try:
      if int_or_float == "i" :
          param = int(r_param)
      elif int_or_float == "f" :
          param = float(r_param)
      else : raise IOError, 'Not integer or float.'
      return param
      break
    except ValueError:
      if r_param == "":
        param = default
        return param
        break
      else:
        print warning
        repeat = repeat - 1
        if repeat < 0:
          raise IOError, 'Wrong value entered as an answer. '



def temp_numpy(x):
  """Function for calculation of temperature in x. """


  return (276.29143 - 1.50298 * x - 0.00507 *sqr(x)) #According to
origin fit function


def  yes_not(message,  yes_string="yes",no_string="no",  repeat=4,
warning='Wrong entry'):
  """Function asking question yes or not and returning 1 or 0."""
  while 1:
    ok = raw_input(message)
    if ok in (yes_string[0], yes_string): return 1
    if ok in (no_string[0], no_string): return 0
    repeat = repeat - 1
      if repeat < 0: raise IOError, 'Wrong value entered as an
```

```
answer'
    print warning


class progressBar:
     def __init__(self, minValue = 0, maxValue = 10,
totalWidth=12):
          self.progBar = "[]"     # This holds the progress bar
string
          self.min = minValue
          self.max = maxValue
          self.span = maxValue - minValue
          self.width = totalWidth
          self.amount = 0        # When amount == max, we are 100%
done
          self.updateAmount(0)  # Build progress bar string

     def updateAmount(self, newAmount = 0):
          if newAmount < self.min: newAmount = self.min
          if newAmount > self.max: newAmount = self.max
          self.amount = newAmount

          # Figure out the new percent done, round to an integer
          diffFromMin = float(self.amount - self.min)
          percentDone = (diffFromMin / float(self.span)) * 100.0
          percentDone = round(percentDone)
          percentDone = int(percentDone)

          # Figure out how many hash bars the percentage should be
          allFull = self.width - 2
          numHashes = (percentDone / 100.0) * allFull
          numHashes = int(round(numHashes))

          # build a progress bar with hashes and spaces
          self.progBar = "[" + '#'*numHashes + ' '*(allFull-
numHashes) + "]"

          # figure out where to put the percentage, roughly
centered
          percentPlace = (len(self.progBar) / 2) -
```

```
len(str(percentDone))
          percentString = str(percentDone) + "%"


          # slice the percentage into the bar
          self.progBar     =     self.progBar[0:percentPlace]     +
percentString + self.progBar[percentPlace+len(percentString):]


     def __str__(self):
          return str(self.progBar)
##########################################################################
############


#Main body


# Get input data
arg = get_arguments()


  M2 = get_param("Mass of gas in amu (CO = 28): ", 28)
  d2 = get_param("Density of gas in g/cm3: ", 1.25)
  P  = get_param("Pressure of gas in bar : ", 1)
  p0 = get_param("Period of oscillation in 10e-12 s (0.2): ", 0.2)
  particles  = get_param("Number of particles : ", 10000,'i')
  Q  = get_param("The STP flow rate of gas through column (cm3/s):
", 10)
  halflife = get_param("Half-life of the nuclide in s: ", 2.5)
   M1 = get_param("Molecular weight of the substance in g/mol: ",
331)
  d1 = get_param("Density of the substance in g/cm3: ", 1.96)
  dHa1 = get_param("The adsorption enthalpy to start with: ", -10)
  dHa2 = get_param("The adsorption enthalpy to stop with: ", -100)
  dHastep = get_param("How many steps in enthalpy (5): ",1,'i')
  length = get_param("Length of column in cm: ",65)
  radius = get_param("Dimension of radius a in cm: ", 0.2)
  hist_steps = get_param("How many values in result histogram (13):
",13,'i')


R =  8.31432e+7 #Universal gas constant cgs


prog = progressBar(0, particles, 77) #Initialise progress bar
```

```
oldprog = str(prog)


print
"-----------------------------------------------------------------
-----"



cross_section = pi* sqr(radius)



print cross_section


D298 = 0.0044 * pow(298.15,1.5) * sqrt(1.0/float(M1)+1.0/float(M2))
/
(float(P)*sqr(pow(float(M1)/float(d1),1.0/3)+pow(float(M2)/float(d2
),1.0/3)))   #   Calculate   diffusion   coefficient   using   proper
Gilliland's formula


T0 = temp_numpy(0) #Temperature at the entry of the column
TE = temp_numpy(length) #Temperature at the end of the column
print "T0: ", T0-273.15, "TE: ", TE-273.15



#Prepare array of results
results=[]
hist=[]
for k in range(hist_steps+1):
    hist.append(0)

#Simulation
for j in range(dHastep+1):
  dHa = dHa1+(dHa2-dHa1)/dHastep*j

  for k in range(hist_steps+1): # Setting hist to zero
    hist[k] = 0
  print ""
  print "Calculating enthalpy",dHa,": "
```

```
  for n in range(particles): # For all particles
    #print ”New particle”
    prog.updateAmount(n) #make progress bar
    if oldprog != str(prog):
        print prog, ”\r”,
        oldprog=str(prog)

    xi = float(0) # Starting at zero
    tf = float(0) # Time of jump
    tt = float(0) # Processing time of particle
    ta = float(0) # Time the particle spends staying on the surface
     td = (-halflife / log(2))*log(1-random()) # Generate random
life time for nuclide
    #print ”\nParticle #”,n,”Half-life je ”,td
    Ro = float(1)
    while tt < td :
      T1 = temp_numpy(xi) # Calculate temperature in xi
          Dcoff = D298*pow(T1/298.15,1.5) # Calculate Diffusion
coeficient at the T(xi)
      if tf <> 0 :
        Ro = tf / (tf + ta) # Calculate Ro - ratio of the velocity
of the carrier gas to the  mean migration velocity of the zone
        # Particle jumps

      Nm = cross_section * Dcoff / (Q*T1/273.15) + (11 - 16 *Ro + 6
*sqr (Ro))*((Q*T1/273.15)/(48*pi *Dcoff))
      Ni = - Nm * log(1-random())
      xi = xi + Ni # Calculate new position
        #xi = xi - Nm *log(1-random())
        if xi > length : break # If particle flies through the
column, we will find it in the filter
      T2 = temp_numpy(xi) # Calculate temperature in new position
           #Nm = 1/((Q/cross_section)*(T1/273.15))*(Dcoff+((11 -
16*Ro+6*sqr(Ro)*sqr((Q/cross_section)*(T1/273.15))*sqr((cross_sectio
n)/(96*Dcoff)))))
      #Ni = - Nm * log(1-random()) # Generate random jump length
      tf = 2 * cross_section * Ni / ((Q*T1/273.15)+(Q*T2/273.15)) #
Calculate flight time (assume that flight time was Ni/Velocity;
Velocity= Qi/cross_section
      tt = tt + tf # Processing time of particle increases
```

```
      #print "Time after flight: ", tt
      if tt > td:  break # particle decays


      # Particle stays on the surface for some time
      tm = p0 * (10e-12) * exp((-dHa*(1e10))/(R*T2)) # Mean time to
stay on surface
       vi = radius /(Q*T2/273.15) * sqrt(2*pi*R*T2/M1) #Mean number
of collisions
      #vi= sqrt(pi*R*T2/(2*M1))*(2*side_a*side_b)/(4*(Q*T2/273.15))
       ta = -vi * tm * Nm * log(1-random()) # Generate random time
the particle spends staying on the surface
      tt = tt + ta #  Processing time of particle increases
       #print "Dcoff: ", Dcoff, "Colisions:",vi, "Mean stay: ",tm,
"Mean jump :",Nm, "Time of stay: ", ta


     if xi > length : # If particle flies through the column, we
will find it in the filter
        k = len(hist)-1
        hist[k] = hist[k] + 1
    else :
      k = int ((xi/length)*hist_steps)
      #k = int ((length/xi) * hist_steps)
      hist[k] = hist[k] + 1
  results.append(map(int,hist)) # Save results for this enthalpy in
the array of results


#Results
#print results
print D298
part_ord = int(0.5+log10(particles))
devider = "+"+8*"-"+"+"+("-"*4+"+")*hist_steps+7*"-"+"+"
print devider
print "|Enthalpy"+"|",
for k in range(hist_steps):
  print "%3d|" %(k+1),
print "Filter|"
print devider

for j in range(dHastep+1):
```

```
  dHa = dHa1+(dHa2-dHa1)/dHastep*j
  line = results[j]
  print "|%8.1f|" %(dHa),
  for k in range(hist_steps):
    print "%3d|" %(line[k]),
  print "%6d|" %(line[k+1])
#  print "Enthalpy:",dHa,":",results[j]
print deviser
```

3) For thermochromatography experiments with COMPACT

```
# Monte Carlo simulation of thermochromatography using a
#microscopic model proposed by. I. Zvara. in
# Simulation of Thermochromatographic Process by the Monte Carlo
#Method),
# Radiochimica Acta 38, 95-101 (1985)
#
# Original BASIC program made by A. Tuerler from 10/05/94
# rewritten by J. Dvorak in Python 30/05/2005
#
# Changes made to use numpy instead of ScientificPython, which is
# incompatible with python 2.5 under Windows
#
# Changed by J.Even 2010/2011  -
# ONLY for rectangular TC-channel!!!!
# fit function for the temperature gradient was defined with
# origin,
# has to be changed in the program for every new gradient!!!
##############################################################
############
#Some definitions

from numpy import *
from random import random
from math import *
from string import *
import sys

def sqr(x):
  """Make x^2. """
  return x*x
```

```
#Asking for parameters
def get_param(message="Enter value: ", default=0, int_or_float="f",
repeat=3, warning="Wrong value! "):
  """Function asking for parameters


  Asks for parameter, checks if OK and returns.
  """
  while 1:
    r_param = raw_input(message)
    try:
      if int_or_float == "i" :
          param = int(r_param)
      elif int_or_float == "f" :
          param = float(r_param)
      else : raise IOError, 'Not integer or float.'
      return param
      break
    except ValueError:
      if r_param == "":
        param = default
        return param
        break
      else:
        print warning
        repeat = repeat - 1
        if repeat < 0:
          raise IOError, 'Wrong value entered as an answer. '



def temp_numpy(x):
  """Function for calculation of temperature in x. - function was
estimated by fitting the measured temperature with Origin for every
single experiment """
     return (285.21286-0.32509*x-0.1081*sqr(x))
def yes_not(message, yes_string="yes",no_string="no", repeat=4,
```

```
warning='Wrong entry'):
  """Function asking question yes or not and returning 1 or 0."""
  while 1:
    ok = raw_input(message)
    if ok in (yes_string[0], yes_string): return 1
    if ok in (no_string[0], no_string): return 0
    repeat = repeat - 1
    if repeat < 0: raise IOError, 'Wrong value entered as an
answer'
    print warning


class progressBar:
     def __init__(self, minValue = 0, maxValue = 10,
totalWidth=12):
          self.progBar = "[]"   # This holds the progress bar
string
          self.min = minValue
          self.max = maxValue
          self.span = maxValue - minValue
          self.width = totalWidth
          self.amount = 0       # When amount == max, we are 100%
done
          self.updateAmount(0)  # Build progress bar string


     def updateAmount(self, newAmount = 0):
          if newAmount < self.min: newAmount = self.min
          if newAmount > self.max: newAmount = self.max
          self.amount = newAmount


          # Figure out the new percent done, round to an integer
          diffFromMin = float(self.amount - self.min)
          percentDone = (diffFromMin / float(self.span)) * 100.0
          percentDone = round(percentDone)
          percentDone = int(percentDone)
```

```
          # Figure out how many hash bars the percentage should be
          allFull = self.width - 2
          numHashes = (percentDone / 100.0) * allFull
          numHashes = int(round(numHashes))

          # build a progress bar with hashes and spaces
          self.progBar = "[" + '#'*numHashes + ' '*(allFull-
numHashes) + "]"

          # figure out where to put the percentage, roughly
centered
          percentPlace = (len(self.progBar) / 2) -
len(str(percentDone))
          percentString = str(percentDone) + "%"

          # slice the percentage into the bar
          self.progBar = self.progBar[0:percentPlace] +
percentString + self.progBar[percentPlace+len(percentString):]

     def __str__(self):
          return str(self.progBar)



def usage():
  print "Possible arguments are: \n -h   help \n -i   input file \n
-o   output file"

def get_arguments():
    args = sys.argv[1:]
    arguments={}
    for arg_nr in range(len(args)):
      if args[arg_nr] in ["-h", "--help"]:
        usage()
        sys.exit(2)
      elif args[arg_nr] in ["-i", "--input"]:
```

```
        arguments['input_file'] = args[arg_nr+1]
      elif args[arg_nr] in ["-o", "--output"]:
        arguments['output_file'] = args[arg_nr+1]
    return arguments



##################################################################
############

#Main body

# Get input data
arg = get_arguments()

M2 = get_param("Mass of gas in amu: ", 6.8)
d2 = get_param("Density of gas in g/cm3: ", 0.3)
P  = get_param("Pressure of gas in bar: ", 1.0)
p0 = get_param("Period of oscillation in 10e-12 s (0.2): ", 0.2)
particles  = get_param("Number of particles : ", 50,'i')
Q  = get_param("The STP flow rate of gas through column in cm3/s:
", 12.0)
halflife = get_param("Half-life of the nuclide in s: ", 15.0)
M1 = get_param("Molecular weight of the substance in g/mol: ",
333.0)
d1 = get_param("Density of the substance in g/cm3: ", 4.0)
dHa1 = get_param("The adsorption enthalpy to start with: ", -30.0)
dHa2 = get_param("The adsorption enthalpy to stop with: ", -50.0)
dHastep = get_param("How many steps in enthalpy (5): ",2,'i')
length = get_param("Length of column in cm: ",32.0)
side_a = get_param("Dimension of side a in cm: ", 1.0)
side_b = get_param("Dimension of side b in cm: ", 0.06)
hist_steps = get_param("How many values in result histogram (32):
",32,'i')
```

```
R =  8.31432e+7 #Universal gas constant cgs

prog = progressBar(0, particles, 77) #Inicialise progress bar
oldprog = str(prog)

print
"-----------------------------------------------------------------
-----"
#Calculate some values
cross_section = side_a*side_b
print cross_section

D298 = 0.0044 * pow(298.15,1.5) * sqrt(1.0/float(M1)+1.0/float(M2))
/
(float(P)*sqr(pow(float(M1)/float(d1),1.0/3)+pow(float(M2)/float(d2
),1.0/3))) # Calculate diffusion coefficient using proper
Gilliland's formula

T0 = temp_numpy(0) #Temperature at the entry of the column
TE = temp_numpy(length) #Temperature at the end of the column
print "T0: ", T0-273.15, "TE: ", TE-273.15



#Prepare array of results
results=[]
hist=[]
for k in range(hist_steps+1):
    hist.append(0)

#Simulation
for j in range(dHastep+1):
  dHa = dHa1+(dHa2-dHa1)/dHastep*j

  for k in range(hist_steps+1): # Setting hist to zero
    hist[k] = 0
  print ""
```

```
  print "Calculating enthalpy",dHa,": "


  for n in range(particles): # For all particles
    #print "New particle"
    prog.updateAmount(n) #make progress bar
    if oldprog != str(prog):
        print prog, "\r",
        oldprog=str(prog)

    xi = float(0) # Starting at zero
    tf = float(0) # Time of jump
    tt = float(0) # Processing time of particle
    ta = float(0) # Time the particle spends staying on the surface
    td = -halflife / log(2)*log(1-random()) # Generate random life
time for nuclide
    #print "\nParticle #",n,"Half-life je ",td
    #Ro = float(1)
    Rp = float (1)
    while tt < td :
      T1 = temp_numpy(xi) # Calculate temperature in xi
      Dcoff = D298*pow((T1/298.15),1.5) # Calculate Diffusion
coeficient at the T(xi)
      if ta <> 0: Rp = ta/(tf+ta)
      # Particle jumps
      Nm = ((2 * side_b *side_a* Dcoff) / (Q*T1/273.15))+((7.301 +
21.673 * Rp + 31.872 * sqr(Rp))*(Q*T1/273.15)*sqr(side_b))/
(cross_section*105 * Dcoff*sqr(1+Rp))
      # Calculate mean jump length
      #print Nm
      Ni = - Nm * log(1-random()) # Generate random jump length
      xi = xi + Ni # Calculate new position
      if xi > length : break # If particle flies through the
column, we will find it in the filter
      T2 = temp_numpy(xi) # Calculate temperature in new position
      tf = 2 * cross_section * Ni / ((Q*T1/273.15)+(Q*T2/273.15))
```

```
      # Calculate flight time (assume that flight time was
Ni/Velocity; Velocity= Qi/cross_section
      tt = tt + tf # Processing time of particle increases
      #print "Time after flight: ", tt
      if tt > td:  break # particle decays


      # Particle stays on the surface for some time
      tm = p0 * (1e-12) * exp((-dHa*(1e10))/(R*T2)) # Mean time to
stay on surface
      #vi = ((side_a + side_b)/cross_section) * sqrt(2*R*T2/
(pi*M1))
      vi = ((side_a + side_b) /(Q*T2/273.15)) * sqrt(2*R*T2/
(pi*M1)) #Mean number of collisions
      ta = -vi * tm * Nm * log(1-random()) # Generate random time
the particle spends staying on the surface
      tt = tt + ta #  Processing time of particle increases
      #print "Dcoff: ", Dcoff, "Colisions:",vi, "Mean stay: ",tm,
"Mean jump :",Nm, "Time of stay: ", ta


    if xi > length : # If particle flies through the column, we
will find it in the filter
        k = len(hist)-1
        hist[k] = hist[k] + 1
    else :
        k = int (xi)
        hist[k]= hist[k]+1
      #print "T2: ",T2-273.15
      #for k in range(hist_steps+1): # Particle is somewhere in the
column, calculate where
        #if ((T2 < ((TE-T0)/hist_steps*k+T0)) and (T2 > ((TE-
T0)/hist_steps*(k+1)+T0)) ):
       #print "Fitting temperature: ", k, ((TE-T0)/hist_steps*k+T0-
273.15), "--" ,((TE-T0)/hist_steps*(k+1)+T0-273.15)
          #hist[k] = hist[k] + 1
  results.append(map(int,hist)) # Save results for this enthalpy in
the array of results
```

```
#Results
#print results
print D298
part_ord = int(0.5+log10(particles))
devider = "+"+8*"-"+"+"+("-"*4+"+")*hist_steps+7*"-"+"+"
print devider
print "|Enthalpy"+"|",
for k in range(hist_steps):
  print "%3d|" %(k+1),
print "Filter|"
print devider

for j in range(dHastep+1):
  dHa = dHa1+(dHa2-dHa1)/dHastep*j
  line = results[j]
  print "|%8.1f|" %(dHa),
  for k in range(hist_steps):
    print "%3d|" %(line[k]),
  print "%6d|" %(line[k+1])
#  print "Enthalpy:",dHa,":",results[j]
print devider
```

B) Parameters used in the simulations

Page106, Figure 50:

Mass of the gas in amu: 28
Density of the gas in g/cm^3: 1.25
Pressure of the gas in bar: 1.32
Period of oscillation in 10^{-12} s: 0.2
Number of particles : 10000
Flow rate of the gas through column in cm^3/s: 10
Half-life of the nuclide in s: 60 / 35.6
Molecular weight of the substance in g/mol: 280 /281
Density of the substance in g/cm^3: 1.96
Length of column in cm: 191
Radius of column in cm : 0.1
Temperature of the column to start with in K: 293
Temperature of the column to stop with in K: 183
Number of steps in temperature: 14

Page 107, Figure 51:

For the Tc-isotopes:

Mass of the gas in amu: 28
Density of the gas in g/cm^3: 1.25
Pressure of gas in bar: 1.32
Period of oscillation in 10^{12} s: 0.2
Number of particles : 10000
Flow rate of gas through column in cm^3/s: 10
Half-life of the nuclide in s: 54.2 / 35.6 / 21.2
Molecular weight of the substance in g/mol: 243 / 246/ 247
Density of the substance g/cm^3: 2
Length of column in cm: 191
Radius of column in cm : 0.1
Temperature of the column to start with in K: 293
Temperature of the column to stop with in K: 183
Number of steps in temperature: 14

For Mo – isotopes:

Mass of the gas in amu: 28
Density of the gas in g/cm^3: 1.25
Pressure of gas in bar: 1.32
Period of oscillation in 10^{-12} s (0.2): 0.2
Number of particles : 10000
Flow rate of gas through column in cm^3/s: 10
Half-life of the nuclide in s: 67.5 / 8.4 /3.5
Molecular weight of the substance in g/mol: 279 /282 /283
Density of the substance in g/cm^3: 1.96
Length of column in cm: 191
Radius of column in cm: 0.1
Temperature of the column to start with in K: 293
Temperature of the column to stop with in K: 183
How many steps in temperature: 14

Page 108, Figure 52:

For ^{109}Rh:

Mass of the gas in amu: 28
Density of the gas in g/cm^3: 1.25
Pressure of gas in bar: 1.32
Period of oscillation in 10^{-12} s (0.2):
Number of particles : 10000
Flow rate of gas through column in cm^3/s: 10
Half-life of the nuclide in s: 80
Molecular weight of the substance in g/mol: 221
Density of the substance in g/cm^3: 2
Length of column in cm: 191
Radius of column in cm: 0.1
Temperature of the column to start with in K: 293
Temperature of the column to stop with in K: 183
How many steps in temperature: 14

For ^{109}Ru:

Mass of the gas in amu: 28
Density of the gas g/cm^3: 1.25
Pressure of gas in bar: 1.32
Period of oscillation in 10e-12 s (0.2):
Number of particles : 10000
Flow rate of gas through column in cm^3/s: 10
Half-life of the nuclide in s: 34.5
Molecular weight of the substance in g/mol: 249

Density of the substance in g/cm^3: 2
Length of column in cm: 191
Radius of column in cm : 0.1
Temperature of the column to start with in K: 293
Temperature of the column to stop with in K: 183
How many steps in temperature:14

Page 109, Figure 53:

Mass of the gas in amu: 28
Density of the gas g/cm^3: 1.25
Pressure of gas in bar: 1.32
Period of oscillation in 10^{-12} s: 0.2
Number of particles : 10000
Flow rate of gas through column in cm^3/s: 3.833
Half-life of the nuclide in s: 60
Molecular weight of the substance in g/mol: 272
Density of the substance in g/cm^3: 1.96
Length of column in cm: 65
Dimension of the column radius in cm: 0.135
How many values in result histogram: 13
Temperaturegradient form +23°C to -118 °C

Page 110, Figure 54:

Mass of the gas in amu: 28
Density of the gas in g/cm^3: 1.25
Pressure of gas in bar: 1.28
Period of oscillation in 10^{-12} s: 0.238
Number of particles : 10000
Flow rate of gas through column in cm^3/s: 8.333
Half-life of the nuclide in s: 60
Molecular weight of the substance in g/mol: 272
Density of the substance in g/cm^3: 1.96
Length of column in cm: 65
Dimension of column radius in cm: 0.2
How many values in result histogram: 13
Temperature gradient from +3 °C to -116 °C

Page 111, Figure 55:

Mass of the gas in amu: 28
Density of the gas in g/cm^3: 1.25
Pressure of gas in bar: 1.28
Period of oscillation in 10^{-12} s: 0.238

Number of particles : 10000
Flow rate of gas through column in cm^3/s: 8.333
Half-life of the nuclide in s: 21.2
Molecular weight of the substance in g/mol: 247
Density of the substance in g/cm^3: 2
Length of column in cm: 65
Dimension of column radius in cm: 0.2
How many values in result histogram: 13
Temperature gradient from +3.1 °C to -116 °C

Page 111, Figure 56:

Mass of the gas in amu: 28
Density of the gas in g/cm^3: 1.25
Pressure of gas in bar: 1.32
Period of oscillation in 10^{-12} s: 0.2
Number of particles: 10000
Flow rate of gas through column in cm^3/s: 3.833
Half-life of the nuclide in s: 21.2
Molecular weight of the substance in g/mol: 247
Density of the substance in g/cm^3: 2
Length of column in cm: 65
Dimension of column radius in cm: 0.135
How many values in result histogram: 13
Temperature gradient from 22.9 °C to -117.6 °C

Page 112, Figure 57:

Mass of the gas in amu: 28
Density of the gas in g/cm^3: 1.25
Pressure of gas in bar: 1.57
Period of oscillation in 10^{-12} s: 0.2
Number of particles: 10000
Flow rate of gas through column in cm^3/s: 8.33
Half-life of the nuclide in s: 11
Molecular weight of the substance in g/mol: 243
Density of the substance in g/cm^3: 2
Length of column in cm: 65
Dimension of column radius in cm: 0.2
How many values in result histogram: 7
Temperature gradient form +3 °C to 121°C

Page 113, Figure 58:

Mass of the gas in amu: 28
Density of the gas in g/cm^3: 1.25
Pressure of gas in bar: 1.28

Period of oscillation in 10^{-12} s: 0.238
Number of particles : 10000
Flow rate of gas through column in cm^3/s: 8.333
Half-life of the nuclide in s: 80 / 11
Molecular weight of the substance in g/mol: 221 / 223
Density of the substance in g/cm^3: 2
Length of column in cm: 65
Dimension of the column radius in cm: 0.2
How many values in result histogram: 13
Temperature gradient from +3 °C to -116 °C

Page 128, Figure 69:

Mass of the gas in amu: 16
Density of the gas in g/cm^3: 0.711
Pressure of gas in bar: 0.8
Period of oscillation in 10^{-12} s: 0.2
Number of particles : 10000
Flow rate of gas through column in cm^3/s: 14.17
Half-life of the nuclide in s: 2.75
Molecular weight of the substance in g/mol: 331
Density of the substance in g/cm^3: 2.65
Length of column in cm: 32
Dimension of side a in cm: 1
Dimension of side b in cm: 0.06
How many values in result histogram:32
Temperature gradient from +21°C to -112 °C

Page 129, Figure 71:

Mass of the gas in amu: 16
Density of the gas in g/cm^3: 0.711
Pressure of gas in bar (1.0): 0.8
Period of oscillation in 10^{-12} s: 0.2
Number of particles: 10000
Flow rate of gas through column in cm^3/s: 14.17
Half-life of the nuclide in s: 2.75
Molecular weight of the substance in g/mol: 332
Density of the substance in g/cm^3: 6
Length of column in cm: 32
Dimension of side a in cm: 1
Dimension of side b in cm: 0.06
How many values in result histogram: 32
Temperature gradient from +21°C to -112 °C

Page 130, Figure 73:

Mass of the gas in amu: 16
Density of the gas in g/cm^3: 0.711
Pressure of gas in bar: 0.8
Period of oscillation in 10^{-12} s: 0.2
Number of particles : 10000
Flow rate of gas through column in cm^3/s: 14.17
Half-life of the nuclide in s: 4.4
Molecular weight of the substance in g/mol: 332
Density of the substance in g/cm^3: 2.65
Length of column in cm: 32
Dimension of side a in cm: 1
Dimension of side b in cm: 0.06
How many values in result histogram: 32
Temperature gradient from +21°C to -112 °C

Page 131, Figure 75:

Mass of the gas in amu: 8.8
Density of the gas in g/cm^3: 0.39
Pressure of gas in bar: 0.8
Period of oscilation in 10e-12 s (0.2): 0.2
Number of particles: 10000
Flow rate of gas through column in cm^3/s: 13.67
Half-life of the nuclide in s: 2.75
Molecular weight of the substance in g/mol: 331
Density of the substance in g/cm^3: 2.65
Length of column in cm: 32
Dimension of side a in cm: 1
Dimension of side b in cm: 0.06
How many values in result histogram: 32
Temperature gradient from 12 °C to -115°C

Page 134, Figure 78:

Mass of the gas in amu: 16
Density of the gas in g/cm^3: 0.711
Pressure of gas in bar: 0.8
Period of oscillation in 10^{-12} s: 0.238
Number of particles: 10000
Flow rate of gas through column in cm^3/s: 12.17
Half-life of the nuclide in s: 6
Molecular weight of the substance in g/mol: 332
Density of the substance in g/cm^3: 2.65

Length of column in cm: 32
Dimension of side a in cm: 1
Dimension of side b in cm: 0.06
How many values in result histogram: 32
Temperature gradient from +14 °C to -150 °C

Page 135, Figure 80:

Mass of the gas in amu: 6.4
Density of the gas in g/cm^3: 0.29
Pressure of gas in bar: 0.73
Period of oscillation in 10^{-12} s: 0.239
Number of particles : 10000
Flow rate of gas through column in cm^3/s: 21.33
Half-life of the nuclide in s: 6
Molecular weight of the substance in g/mol: 332
Density of the substance in g/cm^3: 2.65
Length of column in cm: 32
Dimension of side a in cm: 1
Dimension of side b in cm: 0.06
How many values in result histogram: 32

Page 140, Figure 85:

Mass of the gas in amu: 16
Density of the gas in g/cm^3: 0.7145
Pressure of gas in bar: 0.75
Period of oscillation in 10^{-12} s: 0.2
Number of particles: 10000
Flow rate of gas through column in cm^3/s: 12.2
Half-life of the nuclide in s: 7.3
Molecular weight of the substance in g/mol: 310
Density of the substance in g/cm^3: 2.5
Length of column in cm: 32
Dimension of side a in cm: 1
Dimension of side b in cm: 0.06
How many values in result histogram:32
Temperature gradient from +12 °C to -109 °C

Page 141, Figure 87:

Mass of the gas in amu: 8.8
Density of the gas g/cm^3: 0.39
Pressure of gas in bar: 0.73

Period of oscillation in 10^{-12} s: 0.2
Number of particles: 10000
Flow rate of gas through column in cm^3/s: 18.13
Half-life of the nuclide in s: 7.3
Molecular weight of the substance in g/mol: 310
Density of the substance in g/cm^3: 2.5
Length of column in cm: 32
Dimension of side a in cm: 1
Dimension of side b in cm: 0.06
How many values in result histogram: 32
Temperature gradient form +12 °C to -112 °C

Page 143, Figure 90:

Mass of the gas in amu: 16
Density of the gas in g/cm^3: 0.711
Pressure of gas in bar: 0.94
Period of oscillation in 10^{-12} s: 0.239
Number of particles: 10000
Flow rate of gas through column in cm^3/s: 4
Half-life of the nuclide in s: 19.2
Molecular weight of the substance in g/mol: 312
Density of the substance in g/cm^3: 2.5
Length of column in cm: 32
Dimension of side a in cm: 1
Dimension of side b in cm: 0.06
How many values in result histogram: 32
Temperature gradient from +11 °C to -153 °C

Page 144, Figure 92:

Mass of the gas in amu: 8.8
Density of the gas in g/cm^3: 0.39
Pressure of gas in bar: 1
Period of oscillation in 10^{-12} s: 0.239
Number of particles: 10000
Flow rate of gas through column in cm^3/s: 13.67
Half-life of the nuclide in s: 19.2
Molecular weight of the substance in g/mol: 312
Density of the substance in g/cm^3: 2.5
Length of column in cm: 32
Dimension of side a in cm: 1
Dimension of side b in cm: 0.06
How many values in result histogram: 32
Temperature gradient from +16 °C to -147 °C

Page 145, Figure 94:

Mass of the gas in amu: 16
Density of the gas in g/cm^3: 0.711
Pressure of gas in bar: 0.99
Period of oscillation in 10^{-12} s: 0.239
Number of particles : 10000
Flow rate of gas through column in cm^3/s: 12.17
Halflife of the nuclide: 19.2
Molecular weight of the substance: 312
Density of the substance: 2.5
Length of column in cm: 32
Dimension of side a in cm: 1
Dimension of side b in cm: 0.06
How many values in result histogram: 32
Temperature gradient from + 11°C to -153 °C

Page 150, Figure 98:

Mass of the gas in amu: 8.8
Density of the gas in g/cm^3: 0.39
Pressure of gas in bar: 1
Period of oscillation in 10^{-12} s: 0.2
Number of particles : 10000
Flow rate of gas through column in cm^3/s: 9.1
Half-life of the nuclide in s: 12
Molecular weight of the substance in g/mol: 290
Density of the substance in g/cm^3: 3
Length of column in cm: 191
Radius of column in cm: 0.1
Temperature of the column to start with in K: 293
Temperature of the column to stop with in K: 183
How many steps in temperature: 11

Page 156, Figure 103:

Mass of the gas in amu: 8.8
Density of the gas in g/cm^3: 0.39
Pressure of gas in bar: 1
Period of oscillation in 10^{-12} s: 0.2
Number of particles: 10000
Flow rate of gas through column in cm^3/s: 9.1
Half-life of the nuclide in s: 9.2
Molecular weight of the substance in g/mol: 310
Density of the substance in g/cm^3: 2.5
Length of column in cm: 191

Radius of column in cm: 0.1
Temperature of the column to start with in K: 293
Temperature of the column to stop with in K: 203
How many steps in temperature: 9

Acknowledgements

Curriculum Vitae: